Synthesis, alignment, growth mechanism and functional properties of carbon nanotubes and their hybrid materials with inorganic and biomaterials

Dissertation von Ravi K. Joshi, M.S. aus Solapur, Indien
September 2010 — Darmstadt — D 17

TECHNISCHE UNIVERSITÄT DARMSTADT

Fachbereich Anorganische Chemie
Eduard Zintl Institut für Anorganische und Physikalische Chemie

Synthesis, alignment, growth mechanism and functional properties of carbon nanotubes and their hybrid materials with inorganic and biomaterials

Vom Fachbereich Chemie

der Technischen Universität Darmstadt

zur Erlangung des akademischen Grades eines

Doctor rerum naturalium (Dr. rer. nat.)

genehmigte

Dissertation

eingereicht von

M.S. Ravi K. Joshi

aus Solapur, Indien

Referent:	**Prof. Dr. Jörg J. Schneider**
Korreferenten:	**Prof. Dr. Christian Hess**
	Prof. Dr. Ulrich Simon (RWTH Aachen)
Tag der Einreichung	**06. September 2010**
Tag der mündlichen Prüfung	**01. November 2010**

Darmstadt - D17 2010

Dedicated to my parents,

(who spent their life for career of their kids)

to my beloved brother and soul love of my life

संगच्छध्वम् संवदध्वम् सम्वो मनांसी जानताम् ।

– ऋग्वेद ।

Sangacchadhwam, Samvadadhwam, Samvo Manamsi Jaanatham

– a sukta from Rigveda

(Let's walk together, let's speak the same language & let all this happen after knowing the each other's mindset)

(This sukta explains that, as objective of our work is same, lets talk over it, try to understand each other's point of view; put heart and soul into efforts so that a settlement could be reached amicably.)

Acknowledgment

I express my sincere gratitude towards **Prof. Dr. Jörg Schneider** for allowing me to be a part of his research group, offering me a fair work bench, his valuable time and closely following my work during the course of my doctoral thesis. I appreciate his constant motivation throughout this period and his support in professional as well as personal life.

I am indebted to **Dr. Jörg Engstler** and **Dr. Jayprakash Khanderi** for their invaluable time they gave in discussing various issues of my ongoing work. These discussions were of great importance to me from the aspect of experimental work, stimulating ideas and evaluation of the system. I am also thankful to both of them for their moral support in hard phase of this period, without which, it would have been difficult for me to arrive at this stage. Any amount I appreciate their help, it is not enough. Jörg shares extra gratitude for helping me to learn various characterization techniques.

I reserve my special thanks for **Dr. Oktay Yilmazoglu** for a cooperative work, lengthy discussions, and constructive ideas. I really enjoyed working with him. I am also thankful to **Christoph Nick** for a collaborative work. The work we carried out together added a new dimension to my thesis.

I take this chance to mention my cordial thanks to Deutsche Forschung Gemeinschaft (DFG, German Research Foundation) for financing my studies through the project.

I have my heartfelt thanks to many people for constantly rendering help during this research activity. Few names those I remember are, **Dr. Alexander Issanin** for XPS measurements, **Dr. Kathrin Hofmann** and **Jens Suffner** for XRD measurements, **Jens-Peter Biethan** for electrical measurements, **Dr. Stefan Lauterbach** for helping to learn and operate TEM, **Dr. Hergen Breitzke** for MAS-NMR measurements **Dr. Erwin Hildebrandt** for SQUID measurements, **Dr. Emanuel Ionescu** for raman spectroscopy and **Dr. Rudolf Hoffmann** and **Carina Vogel** for oximato work. I specially mention the name of my friend **Kamalpreet Kaur** who gave me bunch of silicon wafers to initiate this thesis work. I am thankful to couple of my friends **Dr. Jitendra Kumar, Sapthagireesh Subbarayan, Anuj Chopra** and **Rahul Kulkarni** from different parts of the world who patiently fulfilled my literature need.

During this Ph.D. tenure, I have really enjoyed my work in this group. I had enormous fun with almost every person of my group. It was my first cross cultural experience and I really found

my group mates warm and I never felt that I am anyway different from them. In particular **Dr. Mathias Nowotny, Hermann Tempel and Ildiko Balog** made my stay indisputably enjoyable. I enjoyed learning German from these Germans and understanding blunders I did while showing my speaking talent. These are unarguably few best moments of my life.

During this stay in Darmstadt, I really had joy to spend time and make trips with Rajeev, Parag, Atul and his wife Meghana. It was undoubtly wonderful experience with different experiments in the kitchen.

I am forever grateful to my parents and beloved brother for their understanding, moral support and continuous encouragement throughout my life. The secret of my success is hidden in the hard work they did to financially support my education. I feel myself fortunate to have such kind parents. Another strength of my life is Parisa, a soul love of my life. Over the last five years of my life, she is and will be the reason for my eternal happiness.

There is an active and passive role of many people who helped me to arrive at this milestone. I may have forgotten to mention their names, but the help they offered has certainly made a home in my heart.

Ravi K. Joshi

Abstract

Carbon nanotubes with unique properties are interesting materials for various sensors (gas, light, or bio), electrical devices (transistors, cold cathodes), catalysis, and energy related applications. However, the real hindrance in visualizing state of the art applications of CNTs is lack of a technique for selective and qualitative growth of CNTs at a predefined position. Also, in order to visualize various sensors and device architectures, CNTs alone will not suffice. CNTs structures need to be modified using other materials to develop new hybrid materials. The present work addresses the need of growth of qualitative CNTs, pinpoint their growth mechanism and methodologies to develop its hybrid materials.

Carbon nanotubes are synthesized using water-assisted chemical vapor deposition method (WCVD). Using this method, synthesis of crystalline, aligned, impurity-free, double walled CNTs of high aspect ratio ($\sim 10^6$) is achieved. Carbon nanotubes, as per need, are grown in vertical direction perpendicular to the substrate or even along the horizontal direction. A detailed study investigating different growth parameters in WCVD method is carried out to maximize the growth rate and quality of CNTs synthesized. Based on the experimental understanding, a conclusive growth mechanism elucidating the exact role of water as a catalyst activator is put forth. Also, a straight forward method to pattern the catalyst and thereby a possibility to achieve structured growth of CNTs is demonstrated.

Pristine CNT structures are modified using various metal oxides (ZnO, TiO_2, Fe_3O_4), platinum nano particles as well as nerve cells to form various hybrid materials. Deposition of metal oxides is carried out using various methodologies to obtain their nano particulate layers or thin films on CNTs. Platinum nano particles (2 to 4 nm) are deposited on 2D-aligned CNT film using self reduction technique for fuel cell applications. Additionally, different block structures of CNTs are used as a substrate to grow nerve cells. The selective growth of nerve cells on CNTs structures and inter bridging of CNT blocks are additional key points of this work.

Carbon nanotubes based devices such as field emission and field effect transistors are successfully realized. CNT based hybrid materials are tested for the potential applications such as modified field emission, super para magnetic applications, light sensors, fuel cells and gas sensors. Various other modules of CNT or its hybrid materials for are currently being tested for devices viz. photo catalysis, dye sensitized solar cells, magnetic actuators.

Contents

Abbreviations

AFM - Atomic force microscopy
CNT - Carbon nanotube
CVD - Chemical vapor deposition
DMF - Dimethyl formamide
DOS - Density of states
DWNT - Double walled carbon nanotubes
e-beam - Electron beam
EDAX - Energy dispersive analysis of X-rays
EELS - Electron energy loss spectroscopy
FE - Field emission
FET - Field effect transistor
FN - Fowler - Nordheim
FWHM - Full width half maximum
GDL - Gas diffusion layer
GIXRD - Grazing incidence x-ray diffraction
HiPCo - High pressure carbon monoxide
IR - Infra red
MAS - Magic angle spinning
MEA - Membrane electrode assembly in fuel cell
MEA - Multi electrode assembly
MEMs - Micro electro mechanical systems
MWNT - Multi walled carbon nanotube
NEMs - Nano electro mechanical systems
NMR - Nuclear magnetic resonance
PAOX - Porous aluminum oxide template
PBS - Phosphate based solution
PEG - Poly ethylene glycol
PEM - Proton exchange membrane
PL - Photo luminescence
PPM - Parts per million
RBM - Radial breathing mode
SAED - Selected area electron diffraction
sccm - Standard cubic centimeter per minute
SEM - Scanning electron microscope
STEM - Scanning in transmission electron microscope
STP - Standard temperature and pressure
SQUID - Super conducting quantum interface device
SWNT - Single walled carbon nanotube
TEM - Transmission electron microscope
TEP - Thermo electric power
TGA - Thermo-gravimetric analysis
TG-MS - Thermogravimetric - mass spectrometry
THF - Tetrahydrofuran
UV-Vis - Ultraviolet - visible
VLS - Vapor solid liquid
WCVD - Water assisted chemical vapor deposition method
XPS - X-ray photoelectron spectroscopy
XRD - X-ray diffraction

Symbols

a_1, a_2 - Unit vectors of graphene sheet

θ - angle

(n, m) - Two integers

d_t - Diameter of carbon nanotube

d_1, d_2, d_3 - Distance of diffraction points from equatorial plane

β - Field enhancement factor

ϕ - Work function of carbon nanotubes

I_{ds} - Current applied between source and drain

V_{ds} - Voltage applied between source and drain

V_g - Gate voltage

Oe - Ostered

H - External magnetic field

H_c - Coercivity

M_r - Remant magnetic field

Claim not perfection, perfection is divine. Aim at perfection to manifest in yourself divine, have confidence in your work & faith in divine, divine helps those who in themselves manifest divine.

1 Introduction

1.1 From the element carbon to carbon nanotubes

The carbon is sixth element in periodic table. It is found to have three allotropes, i.e. various stable forms, namely diamond, graphite and amorphous carbon. These allotropes show peerless qualities in terms of heat, electrical conductivity, transparent or absorbency, hardness or soft behaviour etc.

The carbon phase diagram depicted in a figure 1.1 shows various allotropes of carbon corresponding to varied value of pressure and temperature [1, 2]. At high temperature and high pressure sp^3 bonded cubic diamond is stable and while graphite at lower pressure and high temperature. Graphite constitutes of three in plane $sp^2(\sigma)$ bonds and one out of plane π bond. This creates the planar hexagonal network, in which each carbon atom is bonded with another 3 atoms, with bond length of 1.4 Å. Such hexagonal network is called as graphene sheet and many of such sheets are stacked parallel to each other following ABAB arrangement. Such stacking with ABAB arrangement is known as "Bernal stacking". The inter planar distance in Bernal stacking is 0.3354 nm.

If Bernal stacking (AB) is admixed profoundly with rombohedral (ABC) stacking arrangement, 'turbostratic graphite' is obtained. In it, stacking of graphene layer becomes irregular, increase in inter planar distance to a value as high as 0.3442 nm is observed. If crystalline disorder further increases, reducing thereby in plane ordering of graphene sheets, electronic properties of ideal 2D graphite will be modified giving rise to effective energy gap. Same structural changes

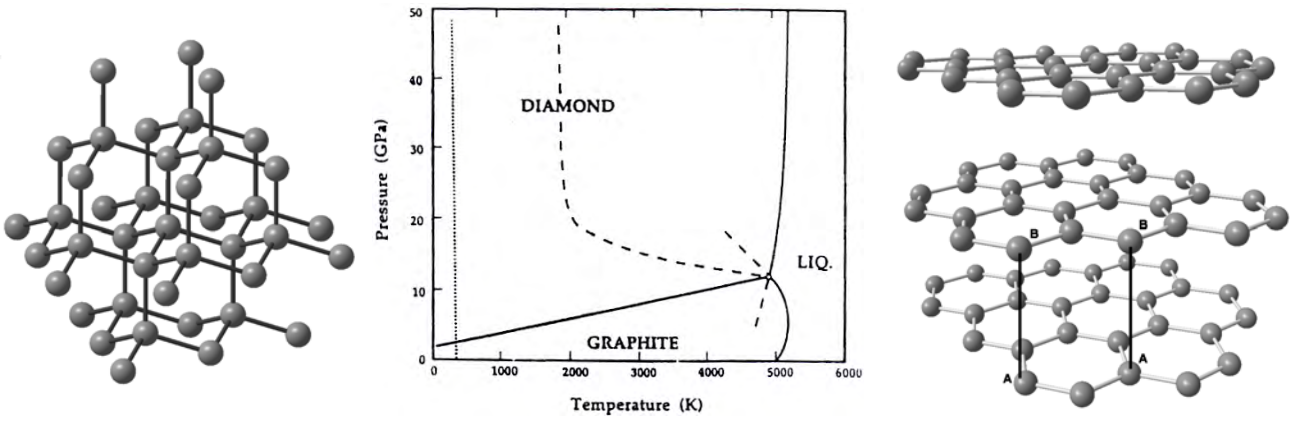

Figure 1.1: Pressure temperature phase diagram of element carbon [1,2] along with crystal structure of diamond(left) and graphite(right)

are partially visible in carbon nanotubes, which will be covered later in the text. The allotrope graphite is recently observed in various other forms explained below shortly.

Graphite whiskers consist of rolled up form of graphene sheet into scroll. It can be up to 3 cm long and 1 to 5 μm in diameter. Graphite whiskers are grown by arcing between two electrodes using direct current in high pressure (92 atm.) inert atmosphere. These whiskers exhibit great extent of crystalline nature, high electrical conductivity and elastic modulus setting a bench mark for performance of carbon fibers.

Carbon fibers are another important form of graphitic material and resembles more close to carbon nanotubes in terms of structures and properties. Carbon fibers have various morphologies such as 'onion skin' or 'tree ring'. After heat treatment at higher temperature (2500 to 3000 °C) structure resembles more close to graphite or even may develop facets on outer region. Typical carbon fiber diameter is ~ 7 μm and they can be very long, often bundled to form tows and then wound up as a continuous yarn on the spool.

Various forms of graphitic carbon are classified in figure 1.2 on the basis of their size. Among them carbon nanotubes and fullerenes are of nanometer size. These two allotropes of graphite have been discovered over last few decades. In year 1985, Herald Kroto together with Robert Curl Jr. and Richard Smalley awarded by noble prize for discovery of fullerenes. Thereafter, in year 1991, Sumio Iijima discovered carbon nanotubes [4].

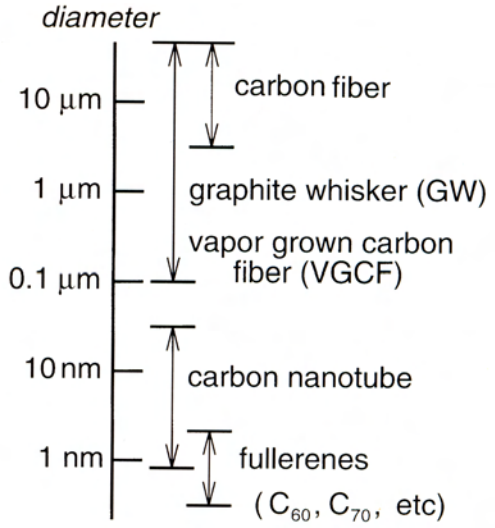

Figure 1.2: Comparison of diameters of various forms of graphitic carbon [3].

Carbon nanotubes (CNTs) are seamless hollow cylinder made up of sp^2 graphitic carbon. Circular curvature form results into quantum confinement leading to σ - π re hybridization causing σ bonds bending out of plane and π bond more delocalized outside the tube. As if graphite consists of many basal planes of carbon, CNTs also exists in single or many layers of such basal planes called graphene. If CNT consists of only one rolled in graphene layer, its called Single Walled (carbon) NanoTubes or SWNTs, DWNT for double walled and M for many walled in MWNTs. However, CNTs, due to their curvature, have neither AB stacking (Bernal Stacking) nor ABC stacking and thus gives a sense of turbostratic stacking as in graphite. On the other hand, existence of interlayer site correlations between carbon atoms in tubules, especially regarding the tubule axis, stacking is not completely turbostratic.

Properties of carbon nanotubes are based upon three of its important structural parameters; diameter, chirality, and handedness. Diameter is geometrical dimension of tubule, chirality is a angle with which honeycomb structure rotates along the axial length of CNTs as if thread on the bolt. As threads are left or right handed threads, chirality also posses left or right handedness. MWNTs are often metallic in nature, while SWNTs or DWNTs depending on their diameter and chirality can be metallic or semi conducting in nature. Carbon nanotube with known diameter can possess three different types of chirality as shown in the following figure 1.3b. Depending upon chirality, CNTs are classified into three following different types -

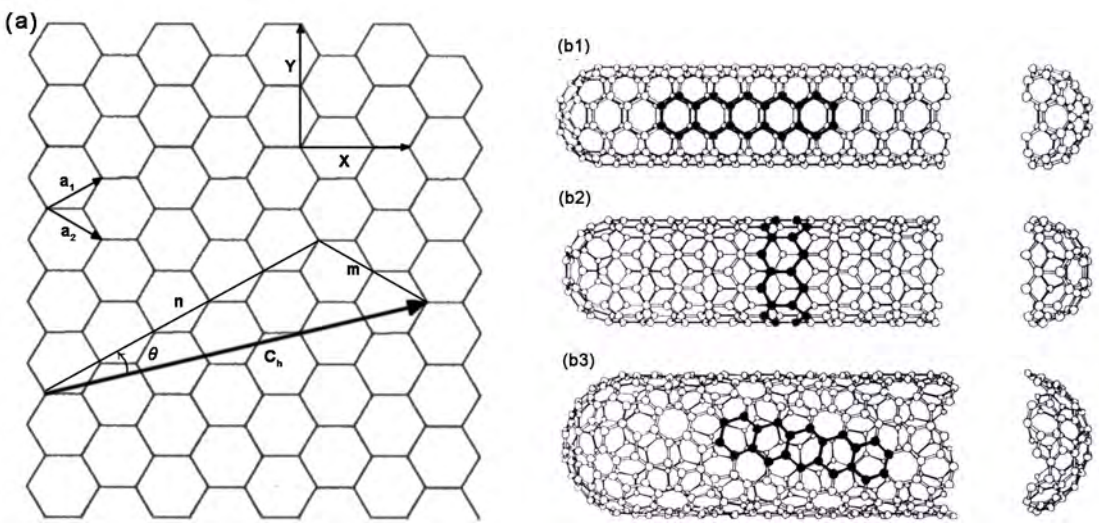

Figure 1.3: (a)Chiral vector representation on honeycomb lattice of carbon atoms along with unit vectors $\overline{a}_1$, $\overline{a}_2$ and schematic models of carbon nanotubes; (b1) armchair type (b2) zigzag type (b3) chiral type CNT

1. Arm chair (n=m, & $\theta = 30^\circ$)
2. Zigzag (n,0 & $\theta = 0^\circ$)
3. Chiral (n,m & $\theta = 0$ to 30°)

These three types can be easily distinguished on the basis of orientation of the carbon-carbon bond with respect to the axis of the tube, often called needle axis of the nanotube. This orientation is reflected in the value of the chiral angle (θ), as shown in figure 1.3a. In first two types, at least one carbon-carbon bond of hexagon array will be either parallel or perpendicular to the axis of the nanotube or the needle axis. The chirality displayed by a CNT is often denoted by two integers placed within parenthesis (n, m). Based on the values of n, m, it is possible to determine if the nanotubes are of the armchair type, or zigzag type, or chiral type. CNTs having carbon-carbon bond perpendicular to needle axis are called armchair nanotubes, designated as (n, n) nanotubes and their chiral angle (θ) equals 30°. Zigzag nanotubes have chiral angle $\theta = 0^\circ$ with carbon-carbon bond parallel to needle axis and are designated as (n, 0) nanotubes. Chiral nanotubes have a chiral angle between 0 to 30°, with (n, m) designation. In armchair nanotubes, hexagonal arrays are aligned along the needle axis, while in zigzag it is perpendicular to it. It follows spiral path in chiral nanotubes with lead angle exactly equal to the chiral angle. These three structures are depicted in figure 1.3b with highlighted part of honeycomb structure. Perimeter of carbon nanotube is expressed in terms of chiral vector using two unit vectors, $\overline{a}_1$ and $\overline{a}_2$, (see fig 1.3a) of the hexagonal honeycomb lattice of graphene sheet.

$$C = n\overline{a}_1 + m\overline{a}_2 \tag{1}$$

Diameter (d_t) and chiral angle (θ) of CNT can be measured using following equations.

$$d_t = \sqrt{3}a_{c-c}(m^2 + nm + n^2)^{1/2}/\pi \tag{2}$$

and

$$\theta = \tan^{-1}[\sqrt{3}n/(2m + n)] \tag{3}$$

.....a_{c-c} is carbon-carbon bond length

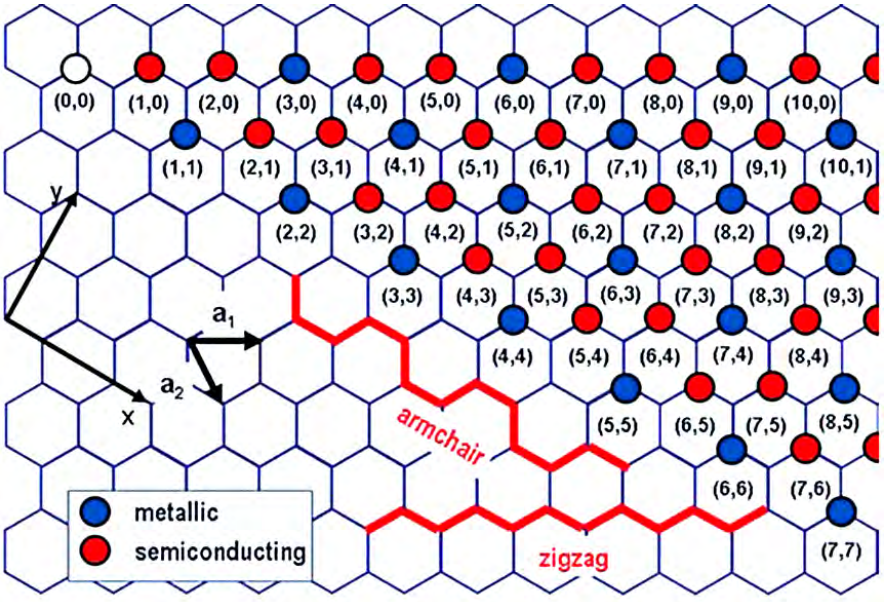

Figure 1.4: Schematic elaborating possible (n,m) integer permutations and tendency of forming semi conducting or metallic nanotube as per equation n-m = 3q [5].

Depending upon the band crossing calculations, a carbon nanotube will be metallic if,

$$n - m = 3(q) \tag{4}$$

.....Where q is any integer

This gives the probability that at least two third of carbon nanotubes can show semi conducting behaviour and one third metallic. Also, as per this equation, the small diameter SWNTs will predominantly behave semi conducting. This is because, for such small diameter, chances that the difference between n and m will be multiple of three are low. In figure 1.4, a scheme is elaborated in order to visualize possible combinations with n,m integers on graphene plane. From equation (4), every armchair type CNT will behave metallic in nature and zigzag and chiral depending upon their tube diameter and chirality. The band gap of 1 nm wide semi conducting tube lies in range of 0.7 to 0.9 eV. This is experimentally confirmed using STM measurements [6]. Inter tube coupling needed to be considered in case of SWNT rope, synthesized in arc discharge or in case of MWNTs. It induces small band gap in certain metallic tubes and reduced band gap by 40% semi conducting tubes in a SWNT rope.

Apart from its atomic structure, carbon nanotube have further different morphologies. Single, double or multi walled carbon nanotubes have already been defined before. In addition to

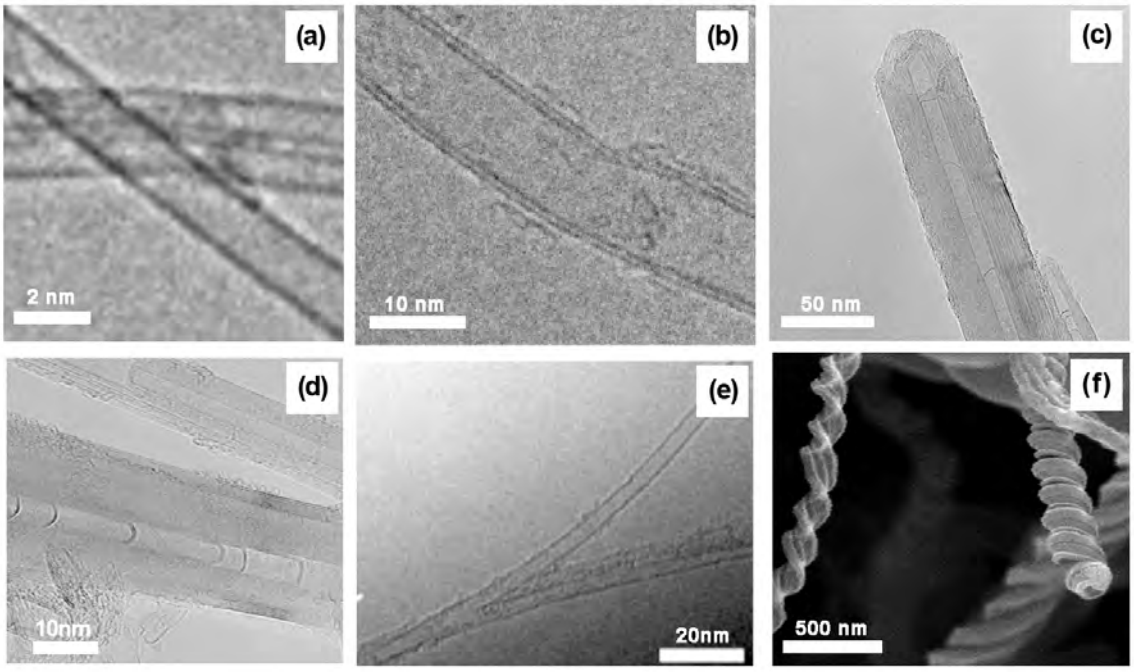

Figure 1.5: Electron micrographs of various possible morphologies of carbon nanotubes, (a) SWNT [7] (b) DWNT (c) MWNT (d) bamboo structured CNT (e) Y-junction CNT [8] (f) coiled CNTs.

them, coiled carbon nanotubes, Y-junction nanotubes, truncated or bended junction, bamboo structured CNTs are rigorously studied (see fig.1.5).

In order to generate such complex morphologies, change in the direction within the graphene film is demanded. This change in direction can not possibly be achieved just by bending a honeycomb structure. Such change in direction as drastic as 90° turn can be achieved by inserting penta or heptagonal ring or rings replacing hexagonal ring in honeycomb structure at requisite location. Pentagonal defects gives rise to positive curvature (bending in) and heptagonal are responsible to negative curvature (bending out). Such defects are called 'topological defects'. In the figure 1.6, a schematic helps to visualize how the topological defects bring in curvature change in a graphene sheet. Removing one C-C bond, and there by triangular area marked black,(as shown in figure 1.6a) from the central hexagonal ring forces the film to bend in a dome like hemispherical cap as shown in figure 1.6b. Presence of such disinclination leads to large strain in folded graphene sheet, resulting large increase in energy of the system. If it is done in reverse manner, i.e. instead of removing if we add a extra C-C bond in hexagon, additional plane, equivalent to triangle explained before, is added to system resulting in outwards bending of the film, giving negative or concave curvature. Pentagon and

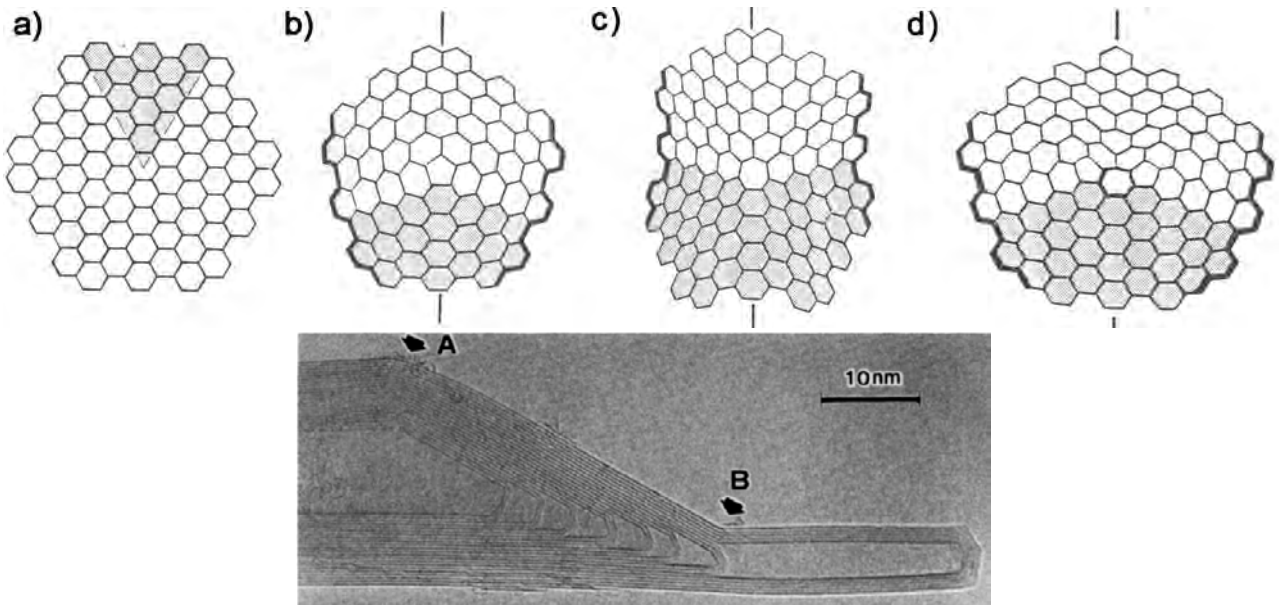

Figure 1.6: (a to d) Schematic elaborating the effect of penta or heptagon rings on the curvature of a carbon nanotube and representative TEM micrograph of CNT showing both defects [11].

heptagon seating aside each other often neutralizes the effect. In figure 1.6e, position marked by 'A' and 'B' are result of pentagon and heptagon insertion in the graphene film. If these topological defects are inserted in SWNTs or semi conducting nanotubes, intra molecular single electron transport devices can be miniaturized [9, 10].

Since after discovery in year 1991, carbon nanotubes have been exotically studied. The reason lies in wide spectrum of properties that CNTs displays. Below, a perspective of the exceptional properties of CNTs and applications based on them is given in brief.

1.2 Properties and potential applications of carbon nanotubes

1.2.1 Mechanical properties of CNTs

Carbon nanotubes show exceptional mechanical properties. A comparative summary of various type of CNTs is listed in table 1.1. These values were experimentally calculated using various characterization tools [12–14]. CNTs have not only high mechanical strength but also they have highly elastic behaviour. Falvo et. al. have bend the CNT using AFM tip to an angle of about 180° and upon release, MWNT acquires back its original configuration. Most of the hard material, cant sustain strain more than 1% and fail. CNTs, however, can sustain upto 15% tensile strain before fracture [15].

Table 1.1: Mechanical properties of carbon nanotubes in comparison to steel. [6]

CNT Type	Young's Modulus (GPa)	Tensile Strength (GPa)	Density (g/cm^3)
MWNT	1200	~150	2.6
SWNT	1054	75	1.3
SWNT bundle	563	~150	1.3
Graphite (in plane)	350	2.5	2.6
Steel	208	0.4	7.8

Carbon nanotubes can be utilized well due to their nano shape in building micro or even nano electromechanical systems(MEMs or NEMs). Using source, drain and gate structure made up of CNT blocks or film itself, one can fabricate an actuator or arrays of them [16]. High frequency resonators have been fabricated out of SWNTs [17]. Being good conductor of heat and electricity, CNTs can be employed as a reinforcement for preparing conducting polymer composites [18, 19]. CNT composites with proper binding matrix material have been tested as an electro or even photo actuator [20, 21].

Although CNTs considered as a ideal reinforcement for composite materials as they exemplify unique strength and elastic properties in a way elastic modulus of CNTs is considered far better than ideal graphite fibers; the real challenge is to maximize the utilization of CNT strength in a composite. It can be achieved by developing good interface between the matrix material and reinforced CNTs. Functionalizing the side walls of CNTs using long chain polymer secures good bondage with matrix material and there by a high strength composite can be visualized [22–24].

1.2.2 Electrical properties of CNTs

Carbon nanotubes are considered as an answer to the technological hurdles the present semiconductor industry might face in coming decade. Small size and highly symmetric structure allow remarkable quantum effect and enhanced electronic properties. CNTs with small tube diameter, specifically SWNTs, predominantly behave semi conducting. Their band gap is diameter dependent, and is 0.8 eV for 1 nm diameter tube.

The density of states (DOS) for CNTs can be easily calculated without considering small band gap effect following an approach of Mintmire and White [25]. The DOS is 4 fold smaller for CNTs than that of metals which should normally result in bad conductivity. However, one dimensional

nature results in huge free path of order 1-10 μm contrast to 40 nm for copper. The measured lowest possible resistance of SWNT is $\sim$ 6.5 kΩ. The measured resistance of CNT is strongly dependent upon the contact miniaturization [26].

Individual SWNTs considered for fabricating transistors, memories, logic devices [27–29] while DWNT or MWNTs are considered for manufacturing stable field emission devices. Major advantages of CNTs as a material for cold cathode emission are high electron mobility and stronger field enhancement effect. Thus for field emission displays, CNTs seems to be a promising candidate. A model of colored field emission display is already manufactured by Samsung company [30]. Not just SWNTs, Y-junction CNTs, sharp bends generated in CNT structure due to topological defects, have been studied for nanoelectronics devices [10]. Other promising applications of carbon nanotubes are gas sensors, batteries, fuel cells, super capacitors etc. [31–33].

1.2.3 Thermal conductivity of CNTs

Carbon nanotubes have reported high thermal conductance, as high as $\sim$ 3000 W/m-K (for single MWNT), surpassing that of diamond ($\sim$ 2000 W/m-K) [34]. For SWNTs, this value is in range of 200 to 6000 W/m-K. Thermal conductance depends upon quality of CNT, diameter distribution, alignment etc. Thermal conductivity in CNTs is uni dimensional as if electrical conductivity. Therefore in metallic CNTs, heat is carried away via electrons as well as phonons. However, heat conduction via phonons is predominant [35]. For purely ballistic phonon transport, thermal conductivity (λ_{ph}) behaves linearly with respect to tube length. It follows the power law behaviour ($\lambda_{ph} \propto L^{\alpha}$) if length (L) is bigger than 100 nm and exponent α is estimated to value of 0.25 at 300 K [36].

Thermal contact resistance effectively reduce the thermal conductivity of CNTs [37]. Thermal boundary resistance of CNTs in contact with various metals and polymers has been measured [38]. Surprisingly, CNT-polymer junction or boundary resistance is found to be lower than CNT-metal contact resistance. It is suggested that, lower phonon transmission coefficient at metal-CNT interface is responsible for such behaviour. Efforts have been put forth deduce experimental values for 'thermo electric power' (TEP) for CNTs. When bias is applied across the CNT axis, temperature gradient will develop across its length through joule heating. Room

temperature TEP values reported for SWNT and MWNT are 280 μV/K and 80 μV/K respectively [35, 39].

1.2.4 Optical properties of CNTs

Defect free SWNTs offer a direct band gap, ideal for optical and optoelectronic applications. Optical spectra of individual SWNTs have been already established using Raman, UV-VIS-IR spectroscopy. In addition, experiments demonstrating electrically induced optical emission [40, 41] and photo detection effect [42] in infra red region by SWNTs are carried out. Unlike conventional solid state optoelectronic devices, SWNT can emit light upon injecting electrons and hole from either side of contacts. Light emission in the range of 600 to 1000 nm wavelength for aligned SWNTs is successfully demonstrated [43]. Recently, the electro luminescence from SWNT built in transistors [44] and photo voltaic effect in junction between n-doped gallium arsenide and carbon nanotubes was reported [45].

1.2.5 Other important properties of CNTs

CNTs exhibit strong sensitivity against chemicals and different gases. This make them a potential candidate for chemical and biological sensors. In order to calibrate their response, change in electrical properties, such as resistance, current flux can be easily measured. This makes CNTs a potential candidate for chemical, biological sensors or detectors.

Large specific surface area can be utilized for energy applications viz. hydrogen storage, lithium ion batteries etc. Same is optimal for catalyst support in various catalyst processes and also ideal material for fuel cell applications. Nitrogen doped CNT arrays are successfully tested for oxygen reduction activity [46]. For CNTs, enhanced molecular adsorption and charge transfer was observed even at room temperature. This can be utilized in catalysis, sensing applications. Small diameter CNTs have ability to reduce noble metals from their salt solutions without supply of any external energy (such as UV illumination) [47]. The phenomenon takes place as CNT/Au^{3+} or CNT/Pt^{2+} form redox pair as if zinc metal against copper ions in a galvanic cell.

CNTs show characteristic bio-compatibility and many investigations have taken place to study how biological cells behave in vicinity or in contact with CNTs [48, 49]. Parallely preliminary studies are undergoing to investigate potential of CNTs in drug delivery system. CNTs are

comparatively less explored in concern to biological applications although deposition or growth of biological material (DNA, RNA, nerve cells, peptides etc.) on CNTs is picking up the pace. Free standing CNT films show extraordinary behaviour to adhere foreign substrates using Van der Waals interactions. Such behaviour can be used to mimic artificial gecko feet [50].

1.3 Methods for synthesizing carbon nanotubes

While working with arc discharge setup, accidental discovery of carbon nanotubes by Iijima gave a new dimension to graphitic carbon material [4]. Within few years after the discovery, two new methods namely laser ablation [51] and chemical vapor deposition (CVD) method [52] have been introduced. First two methods are high temperature methods, while CVD operates at relatively lower temperature. These three methods are explained below along with their merit and demerits.

1.3.1 Arc discharge method

In this method arc is struck between two electrodes made up of graphite rods. The anode is typically smaller in size than the cathode, is a consumable electrode, and is often stuffed with a catalyst. Arc is struck using a DC power supply providing $70 - 150$ A current and voltage in the range of $20 - 40$ V. A schematic of the experimental setup is shown in figure 1.7. The anode, consisting of graphite and catalyst, is evaporated and deposited on the cathode surface

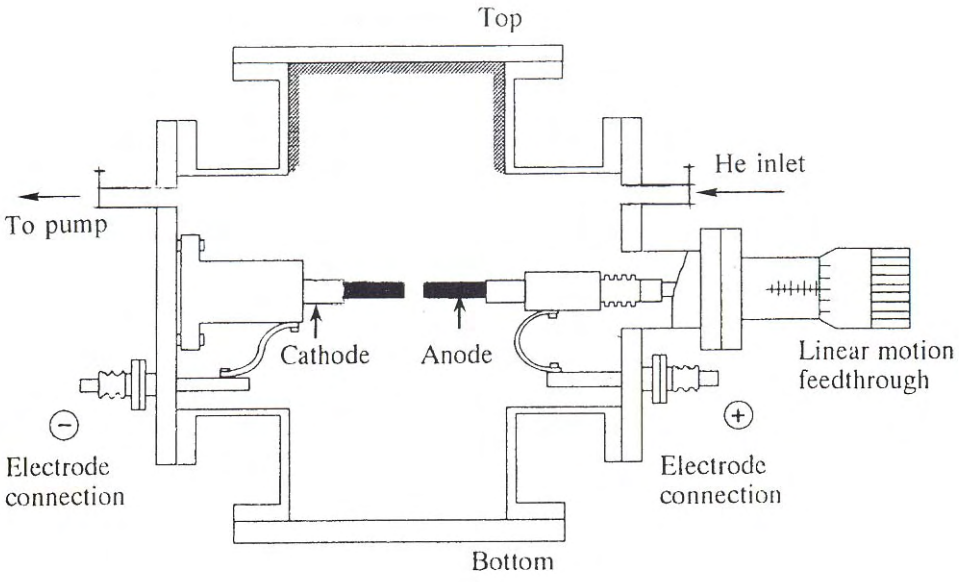

Figure 1.7: Schematic of arc discharge setup [53].

and the deposit produced contains carbon nanotubes [54, 55]. Typically, the arcing is carried out under a controlled atmosphere consisting of either argon, or helium [56], or methane [57] or nitrogen [58]. Of these, helium atmosphere is most frequently used, typically at 500-600 Torr. This version of the arc discharge method is the conventional approach for production of single walled and double walled CNTs and may result in the formation of bundles of single walled nanotubes [59]. In the arc discharge process, plasma temperature plays a vital role in quality of CNTs deposited at cathode end. The arcing current, gaseous atmosphere used, and a gap between two electrodes are few important experimental factors which control the plasma temperature. Concave shape of anode end after arcing, indicates that a high temperature zone exists in the central area of the anode and may lead to sintering of the CNTs produced.

1.3.2 Laser ablation method

In this method, a metal-graphite composite rod is evaporated with the help of a high intensity laser which results in the formation of SWNTs. A schematic of the experimental setup is shown in figure 1.8. A typical 10 ns duration, 300 mJ laser pulse evaporates the target in the presence of argon gas preheated to 1200 °C [60]. The surface temperature of target rises up to 6000 °C when struck by the laser beam, carbon vapor formed near the target surface expands with supersonic velocity to detach and propagate through the background gas. The initial carbon vapor consists of C_2 and C_3 species [53]. These carbon species get condensed or deposited on pre structured substrate growing into CNTs. In the buffer gas, the carbon vapor in combination with metal ions, called a 'plume', cools down, forming SWNTs. Maximum yield of nanotubes

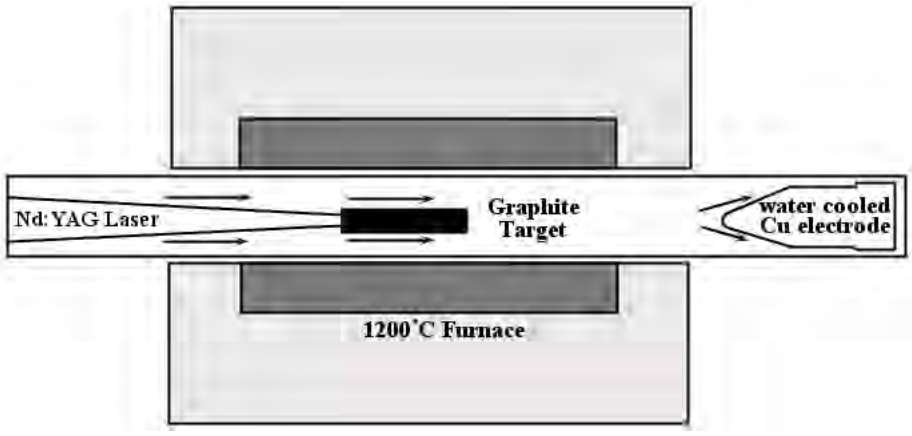

Figure 1.8: Schematic of laser ablation setup.

was obtained with a furnace temperature of 1200 °C, while no SWNT formation was observed below 800 °C and above 1300 °C. Argon gas flow in the laser reactor also influences SWNT yield due to the temperature decrease that can be caused by high velocity of argon.

1.3.3 Chemical vapor deposition method

Chemical vapor deposition method (CVD) is comparably low temperature method in which carbon source is thermally decomposed to produce the carbon species and ultimately CNTs. This process can be driven using a template or a substrate and with or without usage of catalyst. A variety of carbon precursors are used in this process, few popular among them are hydrocarbons such as methane, ethane, propylene etc, or organic solvents xylene, pentane, heptane etc., [61] or even carbon monoxide [62]. Transition metals having limited carbon solubility such as iron, cobalt, nickel or metallocenes and carbonyl complexes of these metals are often used as catalyst. A substrate (Si-wafer, quartz glass, metal foils) or a template (anodized aluminum oxide template) is inserted inside a tubular oven and heated to the desired temperature under inert atmosphere. The CVD temperature varies upon selection of precursor, however good quality CNTs are generally synthesized in range of 700 to 1300 °C. At desired temperature, a mixture of various gases, mostly argon or helium, mixed with hydrogen, carbon source and catalyst if its in chemical form, is introduced into the oven at a predetermined rate. Finally, the oven is cooled down to room temperature under insert atmosphere. Quality of CNTs produced in this method is strongly process dependent. A schematics of CVD setup is as shown in figure 1.9. Below, few important CVD methods are explained in short.

The high pressure carbon monoxide process, also known as HiPCo is one of the excellent methods to grow high quality CNTs [62]. In this process carbon monoxide gas along with iron pentacarbonyl [$Fe(CO)_5$] is pumped through a small nozzle hole in an oven, previously heated to 1100 to 1300 °C. Iron complex cracks to produce smaller iron nanoparticles, which then react with gas to grow carbon nanotubes. As size of iron nanoparticle obtained in this process is very small, preferably single walled CNTs are synthesized.

Template assisted process is another method in which, carbon nanotubes are synthesized in side nanopores of porous aluminum oxide (PAOX) template. PAOX template is synthesized by electro-oxidation of aluminum plate in acidic bath leading to formation of nanopores in aluminum (see figure 1.9) [63]. Hydrocarbon gas is decomposed inside these nanopores, and

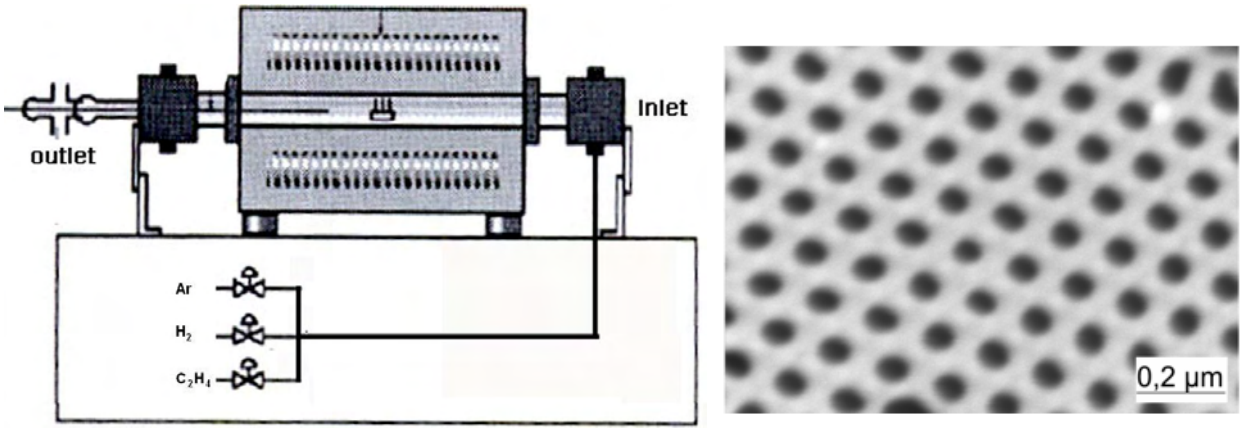

Figure 1.9: Schematic showing standard experimental setup used in chemical vapor deposition method. Beside it, a SEM micrograph of porous aluminum oxide template used in same method to grow CNTs [53, 65].

carbon in form of graphitic layers is deposited on the side walls of these nanopores [64]. CNTs can be grown with the help of proper metal catalyst, however its not mandatory. After CNTs synthesis, the template is etched away using concentrated hydrofluoric acid. This method has unique advantage that it delivers highly ordered CNTs, however they are often multi walled, less graphitic and includes high level of defects.

Chemical vapor deposition using hydrocarbon gas, metal catalyst and a substrate is often used method for growing carbon nanotubes. This method is explored by manipulating various growth parameters, chemicals, synthesis temperature, gas flow rates in order to produce good quality CNTs. In this process, carbon species generated in gas phase are dissolved in the catalyst, until it saturates. This process is termed as "Vapor Liquid Solid" (VLS) process. (hydrocarbon vapor, carbon-metal liquid, crystalline carbon solid) [5]. In this method, catalyst deposited substrate is heated to CVD temperature under controlled inert atmosphere. At desired temperature, growth of CNTs take place by decomposition of hydrocarbon in presence of different gases.

Although this method produces good quality of carbon nanotubes, relatively free from catalyst and highly graphitic in nature, still a broad distribution of CNT diameters and control over their typology were problems to be resolved. The answer to these problems is modified version of CVD method called "Water assisted chemical vapor deposition" method. This method is discussed in detail in upcoming part of thesis. Figure 1.10 shows the time line of evolution of various methods employed for synthesis of carbon nanotubes after their initial discovery in year 1991.

Arc discharge **1991** [4]	Laser ablation **1996** [51]	CVD method **1996** [52]	HiPCo process **1999** [62]	Alcohol CVD **2002** [66]	Water assisted CVD **2004** [7]	Low temp. CVD **2006** [67]

Figure 1.10: A time line showing evolution of important methods for synthesis of CNTs right from the discovery till today.

Water assisted chemical vapor deposition (WCVD) method is a unique way to grow carbon nanotubes up to a millimeter length. This gives CNTs an aspect ratio of an order $\sim 10^6$ to 10^7. WCVD is a modified version of the normally used chemical vapor deposition method explained above. During the growth phase, along with mixture of hydrocarbon, argon and hydrogen gas, a small amount of water vapor is supplied. The change is minute but very important in order to keep the catalyst active for longer time, to make sure growth will continue for longer duration. Water is proposed to be a weak oxidant, cleaning and preserving the catalyst active. Using proper amount of water, growth rate as high as 2.5 mm in ten minutes has been achieved. By engineering the iron catalyst used in this process, one can fine tune the diameter or even typology of CNTs grown. A number of research groups have demonstrated growth of single, double and multi walled CNTs growth using this method [7, 68]. A patterned growth of CNTs at a required place in order to miniaturize the engineering devices is made possible with this technique.

1.4 Methods for characterizing carbon nanotubes

Various classical methods used to characterize CNTs are listed below and some of the aspects associated with characterizing CNTs using these techniques are highlighted.

1. Raman spectroscopy
2. Scanning electron microscopy
3. Transmission electron microscopy
4. atomic force microscopy
5. X-ray diffraction
6. Thermo-gravimetric analysis

1.4.1 Raman spectroscopy

This characterization tool is a non destructive method for characterizing CNTs. It can give qualitative as well as quantitative information about the CNTs obtained using various methods. A typical plot obtained using Raman spectroscopy on a sample containing carbon nanotubes, is shown in figure 1.11. As per literature [69, 70], presence of graphitic structure leads to the existence of a 'G band peak', in between 1580 to 1590 cm^{-1} wave numbers. Dangling or defect band peak, 'D', is sensitive to incident laser energy and can be seen in between 1340 to 1350 cm^{-1}, if sample is excited by 514 nm argon laser. The first over tone of D band, often called G' band found between 2450 to 2650 cm^{-1} and combination of D and G band is found in between 2775 to 2950 cm^{-1}. Radial breathing mode peaks (RBM), corresponding to the diameter of single walled nanotubes, are found at wavenumber below 200 cm^{-1}. [69]. Rao and his coworkers in year 1997 [70] studied a range of wavelengths and observed an inverse relationship between diameter of SWNTs (d_t) and the wave number scattered (ω_{RBM}) corresponding to the radial breathing mode peak. The equation for inverse variation is given by

$$\omega_{RMB} = \frac{A}{d_t} + B \tag{5}$$

.....Where A and B are constants

Further work to determine the constants A and B, was carried out by various research groups using different modeling methods. The values of A and B reported in the literature have minute error and widely accepted. The value of A = 224 [71] or 227 [72](with 'd_t' in nanometers) for SWNT and A = 234 and B = 10 cm^{-1} for bundle of SWNTs [73]. The up shift of frequency is observed normally due strong inter tube Van Der Waals interaction. Filho and his co workers [74] have studied G' band peak for SWNTs. They have observed two peak structure in some special raman spectra for SWNTs. However typically, only one peak was found at approximately twice the wavenumber corresponding to the D band (1350 cm^{-1}) peak. Polarized raman [75], surface enhanced raman [76], and z-breathing raman spectroscopy studies are some of the recent studies being carried out in this context.

From a utility point of view, Raman spectroscopy can be used to calculate diameter of SWNTs present, while ratio of D band (I_D) and G band (I_G); I_D/I_G gives approximate indication of

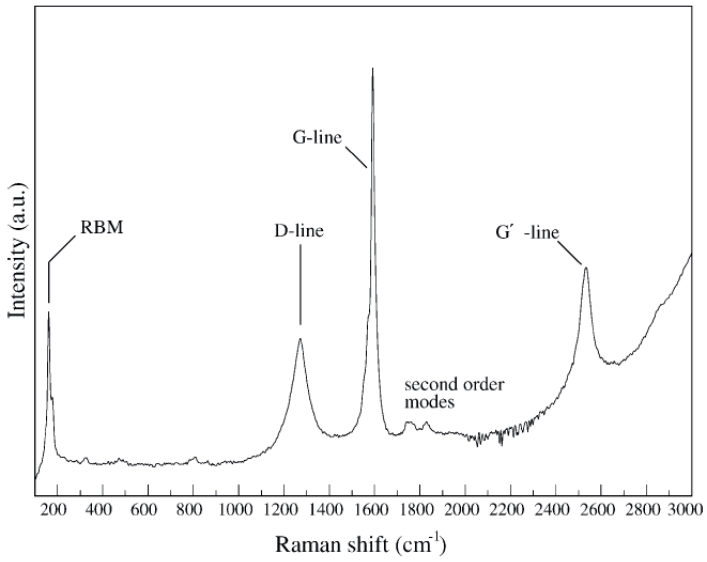

Figure 1.11: Raman spectroscopy of graphitic carbon nanotubes [69].

quality of nanotubes soot. Smaller the ratio; higher is crystalline nature of CNTs and thus smaller will be the defect level. Also raman spectroscopy is used to study oxidation of soot, and hence used as a tool to investigate effectiveness of purification techniques.

1.4.2 Transmission electron microscopy (TEM)

This is an important tool in the field of nano science and for the study of CNTs as well. Ever since the discovery of CNTs [4], extensive study of this nano structured material has been carried out using the TEM. Reciprocal space representation and a typical diffraction pattern obtained from CNTs, is shown in figure 1.12a. Sp^2 hybridized graphite shows hexagonal diffraction pattern and since CNTs are made up of curved sp^2 hybridized graphene plates, it has same hexagonal diffraction pattern similar to HOP graphite first elaborated by Iijima [4]. The diffraction pattern contains (hk0) spots and (002) spots in the radial direction. The number of sets of these (hk0) spots and (002) spots varies according to chirality and number of walls of carbon nanotubes (single, double or multi walled) for which diffraction is taken. The top and bottom part of any chiral nanotube will have honeycomb pattern differing by angle 2θ or twice the 'chiral angle' present in hexagonal arrays. The diffraction pattern will therefore consist of double hexagonal patterns separated by twice the chiral angle measured at the center spot formed by the transmitted beam. In case of achiral nanotubes, i.e. armchair or zigzag type of carbon nanotubes, these two hexagonal patterns will superimpose on each other giving only one set

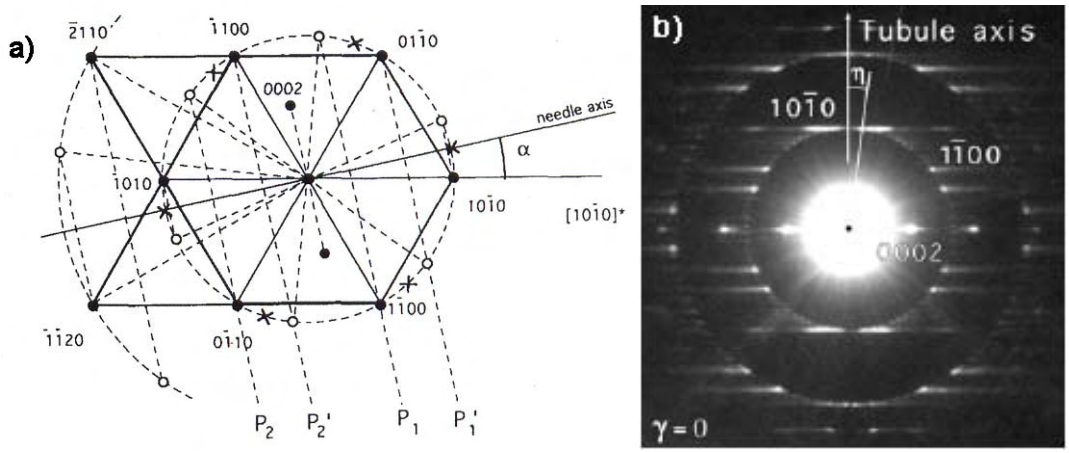

Figure 1.12: (a) Schematic showing reciprocal space construction for a carbon nanotube [78], (b) showing real time diffraction pattern of multi walled carbon nanotube [79].

of spots. A computer generated SAED images for zigzag, armchair and chiral nanotubes are as shown in figure 1.13 [77].

In the year 1994, Liu and Cowley, published their work on TEM analysis of different types of multi walled CNTs with different wall sizes. The relationship between helicity and geometry of nanotubes was also explained [80]. Diffraction pattern and evidence of polygonal multi walled nanotubes were also indicated them. Zhang et. al. studied CNTs with TEM with particular reference to helical diffraction pattern. They explained the geometry of the diffraction with the help of reciprocal lattice and a detailed analysis of the diffraction planes (fig 1.13b). Angular relations and tilt effect calculations were precisely worked out [78]. A practical method to determine handedness of carbon nanotubes has been proposed in year 2005 by Liu and Qin [81] When carbon nanotube is twisted, spacing of diffraction layer lines (marked by P1, P2, P1' and P2' in fig 1.12a) will change. Thus, the ratio of layer line spacing can be correlated with known angle of twisting to evaluate handedness of carbon nanotube.

A method to calculate helicity or chirality along with handedness of CNTs was also explained [82]. Another simple but effective method to calculate helical angle of hexagonal arrays was identified by Gao et. al. group [83]. Chiral angle was measured with the help of "equation (6)" and by measuring distances of diffraction spots from the equatorial plane (see figure 1.13b) and also diameter of nanotube by equatorial oscillations. Cowley et. al. studied SWNTs bundles for chirality with dark field imaging and found that most of the tubes in bundles produced with laser ablation showed no chirality or same chirality [84].

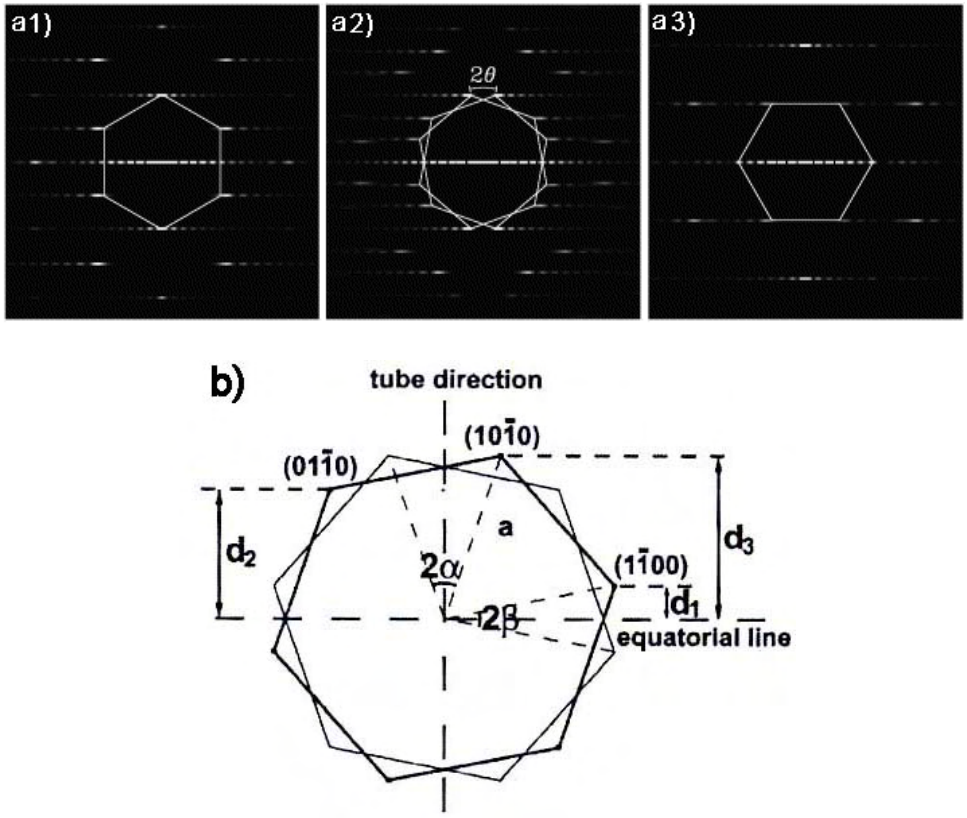

Figure 1.13: Computer simulated diffraction pattern for (b1) zigzag type (19,0),(b2) chrial type (17,4) & (b3) armchair (10,10) type CNTs [77] and (b) Schematic showing diffraction pattern of SWNT. Two hexagonal rings represent first order $(10\bar{1}0)$ reflections from top and bottom of carbon nanotube [83].

$$\theta = tan^{-1}\left[\frac{1}{\sqrt{3}} \times \frac{(d_3 - d_2)}{d_3}\right] \qquad OR \qquad \theta = tan^{-1}\left[\frac{1}{\sqrt{3}} \times \frac{(d_2 - d_1)}{d_3}\right] \qquad (6)$$

.....d_1,d_2,d_3 are marked in figure 1.13b

Another important part of transmission electron microscopy is scanning in transmission electron microscopy. This is advanced tool, with which one can generate micrographs revealing atomic structure of carbon nanotube or its catalyst particle. one of such tunneling electron micrograph is published by Baughman in his review on carbon nanotubes and their applications [30]. In summary, use of TEM for characterization of CNTs has therefore had a significant impact in the efforts to narrow experimental parameters to increase yield and quality of tubes.

1.4.3 Atomic force microscopy (AFM)

Atomic force microscopy is gaining importance in the characterization of CNTs. It can measure diameter as well as chirality of CNTs. The nanotube diameter is lateral direction is overestimated due to convolution of tip, however height measured along the direction of scanning can give reliable information about the diameter of carbon nanotubes. This tool is used to for imaging single or bundles of CNTs, can also used as mechanical manipulator for CNTs. AFM can thus deliver information about the mechanical properties of CNTs such as tensile or torsional strength [85]. In scanning tunneling mode, one can generate high resolution image showing atomic structure of CNT clearly showing its chiral structure. However, use of this method to characterize CNTs requires further refinement since extensive calculations are required to compensate the effect of curvature of the nanotubes. Some preliminary work has already been done to measure helicity of hexagonal arrays of CNTs using STM [86]. This characterization tool is often used to investigate the mechanical properties of carbon nanotubes of various morphologies [87].

1.4.4 Scanning electron microscopy (SEM)

Scanning electron microscope (SEM) is an important tool to primarily investigate the product synthesized using various methods. It can give primary results in order to evaluate the impact of change in experimental parameter on the synthesis conditions. Using this tool, one can collect vital information about morphology, topography, alignment of CNTs synthesized. It can also help in elemental analysis using technique energy dispersive analysis of x-ray, famously called EDAX. This tool can play a vital role in understanding the growth mechanism.

1.4.5 X-ray diffraction (XRD)

This characterization method is used to measure the extent of graphitization as well as provides information about degree of nanotube alignment. X-ray diffraction data obtained from a sample containing carbon nanotubes contains a graphitic peak corresponding to (002) and a family of (hk0) peaks. Using the (002) graphitic peak, interlayer spacing can be calculated. Peak position is approximately 26° 2θ for SWNTs, which differs slightly from 26.5°, the value reported for HOPG. The (hk0) peaks possesses an asymmetric shape due to curvature of carbon nanotubes. The (hkl) reflections will appear only in XRD patterns with regular stacking of layers [69]. X-ray diffraction has been used to specify a relation between the degree of carbon nanotube alignment

and the intensity of the graphitic (002) peak [88]. A monotonous decrease in the intensity of the graphitic peak with increase in degree of alignment of CNTs is observed.

1.4.6 Thermo-gravimetric analysis (TGA)

A study on temperature dependent weight loss can also give characteristic signature for nano materials. CNTs have carbon as a base element, thus depending on extent of graphitization, quality of CNTs synthesized can be determined using thermogravimetric analysis technique. using TGA, one can determined extent of graphitization, presence or absence of amorphous or other forms of carbon, extent defects in CNT structure. All other forms of sp^2 hybridized non nanotube carbon material burns before 600 °C. When CNTs are subsequently heated further, it starts losing weight at temperatures close to 600 °C. A dramatic decrease in weight occurs up to 700 °C, if the analysis is carried out in ambient atmosphere. Depending upon quality as well as typology of CNTs (single or many walled), the data obtained from TGA will appear bit differently. If metal catalysts are employed during the synthesis of nanotubes, then oxidation of metal catalyst results in the appearance of a slight weight gain in the TGA data. This method is typically used to study the effect of the purification processes employed. For example, it is used to study effect of oxidation and acid treatment on CNTs produced by various methods. TGA is usually carried out in open air for carbon nanotube samples.

1.5 **Methods of purification and funtionlization of carbon nanotubes**

Carbon nanotubes can be synthesized using various techniques explained above. Depending upon usage of metal catalysts (Fe, Ni, CO, Y), and method of synthesis, a special acid treatment is needed to remove the metal catalyst as well as other non nanotube impurities. As these metal particles are completely covered by graphite shell, a heated mixture of concentrated sulphuric acid and nitric acid is used [89]. These concentrated acids tends to attack carbon nanotubes profoundly at defect sites or at the ends. This leads to partial destruction of the graphitic structure by creating holes in the side wall of CNTs. If CNTs are produced using the WCVD method, catalyst particles are not incubated within CNTs. Also, CNTs produced in this process are very crystalline, free of any amorphous carbon. Therefore, purification treatment is not required for WCVD grown CNTs. The oxygen plasma can functionalize CNTs by creating

carboxyl, aldehyde functional groups at dangling bond sites, reducing the hydrophobicity of the CNT film [6].

1.6 Growth mechanism of carbon nanotubes

1.6.1 General growth mechanism of CNTs

Carbon nanotubes have several potential applications in field of electronics and material science. The specific need of these application potentials is to grow the carbon nanotube of specific variety, length, chirality, or quality. This need will only be satisfied only if the exact growth mechanism of carbon nanotube is known. Within few years after the discovery of CNTs, many postulates depending upon the TEM investigation are presented. Many of them explain how the growth happens, exact role of the catalyst during growth. Depending on the method or process of synthesis, growth mechanism will differ. Many well understood growth mechanisms are published for arc discharge, laser ablation as well as chemical vapor deposition method. There is minute difference between a growth mechanism for arc discharge and laser ablation method, however mechanism explaining chemical vapor deposition method is unique and altogether different from that of arc discharge process. Some of the important studies explaining growth mechanisms for chemical vapor deposition are highlighted below.

In "vapor-liquid-solid" method (see fig. 1.14), hydrocarbon gas is decomposed by supplying thermal energy to generate carbon species. These carbon species are dissolved in the catalyst

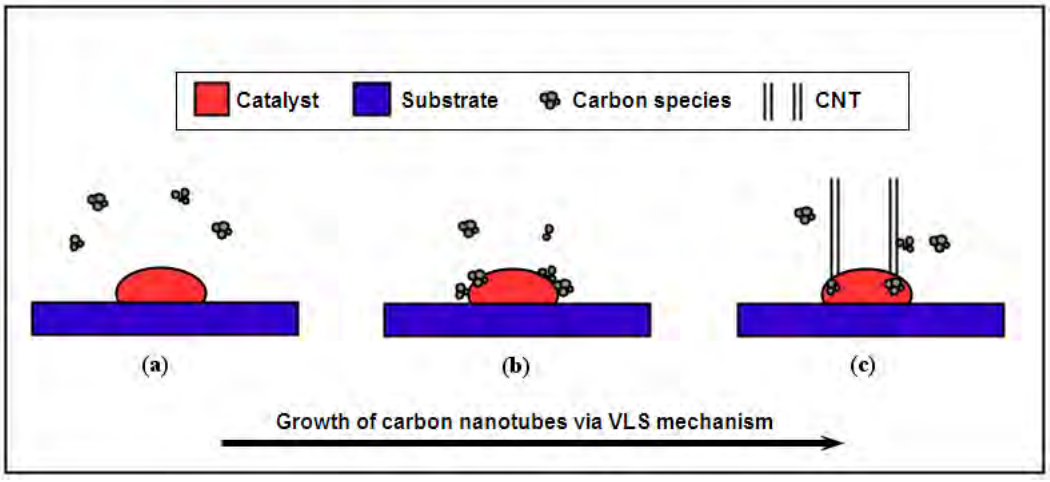

Figure 1.14: A pictorial representation of Vapor-Liquid-Solid (VLS) mechanism demonstrating the growth of CNTs. (a) Formation of carbon species in vapor phase, (b) docking of same species on the metal catalyst forming liquid-solid junction and (c) growth of crystalline CNTs.

particle. As catalyst (Fe, Co, Ni) have limited solid solubility for carbon, it results in expulsion of excess of carbon in crystalline form out of particle from another end, growing carbon nanotube. The growth process continues as long as carbon is dissolving in and precipitating out of the catalyst.

The key parameters in nanotube CVD growth are choice of hydrocarbon, nature of catalyst and growth temperature. Among various possible options, methane (CH_4), ethene (C_2H_4), propylene (C_3H_8) and acetylene (C_2H_2), ethene is selected. In absence of double of triple bond, methane demand higher decomposition temperature and generate moderate amount of carbon species. On the other hand, propylene or acetylene decompose easily but generate high amount of carbon. This leads to growth of CNTs with high degree of defects as well as amorphous carbon. Although, recent studies suggest presence of carbon species such as ethylene and acetylene are essential for growth of SWNT [90]. These species are formed in gas phase during the growth period. Growth temperature can control the decomposition of hydrocarbons and formation of carbon species there after. However inappropriate growth temperature affects the carbon solubility in catalyst and CNTs tend to grow less graphitic in nature. Ethene, therefore, is an optimal choice, as it decomposes at moderate temperature, delivers optimal amount of carbon and decomposition rate is easy to maneuver by controlling thermal energy or hydrogen gas supply.

Choice of proper catalyst is another important parameter in CVD process. Metals such as cobalt, nickel, iron are chosen, due to limited solubility of carbon. It means, metal should have finite solubility that carbon can dissolve, supersaturation will take place and carbon can recrystallize tubular form. Also, size of metal catalyst particle strongly influences the diameter of CNT, that will grow on it. In order to increase the catalyst activity and reduce its particle size, researchers have came out with idea to use bimetallic catalysts such as iron-molybdenum or forming metal oxide supported catalyst such as iron on magnesia, alumina or silica etc. Instead of silica, single crystalline Si wafer with thin layer of SiO_2 proved to be ideal substrate for growing CNTs. Iron catalyst evaporated on the silicon substrate interact strongly with substrate leading to root growth mechanism instead of tip growth. These two mechanisms are responsible for growth of CNTs using CVD method, explained below.

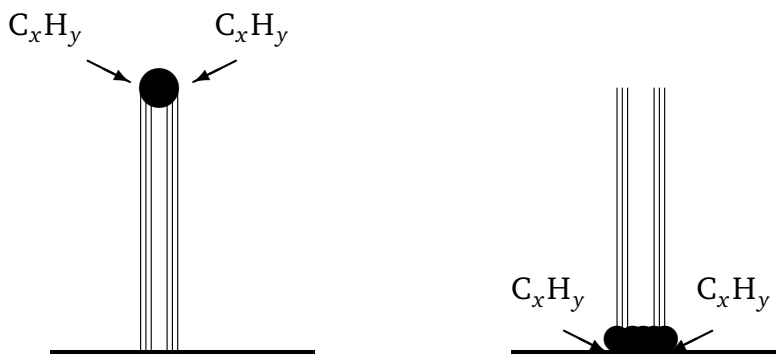

(a) Tip growth mechanism **(b) Root growth mechanism**

Figure 1.15: Schematic model showing root growth and tip growth mechanism, dark circle and oval represent catalyst particle.

Carbon nanotubes have similar growth mechanism as that of carbon filament, first discovered by Baker and coworkers in year 1972 [91, 92]. These mechanisms are termed as "root growth" and "tip Growth" mechanism. The major difference between these two mechanisms is location of the catalyst during CNT growth. As name suggests, If the catalyst particle is seating at the root of the CNT, sticking hard to substrate, the growth process is termed as a Root growth. On the other hand, if catalyst particle is lifted off the substrate and seats at the top apex of carbon nanotube growth, the mechanism is termed as a Tip growth mechanism. Surface activation energy between the substrate and catalyst particle decides which growth mechanism CNT will follow. Both mechanisms are displayed in figure 1.15. During the growth process, carbon will be dissolved into metal particle till supersaturation of metal takes place. At supersaturated condition, carbon starts re precipitating. Depending upon the surface energy, growth will follow tip or root growth mechanism.

If the catalyst particle wets the surface of the substrate well and is good grafted underneath, the catalyst particle is hard to lift off. In such a case, the precipitation of crystalline carbon will take place from the top side of particle and CNT will grow in length at its root. Another possibility is, if surface activation energy of substrate is high, and catalyst particle seats as if water droplet on a lotus leaf, saturated carbon precipitates out from bottom side of the catalyst particle. In this situation, catalyst particle is lifted off the substrate, leading to tip growth

mechanism as shown in figure 1.15a. Root growth mechanism is favorable in a aspect, catalyst particle is seating fixed on substrate eliminating possibility of incubation inside the CNT grown and thus eliminates the need of post purification procedure. Iron on Si or SiO_2 substrates lead to root growth conditions while a thin layer of nickel on quartz glass gives rise to tip growth mechanism [52].

1.6.2 Growth mechanism of water assisted chemical vapor deposition (WCVD)

Water assisted chemical vapor deposition method is a advanced version of the chemical vapor deposition method. Here, a small amount of water is used to keep the catalyst active for longer time, in order to grow CNTs of millimeter length. A thin layer of aluminum is deposited on substrate prior to catalyst, i.e. iron deposition. This is called buffer layer. The Al layer not only lead to root growth mechanism, but also helps in forming small nano islands of catalyst to grow carbon nanotubes. Smaller islands lead to growth of few walled CNTs having narrow diameter distribution. Another important role this buffer layer plays in enhancing catalyst life. This role will be explained in detail in synthesis part of this thesis.

Water vapor is introduced in the system by bubbling a part of carrier gas through a water bubbler. The gas will carry small amount of water vapor governed by the equation (7) given below. This introduced water vapor reacts with amorphous or unused carbon to convert it into carbon dioxide as per following the equation (8).

$$M_w = M_g \left[\frac{P_w}{(P_w) - (P_g)} \right] \tag{7}$$

...M & P are molar mass and partial pressure, w & g denote water vapor and gas bubbled

$$C + 2H_2O \leftrightharpoons CO_2 \uparrow + 2H_2 \uparrow \tag{8}$$

The water molecule is supposed to be reacting with amorphous carbon that is continuously deposited on the active surface area of catalyst. The CNT growth temperature is high enough to keep the equation balance on right side to successfully convert the amorphous carbon to carbon monoxide or carbon dioxide gas. In absence of such a cleaning activity, catalyst will be poisoned

losing its active surface area, a location where fresh carbon diffuses into the catalyst. Such lose of active surface area is termed as a "catalyst poisoning" which leads to no CNT growth condition.

Apart from water, numerous other catalyst activators, those can deliver required oxygen have also been studied. Carbon dioxide as a catalyst activator (CO_2) is used by Magrez research group [93]. Maruyama could even grow centimeter long carbon nanotube in a single batch using ethanol precursor. Remarkable to note, here ethanol (C_2H_5OH) was serving a dual purpose, as a carbon source and as an oxygen supplier. Recently, A complete study investigating various chemicals such as carbon dioxide, tetrahydrofuran, acetone, ethanol etc for their possible candidature as a weak oxidants is published [94]. Along with these oxygen containing organic molecules, ammonia (a gas without oxygen content) is also investigated as a carbon etching agent. Ammonia fails to show any growth enhancing effect at all. Depending upon tendency of decomposition, stability against thermal energy and oxygen species a chemical molecule can deliver, each compound varies in its supply (from 100 to 1000 ppm) in order to achieve efficient growth rate.

Another possible method for efficient growth is to decrease the carbon supply or dilute it to a extent efficient growth occurs without or minimized effect of catalyst poisoning. If the hydrogen content is increased in the system, increase in the partial pressure of hydrogen tends to suppress hydrocarbon decomposition or can help to etch away carbon that is deposited on the catalyst [95]. This effect can be used in order to decrease catalyst poisoning there by leading to super growth of CNTs [96].

In this present work, water is used as an oxidant, and more light will be thrown on the exact role of it. A growth mechanism will be put forth explaining its selective activity against of the catalyst poisoning by amorphous carbon.

1.7 Aim of the present work

A rich blend of qualitative carbon nanotubes together with various inorganic as well as bio-materials have superior physical and chemical properties and thus serves a broad field of application. However, inheritance of new properties of such a composite material is co-related to quality of its constituent elements. Therefore, the present work comprises of studies on the synthesis and systematic investigation of growth mechanism of carbon nanotubes in water assisted CVD method as well as various methodologies to blend as grown CNT structures to develop new "hybrid materials".

Water assisted CVD method is employed to grow diameter selective, aligned and structural growth of CNTs. However, the process is quite complicated and incorporates numerous parameters those are interdependent of each other. In order to understand such a complex system, stepwise and pragmatic investigation of each growth parameter is necessary. By scrutinizing various experimental parameters, the selective activity of water driving ultra-long growth of CNTs can be understood.

The second major part of the present work conceptualizes various methodologies to produce a rich blend of carbon nanotubes structures with inorganic and bio-materials. Various metal oxides, noble metals at nano scale and neuronal cells are integrated with as synthesized CNT structures to derive new hybrid materials. At the end, CNTs and their hybrid materials are integrated in a form of micro structured devices demonstrating potential applications in field of electronic, sensing and energy applications.

2 Synthesis of carbon nanotubes

2.1 Synthesis of carbon nanotubes using water assisted chemical vapor deposition method.

Chemical vapor deposition method is a classical method used in the semiconductor industry, in which, a precursor is decomposed using thermal energy in order to form chemical species in vapor phase. These species are then deposited on substrate. Often, during the process many volatile by-products are generated, which are removed using high stream of inert gases from the reaction chamber. The work presented here uses an advanced version of this process called water assisted chemical vapor deposition method (WCVD).

Carbon nanotubes were grown at 800 °C using hydrogen, argon, ethene (C_2H_4) and small amount of water vapor (200 ppm). Water vapor was carried into an oven by bubbling small amount of carrier gas through a water bubbler built into the system. The growth is catalyzed by bimetallic catalyst nano particles composed of iron and aluminum. A schematics of the growth process is as shown in figure 2.1. both metals, Fe (1 nm) over Al (10 nm), were deposited on the substrate using metal evaporation technique. Upon heating to CVD temperature, both metals build up a inter metallic phase and thereby small nano particles of same phase. The growth of carbon nanotubes is catalyzed by these nano particles and a dense film of CNT grow on the substrate.

Carbon nanotubes were grown at a rate of 30 to 40 μm per minute. At this rate, 1 mm long CNTs were grown in a time span of half an hour. A millimeter thick film, formed by aligned growth of carbon nanotubes on silicon wafer is as shown in figure 2.2a. The average diameter

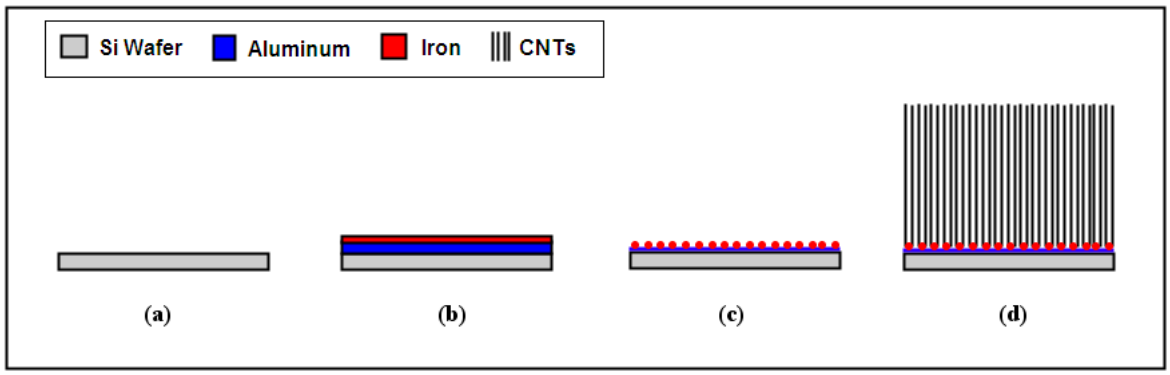

Figure 2.1: Schematic layout of growth process of carbon nanotubes (a) cleaned Si wafer (b) Al and Fe deposition (c) formation of catalyst nano particles upon heating (d) growth of CNTs using WCVD method .

of CNT is 4 to 6 nm and are mostly doubled walled. An electron micrograph beside it (fig 2.2b), shows a CNT film grown in absence of water vapor. Due to lack of water supply, growth is limited to 150 μm length. The growth rate for the fresh catalyst is 30 to 40 μm per minute; same as that of standard conditions. However, approximately 2 to 4 minutes after the commence of CNT growth, catalyst is completely poisoned and therefore no further growth is possible.

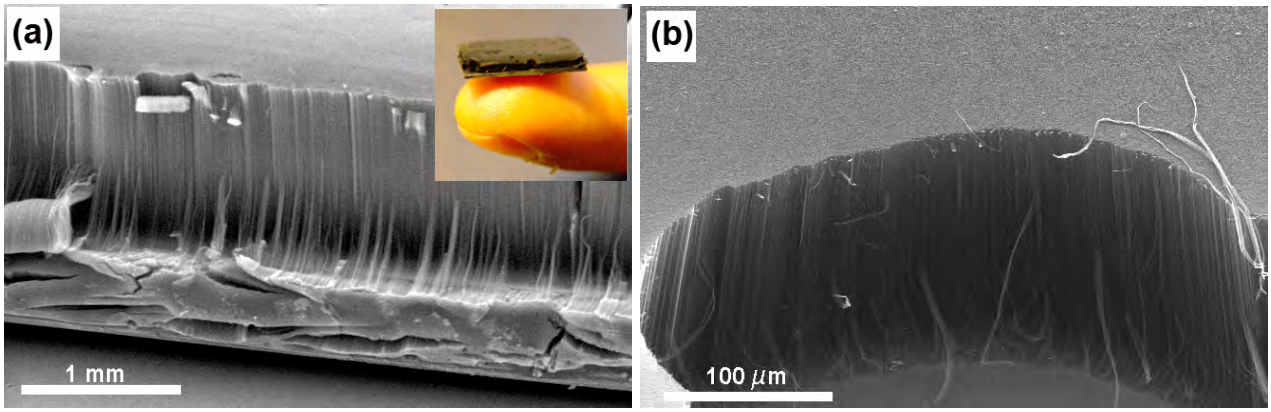

Figure 2.2: (a) SEM micrograph and an optical image (inset) of a film of 1 mm long CNTs grown using 200 ppm of water supply (b) SEM of CNT film grown without supply of water.

Further study revealed, the growth rate is strongly dependent upon flow rate of reactant gases. If the gas flow rate is increased, the growth rate will increase with it and so will be the rate of catalyst poisoning. It means, in order to keep CNTs growing at constant rate, quantity of water required to keep catalyst active is directly depends upon flow rate of carbon precursor. In other words, ratio of number of reactant chemical species to that of water molecules per cubic meter of reaction zone is deciding factor. This ratio has to be constant in order to have continual growth for desired time. A detailed study evaluating the impact of this ratio on growth rate is systematically represented in upcoming part of this section. The flow rate of 100 sccm of ethylene together with 200 ppm of water vapor supply gives rise to maximum achievable growth rate. Higher flow rate of the precursor gas was avoided as higher flow rate generates more carbon species. If these species are not utilized for CNTs growth, they may get deposited on already grown carbon nanotubes in form of an impurity [7, 97].

The starting temperature has critical impact on formation of catalyst nano particles. Till 500 °C as a starting temperature, there was no major impact on quality, typology, or even on growth rate of CNTs. However, past 600 °C absolutely no growth is observed. The possible reason for it is, till 500 °C aluminum is still in solid state, has got enough time to get reduced and melt

slowly thereafter. However past 600 °C aluminum layer undergoes thermal stress, melt without getting reduced, leading to loss of nano particle formation. In absence of catalyst particles, did not take place.

2.1.1 Characterization of CNTs grown using water assisted CVD method.

As mentioned in introduction part, carbon nanotubes are grown using the WCVD method consists of 99% crystalline graphitic carbon, free from any amorphous carbon or metal catalyst impurities. A CNT film grown on 1 cm^2 Si - wafer piece for 15 to 20 minutes, i.e. around half millimeter in height, weighs near about 1 milligram. One of such well grown CNT film is investigated using Raman spectroscopy using 488 nm wavelength laser (see fig 2.3a).

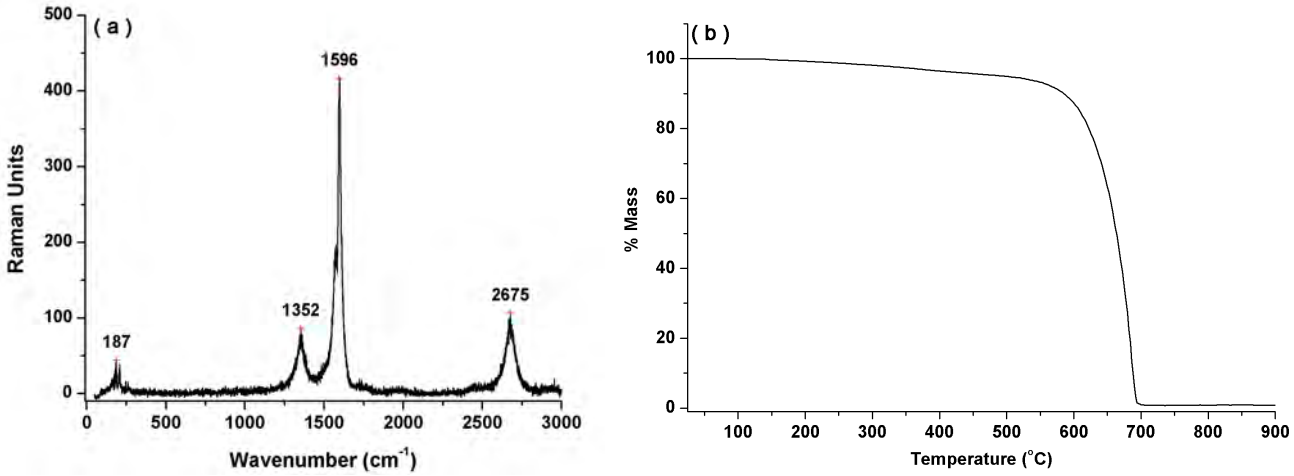

Figure 2.3: (a) Raman spectrum and (b) thermo gravimetric analysis of CNTs grown using water assisted chemical vapor deposition method.

The spectrum shows the distinguishing and sharp peak at 1596 wavenumber denoted as G-band peak. It corresponds to crystalline graphitic nature of carbon nanotubes. The G peak has one sharp shoulder at lower wavenumber. This shoulder represents the semi conducting nature of CNTs grown [59]. Two other peaks at 1352 cm^{-1} and at 2675 cm^{-1} are defect band peak (D band peak) and first overtone of it respectively. The presence of the D band here is presumed to be due to dangling bonds present at the end of the CNT. This ratio of intensity of G band to D band peaks (I_d / I_G ratio) gives qualitative information about crystallinity of CNTs grown. The ratio in this spectrum is lesser than 0.2. At lower wavenumber (peak at 187 cm^{-1}) radial breathing mode (RBM) peaks are seen. The occurrence of RBM peak symbolizes presence of SWNTs or sometime DWNTs peaks [70].

Thermo-gravimetric analysis of carbon nanotubes shows typical oxidation resistance till 500°C in oxygen atmosphere (see figure 2.3b) [7]. Till 550°C, a minor weight lose of 1.5% is seen. This is due to preferencial attack of oxygen molecules at dangling carbon atoms. Thereafter, as CNTs grown here are few walled (1 to 3), their oxidation starts at around 550°C and till 700°C, the whole mass is completely oxidized.

The characteristic peak for carbon nanotube originates at 26° of 2θ from Bragg diffraction of X-rays from its side walls. This is highest intensity peak and termed as (002) or graphitic peak. However, when as grown CNT film on silicon wafer is measured in a range 15 to 90° of 2θ, no (002) peak was seen (see figure 2.4a spectrum 'x'). Instead peaks corresponding to 100 and 004 planes were observed. This is an effect of their aligned growth on the Si-wafer. As CNTs have strong alignment, no side wall could interact with X-rays, leading to loss of (002) or characteristic graphitic peak. This can be proven by measuring the same CNTs after destroying their alignment. The film is lightly ultra-sonicated in ethanol in order to lose their alignment and the drop casted on Si wafer. XRD of drop casted film (spectrum 'Y') has an intense (002) peak and other peaks (100 and 004) were disappeared. The broad (002) peak still shows signature of microscopic alignment [98].

Atomic force microscopy (AFM) image of a single CNT generated using tapping mode is displayed in figure 2.4b. CNTs with high aspect ratio, can practically stick to the probing tip

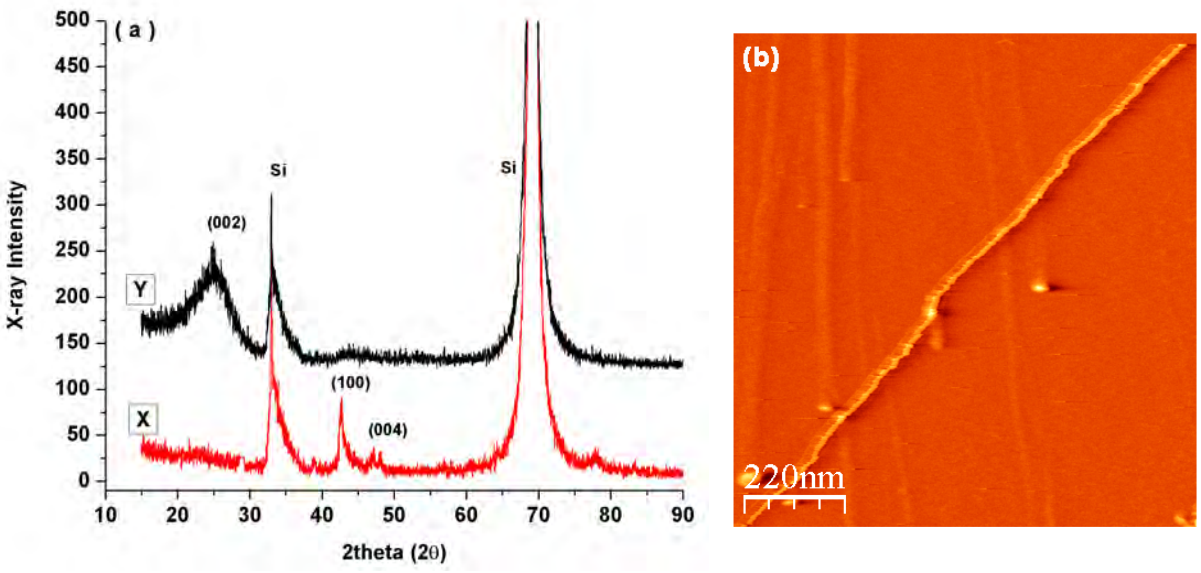

Figure 2.4: (a) X-ray diffraction spectrum of as grown aligned CNT film (spectrum 'x') and unordered film (spectrum 'Y') supported on Si-wafer and (b) Atomic force microscopy image of an individual carbon nanotube. The diameter of CNT is 1.69 nm.

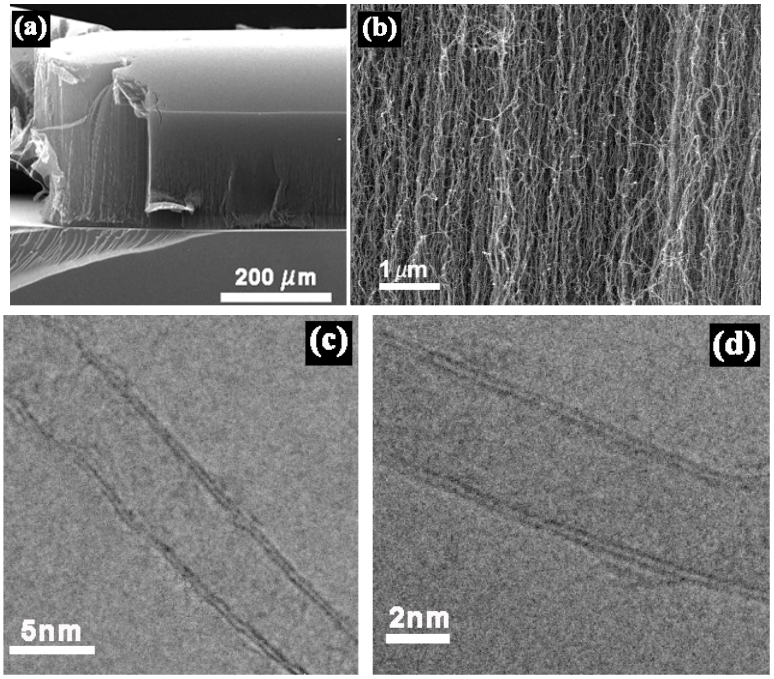

Figure 2.5: Scanning electron micrographs of (a) a CNT film (b) high resolution image of same film showing vertically aligned CNTs, (c & d) transmission electron micrographs of DWNTs.

during investigations, therefore, tapping or non contact mode is recommended to generate an image. The CNT scanned here is measured 1.69 nm in diameter, in which case, it is single walled carbon nanotube.

A few of well resolved scanning along with transmission electron micrographs of carbon nanotubes are displayed in figure 2.5. A high resolution SEM micrograph of a CNT film (2.5b)reveal the vertical alignment of CNTs. More than 90% of CNTs grown on the Si-wafer are DWNTs and rest is mixture of SWNTs and MWNTs. TEM micrographs of displayed in figure 2.5c & d show double walled carbon nanotubes free from any kind of impurity. TEM can also be used in scanning mode, called scanning in transmission microscopy (STEM), a versatile tool delivers high resolved images of the sample even at atomic resolution [30].

The surface area of a half a millimeter thick the CNT film was measured using BET technique (see fig. 2.6). The measurement revealed surface area of 344 m^2 / g. It is not as high as active charcoal, but on the other hand, compared to active charcoal, CNTs are biologically, thermally or chemically more stable. The high surface area can be utilized in catalysis for catalyst support, and to built micro reactors [99].

The as grown carbon nanotube film was studied using X-ray photo electron spectroscopy (XPS). The survey spectrum shows just two major peaks; one for carbon and another for oxygen.

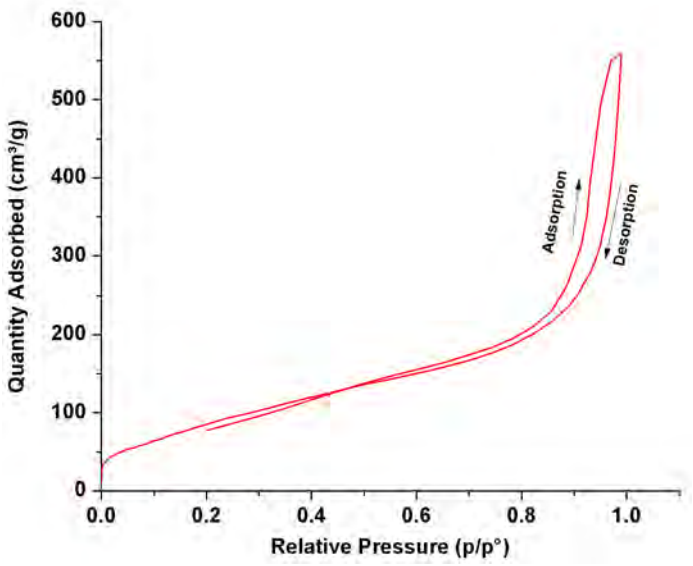

Figure 2.6: Isotherm linear plot displaying nitrogen adsorption and desorption on a CNT film.

The carbon peak was located at 284.5 eV, standardized for graphitic nature of carbon. The small shift in binding energy (<0.35 eV) is considered insignificant [100]. The oxygen peak was located at 532.6 eV of binding energy. This data will be used often as a reference data during characterization of CNTs based metal oxide composites. All spectra are displayed in fig. 2.7.

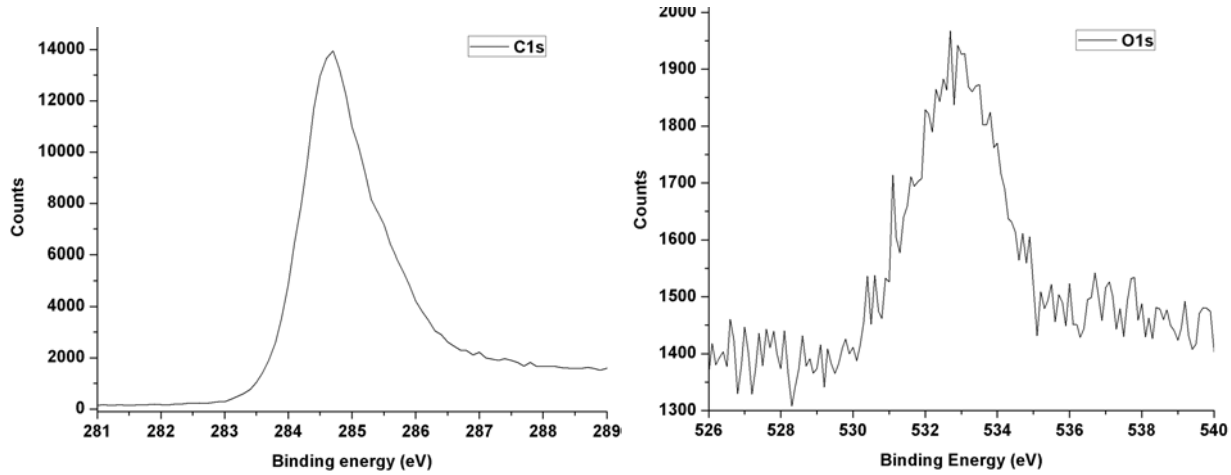

Figure 2.7: XPS spectra of as grown carbon nanotubes (a) carbon C1s and (b) oxygen O1s spectrum.

2.1.2 Engineering the catalyst to grow geometrically confined CNT structures.

A bimetallic catalyst consisting of aluminum and iron is used to grow CNTs in water assisted CVD method. If one of the metal among two is missing, growth will not takes place. This process parameter can be advantageously used in order to grow CNTs as desired location by patterning

one of the two metals. Aluminum deposited on substrate is relatively thicker compared to iron. Therefore, patterning of iron was undertaken. This technique leads to growth of various micro or even macroscopic geometries made up of vertically grown CNTs without aid of costly processes such as lithography. The process is schematically represented in figure 2.8.

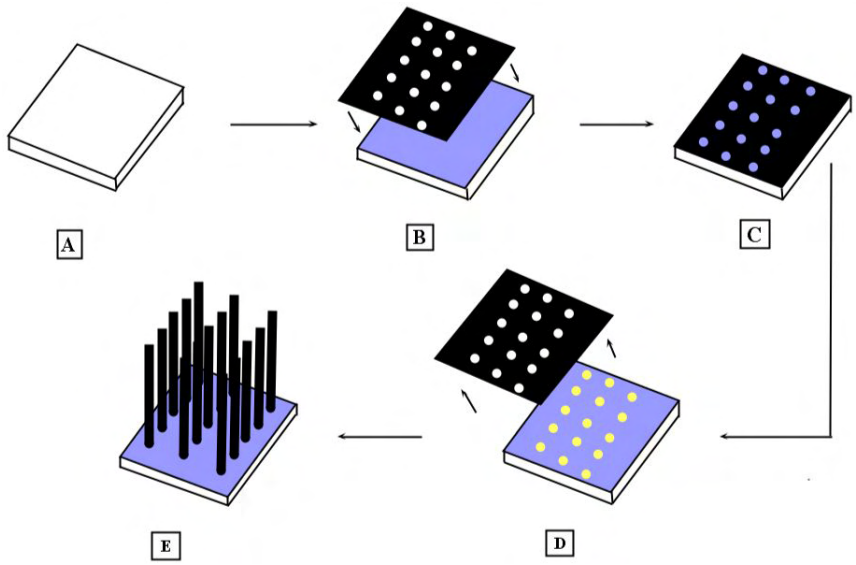

Figure 2.8: Schematic representation of the method used to grow structured CNT blocks. (a) cleaned Si - wafer (b) Al deposition & mask adjustment (c) iron deposition through a perforated mask (d) removing the mask and (e) CNT growth.

Depending upon the application, first Si or SiO_2 wafer are cleaned using iso-propanol. After that a layer of 10 to 11 nm of aluminum is deposited on the wafer using e-beam metal evaporation. Upon this thin layer of aluminum, a shadow mask i.e. perforated metal foil, or woven nylon mesh with predetermined mesh size was fixed. There after, a thin layer of iron 0.8 to 1 nm is deposited by using e-beam technique. Finally, the mask is removed, and CNTs are grown using standard growth process explained previously. Metal iron is deposited through holes of the mesh or grid, exactly where CNT growth will take place. Few SEM images exemplifying perfection and reproducibility of the process are shown in figure 2.9.

Another possibility to structure the iron catalyst is by printing a salt solution or a dispersion of iron nano particles directly on the aluminum deposited silicon wafer. The ink jet printing technique is most suitable for this purpose. After depositing 10 nm layer of aluminum, 0.2 mM concentrated alcohol based solution of iron nitrate ($Fe(NO_3)_3 \cdot 9H_2O$) was directly printed on silicon wafer using commercially available ink jet printer. This technique eliminates the need of masks at all and can print any complicated structure. However, the biggest problem associated

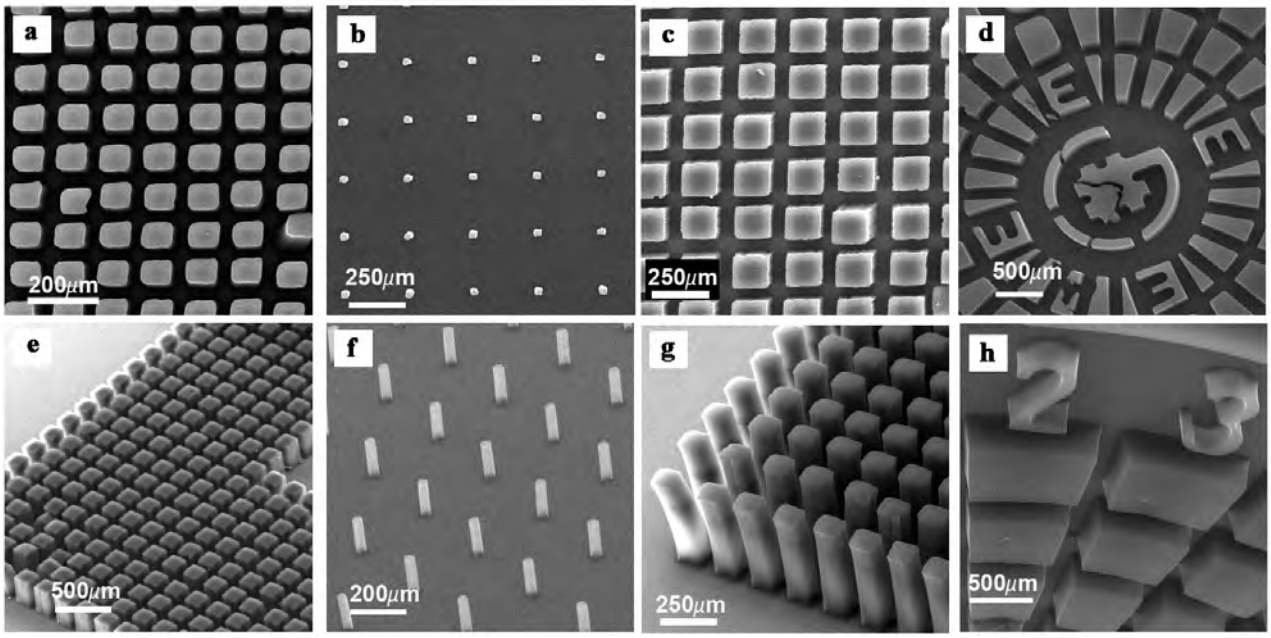

Figure 2.9: SEM micrographs of different CNT block arrays in various shapes and sizes obtained by using various masks.

with this technique is inhomogeneous distribution of the catalyst (solute) after evaporation of the solvent. The effect can be minimized by appropriate choice of a solvent or by adding small amount of a surfactant to the solution. Two SEM micrographs exemplifying the potential of this process are displayed in figure 2.10.

CNT blocks can be grown in any desired form or shape provided appropriate mask is available. It forms sharp edges or corners and such structures found immense interest in various applications fields such as cold field emission, MEMs NEMs actuators as well as a gas or bio sensors.

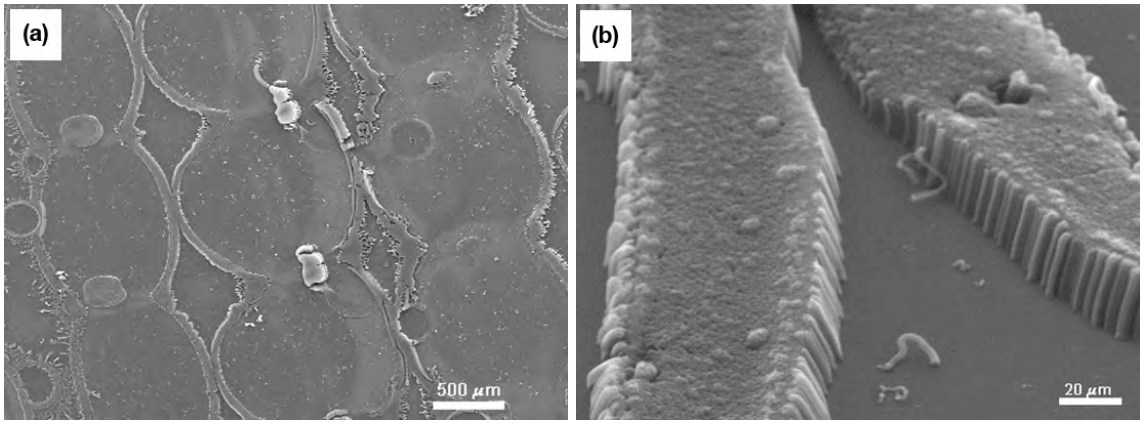

Figure 2.10: SEM micrographs of complicated structure grown by printing the catalyst solution on aluminum deposited silicon wafer with the help of ink-jet printing.

2.2 Study of different growth parameters in WCVD method

Water assisted chemical vapor deposition technique is a process sensitive method. WCVD incorporates numerous parameters, and each of them carry a strong influence on the growth rate as well as on typology of carbon nanotube. Few important parameters those carry noteworthy influence are aluminum, iron, hydrogen and water vapor. A slight change in any one of them will lead to fatal consequences. For example, if thickness of iron is increased by 1 nm over the requisite amount, the process shifts from good growth to no growth conditions. Not only this, above mentioned parameters are interdependent on each other. It means, if one of the parameter is varied slightly (if thickness of Al is increased), other one has to be readjusted to incorporate the change (water vapor amount has to be increased). This increases the degree of complexity in the system.

The only way to understand such complicated system is to investigate every important growth parameter separately by keeping all other parameters unchanged. This pragmatic approach will give inside information about the influence of each parameter, crucial for understanding the complex process. The four above mentioned parameters are investigated in series of experiments as explained below.

2.2.1 Effect of growth parameter : Aluminum

Aluminum plays a vital role in a super long growth of carbon nanotubes. At beginning, aluminum is thought to serve only as a buffer layer. As aluminum melts (at 660 °C) below the CVD temperature, it helps to break the thin layer of the used metal catalyst into small islands, and these islands catalyze the growth of carbon nanotubes. Also, it wets almost all substrate materials, there by fixing the catalyst particle hard to substrate and leading to root growth mechanism. Iron, another component in the bimetallic catalyst, has limited solid solubility and thus acts as a good catalyst for growth of carbon nanotubes. Important to notice if one of these two metals, iron or aluminum is absent, growth will not take place. Therefore, it is ambiguous that aluminum serves only as a buffer layer to form small nano particles of iron and glue them to the substrate. It must or should serve another and vital role in growth of carbon nanotubes. The work explained in this section try to focus on this question.

As stated above, aluminum melts to form small islands and there by the iron film transformed into a shape of small nano particles. In order to investigate this phenomenon, two wafer pieces are deposited with 10 nm aluminum layer and one of them further with 1 nm iron layer. Both pieces are then heated to CVD conditions following the standard procedure. SEM as well as AFM investigations were carried out on both wafers (see fig 2.11). Investigations reveal formation of well ordered small nano particles of average particle size 8 to 10 nm in case of wafer containing layer of aluminum as well as iron. No such particle building took place on a wafer missing the iron layer. The study indicates, aluminum and iron recombine together to form bimetallic nano particles.

As a next step, various other metals have been tried in place of aluminum in order to check if particle formation takes place for other metal combinations as well. For this purpose, titanium, germanium, molybdenum, niobium, along with few other oxides such as titanium dioxide, zinc oxide were selected. For every new candidate element, two tests were carried out. On two pieces of a substrate, 10 nm thick layer of candidate metal was deposited and followed by 1 nm layer of iron. One out of two pieces was heated to CVD temperature and cooled down, other was heated and CNT growth was carried out. Most of the candidate metals fail to show any sort of catalytic activity except titanium and molybdenum. Both metals have shown formation of nano particles as well as aligned CNT growth to a length of 100 μm. Few representative SEM images of CNTs grown and catalyst particles are displayed in figure 2.12. It is worth making

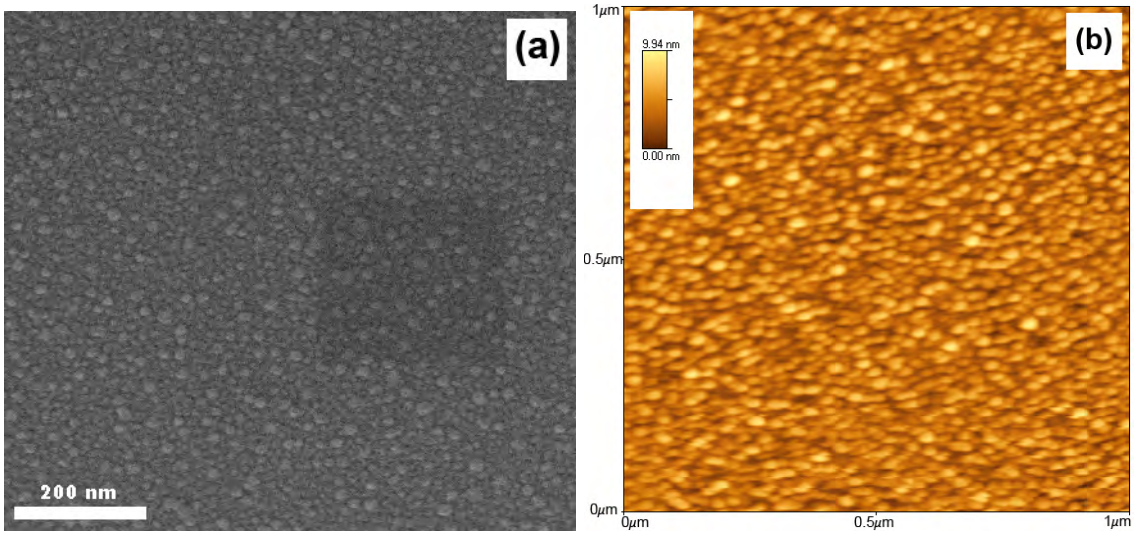

Figure 2.11: (a) Scanning electron microscope and (b) atomic force microscopy image of catalyst nano particles.

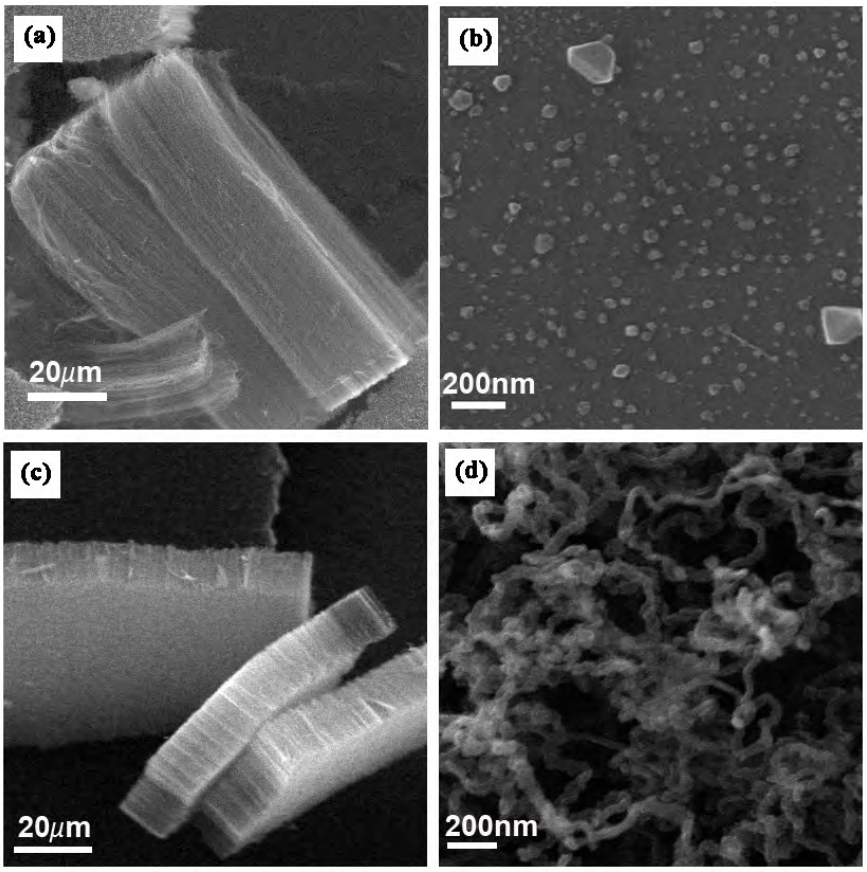

Figure 2.12: Scanning electron microscope of CNTs grown using various other metals as buffer layer. (a) using titanium , (b) nano particles formed using titanium, (c) molybdenum and (d) germanium.

it clear here, aligned growth is possible even without supply of water as seen in figure 2.2b above. However, if CNTs continues to grow past 100 to 150 μm length with the help of water vapor supplied, the catalyst is said to be active for water assisted growth of carbon nanotubes. Both metals show growth but not past this limit. Further experiments for these 2 metals were undertaken for varied thickness (thinner or thicker than 10 nm), different candidate metal to iron ratio as well as for other gas combinations to check out if these two metals support the water assisted growth. None of these experiments were fruitful. The growth continued till maximum film thickness of 100 μm. It enunciates that aluminum plays a vital role in catalytic activity of bimetallic catalyst used in water assisted chemical vapor deposition method. The aluminum seems to be responsible for creating a optimal conditions that water can attack the amorphous carbon which would otherwise poison the catalyst nano particle.

Aluminum and iron have good solid solubility and form numerous inter metallic phases $Al_X Fe_Y$ over the range of temperature. The phase formed depends upon the atomic ratio of metals

deposited. However, as here thickness (neither weight nor mass) of metal deposited is taken into account and obviously deposition is seldom mono layer over mono layer, it's hard to estimate in which bimetallic phase the catalyst exists. As amount of aluminum is higher compared to iron; it's certain that the catalyst composed of aluminum rich Al-Fe bimetallic phase. Keeping iron thickness same, if aluminum thickness is varied by few nanometers, the probability that the phase might change is high. It is intriguing to cross check if all phases of Al-Fe bimetallics support the water assisted growth or only a certain phase does. Thus, for constant thickness of 1 nm of iron, buffer layer thickness was varied from 6 to 15 nm. As a matter of fact, for iron of 1 nm thickness, catalyst particles formed using aluminum in range of 8 to 12 nm show active behavior during the water assisted growth. A detailed study on elemental composition of metal catalyst is explained in the following chapter.

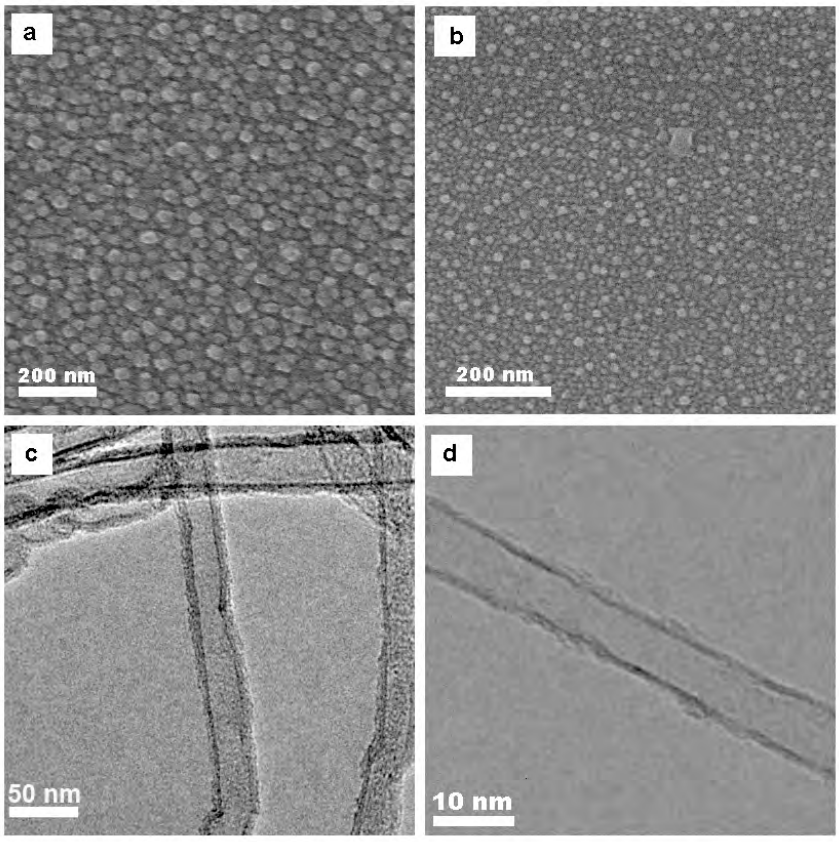

Figure 2.13: Electron micrographs (SEM and TEM) showing impact of metal evaporation technique on (a & b) size of catalyst nano particles and (c & d) typology of CNTs grown on such particles. Catalyst particles were grown by evaporating 1 nm of iron and 10 nm of aluminum by using two different metal evaporation techniques; (a & c) thermal evaporation method (b & d) e-beam evaporation.

As thickness of aluminum is higher compared to that of iron used in standard growth process, the method of deposition can play a good role in controlling the size of catalyst particles formed from metal layer deposited. The energy of the evaporated atoms will vary depending upon the method of evaporation, which in turn will affect the density of the metal film deposited. If the film is dense enough, atoms having less surface energy will hardly need to relocate themselves. Therefore, nano particles grown out of dense film will have smaller diameter than those grown out of less dense film. Such an effect is visualized experimentally if, aluminum evaporated using two different techniques, thermal evaporation leading to bigger size of catalyst particle and electron beam evaporation giving rise to smaller catalyst particles. Using both methods, 10 nm of aluminum was evaporated on separate substrates and then 1 nm of iron was sputtered on both films simultaneously. Using the standard growth conditions, CNTs were grown on the substrates and SEM investigations are carried out on both samples.

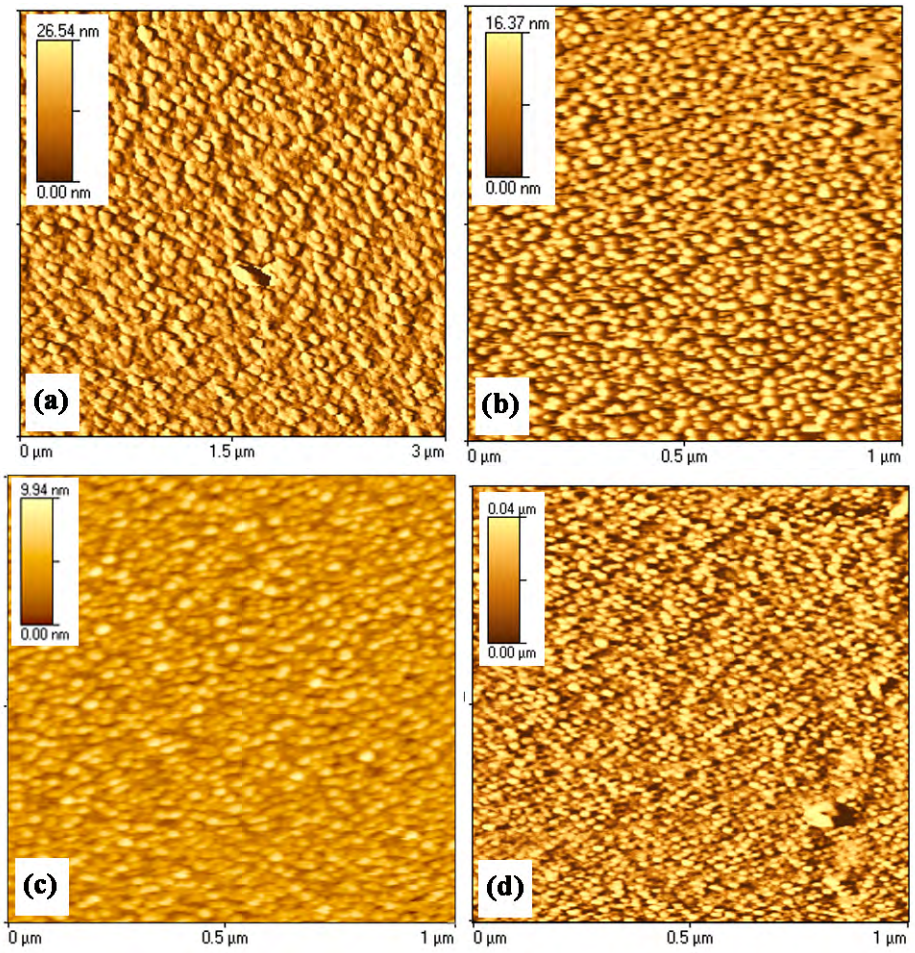

Figure 2.14: Atomic force microscope images of bimetallic catalyst nano particles formed by 1 nm iron deposited over (a) 6 nm, (b) 8 nm, (c) 10 nm and (d) 12 nm thick aluminum.

Catalyst particles grown using the thermal evaporation method show average particle size of 30 to 40 nm and CNTs grown on them are multi walled; 4 to 6 walls per tube (see fig. 2.13a&c). By e-beam method, particles generated have average size in range of 6 to 10 nm and CNTs grown on them are mostly DWNTs (see fig. 2.13b&d). It confirms the fact that mode of metal evaporation or density of the film deposited plays a deciding role in determining the size of catalyst nano particles formed [68].

The change in the aluminum or iron thickness will certainly create an impact on size of the catalyst particle and there by on CNT diameter or may on typology. For standard 10 nm Al/ 1 nm iron thickness, average size of catalyst particles was 6 to 10 nm. Few other combinations in which aluminum varied from 6 to 15 nm in thickness and iron accurately 1 nm were studied. After deposition of metals, wafers were heated to 800 °C and investigated using AFM technique. The AFM micrographs for selected samples are displayed in figure 2.14. Catalyst particles grown by heating in controlled atmosphere found to have same spherical morphology, however strong change in average size. For smaller thickness of aluminum (6 nm), particles were grown to an average size of 20 nm. The size decreases with increasing amount of aluminum. For 10 nm Al thickness, particle size is reduced to as small as 6 nm. Past 10 nm, the particle size starts building up again. For 12 nm Al thickness, particles as big as 15 nm were recorded. In order to understand the complete effect of Al and Fe thickness on morphological aspects of bimetallic catalyst particles, a detailed study was undertaken. Aluminum was varied from 6 to 12 nm and iron from 0.8 to 2.0 nm. Various samples from this matrix of Al and Fe thickness were scanned using AFM technique. with increasing amount of iron or aluminum, particle building become more and more inhomogeneous. A table summarizing the mean size of particles against the thickness of aluminum and that of iron is given below (see table 2.1).

Table 2.1: A table comparing the size of catalyst nano particles formed for a thickness of aluminum and iron deposited.

Fe (nm)→ Al (nm)↓	0.8	1.0	1.2	1.6
6	4	5	6	20
8	8	6	10	7
10	4	5	8	6
12	4	7	13	7

2.2.2 Effect of growth parameter : Iron

Similar to aluminum, an impact of thickness of iron deposited is studied. Iron, in absence of aluminum, agglomerate forming nano particles due to high temperature annealing. For 1 nm iron, particles of size 1 to 2 nm were obtained (see fig. 2.15a). However, no aligned water assisted CNT growth was observed using these particles. On few other wafers, 10 nm thick layer of aluminum was deposited prior to iron deposition. On it, iron thickness was varied from 0.4 nm till 2.0 nm. After annealing in hydrogen atmosphere, no particle resembling morphologies were observed in AFM investigations for iron thickness less than 0.6 nm. Above 0.7 nm particle building starts and particle size grows with increasing amount of iron as seen in figure 2.15b-e. For iron thickness of 2.0 nm and above, particles were non homogeneously distributed and a broad size distribution was observed. The CNT growth on such particles was also inhomogeneous and was not reproducible [101].

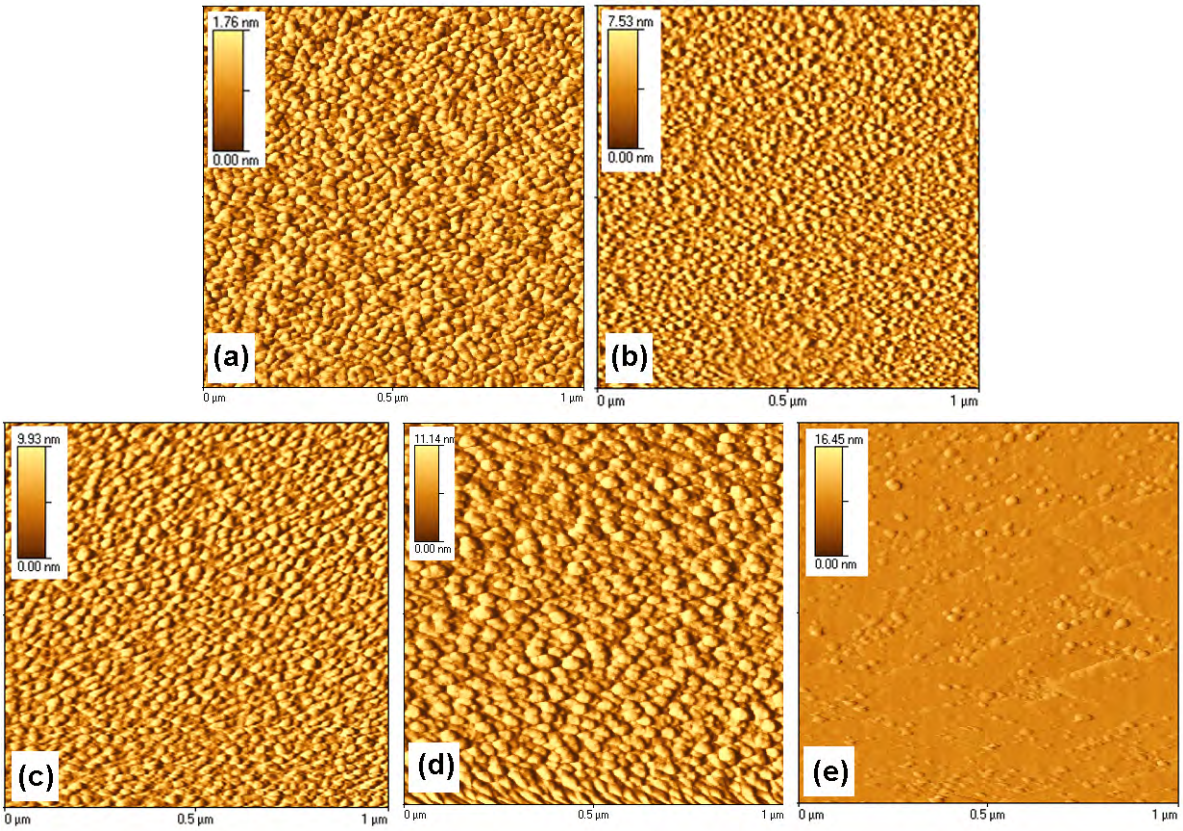

Figure 2.15: Atomic force microscope images of bimetallic catalyst nano particles grown on Si wafer using (a) just 1 nm iron (no aluminum) while (b) 0.8 nm, (c) 1.0 nm, (d) 1.6 nm and (e) 2.0 nm of iron on 10 nm of aluminum.

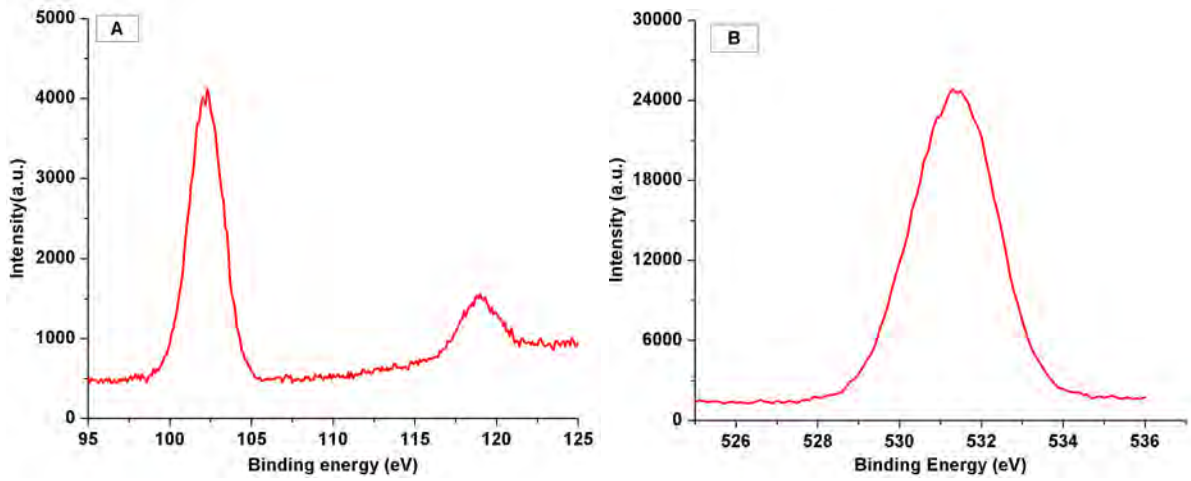

Figure 2.16: XPS spectra of Al layer deposited and heated on Si wafer. (a) AlSi 1s spectrum and (b) oxygen 1s spectrum.

Aluminum and iron have good affinity towards each other to form inter metallic phases. X-ray photo electron spectroscopy (XPS) study of aluminum deposited on Si-wafer substrate revealed the formation of aluminum silicide phase upon heating. Aluminum reacts with the silicon from the substrate forming aluminum silicide only in absence of iron. If iron is present, no such phase was detected. Instead aluminum and iron combine with each other forming the catalyst nano particles as explained above. This is another indication towards necessity of presence of iron as well as aluminum, if water assisted mechanism has to work successfully. XPS spectra are displayed in fig. 2.16.

2.2.3 Effect of growth parameter : Hydrogen

Hydrogen gas is one of the most often used reactive gases in chemical vapor deposition method. Hydrogen has smallest atom size and can behave very reactive element at high temperature; specially against bi-products generated by decomposition of precursor compound. These bi-products if not chemically modified and flushed out of reactive area fast enough, they might incorporate into deposited material as an impurity. Many speculative studies deduce a role for hydrogen as a agent controlling the rate of hydrocarbon decomposition in the CVD process. Some other demonstrative studies reveal hydrogen can preferentially etch the amorphous carbon [68, 95]. In order to bring the facts under light, a systematic study is undertaken to understand the exact role hydrogen plays.

In order to investigate the role of hydrogen, flow rate of hydrogen is varied stepwise in series of experiments between 0 to 800 sccm; keeping all other growth parameter constant. Such a change was found to have a direct impact on the growth rate of CNTs. Therefore, change in height of CNT film is considered to evaluate the impact of hydrogen gas. Along with it, selected samples were studied using TEM to see the impact of same on typology and quality of CNTs grown.

For no hydrogen gas supply (0 sccm), a minimal growth of 20 μm was obtained. With stepwise rise in amount of hydrogen gas flow, 100 sccm per experiment from 0 to 400 sccm, almost linear increase in CNT film height (or growth rate) is obtained. The CNT film found to have 540 μm height for hydrogen flow rate of 400 sccm. In other words for 4 times increase in hydrogen flow rate, growth rate increased approximately 4 folds. There after, with further increase in the flow rate of hydrogen, negative impact was observed. At 600 sccm flow rate of hydrogen, the growth rate declined and film was 290 μm in height. The growth rate sunk further, with further rise in hydrogen flow rate, however not as drastically as before. The growth rate attends more or less steady state showing minimal change for further increase of hydrogen flow rate. The graph of growth rate vs. hydrogen flow rate is presented in figure 2.17.

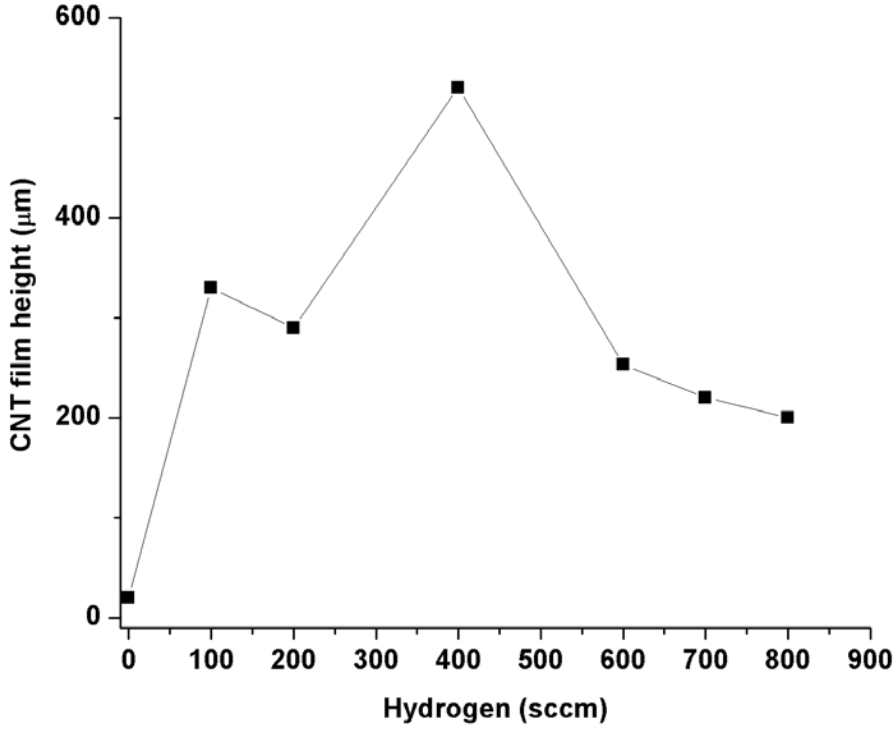

Figure 2.17: Graphical representation of effect of flow rate of hydrogen on CNT growth rate.

The hydrogen content has a indirect influence on the decomposition rate of ethylene. Upon decomposition of ethylene, along with carbon species, hydrogen atoms are released. If the partial pressure of hydrogen in the system is already high, release of hydrogen species or in other words, decomposition of ethylene will be suppressed. In this way, generation of carbon species will be hindered and thus for same amount of water supply, catalyst particles have less carbon species to react with. It delays the catalyst poisoning effect. This effect propagates as a substantial increase in the growth rate of CNTs upon increase in the hydrogen flow rate from 0 to 400 sccm. With further increase in flow rate of hydrogen, decomposition is more suppressed, reducing the supply of carbon species further. Close to 600 sccm of hydrogen flow rate, a stage is reached where supply of carbon species is dropped down to a value lower than requisite for CNTs growth itself. Therefore growth falls down again. Hydrogen can control the decomposition rate of ethylene but cant suppress completely, that is why past 600 sccm flow

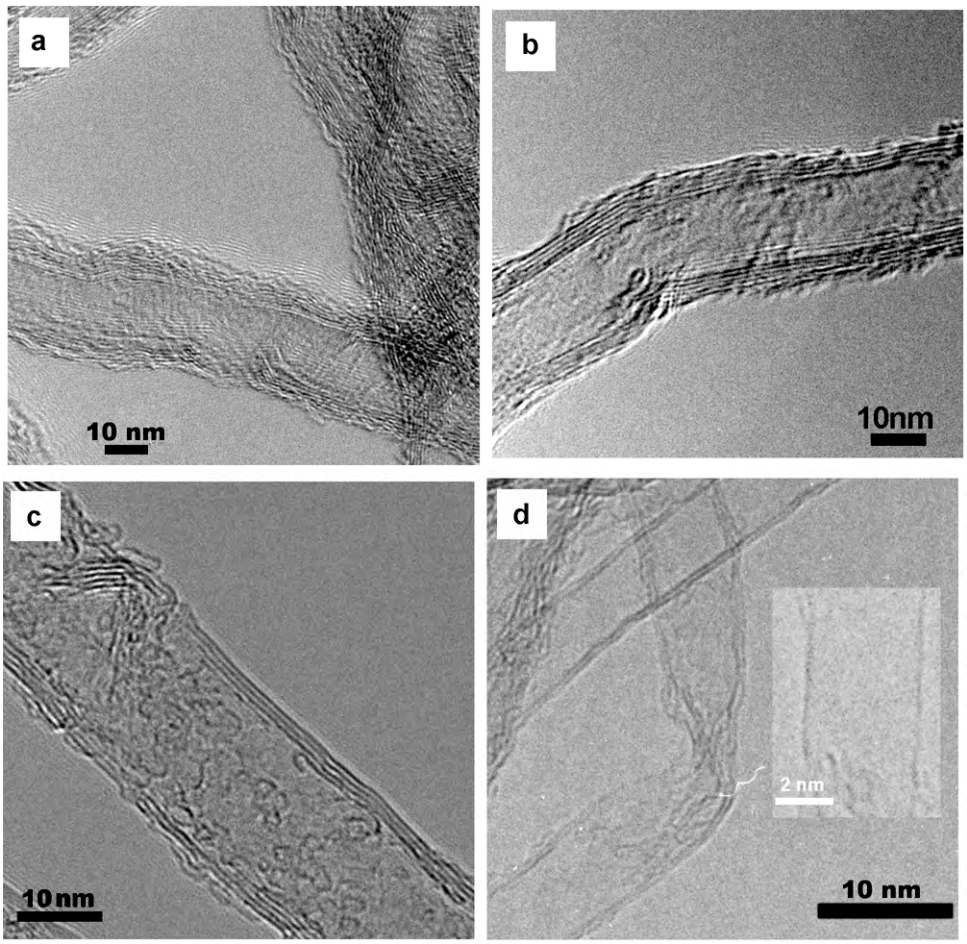

Figure 2.18: TEM micrographs representing the effect of flow rate of hydrogen on CNT typology and purity. The flow rate of hydrogen gas was (a) 100, (b) 200, (c) 300 and (d) 400 sccm.

rate, growth doesn't show any drastic fall in its rate. One can argue, poisoning effect can be nullified for lower flow rate of hydrogen just by increasing the water supply. It is true that higher water supply can be used than using higher hydrogen flow rate. However, hydrogen not only suppress the decomposition of ethylene in order to govern growth rate of CNTs, but also controls the typology of CNTs. Using higher supply of hydrogen, one can fine tune the number of walls of CNTs generated and also level of amorphous carbon impurity; as explained below.

From above experiments, CNTs grown using 100, 200, 300, and 400 sccm of hydrogen were investigated with the help of TEM (see fig.2.18). For lower hydrogen flow rate, a thick layer of amorphous carbon was seen on the side wall of multi walled CNTs. On the other hand for 400 sccm of hydrogen flow, mostly double walled carbon nanotubes were synthesized. A small number of SWNTs were also grown along with DWNTs and CNTs were completely free from amorphous carbon. From TEM micrographs one can confirm, with increase in the hydrogen content CNTs grown were clean and free from amorphous carbon deposits and composed of few graphitic walls (1 to 3). From several experiments, a flow rate of 400 sccm of hydrogen is found to be optimum for the CNT growth.

During heat up the substrate, in order to form nano sized catalyst particles, a flow rate of 600 sccm argon and 400 sccm of hydrogen is used. The flow rate of hydrogen has a minimal effect on the catalyst particle those grown during ramping up, however if at all no hydrogen gas is used during heating up, CNT growth doesn't take place. As explained previously, the thin layer of aluminum and iron tends to oxidize due to air handling. If the film is not reduced before the melting point of aluminum is arrived, particle formation will never take place and so does CNT growth. With higher hydrogen content, lesser will be the reduction time, availing more time for aluminum film to form smaller island. This might influence the particle size determination.

2.2.4 Effect of growth parameter : Water

Water is playing the role of catalyst activator during the growth of CNTs. The oxygen content of water helps in eliminating the poisoning effect of amorphous carbon on catalyst particles. Catalyst stays healthy as long as water supply is on. Inadequate supply of water, more or less, both conditions have adverse consequence on growth rate of CNTs. This effect is studied in detail in this section.

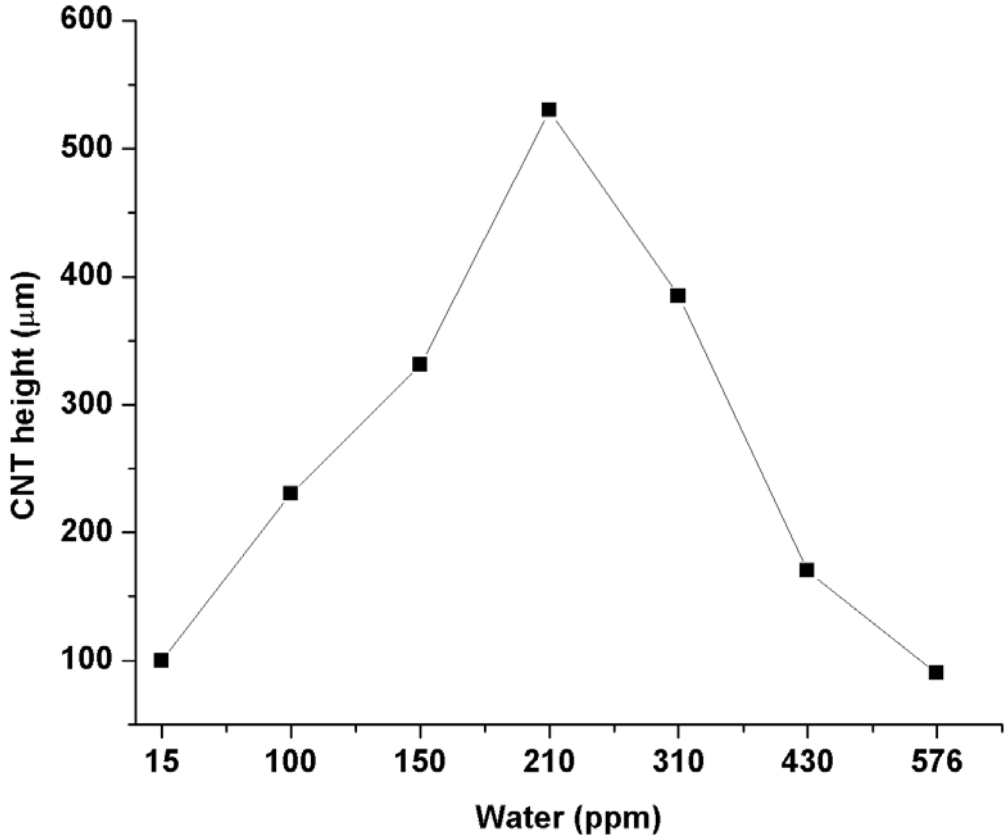

Figure 2.19: Graphical representation of effect of water supply on CNT growth rate.

During the standard growth conditions, 200 ppm of water is supplied by bubbling 30 to 32 sccm of argon through one water bubbler. Using 200 ppm of water, CNTs have been grown with constant growth rate for more than an hour or up to 3 mm length. Even a minor change; few tens of ppm of water have adverse impact on growth rate of CNTs. In order to get experimental evidence, numerous experiments using varying amount of water vapor supply were carried out. Simply, quantity of argon bubbled through the bubbler was manipulated to achieve predetermined ppm value. Starting with 200 ppm, the normal value, 3 sets of data points were obtained on either side. 15 ppm of water content recorded for no argon bubbling through water, 100, 150 ppm for lower side and 310, 430 and 576 ppm above standard value. For every experiments height of CNT film was measured using SEM. A graph showing effect of quantity of water on growth rate of CNTs is as shown in figure 2.19.

From the graph, it is clear that with lower amount of water supply than its needed, at some stage amorphous carbon corrodes the active surface area of catalyst and growth will be terminated. with no supply of water, growth is 100 μm and height of film increases as water amount is increased. At 200 ppm supply, growth rate is modest and catalyst is active for

longer duration. Past the 200 ppm value, the growth rate starts dropping down and for value 576 ppm of water content, growth falls down below 100 μm value. If water content in the system is higher than needed, excess amount of water attack the carbon species responsible for the growth of carbon nanotubes. As carbon species are consumed by excess amount of water; growth retards. It is worth to mention, from higher supply of water, if supply drops down to requisite value, growth will recover. However, once catalyst is poisoned due to lower water supply, it is poisoned and nothing can make it active again. Also apart from the holding catalyst active for longer time, water plays no other role during the growth of CNTs.

The all four important growth parameters were studied to understand their role in water assisted chemical vapor deposition method. The important aspects of this study are summarized below.

- Aluminum not only serves as buffer layer for growth of catalyst nano particles, but also it creates favorable conditions that water can selectively attack the amorphous carbon to hold the catalyst clean.
- Iron has influence on the size of the catalyst particle and thereby on the diameter and typology of CNTs. Thicker iron film will lead to formation of bigger catalyst particles and thus CNTs grown on them will many walled.
- Thickness of iron as well as aluminum should be within predefined range in order to have homogeneous growth of catalyst nano particles of known size.
- Partial pressure of hydrogen indirectly controls the ethylene decomposition rate. This way, it not only supplies requisite amount of carbon for the CNT growth but also controls the typology and quality of CNTs grown.
- Water, a weak oxidant, selectively etch the amorphous carbon to keep the catalyst clean. Inadequate amount, higher or lower, of water is detrimental for CNT growth.

2.3 Study of growth mechanism of water assisted CVD method (WCVD)

2.3.1 Study of morphology and chemical state of the catalyst

The bimetallic catalyst consists of iron and aluminum is a key element in the water assisted chemical vapor deposition method. The detailed study on effect of amount of aluminum, iron

hydrogen as well as water guide to get primary impression that these bimetallic catalyst nano particles should be studied in greater detail in order to understand the exact mechanism of CNT growth. So far it is clear, element aluminum present in the catalyst is responsible for the keeping the catalyst non poisoned and active for longer time. Also from the study of water as a experimental parameter it is clear, in controlled amount, water takes care that amorphous carbon will not corrode the active surface area of catalyst. The question left unanswered is, how two altogether difference processes proceed simultaneously without any conflict. One of them is growth of CNTs via VLS process, in which carbon from vapor phase is dissolved in the catalyst and precipitated from other side in crystalline form. The second process would be preferential activity of water against the amorphous carbon in order to hold the surface area of the same catalyst clean. In order to find an answer to above mentioned question elemental composition, surface chemistry, phase of these catalyst nano-particles should be investigated. To get this information various characterization techniques such as transmission electron microscopy, x-ray photo electron spectroscopy, and gracing incidence x-ray diffraction, attenuated total reflection, Rutherford back scattering tools were employed. Based on these investigations, a growth model for growth mechanism for water assisted chemical vapor deposition method is deduced.

The information about the elemental composition of such small nano particles can only be obtained by using transmission electron microscopy. The major hurdle in carrying out investigation was to find a way with which these particles can be brought on TEM grids. As stated before, aluminum wets the surface of Si-wafer substrate so good that these particles are practically welded to the substrate. The only possible way to investigate catalyst particles in TEM is to grow them directly on TEM sample grids itself. To do so, lacy carbon coated copper grids were chosen as a substrate. As usual, 10 nm thick layer of aluminum followed by 1 nm layer of iron were deposited on carbon coated side these grids. One of them was then inserted inside tubular oven and heated to CVD temperature under same experimental conditions in order to grow catalyst nano particles. On second such grid, CVD was carried out in order to demonstrate growth of CNTs using catalyst particles formed on grid is possible. The demonstration confirming catalytic activity of catalysts particles grown on grid is important to show that they have same nature as of those grown on Si wafer. Both the grids are first investigated in scanning electron microscope to check if particle building has taken place.

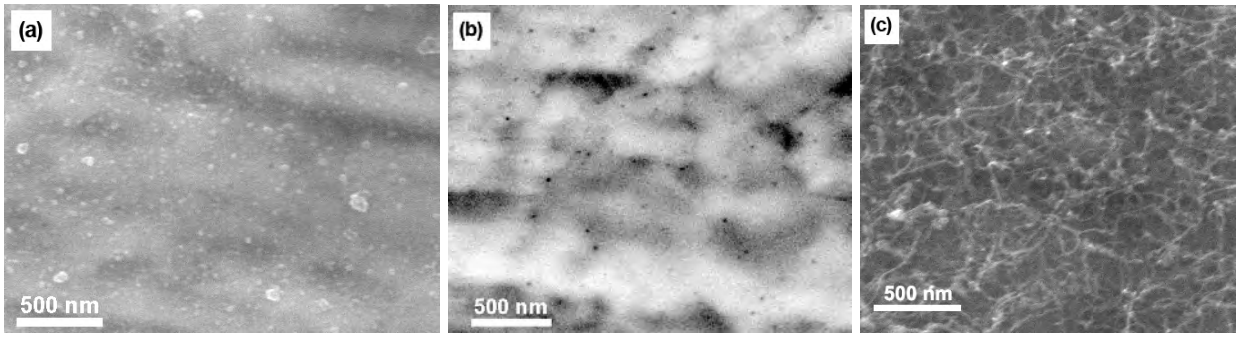

Figure 2.20: Scanning electron micrographs of Al/Fe nano particles grown on different TEM grids (a) on lacy carbon grid (b) on gold grid (c) CNTs grown using Al/Fe particles on TEM grid.

The SEM investigation reveal nano particles composed of iron and aluminum are indeed formed on the TEM grid. Another two grids were deposited one by one with 1 nm iron (no aluminum) and 10 nm thick aluminum (no iron) layer. No particle formation took place in either case. Also TEM grids have an amorphous layer of carbon, therefore those particles can only be formed by inter diffusion of aluminum and iron. SEM micrographs were generated using secondary electrons as well as back scattered electrons. Using back scattered electrons, a good contrasts against the elemental composition can be achieved. From the micrograph depicted in figure 2.20(a and b), one can see the bright contrast of nano particles composed of heavier elements in dark background generated by light carbon. Same particles, if grown on gold grid as a substrate, appear black in contrast against heavier gold that gives rise to brighter background (fig. 2.20b). The micrograph (c) in same figure shows CNTs grown on TEM grid.

The grid consisting Al/Fe nano particles and CNTs were further investigated using scanning in transmission electron microscope (STEM). In TEM machine, the electron beam is generated using 200 KV gun voltage; 10 times more voltage than in normal SEM machine ($\sim$ 20 KV). This serves excellent atomic resolution which is not at all possible in standard SEM. Also,EDAX (energy dispersive analysis of X-rays) and EELS (electron energy loss spectroscopy) were employed to get elemental information about catalyst particles. In addition to them, tomography of one such well grown particles was carried out. Tomography is explained in detail shortly.

Catalyst particles were investigated in scanning mode (see fig 2.21). TEM micrographs revealed a hollow core morphology for the Al/Fe catalyst particles. Each and every particle consists of a cavity at the center surrounded by a bi metallic thin shell. The hollow core diffracts

the electron beam to produce darker contrast. More information about the core can be revealed by producing a dark field image. In dark field mode, image is produced on the screen using the diffracted beam instead of transmitted beam. As the transmitted beam is obstructed by using objective aperture, the part of catalyst originally had brighter contrast produced by transmitted beam, has now darker contrast and the central core part of particle gives rise to brighter contrast. From both the micrographs, one from scanning and one from dark field, one can confirm the presence of a cavity similar morphology rather than through hole.

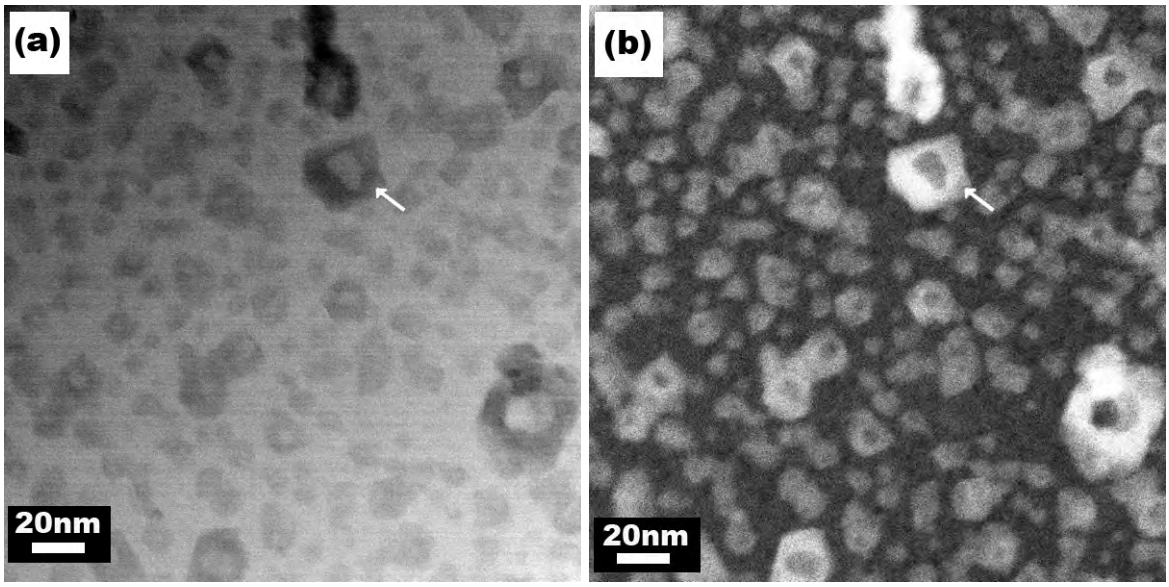

Figure 2.21: Transmission electron micrographs of Al/Fe particles grown on TEM grid (a) bright field image (b) dark field image. Arrows mark the same particle in two different images.

In tomography mode, series of images were taken from different perspective of an object of interest to understand the 3D morphology of it. The different perspectives are made available by tilting the grid holder to a known angle (here over the span of 120°). In order to generate a 3D view of catalyst particle, tomography was carried out on a catalyst particle. A series of snapshots of the tomography video are displayed in the figure 2.22.

The snapshots were taken from different parts of video that lasts for 4 seconds. In order to generate a movie, the complete grid so maneuvered under the electron beam that the center of the solid angle of the grid lies exactly over the center of the particle under attention. Initially at t=0 seconds, the grid is tilted to right extreme position of 60° as shown in figure 2.22a. The pivot point of the tilt is represented by red dot in same figure or red line in snapshot taken at t=0 seconds. The grid is tilted radians by radians in an anti clockwise direction till −60°

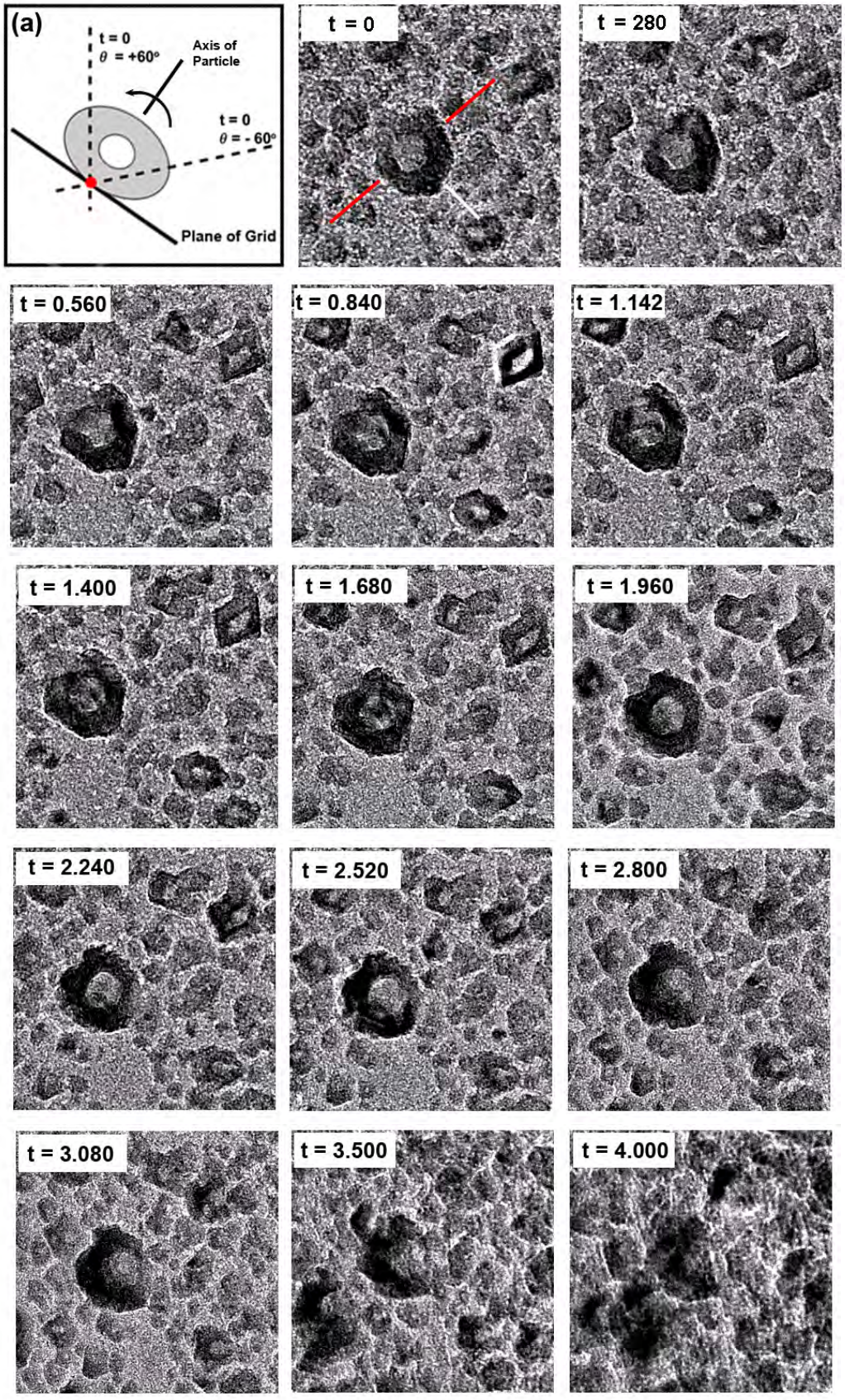

Figure 2.22: Snapshots of the video generated using the tomography tool in TEM to visualize the three dimensional morphology of the catalyst particle. Lap time of taking a snapshot is written on it in milliseconds. (The duration of the video is 4 seconds.) figure (a) is a schematics depicting tilting of a particle inside the microscope.

(total tilt = 120°) position. for every certain degrees of a tilt, an image is taken. The electron beam interacts the particle in a direction perpendicular to plane of the paper. Due to perspective vision, the wall thickness of the particle seem uneven, thinner on left side and thicker on right side of red line. The thickness on the left side starts rising up and on right side it decreases as the grid holding the particle was tilted. At around 2000 milliseconds, the particle is perfectly centered to the electron beam, the axis of particle (white line) and the electron beam are parallel to each other. At this stage, one can confirm the cavity is located perfectly at the central core of the particle. With further tilt, the beam and particle axis are again misaligned giving rise to perspective vision from other side in which wall thickness is thinner on right hand side and thicker on left. Finally, with any further tilt, particle loses the alignment to beam axis completely showing only one side wall at t = 4 seconds.

Tomography leads to confirm the location of the cavity right at the central core of the particle. The formation of such a unique particle morphology is hard to explain and beyond scope of this present work. However, the chemical composition of the catalyst particle is playing a vital role

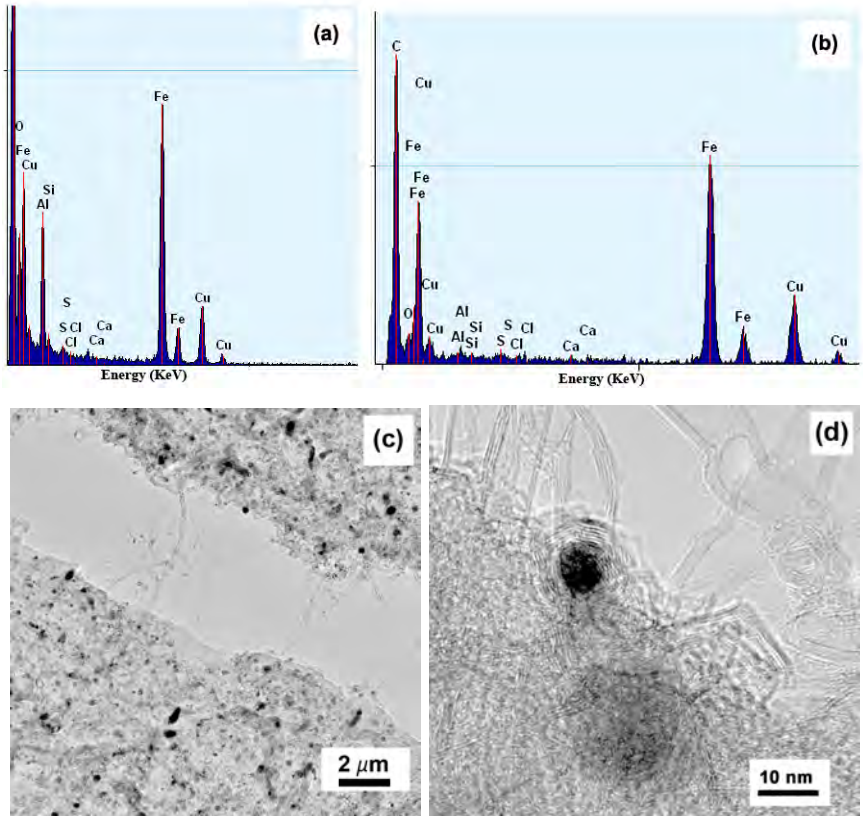

Figure 2.23: EDAX measurement of (a) Al/Fe particles, (b) CNT grown on TEM grid and (c & d) TEM micrographs of same CNTs.

by assisting the growth of CNTs than its morphology. Therefore, further study concentrates on understanding the chemical composition of the catalyst particle.

Energy dispersive analysis of x-ray (EDAX) investigation is carried out on catalyst particles as well as CNTs grown on them. X-rays emitted from the material upon interaction with electron beam possess material characteristics and thus can be studied to find out the elemental information of the particle. Elements iron, aluminum, and oxygen were the constituents of catalysts particles. The other peaks corresponding to elements such as copper are originated from the TEM grid. The composition was not changed even after growth of CNTs. Along with EDAX spectra, electron micrographs of CNTs grown on TEM grids are presented in figure 2.23. The EDAX spectrum gives a broad overview of elemental composition for such small nano particles. Therefore, using a nano probe mode (A mode in which incident electron beam is $\sim$ 1 nm broad) exact elemental distribution of nano particle across its diameter was obtained.

The grid consists of billions of catalyst nano particles. From various parts of the grid, 6 to 8 different particles were scanned using the nano probe mode. One such well resolved particle is displayed in the figure 2.24a. The atomic fringes arose in the micrograph confirms the crystalline nature of the particle. During the measurement, an EELS detector was employed to determine the elemental composition of part of particle interacting with the electron beam. Following the line formed by red dot markings in figure 2.24b, at every dot one EELS spectrum is recorded. The typical EELS spectrum recorded is as shown in fig. 2.24c. From these spectra, a cumulative graph for the concentration of metal across the particle diameter is plotted (see fig. 2.24d-f). Profiles showing distribution of elements iron (fig. 2.24e) and aluminum (fig. 2.24f) across the diameter of a particle are as shown.

The figure 2.24c shows the typical EELS spectrum from numerous catalyst particles for an element iron. During the scan, as soon as the beam approaches the particle leaving the supporting grid, a sudden rise in the intensity of iron and aluminum peaks is observed. The peak intensity keep on rising till the beam reaches the middle point of the particle ring. Past the middle point, the intensity starts falling down. The intensity keep on decreasing till the electron beam reaches the center of the particle. In case of iron, at a center of the particle, energy intensity falls to half of its highest intensity recorded. While for aluminum, it falls completely down to zero value. The intensity profile shows same nature for second half of the particle. It

rises past the center till the middle point of the particle, and then fall down again as and when beam approaches the end of the particle.

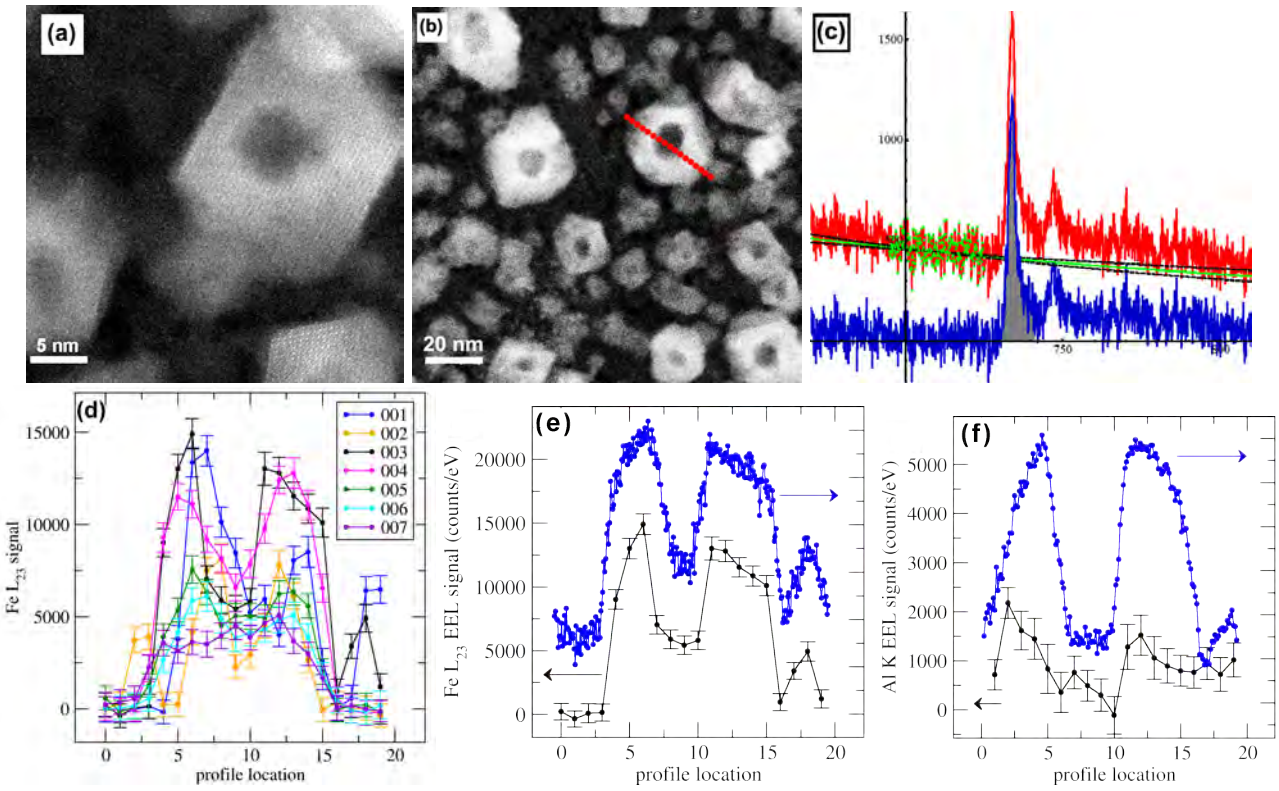

Figure 2.24: (a) High resolution micrograph of Al/Fe particle showing lattice fringes, (b) catalyst particle with scan path, (c) EELS spectrum at one of the scan positions showing Fe peak, (d) cumulative graph of EELS intensity obtained from 7 particles for element Fe, and elemental profile spectra recorded across the particle for elements (e) iron & (f) aluminum.

The catalyst particle consists of two phases. The core is made up of element iron and is surrounded by a mixed phase of aluminum and iron. The formation of such a composition can be a result of complex metallurgical phenomenon. Iron and aluminum both have different density and melting point. The CVD temperature forces aluminum to melt while iron will be still in solid state. As the iron and aluminum have good solubility, atoms of both elements present at intermediate boundary readily form a mixed phase of Al_xFe_y [102,103]. The chemical composition of present catalyst nano particles might be a result of such readily formed inter metallic phase.

X-ray photo electron spectroscopy (XPS) tool is employed to understand the chemical modifications taking place on the surface of these catalyst particles. For this study three samples were investigated. On three cleaned SiO_2 wafers, a fresh layer of 10 nm of aluminum

and 1 nm of iron is deposited. These three wafers were treated to 3 different experimental conditions. Sample No. 1 is heated to CVD temperature and cooled down under standard gas flow conditions. Sample No. 2 is heated to CVD conditions and treated with 200 ppm of water at CVD temperature; 800 °C. The difference of sample 2 over 1 is possible reaction of catalyst particles with water vapor flowing through the system. Third and final sample No. 3 was heated to CVD temperature, CNTs were grown using standard conditions and cooled down. The film was gently peeled off the substrate and the substrate retaining catalyst particles was investigated using XPS technique. All elemental spectra for these three samples are displayed in figure 2.25.

In absence of iron, aluminum reacts with silicon from the substrate wafer to form aluminum silicide as stated before (see figure 2.16). In presence of iron, no aluminum silicide was detected as Al combines with Fe, to form Al/Fe nano particles. The first sample, sample no. 1 has

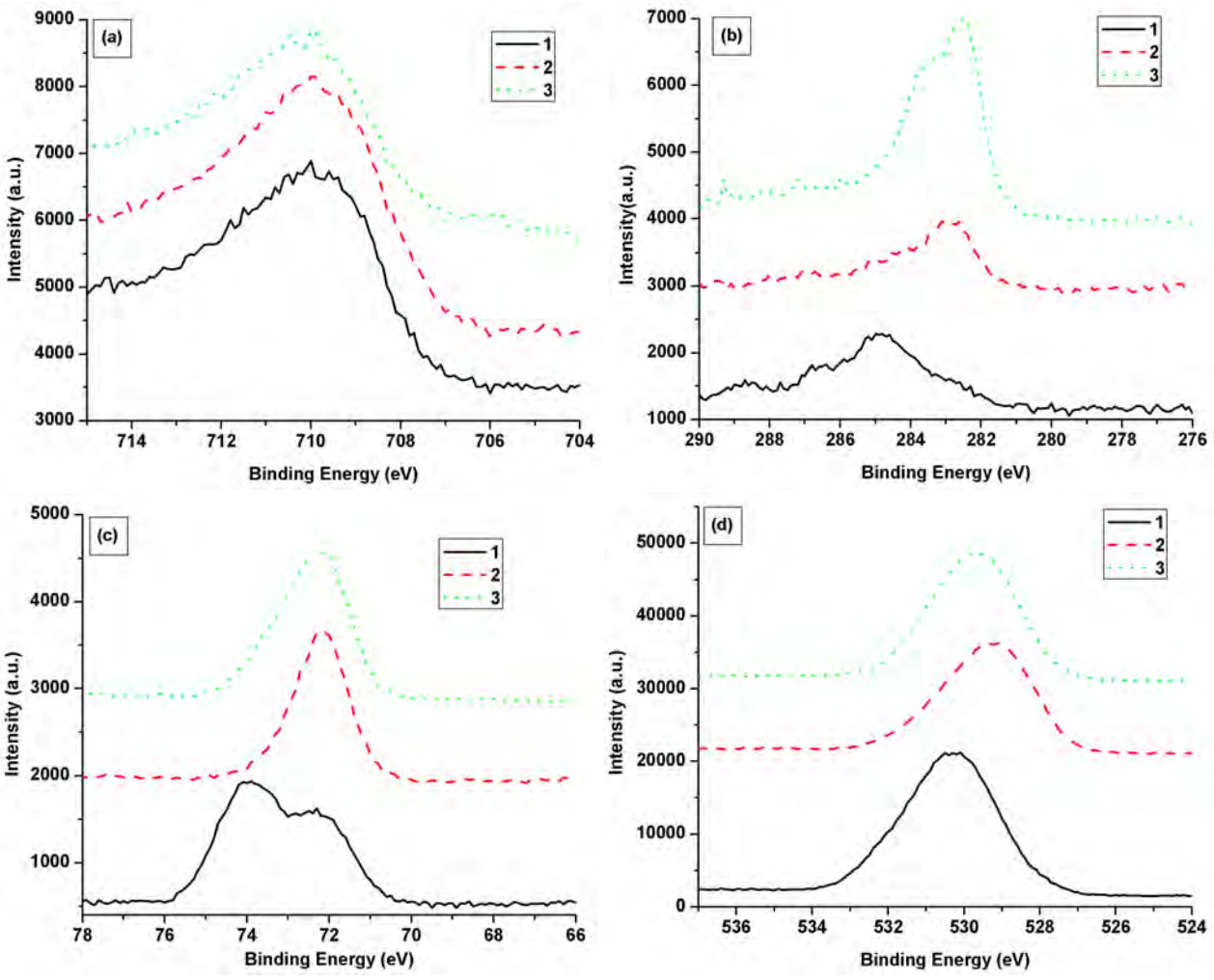

Figure 2.25: X-ray photo electron spectroscopy of Al/Fe catalyst particles supported on Si wafer (a) Fe 3p (b) C 1s, (c) Al 2p (d) O 1s spectra.

aluminum in intermixed phase of metallic aluminum and its oxide (see fig. 2.25c). In other words aluminum is partially oxidized to form Al_xO_y phase [103]. The oxygen comes from the air handling of the sample. The iron peak position is 710.3 eV (see fig. 2.25a) and is also oxidized [104] in similar manner as that of aluminum. Two other elements oxygen (see fig. 2.25d) and carbon (see fig. 2.25b) shows peak position at 530.6 eV and 284.8 eV [105]. The oxygen peak corresponds to oxide state of aluminum and iron while carbon peak symbolizes the presence of graphitic impurity.

The second sample has a minute difference over the first and is treatment with 200 ppm of water before it is cooled down to room temperature. Due to reaction with water, the oxide peak representing deficient aluminum oxide is completely disappeared giving rise to pure metallic aluminum peak. Also the oxygen peak is shifted towards lower energy level. The both spectra ascertain that deficient aluminum oxide reacted with water vapor and is converted to aluminum hydroxide species. This fact is counter confirmed using gracing incidence x-ray diffraction; explained shortly. The peak position for aluminum is recorded at 72.3 eV; 0.6 eV lower than standard value (72.9 eV) [106]. The decrease in the binding energy has several possible reasons. From TEM investigation it is clear, aluminum form the inter metallic mixture with iron, leading to the decrease in the binding energy [107]. Also, as aluminum layer is very thin, and it tends to agglomerate to form clusters upon heating. The small clusters induce further shift in the peak position as well as increase in the peak intensity [103]. Apart from this, carbon peak which was previously at graphitic position (284.8 eV) is shifted to metal carbide position with binding energy of 282.4 eV [108]. This is another effect of water, in which water helps to chemically bind the carbon atoms to metal nano particles.

The third sample, on which CNTs growth was carried out, shows enormous rise in the carbon intensity. The carbon peak, in this case, is composed of two peaks one at 282.6 eV and another at 283.4 eV. The prior peak corresponds to aluminum carbide as explained before. The new born shoulder peak is designated as aluminum oxy carbide(Al-O-C) peak [109–111]. The energy difference between Al 2p peak and oxygen O1s peak is (529.62-72.3) 457.32 eV; much higher than value for aluminum oxide (456.9 eV) [112] confirming the presence of aluminum oxy carbide instead of aluminum oxide. The oxygen peak in both cases, sample 2 and 3 is broad representing various oxygen species viz. hydroxide, oxycarbide, oxy hydroxide. Also the quantitative analysis obtained from XPS spectra give atomic ratio of constituent elements

for all three samples and is listed in the table 2.2 below. The oxygen content is more than 60% on atomic scale for all three samples. The oxide state of iron and aluminum composed of much lesser oxygen atoms. The presence of high amount of oxygen can lead to conclusion that excessive amount of oxygen molecules can only be present in form of adsorbed oxygen species (such as hydroxide or oxyhydroxide) on the surface of catalyst particles. On the other hand, iron was alway in oxidic state, however from its binding energy value, its hard to differenciate whether it is pure oxide or oxy hydroxide. In order to get further clues to confirm the exact state of oxygen Rutherford back scattering, attenuated total reflection, and x-ray diffraction tools were employed. First two techniques fail to deliver any result as nano sized catalyst particles fall below detection limit of these tools. X-ray diffraction in grazing incidence mode gave information about oxidic state of iron as well as aluminum.

Table 2.2: Quantitative elemental analysis (atomic %) of catalyst particles obtained from X-ray photoelectron spectroscopy

sample No.	Iron	Aluminum	Carbon	Oxygen
1	2.2	25.1	8.1	64.6
2	4.6	21.6	12.4	61.4
3	2.3	21.9	22.6	53.2

The sample 1 and sample 3 are prepared once again as described above. Two samples are investigated using the gracing incident x-ray diffraction. X-ray diffraction plots are as shown in figure 2.26. The sample 1 shows nice metallic peaks for aluminum as well as iron. It indicate both deposited metal layers are more or less still in metallic form. These metallic peaks were completely disappeared in the sample 3, giving sharp peaks in the range of 50 to 60° of 2θ. These three peaks corresponding to iron oxyhydroxides, aluminum hydroxide and oxyhydroxides respectively [113, 114]. Aluminum was recorded in dual phase; aluminum hydroxide and aluminum oxyhydroxides. Iron on the other hand, was found only oxyhydroxides phase. XRD results prove the previous prognosis made about presence of excess of oxygen molecules in form of hydroxyl group on surface of catalyst particles. These hydroxyl groups are key players in keeping the active surface area of catalyst clean during the growth of carbon nanotubes and explanation about their role follows shortly. At first, salient points of TEM, XPS and XRD investigations are summarized and listed below.

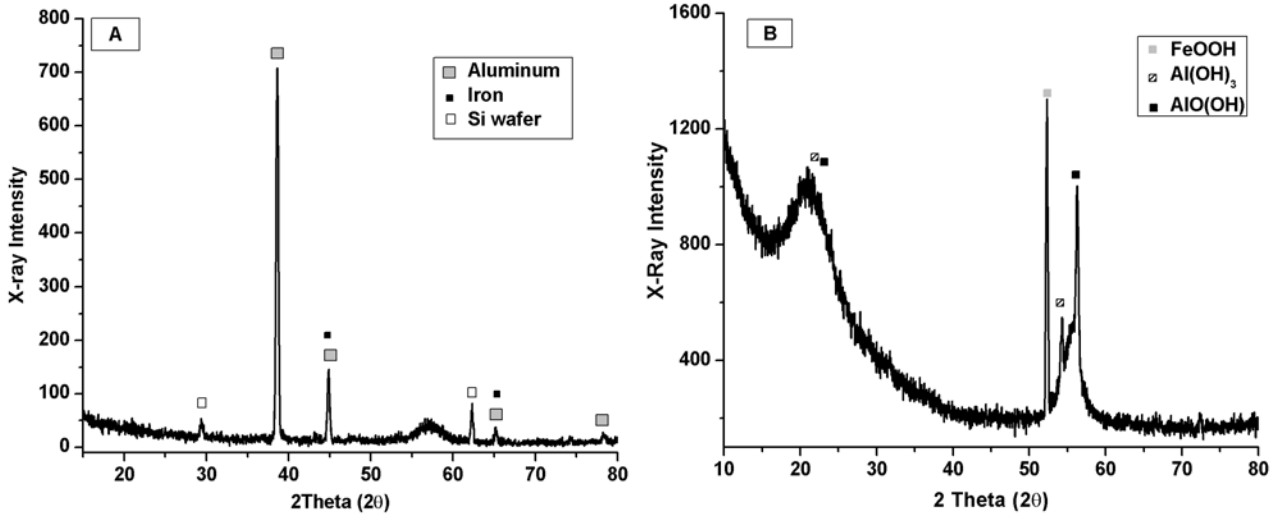

Figure 2.26: X-ray diffraction plots of Al/Fe catalyst particles supported on Si wafer (a) before CVD (b) after CVD.

- Catalyst particle are composed of two parts; central part made up of pure rare earth metal iron and is surrounded by bimetallic phase of iron and aluminum
- Water vapor supplied reacts with catalyst nano particles to form of hydroxyl groups on the surface of catalyst particles.
- The metal catalyst particles were found to be in phase of metal hydroxide, oxyhydroxides form.
- Carbon from gas phase(responsible for catalyst poisoning) is found to be chemically bonded with the catalyst particles by forming surface bonds in form of oxycarbide and carbide species.

Aluminum present in aluminum oxy carbide phase is often trivalent [109, 110]. Apart from having bonds with carbon and oxygen, aluminum is either bonded with neighboring aluminum or iron atom. Recently, a curious behavior of aluminum clusters at nano scale against the water molecules is published [115]. It gives experimental evidence that aluminum indeed reacts with water molecules to generate the hydroxyl groups on its surface. Donut shaped small catalyst nanoparticles composed of iron and aluminum should be emulating same nature as of aluminum clusters against the water molecules. These hydroxyl groups are further utilized to oxidize unused carbon species and convert them into carbon monoxide and carbon dioxide molecules. Such activity is often reported in the catalysis literature of gold supported on metal

oxide particles [116–118]. During oxidation of CO using gold on metal oxide particles, hydroxyl groups present on oxide surface helps in binding CO molecules from gas phase. Same way here, unused carbon species are selectively attacked by hydroxyl groups to convert them into carbon mono or dioxide molecules. Harutyunyan and coworkers have detected CO and CO_2 gas at exhaust during their study on thermodynamics of CNT growth [119]. Depending upon all these results; a growth model is put forth demonstrating a continual process of hydrolysis of the catalyst surface and a precise action of such hydroxyl groups against unused carbon species to keep the catalyst clean and active for longer time in order to grow carbon nanotubes to millimeter long length.

2.3.2 Reaction mechanism of water assisted CVD method

Based on the above mentioned results, a growth model explaining the selective activity of water against the catalyst poisoning is displayed in the figure 2.27. This model demonstrates the activity of water against the unused carbon which is responsible for the deactivation of the catalyst. As the catalyst is held clean and active for longer time, the growth of CNT up to a millimeter length is possible. At beginning, the catalyst particles are not completely free from oxygen species (as seen in XPS investigations). These oxygen atoms are present either in form of hydroxyl groups or partial metal oxide form. Upon the supply of carbon precursor (ethene gas), carbon species are generated by decomposition of ethene. These carbon species are docked on the surface of the catalyst particles. Out of several docked species, many of them diffuse through the catalyst and used to grow CNTs. Few, those unused, stay docked reducing the active surface area of the catalyst. As the process is continuous, the rate at which carbon species interact with the catalyst particle and the rate of usage to grow the CNT should match. If it doesn't, then a alternative method is needed to remove these unused carbon species. By employing an alternative method, total active surface area of catalyst can be held unchanged.

As shown in the growth model, stage I depicts the condition of the catalyst just before the start of CNT growth. During CVD conditions, carbon species generated in the gas phase come in contact with catalyst particle. Most of the carbon species are dissolved in the central core of rare earth metal and with the help of vapor liquid solid (VLS) mechanism and CNT grows from the top side of this catalyst particle. At a same time, carbon species those are not utilized for CNT growth, are bonded to catalyst particles forming carbide and oxycarbide species.

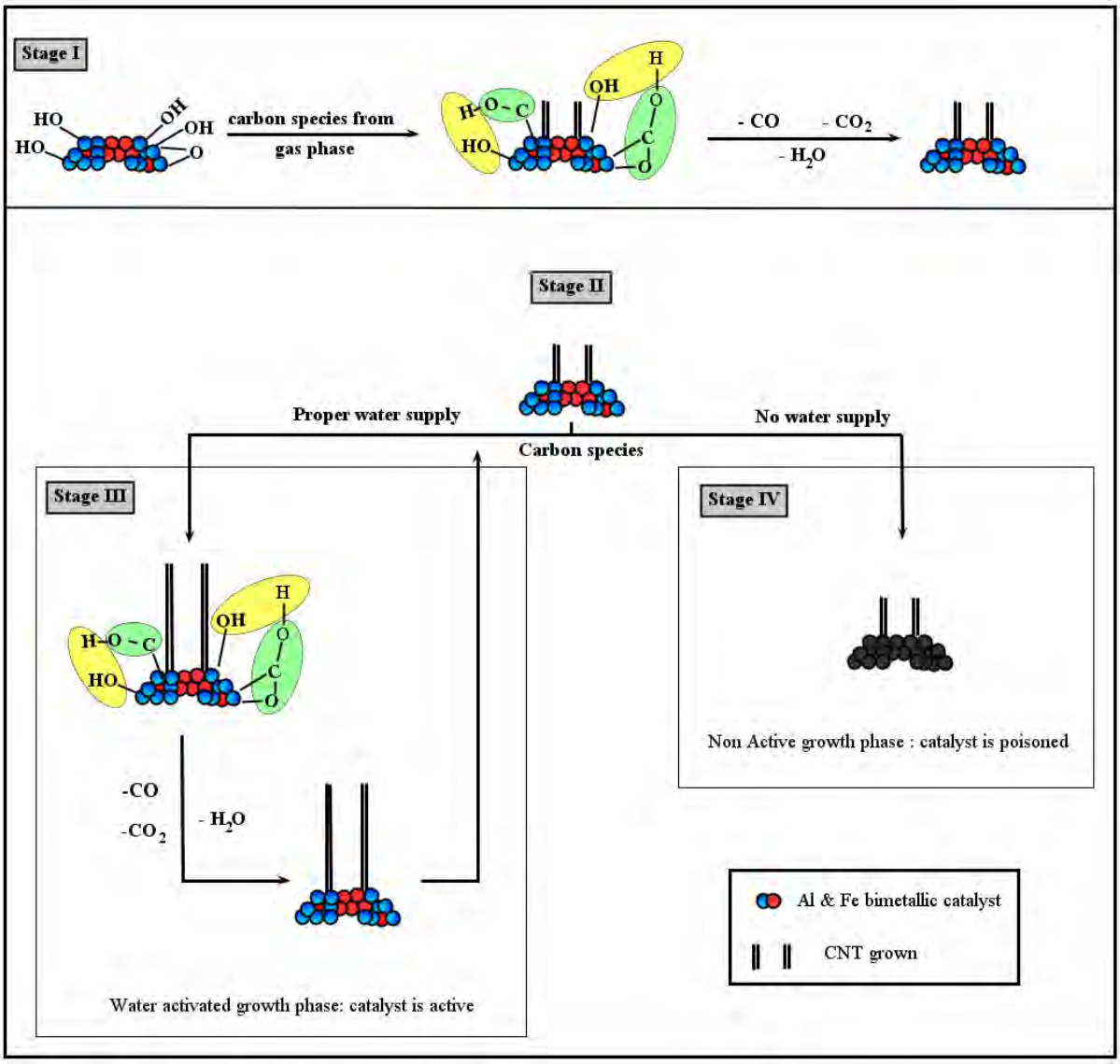

Figure 2.27: Pictorial representation of possible growth mechanism of carbon nanotubes. The mechanism explains how supplied water vapor keeps catalyst active and clean.

Then, these carbon species recombine with oxygen atoms to form carbon monoxide or carbon dioxide and released from the surface into gas phase. The generation of carbon monoxide and carbon dioxide molecules by consumption of oxygen from the catalyst particle is experimentally demonstrated [119]. The consumption of all oxygen atoms present on the surface in form of -OH groups leads to the stage II.

The stage II is condition where the catalyst needs urgent supply of fresh water molecules; those can hydrolyze the catalyst surface creating new -OH groups. In absence of these fresh hydroxyl groups, the catalyst will not be able to keep its surface free from carbon deposition. It means sooner or later catalyst will be completely covered with a thin layer of carbon leaving

behind no place from where new carbon species can diffuse into the catalyst for the growth of carbon nanotubes. This condition is as shown in stage IV. The condition is often termed as catalyst poisoning. Once the catalyst is completely poisoned, any amount of water supply can't regenerate it. This is because thin layer of carbon barricade water to hydrolyze the catalyst surface. The time required to reach the stage IV is 2 to 3 minutes after the start of supply of ethylene gas. Thus, best possible timing to start supply of water is right from the beginning of growth process. This is because any delay between start of carbon precursor and water will lead to lose of active surface area.

On the other hand, at stage II, if adequate amount of water vapor is supplied along with ethylene, formation of new hydroxyl groups on the surface of catalyst will take place. On one side, these fresh hydroxyl groups will continue to etch away the unused carbon species from the catalyst surface and on the other side CNTs keep on growing as carbon continue to diffuse into the catalyst particle. This is termed as stage III. Even in stage III, if supply of water is lesser than adequate amount (200 ppm), catalyst will slowly but certainly get poisoned reaching stage IV. In other case, if water supply is more than 200 ppm, catalyst surface will be excessively hydrolyzed. This leads to drop in CNT growth rate as excessive -OH groups attack carbon species responsible for CNT growth. This effect is experimentally demonstrated in previous part "Effect of water as a growth parameter" (see chapter 2.2.4 above). In order to achieve highest possible CNT growth rate, following three process should carried out in a balanced manner.

1. Adequate supply of carbon species those will diffuse into the catalyst particle in order to grow the CNT.

2. Appropriate supply of water that will hydrolyze the catalyst surface forming appropriate amount of hydroxyl groups.

3. Conversion of non diffused carbon into CO and CO_2 molecules by these hydroxyl groups and there by keeping catalyst surface clean and active.

The growth rate is also depends upon the purity of reactant gases. In an introductory work from Hata et.al., the growth rate as high as 200 μm per minute (2 mm growth in 10 minutes) was achieved by using 99.999998% (termed as 8.8) pure reactant gases [7]. In our case, growth rate is 30 μm per minute (1 mm in half an hour) as purity of gases used is 99.998%

(termed as 4.8); four times poor in quality. Ethylene and argon gas contain other long chain hydrocarbons as an impurity which might decompose to produce other carbon species which might be detrimental for CNT growth.

The growth model is based upon the results of various investigation carried out on the catalyst particle. At present there is no complete experimental understanding about which kind of carbon species are generated and among those generated which species diffuse through the catalyst for CNT growth. From present study it is clear, type or types of carbon species diffuse thought catalyst to grow CNTs, same are responsible for the catalyst poisoning. Future studies should concentrate to understand which kind of chemical state these species bear in order to form chemical bonds with surface hydroxyl groups. This information will help in understanding the phase of the catalyst during the transformation from stage I to stage II.

2.3.3 Analytical understanding of the morphology of bimetallic catalyst nano particles

From the present discussion and results of characterization techniques, it is clear that iron and aluminum film deposited on Si-wafer diffuse to form bimetallic nano particles upon heating. The thickness of aluminum as well as iron carry a intriguing effect on the formation of these nano particles. From previous understanding of particle building from the literature one can vaguely explain the formation of bimetallic nano particles and there by its impact on the growth of CNTs.

The effect of thermal energy on Fe - Al or Fe - Al_2O_3 interfaces is studied by various research groups [103, 107, 120]. The iron layer, irrespective of the substrate, tends to agglomerate upon heating to higher temperature. This is experimentally demonstrated and nice nano particles of iron obtained from 0.8 nm thick film on the Si-wafer are as shown in figure 2.15a. However, if iron is deposited on the aluminum film, during deposition itself, iron and aluminum atoms build up inter metallics layer at the interface. This layer at the interface grow thicker upon heating to higher temperature [103]. Aluminum atoms migrate to dissolve into Al/Fe interface and at the same time, top iron atoms agglomerate to build small nano particles. At certain temperature, presumably close to melting point of aluminum (660 °C), the Al/Fe interface layer completely assimilates with the aluminum layer forming Al rich inter metallic phase of iron and aluminum. This explains the two phase morphology of the catalyst particle with iron core surrounded by metallic mixture of Al and Fe.

At this stage, if quantity of any metal deposited, iron or aluminum, changed drastically, the process of particle building as well as formation of two phases should get affected. To investigate this, 2 nm thick layer of iron was deposited on the 6, 8, 10 and 15 nm of aluminum. The samples were heated to CVD conditions and then cooled down to study using AFM technique (see fig. 2.28). With thicker layer of iron, the particles formed up are relatively bigger and even more importantly inhomogeneous. The particle morphology is inconsistent and instead of regular nano particles of bimetallic phase large grains with small and spherical nano particles were seen.

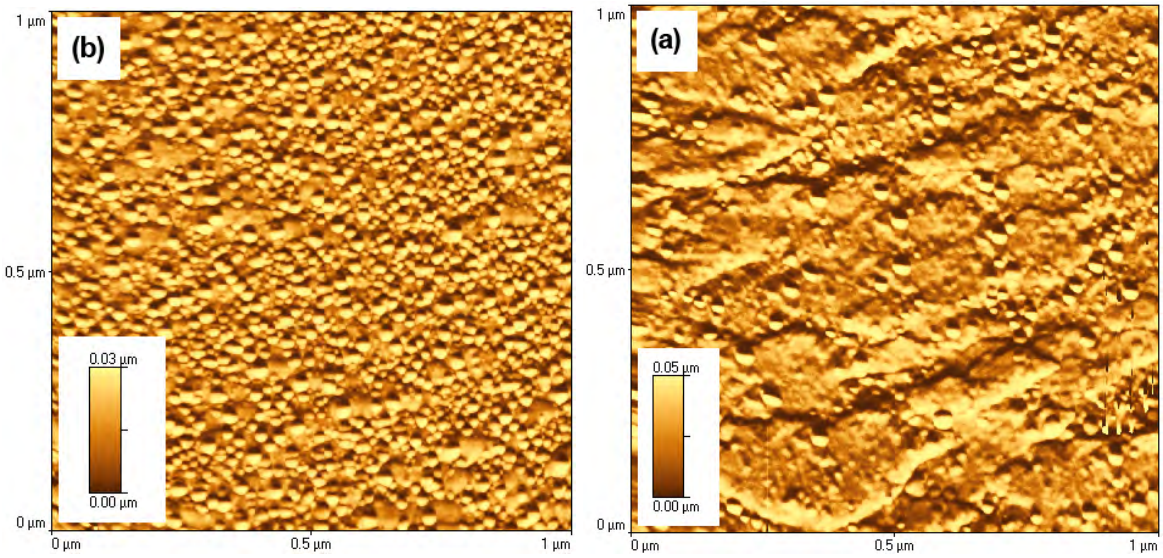

Figure 2.28: AFM micrographs of Al/Fe nano particles obtained by heating bi layer film of composition (a) 2 nm Fe on 8 nm Al and (b) 2 nm Fe on 15 nm Al.

The increase in thickness of iron will lead to building of thicker Al/Fe interface. Thicker the interface, lesser are the chances that it will melt and assimilate with rest of the aluminum to form the homogeneous bimetallic mixture. This is because, compared to previous case, interface layer will be rich in iron and thus need higher temperature for melting (as melting point of iron is higher). On the other hand, in case of thicker aluminum, Al/Fe interface will be thinner. It will melt and assimilate to form Al rich phase. In both cases, requisite composition will not be met. This will lead to formation of inhomogeneous phases. In a situation of lack of proper phase, requisite hydrolytic activity of the catalyst will not be met. It means it can be either too high or too low, which is as explained above detrimental for the CNT growth. Therefore amount of iron as well as aluminum should be in stipulated range.

2.4 Study of morphological aspects of carbon nanotubes

Graphite is considered as a reference material for the study of carbon nantoubes. However, unlike to graphite, CNTs have circular cross section inducing partial sp^3 characteristics in sp^2 hybridized carbon carbon bonds. Such change lead to intriguing effect on the physical properties of carbon nanotubes, one most important among all is their electronic nature. CNTs can be thus metallic or semiconducting in nature; decided by their diameter and chirality. Such an elegant property is inherited from admixing of sp^3 characteristics with sp^2 bond inducing known band gap.

Chirality is another geometrical factor that has strong influence on properties of CNTs. Armchair, zigzag or chiral; type of chirality that CNTs grow with, is defined by the catalyst particle. In other words, chirality of CNTs is decided by the orientation of crystal structure of catalyst particle through which carbon atoms diffuse to form crystalline CNTs. A correlation explaining the dependence of the chirality over the crystal structure of the catalyst is needed.

The effect of curvature on chemical state of carbon atoms can be investigated using nuclear magnetic resonance spectroscopy (NMR) of ^{13}C enriched carbon nanotube. In addition, selected iron clusters made up of 30 to 60 atoms per cluster can be used as a catalyst to grow CNTs. These clusters have defined diameter and crystal structure and thus CNTs grown on such clusters can be studied for their chirality based upon catalyst size and orientation. The both experiments are discussed below.

2.4.1 Nuclear magnetic resonance spectroscopy (NMR) of ^{13}C doped CNTs

Nuclear magnetic resonance (NMR) spectroscopy exploits information about chemical environment of an element. Although NMR measurement is dependent on magnetic spin of nuclear entities, atoms in a molecule can resonate at slightly different frequency depending upon their chemical environment.

In case of carbon nanotubes, the nucleus of a carbon atom consists of 6 protons and 6 neutrons and thus the nucleus is invisible in NMR spectroscopy. Therefore, during growth, ethylene gas with ^{13}C isotope is used along with ^{12}C ethylene to enrich the CNTs. CNTs grown here are double walled and have an average diameter of 6 to 8 nm. Small diameter will lead to curvature effect explained before, giving rise to change in the σ bond angle. Such change in bond angle will

lead to departure of bond from sp^2 characteristics and add in sp^3 properties. With the help of NMR technique, these changes can be detected in terms of a difference in the chemical shift.

The experiment starts with synthesis of ^{13}C doped carbon nanotubes. The CNT growth was carried out using standard procedure (see experimental part) with a minute change. Alike standard growth conditions, 100 sccm of ethene was used, but in this case, coming from two different sources. Out of 100 sccm, 68 sccm ethene was normal ^{12}C isotope, while rest 32 sccm ethene was enriched with ^{13}C isotope. Prior to entering the reaction zone, 32 sccm part of ethene was bubbled through a water bubbler to carry required quantity ($\sim$ 200 ppm) of water vapor. In 20 minutes of growth time, 2.6 mg of CNT mass was synthesized. As 32% of total carbon supply was from ^{13}C isotope, CNT mass grown is presumed to have 32% of ^{13}C enrichment.

The experiment starts by pulsing the sample at 5 KHz. The measurement was carried out at 15 KHz, utilizing pulse sequence with pre-saturation and various relaxation delays; for example 4seconds, 16s, 32 s etc. The best obtained spectrum along with the Gaussian fit is as shown in the figure 2.29. The spectrum is superimposed image of various peaks, 8 precisely, recorded at 135, 127, 119, 114, 109, 105, 95 and 82 ppm relative to TMS. Carbon nanotubes synthesized are mostly (90%) double walled carbon nanotubes with 5 to 10% of single walled CNTs. Also, CNTs depicts metallic as well as semi conducting electronic characteristics. Therefore, numerous permutations are generated. The first two permutations would be in case of small percent single walled carbon nanotubes, those can depicts metallic or semi conducting nature. The next four permutations are for double walled CNTs; both CNTs of DWNT are metallic, both are semiconducting, inner metallic with outer semiconducting and vice versa. In this manner, altogether 6 different permutations are possible. All six permutations are listed in table 2.3. As

Table 2.3: Different permutations for carbon nanotubes grown using water assisted CVD method. (M - metallic & S - semiconducting)

Type of CNT	Inner tube	Outer tube
SWNT	M	-
SWNT	S	-
DWNT	M	M
DWNT	S	S
DWNT	M	S
DWNT	S	M

in case of double or many called CNTs, intertube coupling exists ($\pi - \pi$ interactions) and it will show a pronouced effect on the peak intensity in NMR spectroscopy. Also, not to forget, metallic nanotubes have shorter relaxation time compared to semiconducting [121].

Introductory studies of MAS - NMR studies on CNTs have reported isotropic value of 124 ppm for SWNTs [121, 122]. The peak was deconvoluted in two components, one attributed to metallic while another for semi conducting with separation of 10 ppm [121]. As per literature, two peaks from present spectrum, 127 and 135 ppm , are accounted for single walled carbon nanotubes. The 135 ppm peak can also be attributing DWNT constituting of two co-axial CNTs having metallic characteristics. The semi conducting one are found to be contributing to lower ppm value. Higher the fraction of CNTs those possess semiconducting characters, more will be the shift towards lower value. Hayashi et.al. presented their work showing peak position at 116 ppm. They conclude the shift is due to higher value of semi conducting component [123]. The peaks recorded as 119, 109 and 114, 105 corresponds to DWNTs with permutations inner metallic - outer semiconducting and inner semiconducting - outer metallic respectively. The lowest intensity peaks 94 and 82 arose from DWNTs comprised of semiconducting CNT. CNTs

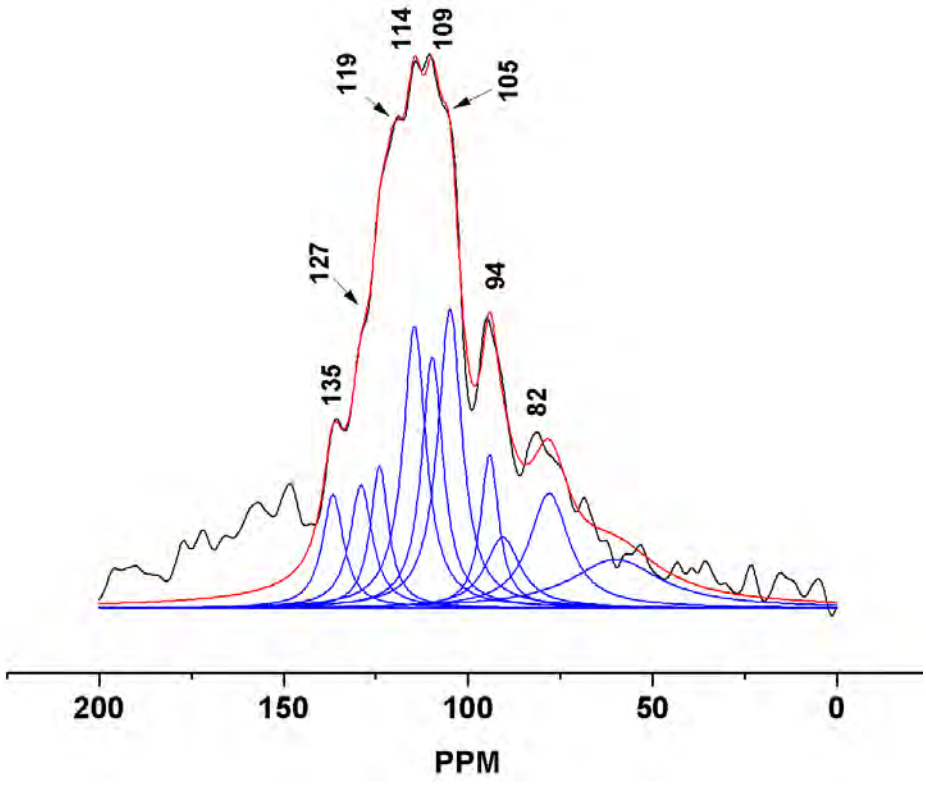

Figure 2.29: ^{13}C MAS-NMR spectrum of carbon nanotubes synthesized using water assisted chemical vapor deposition method.

measured here are pristine or as synthesized, containing neither metallic impurity nor functional groups. Therefore, neither low nor high field peaks are observed corresponding to metal carbide or outer functional groups [121, 123].

NMR gave spectroscopic evidence that CNTs are free from amorphous carbon, metal impurity or even defects. Also from the spectrum obtained, one can confirm that DWNTs have at least one out of two co-axial tubes semiconducting in nature. The diameter difference between two co-axial tubes will be 0.68 nm, too small to produce positive effect. Therefore, it leads to conclusion that, two tubes might have different chirality to depict such altogether different electrical behavior. It's intriguing to separate metallic from semiconducting tubes and study them again in detail. In that case, following experiments are thought out.

As majority of the CNT mass is formed by semiconducting tubes, it would be therefore interesting to cool CNTs below room temperature ($\sim$ 60 K) to convert semi conducting CNTs into insulating one and measure the spectrum again. By this way, only metallic CNTs can be measured. Another possibility would be to deposit nano particles of platinum on CNTs by self reduction method [47] and study the sample in MAS-NMR. Such platinum nano particle will dope the outer CNT, converting them into metallic nature. It would also help to understand electrical interactions between platinum nano particles and CNTs. Also, CNTs having outer shell with semi conducting characteristics will be deposited with metallic nano particles leading to change in electronic behavior or in terms of NMR, relaxation time will decrease. In future, both experiments will be conducted.

2.4.2 Metal clusters mediated growth of CNTs

Metal clusters with defined number of atoms possess particular geometric shape. Such clusters are obtained by laser ablation of metal of interest (which is iron in this case) under ultra high vacuum conditions. These clusters, depending upon their size and number of atoms they are made up of, can bear positive or negative charge or can be neutral. A schematic of an experimental setup used for generating clusters is as shown in figure 2.30 [124]. With the help of Nd:YAG laser, metal is practically evaporated in a helium atmosphere. The generated clusters are accelerated with the help of time-of-flight mass spectrometry (TOF-MS) [125]. The velocity that cluster gains in TOF-MS is directly dependent to their mass. The accelerated stream of metal clusters was then carried through different lens and selective clusters of predetermined

size were separated with the help of a electrostratic mirror. The separated clusters were detected with the help of multi channel plate (MCP) detector and clusters with known number of atoms were deposited on the desired substrate by diverting the beam using an electrostatic mirror (see fig 2.30). A mass spectrum of iron clusters of different sizes generated is as shown in figure 2.30b [124]. Iron clusters deposited on the TEM grids were used to catalyze the growth of carbon nanotubes. More information about the clusters synthesis, quantification and filtering methods can be found in numerous articles [115, 124–126].

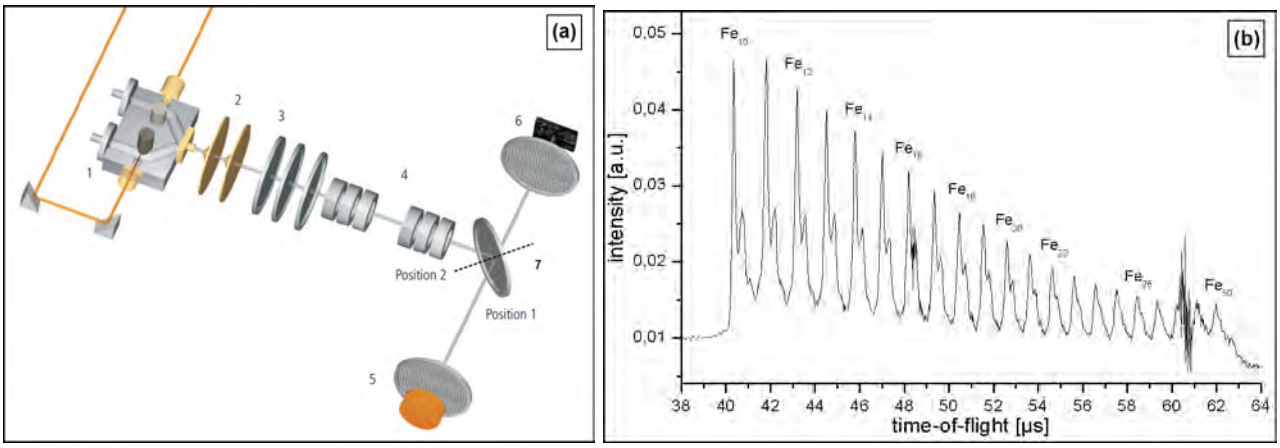

Figure 2.30: (a) A schematic of a standard setup for producing metal clusters. In same figure (1) Nd:YAG laser (2) double skimmer (3) Accelerating grid (4) different lens (5) MCP detector (6) sample to be deposited and (7) electrostatic mirrors. (b) A mass spectrum of iron clusters of different sizes generated [124].

The first important task during this work is to deposit a percent of (1 to 5%) mono layer of these clusters on the substrate and study their behaviour at high temperature (CVD temperature). As the final aim of this work is to study morphological aspect of CNTs grown on size selective clusters with the help of electron microscopy, TEM grid was chosen as a substrate. TEM grids having a thin layer of amorphous carbon or silicon monoxide were selected for this study. Clusters in a range of 20 to 80 atoms comprising size between 0.4 to 1 nm in diameter were selectively deposited on the TEM grids. These small clusters with known shape will catalyze the growth of carbon nanotubes. However, before it, clusters deposited on grid were tested for their stability against annealing at CVD temperature.

Clusters of definite size deposited on TEM grid were heated to 800 °C following the CVD condition and cooled down to room temperature. The study shows, clusters are indeed not stable and tend to agglomerate at higher temperature. TEM investigation show, from clusters

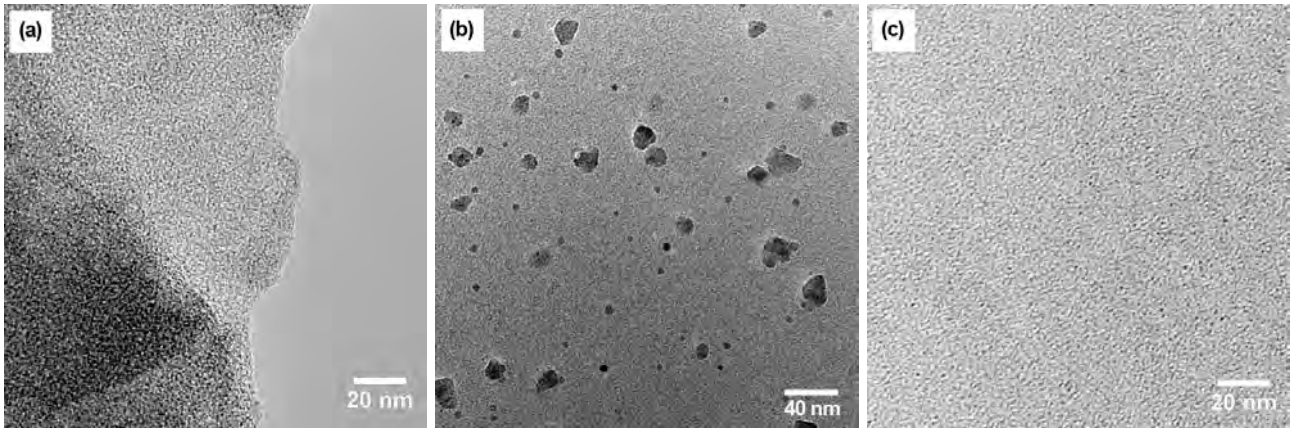

Figure 2.31: Transmission electron micrographs of iron clusters deposited on TEM grid (a) before heating, (b) after heating, (c) implanted in Al layer and after heating.

of 0.6 to 0.8 nm diameter, particles as big as 5 to 8 nm were formed (see fig. 2.31b). During deposition, clusters were accelerated by applying strong electrical field that they practically get implanted in the substrate surface. However, it didn't help much to hinder the agglomeration. As a next step, before depositing clusters on TEM grid, a thin layer of aluminum (10 nm) was deposited on grid and clusters were then implanted in this Al layer. The grid was studied once again in TEM to examine tendency of agglomeration. Indeed, clusters were found to be stable and agglomeration was hindered (see fig. 2.31c). A homogeneous cluster distribution was seen and no agglomerates or bigger particles of iron were observed. TEM micrographs of iron clusters, before and after heating, are as shown in figure 2.31.

Following the methodology explained above, six new TEM grids were deposited by a 10 nm thick layer of aluminum. Upon this layer, clusters of different sizes were deposited. For the present case study, clusters comprising particle size 0.4 to 0.6 nm, 0.6 to 0.8 nm and 0.8 to 1 nm were deposited on 6 different grids. All grids were heated to 800 °C and CNTs were grown using water assisted chemical vapor deposition method. All 6 grids are presently under TEM investigation to study the morphology of CNTs grown on such small clusters.

The diameter as well as chirality of carbon nanotubes grown is strongly influenced by the size and morphology of the catalyst particle. As clusters have definite size and morphology, with the help of high resolution TEM studies, one to one correlation could be found between cluster size and diameter of CNT grown on it. The chirality of CNT grown with the help of catalytic activity of such small clusters will be definite. It will help to tune the growth condition to grow CNTs of selective chirality.

2.5 Horizontal growth of individual carbon nanotubes

Carbon nanotubes depicts semiconducting characteristics with high current carrying capacity [5]. CNTs are therefore, ideal material for fabricating transistors and thereby various devices and sensors. For this purpose, as grown CNTs should be highly crystalline and more important, semiconducting in nature. Even a small amount of metallic characters will lead to loss of ideal conditions and thus sensitivity of the device. For this reason, single walled carbon nanotubes with small diameter (1 to 2 nm) are preferred. The selective growth of small diameter semiconducting SWNTs is not possible with usual methods of mass production. Therefore, either semiconducting CNTs should be separated from metallic ones [127] or an alternative method has to be employed to selectively grow semiconducting CNTs at required location.

Also, functional properties of CNT based field effect transistor are strongly dependent upon contact realization. Non ohmic high resistance contacts demand higher working potential and lead to hysteresis at metal semiconductor junction (CNT-electrode junction) and therefore can influence the device characteristics. The good ohmic contact can be realized during the growth or after the CNT growth. However, the post growth contact realization is a true technical challenge [26]. Instead if, CNTs are grown directly between two contact electrodes, CNTs gain good ohmic contact with electrodes reducing contact resistance and enhancing functional properties of the device.

A conclusive solution to above mentioned problems is a technique to grow horizontally aligned CNTs. CNTs are grown between two electrodes, by using "alcohol - CVD" or "methane - CVD" technique. In both methods, as CNT count is less and diameter distribution of as grown CNTs fall in narrow range, probability that they show semiconducting nature is relatively high. The ethanol-CVD method is first demonstrated by Maruyama and coworkers [66]. By using ethanol as a carbon source, chemical vapor deposition is carried out to grow CNTs. Another way to grow relatively more, well ordered horizontal SWNTs segments is iron catalyzed CVD method by using methane gas. Depending upon the need, one of these two methods is employed to grow CNTs to miniaturize electronic devices such as field effect transistor. Both methods are explained in detail in experimental part of this thesis. Few SEM micrographs of CNTs grown using alcohol - CVD method are displayed in figure 2.32.

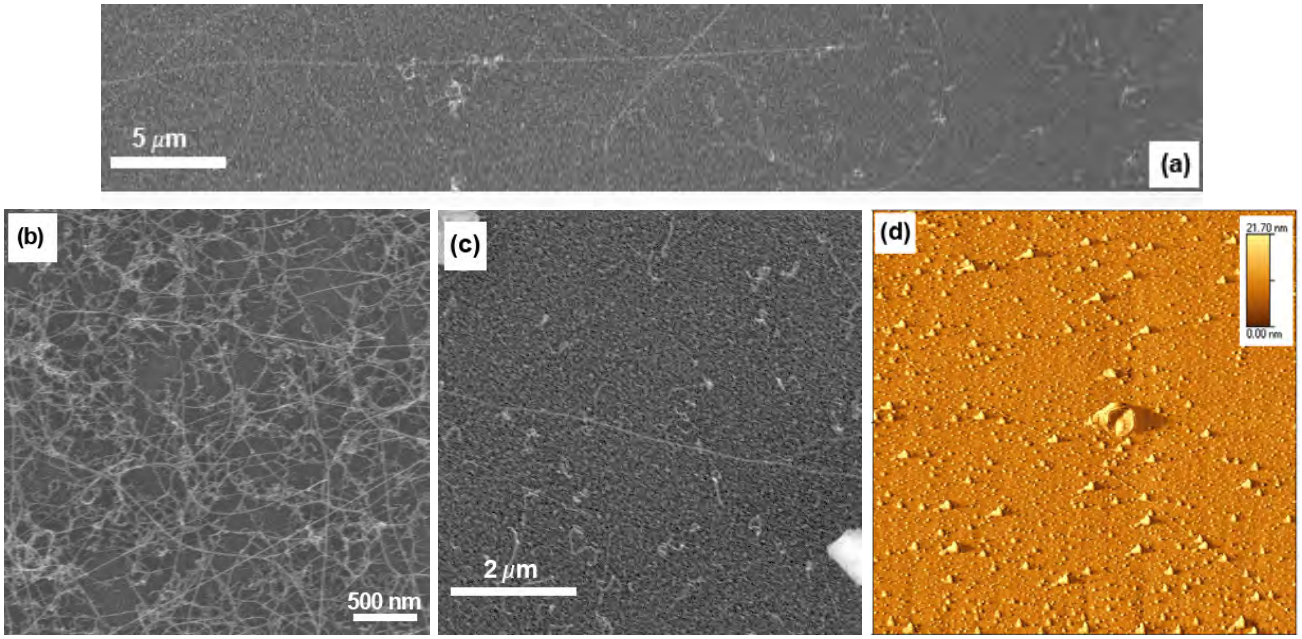

Figure 2.32: Scanning electron micrographs (a, b & c) and (d) atomic force microscope image of carbon nanotubes grown using ethanol-CVD method. In AFM, the diameter of CNT was found to be 1.73 nm.

As seen from micrographs, CNTs grow indeed horizontally and in an unorganized manner. CNTs are grown up to few hundreds of micrometer. It is clear from the figure, most of the catalyst particles fail to show any growth. Upon many other particles, growth process starts but doesn't last longer. Very few catalyst particles could give ultra long CNTs. It concludes not all the catalyst particles are successful to catalyze the CNT growth. Out of those successful, very few can lead the growth to ultra long length. This is because, ethanol is serving here a dual purpose. At 900 °C, ethanol decompose in vicinity of catalyst particle to produce carbon species and oxygen species. Carbon species diffuse through the catalyst particle to grow the carbon nanotubes, while oxygen entities are utilized to keep the catalyst clean. As the supply of carbon species and oxygen entities in comparison to size and surface morphology of catalyst should match to maximize the growth. Few catalyst particles can satisfy this need and thus very few CNTs are found to grow longer in length.

In case of methane-CVD, iron is chosen to catalyze the CNT growth process [128, 129] and methane as a carbon source. Compared to previous method, here, number of CNTs grown per square area of the substrate is high (see fig. 2.33a and b). This will help to drop the resistance between source and drain electrodes and increase the current flowing through the device for a given applied field. This is quite important in certain applications such as high frequency

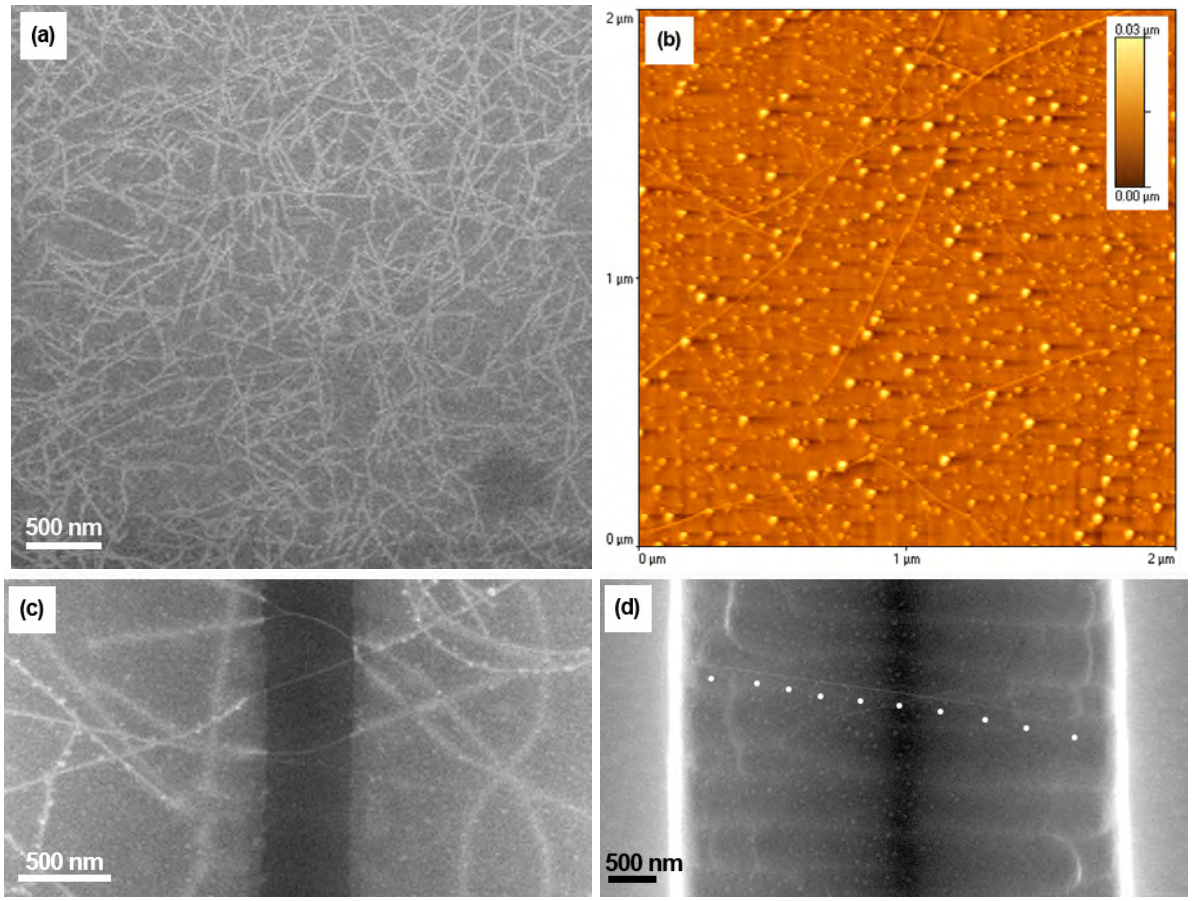

Figure 2.33: Scanning electron micrographs (a, c & d) and (b) AFM micrograph of carbon nanotubes grown using methane-CVD method. (c& d) are micrographs of CNT bridging the plasma etched groove in Si-wafer. (white dots in figure (d) are marked along as CNT grown).

transistors. Apart from this, CNTs grown using methane-CVD method are longer in length compared to one from previous alcohol-CVD method. Therefore, this method can successfully be used grow CNTs to bridge the cavities or grooves as shown in figure 2.33. This offers a possibility to miniaturize sensitive devices such as gas sensors, memory storage applications, motion sensors etc. in the future.

Depending upon the flow rate and carbon source used, using both methods, CNTs depicting semiconducting characteristics were grown on silicon wafer with gold contacts or on silicon pillars. Using various structures or form of gold contacts pads, CNTs were grown for various applications. The introductory work of fabricating CNT based transistors and CNT based gas sensor modules in discussed in up coming application part of this thesis. The fabrication of the device and successful testing of the same will be discussed in detail.

Nano sized metal oxides exhibit excellent electronic, catalytic and photonic potential. Generally, oxides were termed as an insulator due to their very high band gap ($\sim$ 3eV or more). But if synthesized at nano scale, they can be used for harvesting solar energy, as active and stable catalyst, for controlling the environmental pollution, printed circuits and transparent electronics devices. Oxides with different doping elements, mixed oxides phases, oxides of alloys and compounds are gaining interest not only because of their small size inducing profound quantum effect but also due to their unique structure or shape at such nano size.

Metal oxides can be synthesized as zero (nanoparticles) one (nanotubes or nanorods) or even two dimensional (thin films) entities. By tuning oxidation conditions, oxides of titanium, zinc, vanadium and iron can readily be grown as nanoparticles, nanotubes, or nanorods. Peculiarly in zero and one dimensional materials, the limited size brings in high density of corners and edge surface sites. These local sites act as a active locations where catalysis, photon absorption or charge transfer can readily take place. Compared to bulk oxide materials, nano particles have enormous surface area and thus high amount of surface energy. The size induced structural distortion is another important effect and there upon contact with the substrate or the supporting material can lead to formation of new phase that has not been observed in the bulk phase [130, 131].

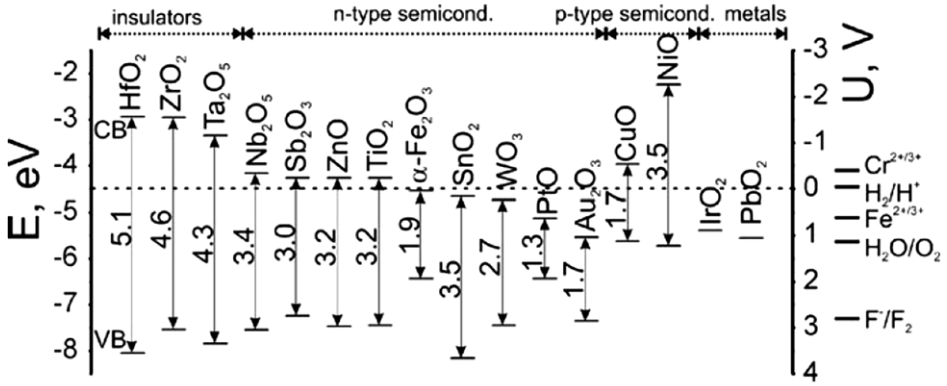

Figure 3.1: Energy structure and band gap of different metal oxides.

Another important effect of size change (from bulk to nano) in oxide materials is the change in electronic properties. Due to decrease in the size, a pronounced quantum effect or confinement effect is seen. The smaller particle size additionally shift the energy of exciton levels or optical band gap to a higher energy [132, 133]. The charge redistribution takes place in metal-oxygen

bonds, and a increase in ionic characters in relevance to decrease in the particle size is estimated [134–136]. The decreasing size and changes in chemical nature of the bond carry impact on physical and chemical properties of the oxide material [137].

The present interesting oxide materials are high band gap oxides as seen in the figure 3.1 [144]. The metal - oxygen bond is essentially formed by transfer of valence shell electrons from metal to oxygen and the magnitude of the band gap is principally governed by electro positivity as well as out shell configuration of metal. In absence of d-electron effect, electro positive metals form essentially large band gap oxides behaving as an insulator, for example hafnia or zirconia as seen in figure 3.1 [137].

The number of charge carriers responsible for electron conduction can be substantially enhanced by introducing non stoichiometry either by doping with an impurity of lower valence (Li in titania) or by controlling the oxygen content (O_2 in ZnO) of nano scaled metal oxides [144–146].

The synthesis of nano scaled metal oxide can be carried out using chemical, physical or physiochemical methods. Few commonly used for synthesis of nano particles of oxides are

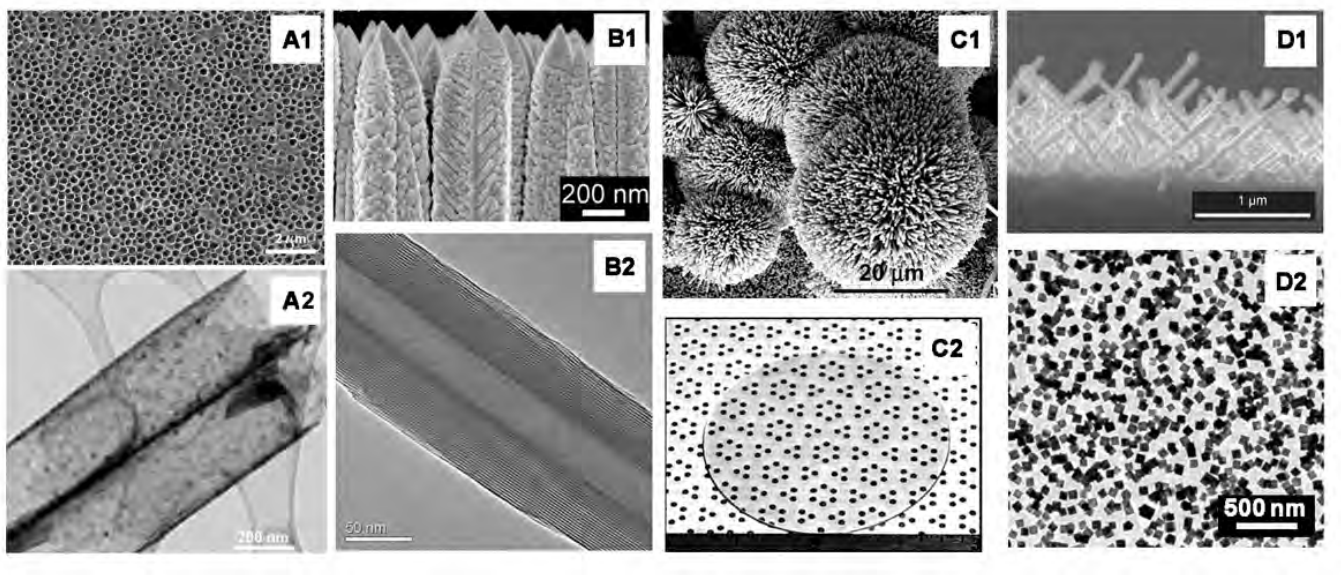

Figure 3.2: Few illustrative micrographs of metal oxides prepared in different shapes and forms. (A1 & A2) self synthesized TiO_2 nanotubes, (B1 & B2) represents vanadia rods and nanotubes respectively [138, 139], (C1 & C2) show ZnO nanorods and single crystal transparent disc (film) [140, 141], and (D1 & D2) represents SnO nanorods and nanocubes of Cu_2O respectively [142, 143]. suffix 1 stands for SEM and suffix 2 for TEM micrograph except for C2; an optical image of ZnO disc.

chemical vapor synthesis, sol-gel method, co-precipitation method [143, 147], vapor-liquid-solid (VLS) method, chemical vapor deposition, for one dimensional species such as nanotubes or nanorods [143, 148] while for thin films, methods such as physical or chemical vapor deposition, atomic layer deposition etc are advised [141, 149]. Along with it, some of the ordered structures for example titania nanotubes can be synthesized using electro-oxidation mode [150, 151]. Few representative images of various structures of different metal oxides are as shown in the figure 3.2.

3.1 Potential applications of various metal oxides

In past few decades, metal oxides are witnessing importance due to their potential applications in various fields. This section is a short overview of recent work on metal oxides from their application point of view.

Numerous high band gap metal oxides are under investigation for potential use in converting solar energy into usable form [152, 153]. Titania is one of the most commonly studied for water splitting applications to generate hydrogen gas [153, 154]. Similarly, other oxides also gaining their place in water splitting applications [138, 155, 156]. Energy in useful form is needed to be stored and for this purpose metal oxides are used again in lithium ion batteries [143, 157].

Industrial catalysis is another important field in which different metal oxides are used. Prominent oxides of this field are titania (TiO_2), zinc oxide (ZnO), tungsten oxide(WO_3), ceria(CeO_2) cuprous oxide (Cu_2O) etc. [137, 158, 159]. Photo catalytic studies are normally carried out using light in range of ultraviolet(UV)-visible energy (300-500 nm) [137]. The major problem of present photo catalytic oxide materials is low quantum efficiency (less than 10%) [137]. Another important application of photocatalysis is to control the pollution by compeleting the oxidation of partially oxidized NO_x, SO_x gases. Also, efforts are taken to convert carbon mono and dioxide gases back to usable fuel such as methane [160].

The major contribution of metal oxide semiconductors is towards electronic devices. The metal oxide films, rods, nanotubes or even nanoparticles are intensely being researched for their possible applications in printable electronics, flexible circuits, transparent electronics field emission displays etc [161–163]. Zinc oxide is one such oxide serving numerous applications [164]. Field effect transistors, single crystal ZnO light detectors have been miniaturized [161, 165]. Tin or indium tin oxides are famous for gas sensing, transparent electrodes, UV light

detectors [142, 166]. Apart from these applications, oxides are also used in abrasive coatings, wear resistance materials, magnetic materials (iron oxide), gas adsorbent and filters etc.

Metal oxides with diverse application potential serve different technological needs. In this work, nano particles or thin films of titanium dioxide as photo catalysis, zinc oxide for electronic applications (photon detector and transistor properties) and iron oxide i.e. magnetite for its magnetic applications are studied. Before elaborating different methods employed to deposit oxide nano particles on CNT structures, a brief introduction about these three oxides is given below.

3.2 Titanium dioxide (TiO_2) as a photo-catalyst

Titania is found to numerous polymorphs among which rutile is most stable polymorph of titania, although it occurs in brookite, monoclinic and anatase phases. Anatase and rutile are tetragonal in structure, while brookite is orthorhombic. In anatase and rutile, each titanium atom is coordinated with 6 oxygen atoms and each oxygen atom surrounded by 3 titanium atoms. Anatase form TiO_6 octahedral with shared edges and rutile tetrahedron [167]. The thermodynamic calculations show the metastable polymorph anatase can also be stable at normal temperature and pressure [168] as transformation to rutile takes place at 600 °C or more [169].

Photo catalytic activity of titania is strongly dependent upon its phase. The anatase phase is more active phase compared to rutile and has several reasons for such activity. The higher band gap of anatase (3.2 eV) gives higher redox potential [170]. In between both phases, anatase has higher charge carriers resulting in more photo activity compared to rutile [171, 172]. However experimentally, powder of titania nano particles composed of both phases yield higher photo activity. Commercially available titania powder consists of 75-80% of anatase phase and the rest rutile (Degussa or AEROXIDE P25). Numerous studies from different aspects were carried out in order to understand the exact reason for the higher photo activity of the mixture [172–174]. A possible answer for higher activity is attributed to the presence of lattice, interfacial, and surface-trapping sites as well as the charge-transfer process across the interface from rutile to anatase [170]. Also, If recombination is hindered by using proper dye, rutile also has similar photo - activity [173]. In most of the photocatalysis or solar energy harvesting studies, anatase phase of titania is used.

Alike most of the oxide materials, titania can also be prepared in different morphologies [170]. The most often studied form is zero dimensional nanoparticles of standard size 5 to 10 nm. There are numerous methods available to grow nano particles; widely categorized in two classes, solution methods and gas phase methods [175–181]. Another form of titania which is intensively researched is nanotubes of titania. First titania nanotubes were synthesized using the electro-oxidation of titanium metal foils [151, 182]. However in this method, dopant insertion for band gap engineering is hard. However, recent studies pave new routes to produce TiO_2 nanotubes with proper doping [153, 183].

Irrespective of mode of synthesis i.e. the gas phase method or solvent method, effect of various dopants is successfully studied to tune the band gap of titania [145, 184, 185]. The post preparation dopant insertion is also possible [154]. Activated carbon, hydrogen, nitrogen, sulphur and metals such as copper, lithium, gold etc have also been tested as a dopants to increase the photo current [144, 145, 153, 154, 185].

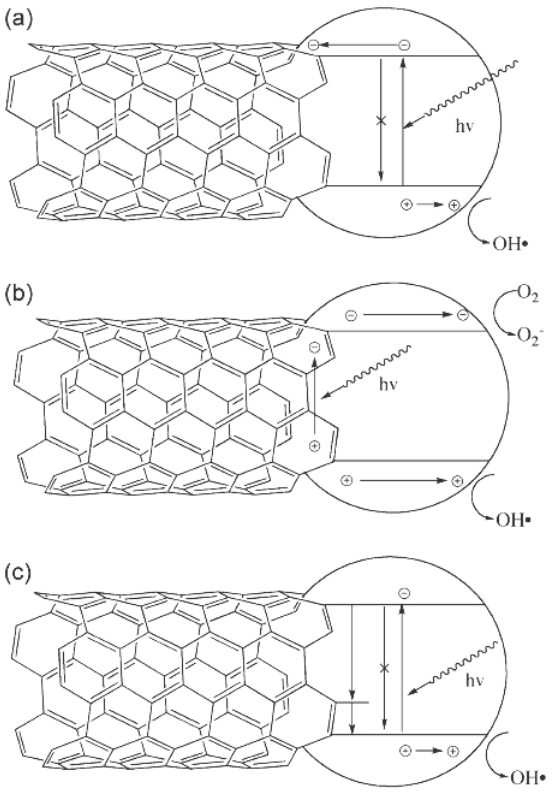

Figure 3.3: Pictorial representation elucidating different mechanisms for enhanced of photo catalytic activity of TiO_2 - CNT composite [170].

The real hindrance in photo catalytic activity of titania is its high tendency of recombination of electron-hole pair generated upon incidence of the light. Therefore, a method is needed to

drive out electrons from the conduction band of titanium dioxide to outer load circuit and holes into the solution. Carbon nanotubes can play a vital role in this aspect. MWNTs can serve metallic contact to semi conducting titania and there by driving electrons to outer circuit prior to recombination. The process works as explained below.

The high surface area of CNTs helps to properly disperse titania nano particles in reaction environment and also makes it easier to separate the photo active material at the end of the reaction. By proper handling with reactive acids, side wall or end of CNTs can be functionalized which can enhance the adsorption of chemical species during photo catalysis. Apart from these all functions, the real role of carbon nanotubes in TiO_2 - CNT composite is to scavenge the electrons excited in to conduction band of TiO_2 by light. There are two possible mechanism explaining this role in the literature.

The first mechanism is explained by Hoffmann and co-workers in year 1995 [186]. According to their theory, the titania nanoparticles deposited on side wall of carbon nanotubes are excited by UV light. UV photons were absorbed and a electron hole pair is generated. The electron from this pair is transfered from conduction band of titania to carbon nanotubes while hole is used to carry out redox reaction. The mechanism is displayed in figure 3.3a. The absorption of electron from CNTs hinder further recombination of electron with hole.

The second model is based on the study of photo degradation of phenol using TiO_2 - CNT composite under visible light illumination [187]. The study suggests, under visible light illumination, CNTs inject an electron in conduction band of titania forcing the formation of oxygen radicals on surface of TiO_2. Then, the positively charged CNT draws an electron from the valence band of titania leaving a hole behind. The positively charged titania with oxygen radicals on its surface lead the catalysis reaction(see fig. 3.3b) [187].

The third figure 3.3c represent the complex model based on carbon-oxygen-titanium bond that helps to absorb the photo light of longer wavelength. The formation of Ti-O-C bond is confirmed by various characterization tools and it also suggest CNTs should possess fewer defects and higher electrical conductivity. The electronic band structure as well as crystalline nature of CNTs play a vital role in photo catalytic behavior of the composite. This is the reason for higher photo efficiency in case of CNTs produced by arc discharge method [170].

Carbon nanotubes synthesized in this present work, are highly crystalline and (see characterization part of section 2) few walled. The structure of CNTs is uniform, consists of

less amount of defects. CNT - TiO_2 composite was synthesized using three different methods viz. chemical vapor deposition method, sol-gel method and metal oxidation method. Every method has unique advantage. Using chemical vapor deposition, nano particles of TiO_2 were deposited on side wall of CNTs. Sol-gel method gives a complete coverage of CNT side wall while metal oxidation method is used to grow bi-layer film of TiO_2 and CNTs. The composite prepared by these three methods are being tested for photo catalysis as well as for the application in field emission.

3.3 Zinc oxide (ZnO) as light sensor

Zinc oxide is binary (II^b-VI) compound of zinc metal and oxygen. The semiconductor crystalline compound takes three different structures namely wurtzite, zinc blend and rock salt. Except wurtzite which has hexagonal unit cell, later two polymorphs typically form cubic arrangement (see fig. 3.4). Wurtzite is thermodynamically most stable phase with two lattice parameters a and c in the ratio c/a = 1.633 cell structure. The ZnO has a substantial ionic characters admixed with covalent bonding, shifting the bond characters on the border of ionic and covalent semiconductors. Therefore the band gap of zinc oxide is as high as 3.424eV [141, 188].

The zinc oxide is direct and large band gap semiconductor. ZnO is transparent to optical light, can operate at high temperature, suitable for high power operations, sustain higher break down voltage and can be used in large electric fields. Undoped ZnO with wurtzite structure behaves as n-type semiconductor with electron density as high as 10^{21} cm^{-3} [141, 189]. Commonly

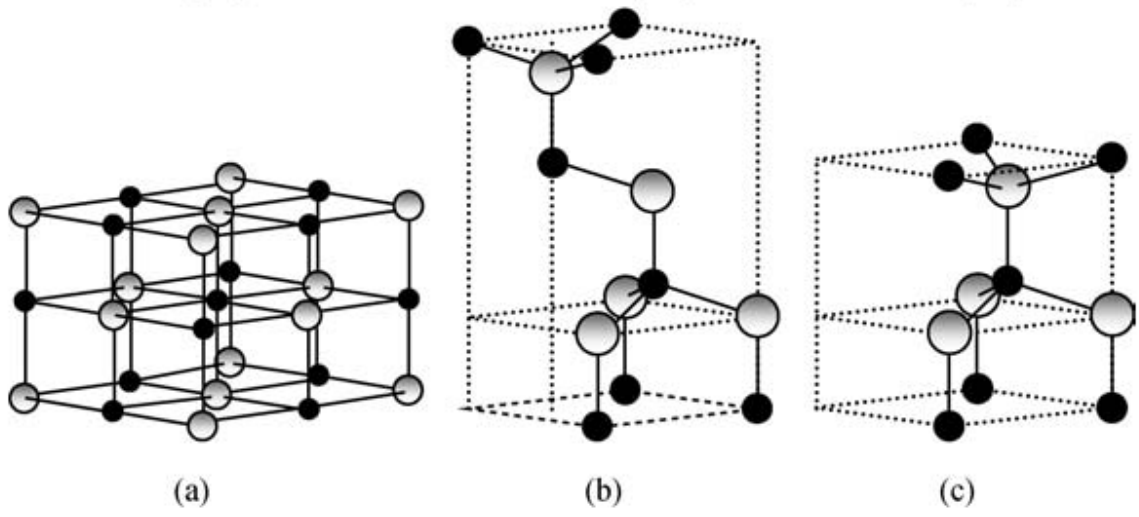

Figure 3.4: Crystal structures of ZnO polymorphs. (a) cubic rocksalt, (b) zinc blende, and (c) hexagonal wurtzite [141].

used n-type dopants are Al, Ga, In and they substitute the zinc atom from the crystal structure. Parallely, modulation of band gap is achieved by bimetallic oxides of zinc with magnesium, Beryllium, cadmium ($A_xZn_{1-x}O$ while A = Mg, Cd, Be)etc. Mg and Be tends to increase the band gap to higher value while Cadmium tends to bring it down [149, 190, 191]. The first p-type ZnO is synthesized in year 1997 [192]. The common doping elements used to make ZnO p-type are N, P, As. The nitrogen is most common dopant as ionic radius of nitrogen is same as that of oxygen [193, 194]. However, the major problem with p-type ZnO is lower hole concentration and mobility [192].

One of the interesting property that zinc oxide exhibit is piezoelectric effect. Every zinc ion in wurtzite crystal of zinc oxide is surrounded by tetrahedra of oxygen ions. This creates polar symmetry (in other words Zn-O bonds aligned along C-direction) and such polarity is responsible for piezoelectric behaviour of zinc oxide [195]. Numerous studies utilized this effect as a tool to convert the small motions or vibrations into electrical energy or vice versa [196, 197].

ZnO is semiconducting and transperent in the optical region. ZnO is thus a potential candidate for transperent electronics, solar cells [198], for developing flexible displays [161, 199] etc. For this purpose, zinc oxide nanoparticles [200], thin films or even nanorods [201] can be used.

Zinc oxide in various form serves as a material for blue laser, LEDs, photo diodes. The electro luminescence properties of ZnO can be exploited using metal-insulator-semiconductor(MIS) structures. Using MIS structures green as well as UV emission is obtained at room temperature [202]. ZnO -polymer based light emitting diodes emitting over a broad range is also demonstrated [199]. ZnO nanowires or rods are intensely investigated for field emission properties [162]. Apart from these major applications ZnO is also considered as potential material for catalysis, gas sensing applications [203].

Similar to tiantia - CNT composite, ZnO - CNT composite is also synthesized using various means. The composite was prepared by depositing zinc oxide on carbon nanotubes using chemical vapor deposition, precursor method and metal deposition and oxidation method. The major aim of such composite material is to fabricate a device able to sense different gases and detect the light of different wavelength.

3.4 Iron oxide (Fe_3O_4) as a magnetic material

Iron oxide appears to have many polymorphs viz. Hematite(α - Fe_2O_3), Maghemite (γ - Fe_2O_3), Magnetite (Fe_3O_4). Hematite weakly or even anti ferromagnetic, maghemite is ferrimagnetic and magnetite exhibits strong ferromagnetic properties [204]. Magnetite has an inverse spinel structure [205, 206] with chemical formula Fe_3O_4. It consists of a mixture of ferrous (Fe^{2+}) and ferric(Fe^{3+}) ions, held at a ratio 1:2 [207]. Magnetite has extremely high curie temperature of order 860K [206]. This polymorph is considered as a potential material for biomedical applications, memory storage, catalysis, sensors etc.

Often magnetic materials are tested for its capability by using a tool abbreviated as SQUID technique. SQUID stands for Superconducting Quantum Interface Device. The measurement begins with application of an external field (H) on target material of magnetic strength (M). The value M increases with increase in H, till the saturation point M_S arrives. Thereafter, upon gradual decrease in the external field (H), if all domains do not return to their original state, a remnant magnetization (M_R) is said to be induced in the material. This is the reason, the measurement reveal standard hysteresis loop as shown in figure 3.5. This effect can only be reversed by applying a coercive field (H_C) in a opposite direction to that of previous field [208]. Based on the value of coercivity, magnets are classified as either soft (for lower value), semi hard (storage media) or hard (permanent) magnet.

The particle size of magnet material has strong influence on its magnetic properties. Smaller the average size of the magnetite, smaller will be its domain size. Magnetite with particle size below 15-20 nm exhibits super paramagnetic behavior at room temperature. Super paramagnetic materials have no hysteresis loop ($H_C \sim 0$) that means, their magnetic domains can quickly realign or change its orientation under the influence of an external magnetic field. This effect is extremely important in certain applications such as magnetic resonance imaging (MRI). Upon rise in the temperature, due to increase in thermal vibrations, loss in magnetic moment is observed. At a certain temperature, termed as Curie temperature, the material becomes completely disordered losing its magnetization.

Magnets are used in varieties of applications such as magnetic seals, inks, magnetic recording media, catalysts, ferro fluids, sensors, high performance magnetic resonance imaging, targeted drug delivery, and various other biological applications [208, 210, 211]. In catalysis applications,

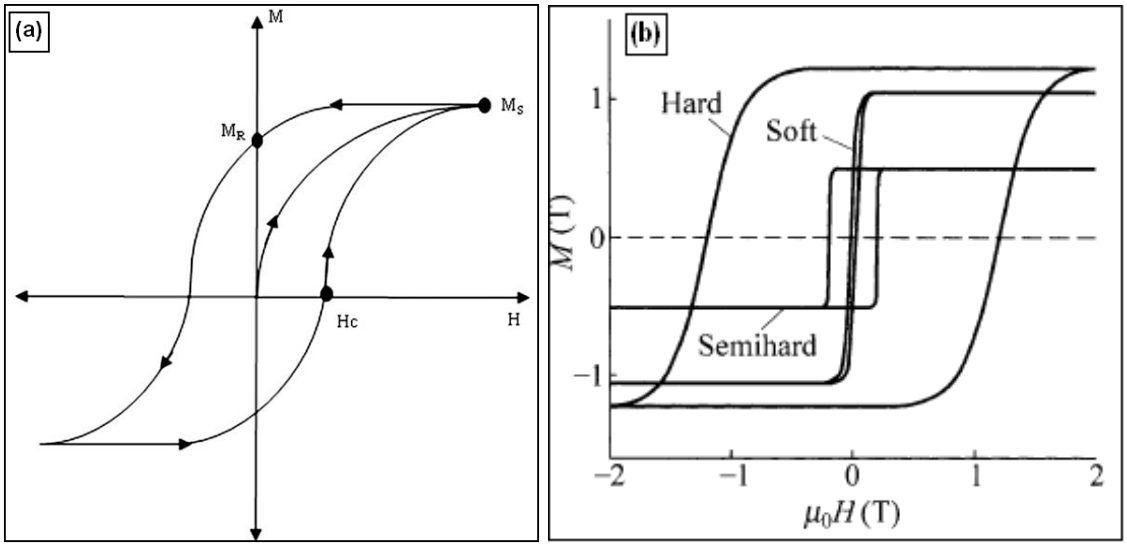

Figure 3.5: Standard hysteresis curve measured for a magnetic material [208] and different shapes of hysteresis curve depicting different kinds of magnets [209].

magnetic property can be well utilized to separate it from the end product. Noble metal decorated magnetic nanoparticles are presently investigated for various catalyst mechanisms [211]. Semi hard magnets can serve as optimal material for multi-tera bit storage devices [212]. The magnetic nanoparticles are typically thought for the purpose of generating a contrast in magnetic resonance imaging [210]. Magnetite nanoparticles are especially attractive for such biological applications due to their super paramagnetic nature at room temperature. The idea behind such usage is targeted drug delivery or for hyperthermia cancer therapy. In alternating magnetic fields, these particles can heat the cancer cells to 41-45 °C introducing irreversible damage in tumor cells.

Various routes have been developed in last few decades to grow magnetite nanoparticles. Majority of methods use chemical or physical method for growing the nanoparticles or thin films. The physical methods are magnetron sputtering, pulsed laser deposition, molecular beam epitaxy etc. On the other hand, chemical modes to prepare the magnetite nanoparticles are co-precipitation [210], hydrothermal [213], micro emulsion technique or thermal decomposition of organic precursors [207]. The chemical routes often use chemical end groups such as amines, sucrose, proteins in order to stabilize nano particles. However, most of the processes needed to be carried out in oxygen free atmosphere. Also, pH of solution, ion concentrations, surfactants carry a critical role during the synthesis [214].

In the present work, super paramagnetic magnetite nanoparticles are synthesized via single step decomposition of iron oximato (Tri[2-(methoxyimino)propanoato]iron(III)) precursor using either UV light or thermal energy. Magnetite nano particles prepared have average size of a order 10 nm. This process eliminates the need of an inert atmosphere, functional end groups or complex synthesis steps. As obtained nano particles will be deposited on carbon nanotubes and material will be characterized for its magnetic properties using SQUID technique and potential use in catalytic applications.

4 Synthesis and characterization of carbon nanotube based hybrid materials

This chapter concentrates on synthesis methodology and characterization of carbon nanotubes based hybrid materials. CNT structures were blended using three metal oxides namely, zinc oxide, titanium dioxide and iron oxide. Apart from metal oxides, carbon nanotubes were combined with biomaterials such as neuron, or cardiac cells as well as noble metals nano particles; platinum for example. Neuron cells were allowed to grow on carbon nanotubes films/blocks in a systematic manner to develop a methodology to study drug delivery applications and miniaturization of bio sensors in future. Carbon nanotube films decorated with platinum nano particles were assembled on either side of nafion membrane to study their potential use in fuel cells applications.

4.1 Deposition of zinc oxide on carbon nanotubes

Carbon nanotubes were grown using the standard technique of water assisted chemical vapor deposition method as explained before. Block structure or film structure, in both cases, the deposition was carried out on CNTs having length of about 400 to 500 μm. In short, the CNT - ZnO composite was synthesized using two different methods. The first method employs a classical CVD technique to deposit ZnO nano particles on the side wall of carbon nanotubes. An alternative solution method using a molecular zinc oximato precursor is also employed. In the CVD technique, zinc acetylacetonate is used as a precursor. In second method, zinc oxide -carbon nanotube bi-layer film is synthesized using metal oxidation method. To achieve bi-layer film, nanometer thick zinc layer was deposited on the CNT film and oxidized in controlled atmosphere. CNT-ZnO hybrid materials prepared here are potential candidates for -

- CNT-ZnO for stable field emission properties
- CNT-ZnO for photon detector & gas sensing
- CNT-ZnO for electro-actuator

4.1.1 Characterization of CNT - ZnO composite material

Using zinc acetylacetonate as a precursor in chemical vapor deposition technique, zinc oxide nano particles were deposited on carbon nanotubes at various deposition temperature. The precursor temperature was held at 135$\pm$ 5 °C i.e. at its sublimation temperature and argon flow

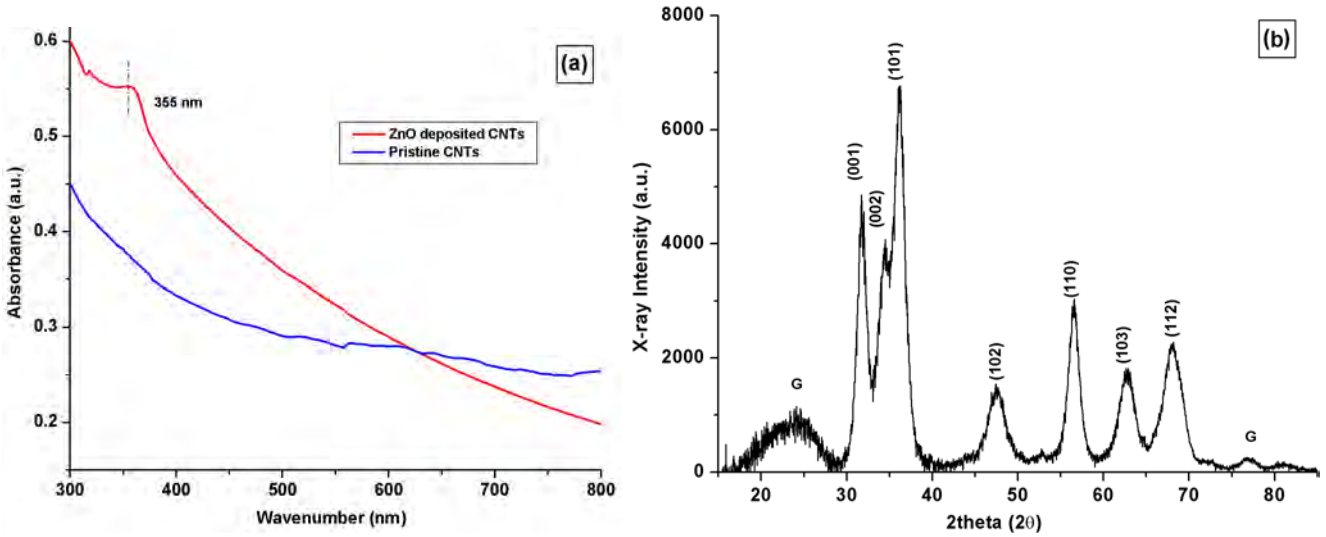

Figure 4.1: (a) UV-Vis spectroscopy and (b) X-ray diffraction of CNT-ZnO composite.

of 100 sccm is used to carry the sublimated precursor inside the oven. On the other hand, CVD temperature was varied from 500 to 800°C, to study its impact on quality of ZnO deposited. The optimal temperature was found to be around 700°C at which homogeneous deposition of zinc oxide with moderate particle size takes place.

The composite material (termed as 'ZnCN-1') synthesized using CVD technique was characterized for the extent of deposition and quality of zinc oxide nano particles. As a preliminary examination, the composite material was examined using UV-Vis spectroscopy and x-ray diffraction. The alcohol based dispersion of ZnCN-1 was examined in UV-Vis range for photon absorption. The spectrum is displayed in figure 4.1a. The spectrum shows sharp absorption edge in UV range; at 355 nm wavenumber. The absorption edge is exactly in a range of band gap of zinc oxide (3.4 eV). The band gap of CNTs is too small (0.7 to 0.8 eV for SWNTs) and therefore pristine CNTs have no absorption in optical or UV region. The blue line spectrum represents pristine CNTs dispersed in same solvent. X-ray Diffractrogram depicted as figure 4.1b having three important major intensity peaks positioned at 31.7, 34.3 and 36.2 ° of 2θ represent <100>, <002> and <101> crystal planes of wurtzite crystal structure of ZnO nano particles. The broad peak marked by letter 'G' represents the graphitic peak characteristics for microscopic bundles of carbon nanotubes.

Electron microscopy of ZnCN-1 sample reveal zinc oxide is completely covering the side walls of carbon nanotubes. Scanning electron micrographs of ZnO - CNT composite are as shown in figure 4.2a & b. Carbon nanotubes were grown in block forms simply by structuring iron

metal on aluminum film (see section 2.1.2 of this thesis). CNT blocks were found to have homogeneous deposition of zinc oxide nano particles across the side wall of carbon nanotubes. A single block consists of around about 1600 nanotubes per μm^2 of area. The inter tube distance between two nanotubes is around 15 to 20 nm. This makes the structure sufficiently porous allowing zinc oxide species to enter in the inter tube voids. The species tend to nucleate on each and every CNT located anywhere in the innermost volume of the block to grow zinc oxide nano particles. The TEM investigation confirm this fact as carbon nanotube without zinc oxide particle nucleated on its side wall were rarely found. The average size of ZnO particle deposited on side wall of CNT was in range of 15 to 20 nm (see fig. 4.2c & d).

As seen from the TEM micrographs, CNTs are indeed covered with ZnO nano particles, however, ZnO particles are not covering the side wall of CNTs in uniform manner. Instead,

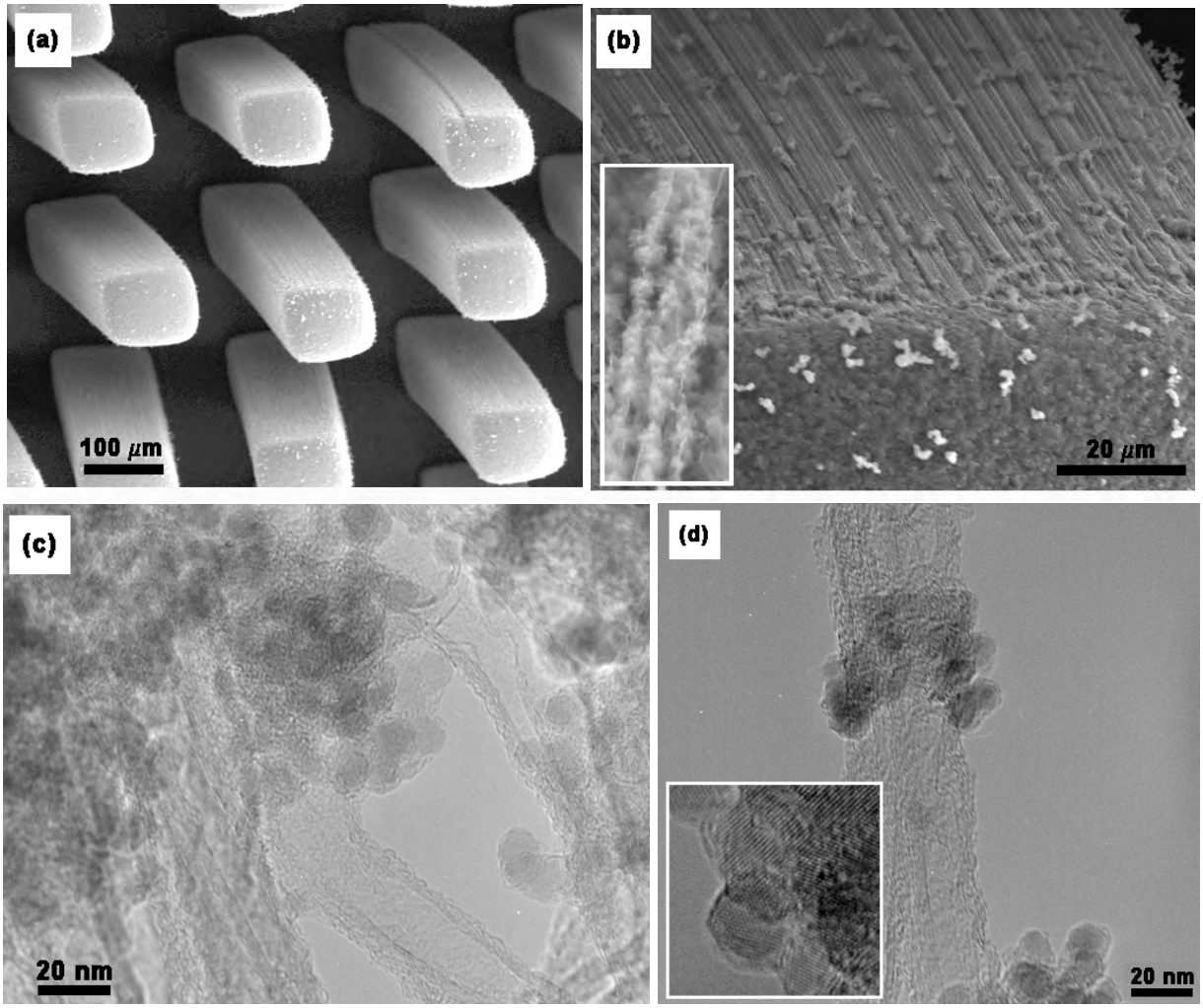

Figure 4.2: (a & b) SEM (c & d) TEM micrographs of CNT-ZnO composite. The inset in (b) is high resolution image of CNT covered with ZnO nano particles and one in (d) shows lattice fringes of ZnO nano particle.

ZnO nano particles seems to have build small clusters type morphology along the length of CNT. The particle are crystalline in nature. The high resolution image obtained from TEM studies shows well ordered lattice fringes of the zinc oxide. The ZnO deposited here is on CNT block structures, however, same results can be obtained with CNT film.

Field emission characteristics of such composite shows, at beginning, electron emission from carbon nanotubes. The testing at higher voltage results in burn out of CNT apex and emission from zinc oxide along with CNTs is observed. The results are explained in detail in upcoming application part of this thesis.

4.1.2 Characterization of CNT - ZnO bilayer material

The bilayer material consists of a carbon nanotube film as a bottom layer and a zinc oxide film as top layer. In order to prepare such bilayer material, zinc metal was evaporated on previously grown carbon nanotube film and oxidized subsequently. The oxidation was carried out under different conditions viz. in open air, in oven under controlled amount of oxygen supply. Depending on oxidation conditions and substrate used, the bilayer film behave photo active and can be used to detect light of different wavelengths.

A thin layer of zinc metal of varying thickness (100 to 200 nm) was deposited on carbon nanotube film as well as glass substrate. The reason of using glass substrate is to investigate the role of porous CNT film over the dense nonporous glass substrate during oxidation and its impact on physical properties of zinc oxide synthesized. During the study four different samples were tested. The nomenclature of those four samples is as follows.

Table 4.1: Synthesis conditions for various bilayer material.

Sample	Oxidation	substrate	O_2 supply
ZnCN-2a	in air	CNT film	air
ZnCN-2b	in oven	CNT film	100sccm O_2 +200sccm Ar
ZnCN-2c	in air	Glass	air
ZnCN-2d	in oven	Glass	100sccm O_2 +200sccm Ar

Zinc films were oxidized in different atmospheres as stated above. Zinc metal was found to be readily oxidizing at temperatures above 250 °C; however most of the experiments were carried out in range of 400 to 500 °C. The upper temperature was limited to 500 °C as otherwise, the CNT film will be oxidized. The dark brown metallic film turns to light blue color upon oxidation.

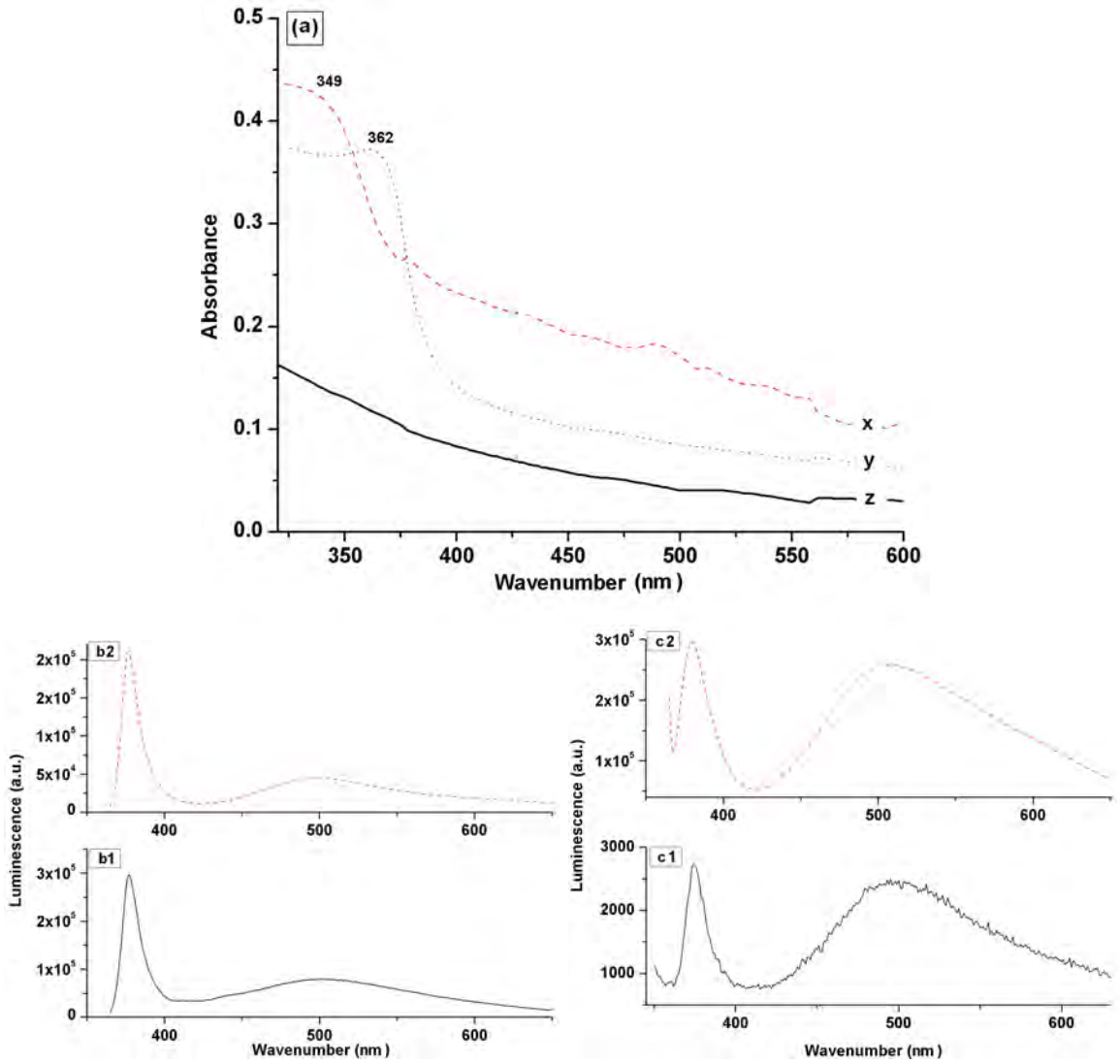

Figure 4.3: (a) UV-Vis spectrum of zinc oxide grown. In same figure, spectrum (x) is for ZnO on CNT, (y) is for ZnO on glass and (z) of pristine CNTs. Also, Photoluminescence spectroscopy of zinc oxide grown (b) on CNTs (c) on glass substrate. In figure (b and c) suffix represents oxidation conditions; 1 in oven while 2 in air.

UV-Vis spectroscopy (see fig. 4.3a) of ZnO grown on different substrates shows an absorption edge in range of 350 to 370 nm. For same experimental conditions, if Zn is oxidized on porous CNTs film instead of glass piece (sample ZnCN-2a and b), the absorption edge was at relatively lower wavelength, at 349 nm. However for ZnO on glass substrate (sample ZnCN-2c and d), the absorption was at 364 nm as seen in figure 4.3. The blue shift in case of ZnO on CNT indicates formation of smaller particle size on CNT film compared to those formed on glass.

As a next step same samples were investigated using photo luminescence (PL) spectroscopy. All four samples listed above were analyzed using xenon lamp as a light source. All spectra are displayed in figure 4.3b & c. Irrespective of oxidation conditions, ZnO grown on CNT film

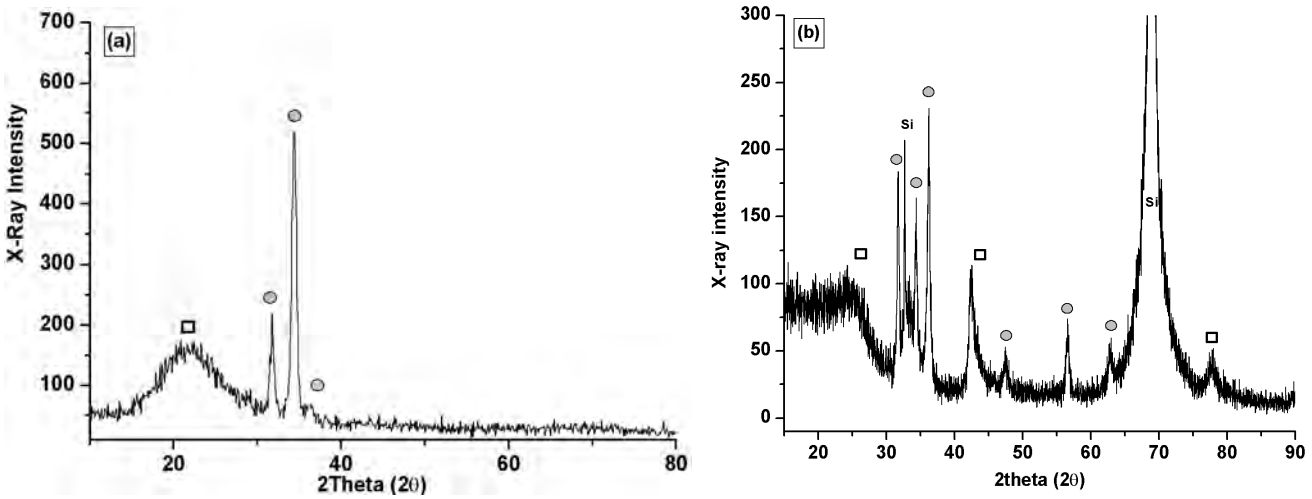

Figure 4.4: X-ray diffraction of ZnO grown on (a) glass substrate and (b) on CNT film. The circle markings denote ZnO peaks while square markings represents respective substrate.

produce strong green luminescence compared to one on glass substrate. In other words, charge carriers in zinc oxide can be easily excited to higher energy level, if CNT film was used as a substrate. The spectrum C2 is from zinc oxidized on CNT film in ambient atmosphere. Although the PL spectrum has almost no difference between two samples (C1 and C2); open air oxidation has a qualitative impact on quality of zinc oxide as explained below.

X-ray diffraction plot of ZnO grown on various substrates helps to visualize impact of substrate on orientation of ZnO nano crystals. Zinc oxide shows three major intensity peaks positioned at 31.7, 34.3 and 36.2° of 2θ corresponding to (100), (002) and (001) crystal orientations. The ZnO film on glass substrate (figure 4.4a) has majority of its crystals orientated along (002) direction while the ZnO grown on carbon nanotubes (figure 4.4b), was polycrystalline in nature showing all three major intensity peaks. In diffractogram of ZnO on CNTs, the broad peak positioned at 26° of 2θ is a graphitic peak (002) arises from carbon nanotubes along with peaks at 43° and 79° of 2θ. The main graphitic peak (002) is broad due to well aligned growth of CNTs.

During oxidation of zinc metal deposited on amorphous glass substrate, energy needed for crystallization of ZnO is quite high compared to that needed by film oxidized on crystalline carbon nanotubes. This is because crystalline substrates promote the nucleation and crystal growth which is not possible in case of amorphous substrates such as glass. The higher requirement of crystallization energy forces zinc on glass substrate to get aligned in an orientation procuring lowest possible nucleation energy. This results into major alignment in

(002) direction. On the other hand, crystalline CNT film helps zinc oxide to crystallize at lower nucleation energy, gaining alignment in all possible directions. The full width half maximum (FWHM) of reasonably narrow (002) peaks of ZnO grown on CNT and glass substrate are 0.005 and 0.013 radians respectively. According to Deybe-Scherrer formula, average crystal size is smaller for zinc oxide grown on CNT film. It resembles well with the blue shift observed in the UV-Vis spectrum. Smaller particle size of the ZnO crystals leads to generation of higher amount of counters and edges. Such locations accounts for interaction with incident photons or behave as active sites for catalysis [137].

The formation of zinc oxide is cross confirmed using Raman spectroscopy and energy dispersive analysis of x-rays (EDAX) during SEM investigations (see fig 4.5a and b). Raman spectroscopy has recorded distinct peaks at lower wavenumber 98, 330 and 437 cm^{-1} represents zinc oxide phase. Two peaks recorded at 1350 and 1595 cm^{-1} represent the defect (D) and the graphitic band (G) peaks for CNTs. The EDAX analysis shows characteristic K-line x-ray intensities for zinc, oxygen, silicon and carbon. The elemental peaks Zn and O arise from zinc oxide while carbon symbolizes carbon nanotubes and silicon from the substrate used for CNT growth.

Scanning electron micrographs of both films are as shown in figure 4.6a to d. ZnO film on glass substrate is almost flat and composed of small plate like morphology of 200 to 300 nm average size (see fig 4.6a and b). On the other hand, zinc oxide film on CNT seem to be composed of smaller particles, either round or dumbbell shaped morphologies (fig 4.6c and d). In either case, the film was densely packed and small particles or flakes constitute to form bigger particles.

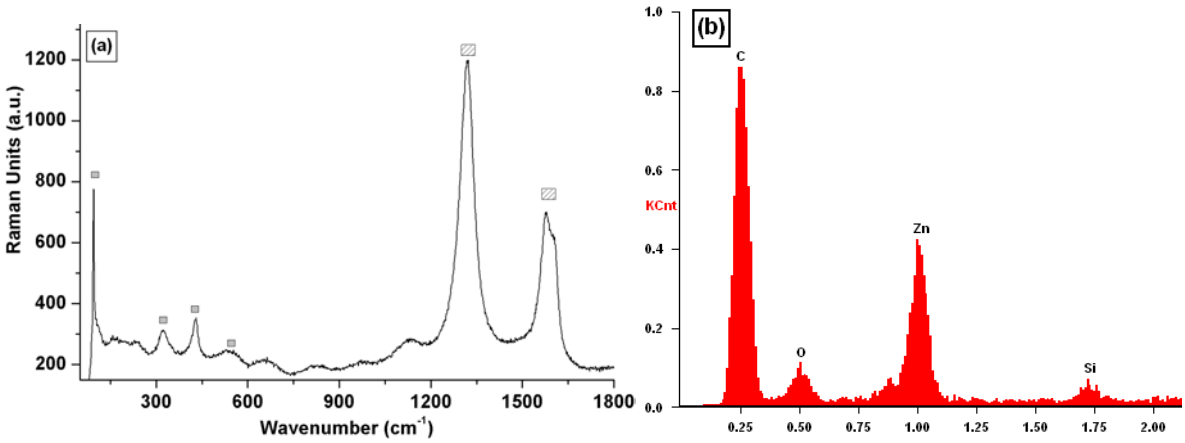

Figure 4.5: (a) Raman spectroscopy and (b) EDAX of ZnO grown on the CNT film.

Transmission electron micrographs (see figure 4.6e & f) confirm the agglomeration of smaller particles building up bigger ones. The agglomeration was hard to hinder. The SAED (inserted as an inset) shows hexagonal pattern for crystalline zinc oxide nano particles evolved from wurtzite type crystal structure. In figure, fig. 4.6f a TEM micrograph shows single crystalline particle of

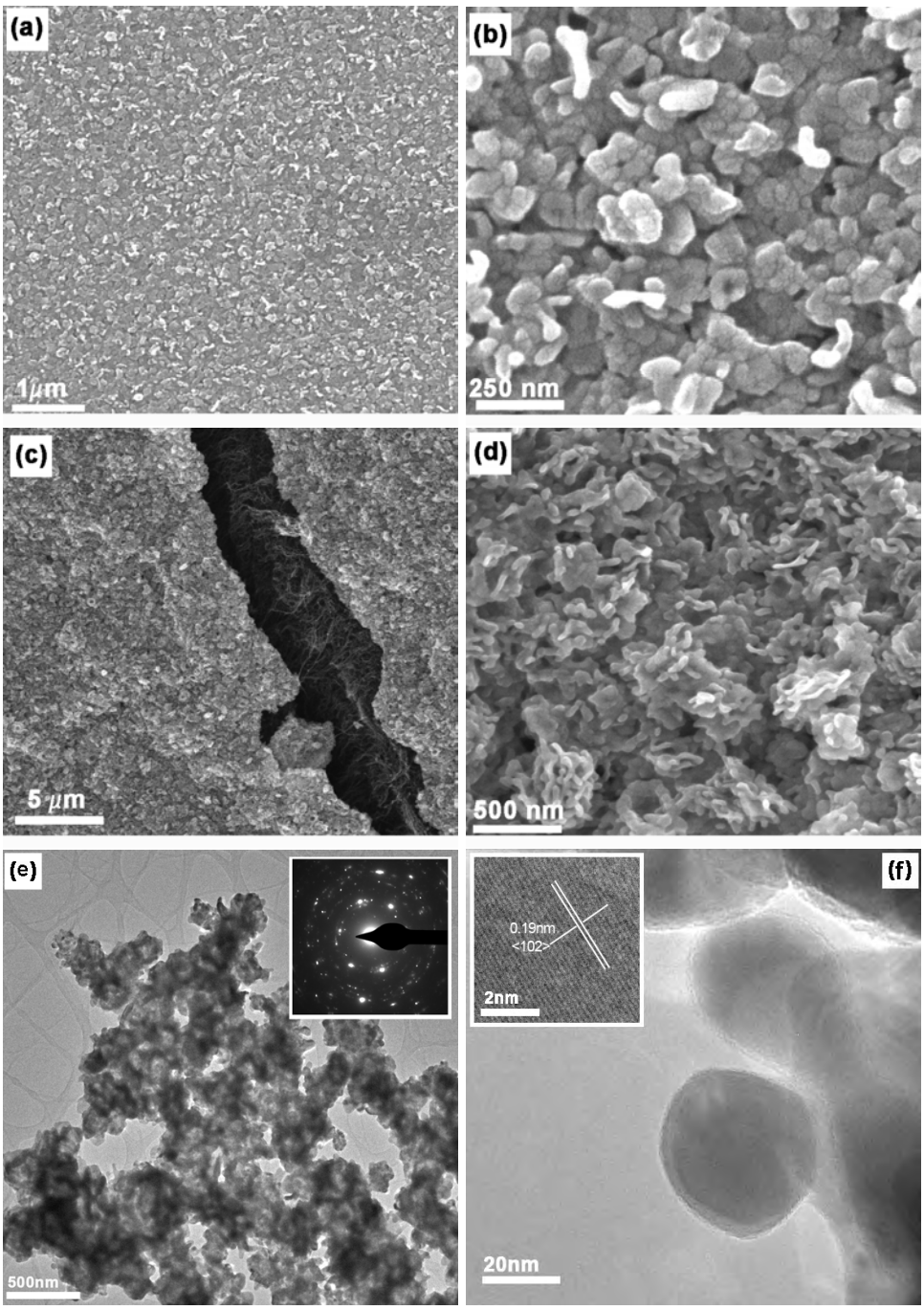

Figure 4.6: SEM investigation of ZnO film grown on (a and b) glass substrate and (c and d) CNT film and (e and f) are TEM micrographs of ZnO grown on CNT film.

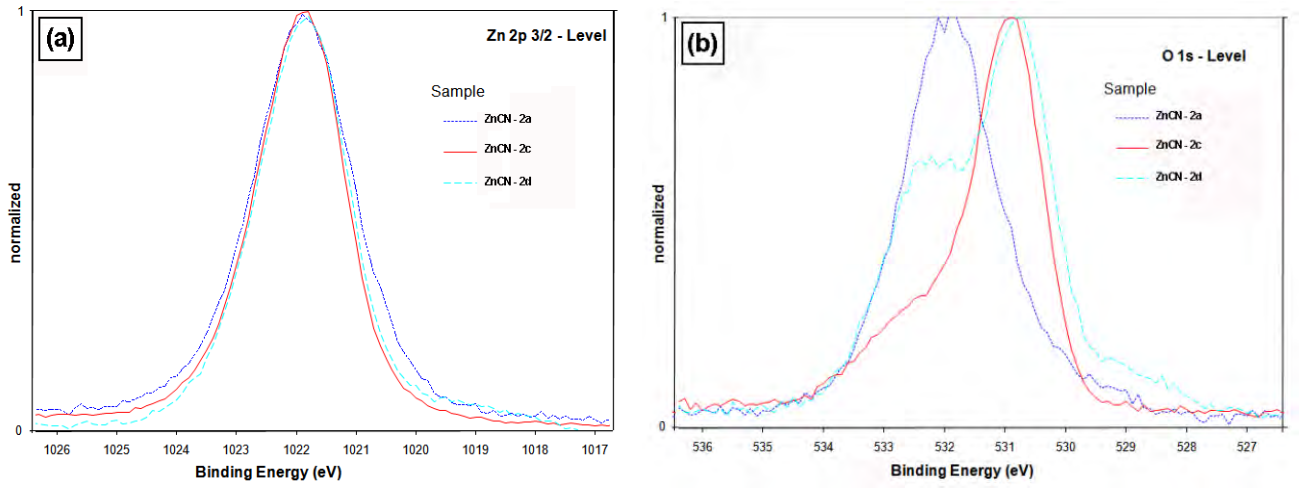

Figure 4.7: X-ray photo electron spectroscopy of ZnO film grown on CNT film (a) Zn 2p3/2 and (b) O 1s spectra.

size 20 to 30 nm in diameter. The inset shows well ordered lattice fringes with an inter planer distance of 1.90 Å perfectly matching with (102) plane of wurtzite crystal structure.

The extent of oxidation, i.e. fact that the zinc metal is oxidized partially or completely across its depth, is still unaccounted. This is important to investigate, as properties of zinc oxide are determined by its oxygen content [141, 146]. In order to find out effectiveness of oxidation treatment, x-ray photo electron spectroscopy (XPS) of all four samples of ZnO was carried out (see fig. 4.7a & b). The survey spectrum of all four samples include major peaks corresponding to zinc, oxygen, carbon (in case of CNT film as substrate). The characteristic zinc 2p3/2 peak was measured at 1021.8 eV for all samples. The 1s carbon peak was recorded for CNT film as substrate at 284.8 eV binding energy; a standard value for graphitic structure of CNTs. The oxygen O1s peak intensity was found to be different for samples prepared under different atmosphere. The binding energy of oxygen atoms in metal oxide compound is reported at 531.6 eV. In case of zinc oxide grown on glass substrate (ZNCN-2c and 2d), O1s peak was recorded at 530.9 eV; about $\sim$ 0.7 eV lesser. In case of ZnO on CNT films (samples ZnCN-2a and 2b), the peak was measured at 531.8 eV matching well with the literature value [161, 203].

A quantitative elemental analysis giving the atomic ratio of elements present in every sample is listed in the table 4.2. Elemental analysis shows ZnO film grown on CNT and oxidized in open air (sample ZnCN-2a) is thoroughly oxidized and such zinc oxide film has stoichiometric amount (1:1) of zinc and oxygen atoms. In case of all other samples (samples ZnCN-2b,2c and 2d), oxidation of zinc metal was never been completed. Curiously, zinc metal on the glass

substrate was alway found to be partially oxidized; irrespective of its oxidation conditions or time of oxidation. A possible explanation for such substrate dependent oxidation mechanism is as follows.

Table 4.2: Elemental analysis of zinc oxide film grown on various substrate.

Sample	Zinc		Oxygen	
	% atoms	Binding energy (eV)	% atoms	Binding energy (eV)
ZnCN-2a	49.44	1021.8	50.55	531.8
ZnCN-2b	26.25	1021.8	73.74	530.9
ZnCN-2c & 2d	37.60	1021.8	64.40	530.8

In comparison to porous CNT film, glass substrate is a dense and non porous medium. During oxidation, oxygen can diffuse into zinc film deposited on the glass substrate only from top side. The diffusion rate is controlled by porous nature of zinc oxide film that is being formed. As and when top layer of Zn is completely oxidized, oxidized layer becomes more and more impermeable for further oxygen diffusion. In absence of proper amount of oxygen supply, high amount of oxygen deficient grains are produced. The oxygen content in ZnO formed on glass does not change much, if oxidation is carried out for longer time or in air or pure oxygen atmosphere. However, in case of zinc metal deposited on the CNT film, case is totally reversed. In contrast to glass, the CNT film is composed of equidistant carbon nanotubes grown with regular intermediate spacing. During oxidation the film acts as a porous medium and supply of oxygen take place from top as well as from the bottom side. Oxygen can diffuse through zinc film from all sides and under better supply of oxygen the zinc metal is oxidized to stoichiometric zinc oxide.

The zinc oxide formed on the CNT film is composed of small nano particles of zinc oxide. The transformation of zinc oxide particles into small nanotubes of zinc oxide can easily be carried out by low temperature solution route reported by [215]. The oxidized Zinc film on carbon nanotubes was immersed into 5% formamide aqueas solution along with small piece of zinc foil and heated to 65 °C for couple of hours. The SEM micrographs of recovered ZnO film reveal formation of small nanotubes of zinc oxide. The micrographs are as shown in figure 4.8.

All four samples were tested for their electrical behavior and light sensitivity. The films grown on glass substrate behave metallic in nature, while those on CNT film are semiconducting and optically active. The bi-layer film of zinc oxide and carbon nanotube is tested for light detection

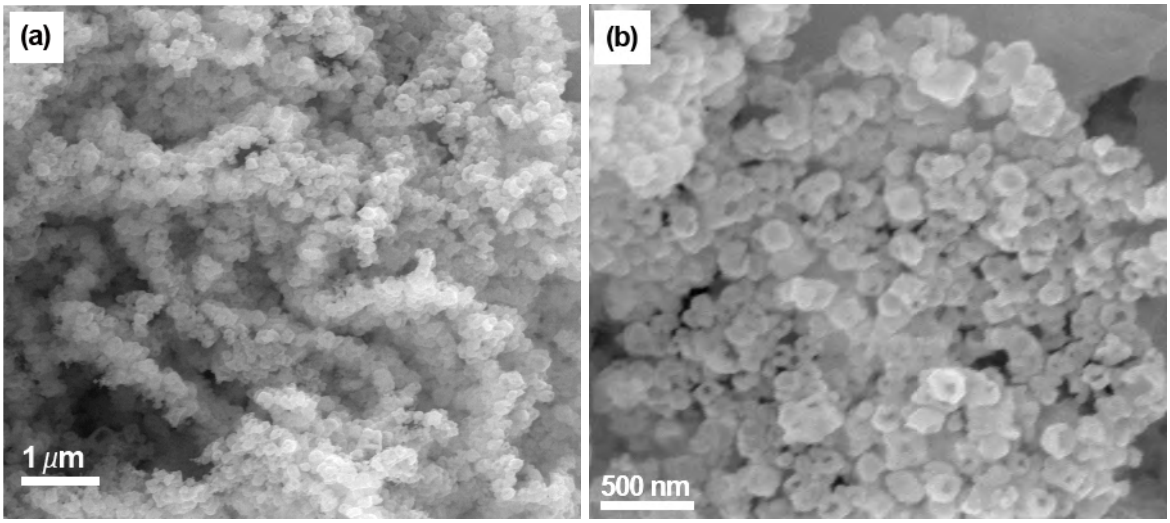

Figure 4.8: SEM micrograph of ZnO nanotubes formed by re oxidation of ZnO film CNTs. Previous particle morphology (see figure 4.6d) is completely disappeared.

application by using low energy lasers of definite wavelength. The electrical characterization of all four films is reported in the application part of this thesis.

4.2 Deposition of titanium dioxide on carbon nanotubes

Titanium dioxide is intensely researched photo catalytic transition metal oxide. The anatase phase with 3.2 eV of energy band gap is most active phase of titania in photo catalytic activity. Due to its high band, an electron hole pair generated by induced photons tends to recombine. A composite with carbon nanotubes will hinder such recombination by driving electrons from conduction band of titania out. However, synthesis of such composite is intriguing process and upon close control of parameters such as quality of CNTs, their electrical behavior, their electrical junction with titania, phase and morphology of titania, its loading rate etc. will results into favorable outcome [170, 187]. Here in this part, a process to synthesize titania - CNT composite by three different ways is explained. The composite prepared in different form, will be further studied for various applications such as water splitting, dye sensitized solar cells, field emission studies etc.

As grown carbon nanotubes of average height 400 to 500 μm were deposited by titania in form of nano particles, a film or a layer using various methods such as chemical vapor deposition method, sol - gel and by metal evaporation and oxidation in suitable atmosphere. The detailed procedure for titania deposition is described in the experimental section.

4.2.1 Characterization of CNT - TiO_2 composite material

The photo catalytic activity of titania depends upon its nano size as well as phase of the nano material [184, 187]. Both factors are important and strongly dependent on process parameters. The particle size and homogeneity depend upon the precursor temperature as well as the synthesis temperature. Numerous experiments were conducted by varying the synthesis temperature and the precursor temperature to gain control over particle size and crystal structure of TiO_2 nano particles deposited on CNTs. Starting experiments from 300 °C, CVD temperature as high as 800 °C was tried. The rutile polymorph is metastable phase of titania and at higher temperature other phases such as anatase or brookite, are converted into rutile by releasing the excess of oxygen. If decomposition of titania precursor is carried out at higher temperature and in presence of oxygen, smaller particle size can be obtained [181, 184]. However, in present case, usage of oxygen will lead to oxidation of CNTs. Therefore, the process was optimized by tuning synthesis and precursor temperatures in order to gain desired quality of titania.

The study starts with CVD temperature of 300 °C and precursor evaporating at 100 °C. Below 500 °C (CVD temperature), amorphous layer of TiO_2 was found to be deposited on the CNT blocks/film. All carbon nanotubes present in the film or block were found to have a homogeneous amorphous layer of titanium dioxide on their side wall. The amorphous layer acts as a barrier film; reducing the conductivity of the CNT film across its width drastically. Each CNT is insulated from each other, showing film resistance of order 500MΩ. On the contrary, as grown CNT film shows conductivity of order 2 to 4 S/cm [216]. The electron micrograph of CNTs with amorphous layer of titania deposited on their side walls is as shown in fig. 4.11. Such composite films can be a potential future material for micro level interconnects [217].

The titania nano particles start nucleating on sidewalls of CNTs at a temperature of about 500 °C. At this temperature, the gas flow rate was kept same, and precursor temperature was varied from 90 °C till 140 °C over series of experiments. With the rise in precursor temperature, more and more dense vapors were generated. The rise in precursor temperature fail to show any major impact on the particle size or the loading rate of titania for temperature below 120 °C. On the other hand, a good homogeneous growth of titanium nano particles began for precursor

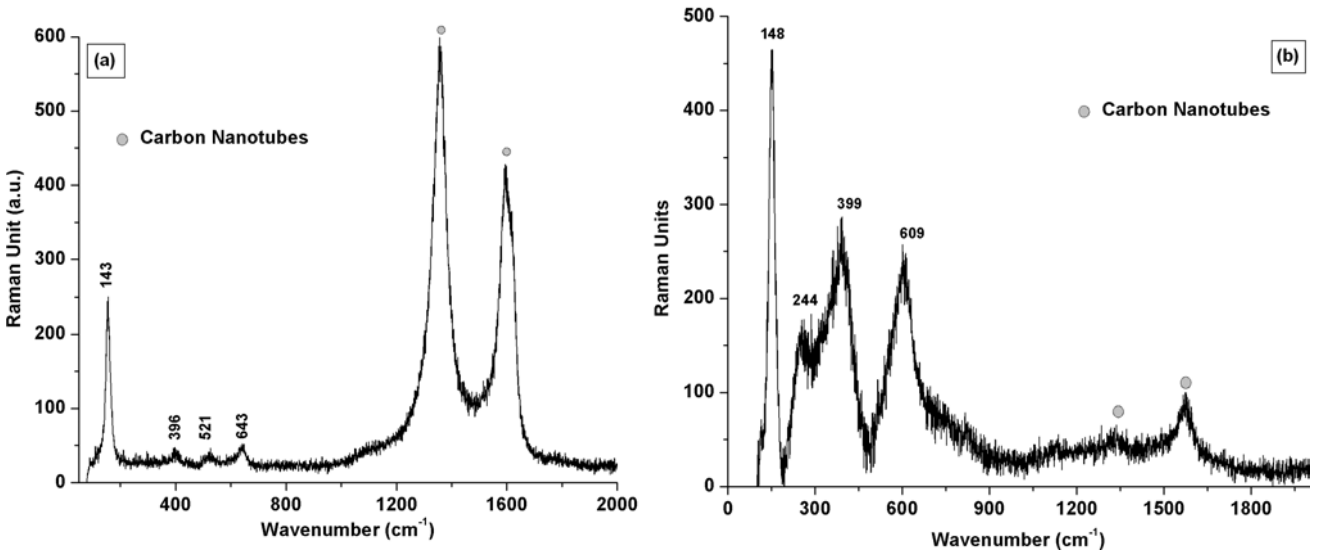

Figure 4.9: Raman spectroscopy of titania-CNT composite prepared by depositing titania at (a) 550 °C and (b)750 °C.

temperature in the range of 130 to 140 °C. SEM investigations reveal that CNTs are uniformly decorated with nano particles of titania.

In order to get homogeneous loading, of crystalline nano particles on side wall of CNT, the precursor temperature and argon flow rate was held constant, and CVD temperature was raised in step of 50 to 100 °C per experiment. Each sample was investigated using Raman spectroscopy. Two samples, synthesized at 550 and 750 °C were investigated for quality of the titania phase. Raman spectroscopy is an optimal nondestructive way for such investigations and spectrum of two samples revealing the exact phase of TiO_2 formed were as shown in figure 4.9. At 550 °C, anatase phase is predominant and results in peak intensities at 144, 399 519 and 639 cm^{-1} (see fig 4.9a). These peaks are attributed to active raman modes of anatase phase symmetries of Eg, B1g, A1g, and Eg, respectively [218]. On the other hand, rutile phase formed above 700 °C, shows peaks corresponding same Raman active modes but at 143, 235, 447, and 612 cm^{-1} wavenumber (refer fig 4.9b). The peak intensity of 144 cm^{-1} is lower in case of rutile in comparison to anatase which is in accord with the literature [218] .

The increase in CVD temperature past 600 °C gives rise to mixed phase of titania composed of anatase and rutile. The percentage of anatase and rutile formed is hard to determine, however, rutile content increases with rise in temperature. At temperature of 700 °C or above, the rutile phase is predominant. Almost at any value of CVD temperature and for given gas flow conditions, the average size of titania nano particles was found to be 5 to 10 nm, confirmed by

TEM investigations described below (see figure 4.11). At standard growth conditions, a good loading rate of titania i.e. in range of 15 to 20 wt % of CNTs was achieved by using 100 sccm of argon flow through the precursor heated at 135 °C. The loading rate was experimentally determined by weighing the CNT film before and after the titania deposition.

Scanning electron micrographs of the composite material confirm uniform loading of titania nano particles on CNT blocks (see figure 4.10). High resolution micrographs reveal uniform deposition of titania nano particles on aligned CNTs. Each CNT block or film structure is composed of uniformly distributed ultra long CNTs. Each nanotube is placed at a distance of 10 to 15 nm, forming a well ordered nano porous micro or even macroscopic film. As the growth of CNT is carried out at atmospheric conditions, and the growth is homogeneous across the film or block structure; the gas flow is certainly reaching the innermost part of such a macroscopic film. Therefore, vapor of titania precursor also be entering the innermost part of

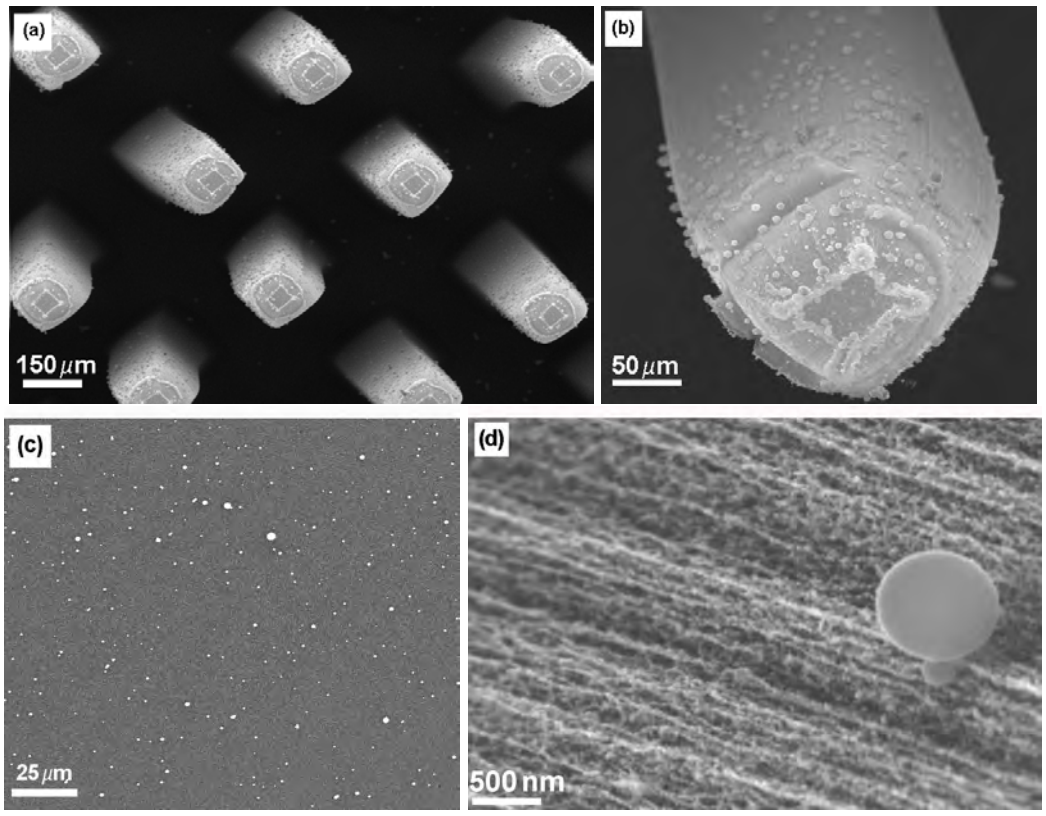

Figure 4.10: Scanning electron microscopy of titania-CNT composite. (a and b) low resolution images of CNTs block structure deposited using titania nano particles (c) top surface of CNT film and (d) high resolution images showing titania nano particle decorated CNTs.

the such CNT blocks depositing more or less same amount and quality of titania as if on outer wall of the block.

In order to determine the size and crystalline nature of titania particles deposited on CNTs, various samples prepared at 300, 550 and 750 °C were individually studied using TEM. The micrographs presenting the morphology of titania deposited at varying temperature are displayed in figure 4.11. As stated before, for CVD temperature below 500 °C, no particulate

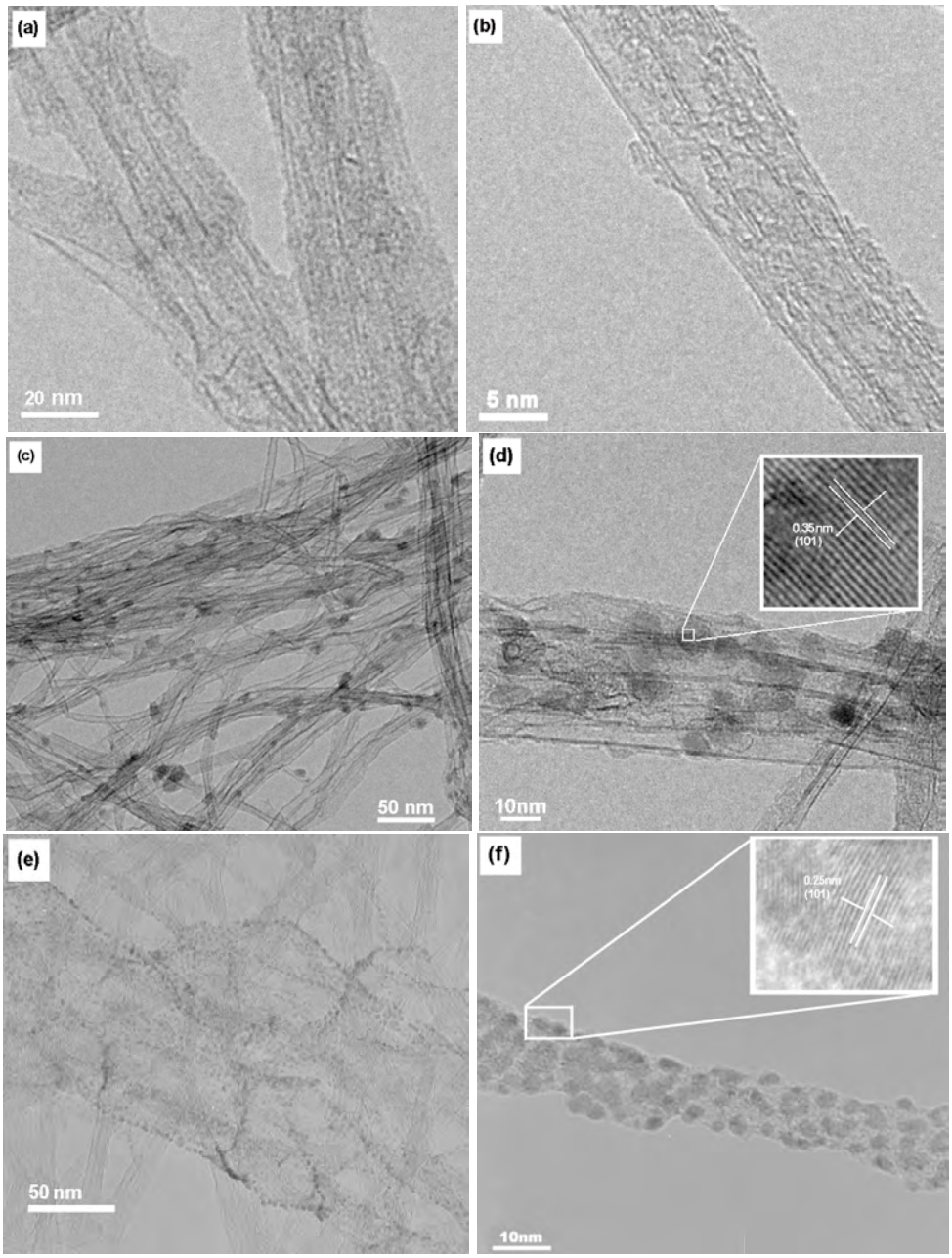

Figure 4.11: Transmission electron microscopy of titania-CNT composite prepared at (a and b) 300, (c and d) 550 and (e and f) 750 °C. Insets in figure (d and f) shows crystalline lattice fringes of respective titania phase.

morphology was seen. Instead, a amorphous layer of titania was uniformly deposited on the side walls of CNTs as seen in fig. 4.11a & b. Upon increase in the growth temperature, nano particles of titania were found to be nucleating with well ordered crystallinity even at temperature as low as 550 °C. TEM micrographs displayed in figures (4.11c & d) and (4.11e & f) show CNTs deposited with titania at 550 and 750 °C respectively. In both cases, the gas flow rate and the precursor temperature was held constant, and therefore CNTs were found to have homogeneous deposition of titania nano particles having more or less the same size. The average particle size obtained is 5 to 10 nm. However, at 550 °C, the anatase phase is predominant while higher temperature gives rise to rutile phase. The inset in the figure 4.11d shows well ordered lattice fringes of titania nano particle. The inter planer distance between lattice fringes was found to be 3.5 Å and 2.50 Å in figures e and f respectively. The inter planer distance matches well for anatase plane (101) in case of samples prepared at 550 °C and for rutile also (101) plane for sample synthesized at 750 °C. The average particle size is in range of 5 to 10 nm.

As anatase phase is more photo active, further study concentrates on titania deposited in anatase phase. X-ray diffraction of the sample synthesized at 550 °C, shows distinguishing peaks of anatase phase. In case of sample prepared at lower temperature, x-ray plot shows peak positions at 25.8, 48.05 and 53.9 ° of 2θ corresponding to crystal planes (101), (200) and (105) of anatase phase and relatively small intensity peaks at 54.2 and 83.2 represents graphitic CNTs.

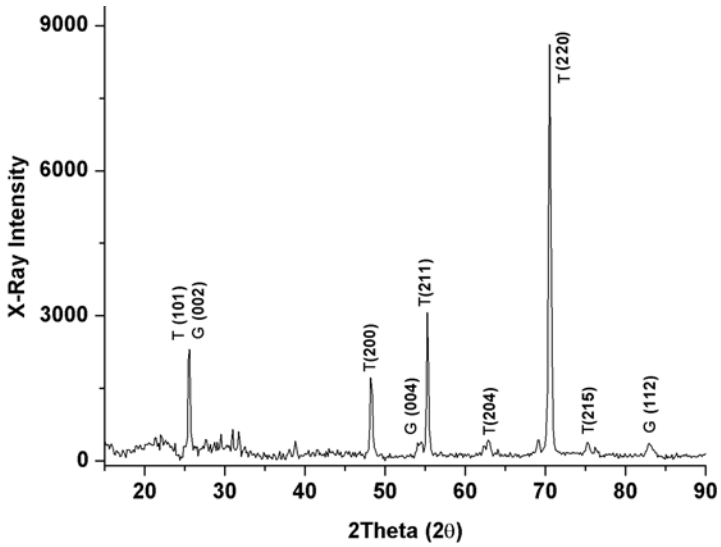

Figure 4.12: X-ray diffraction of titania-CNT composite prepared at 550 °C. The prominent anatase peaks are seen.

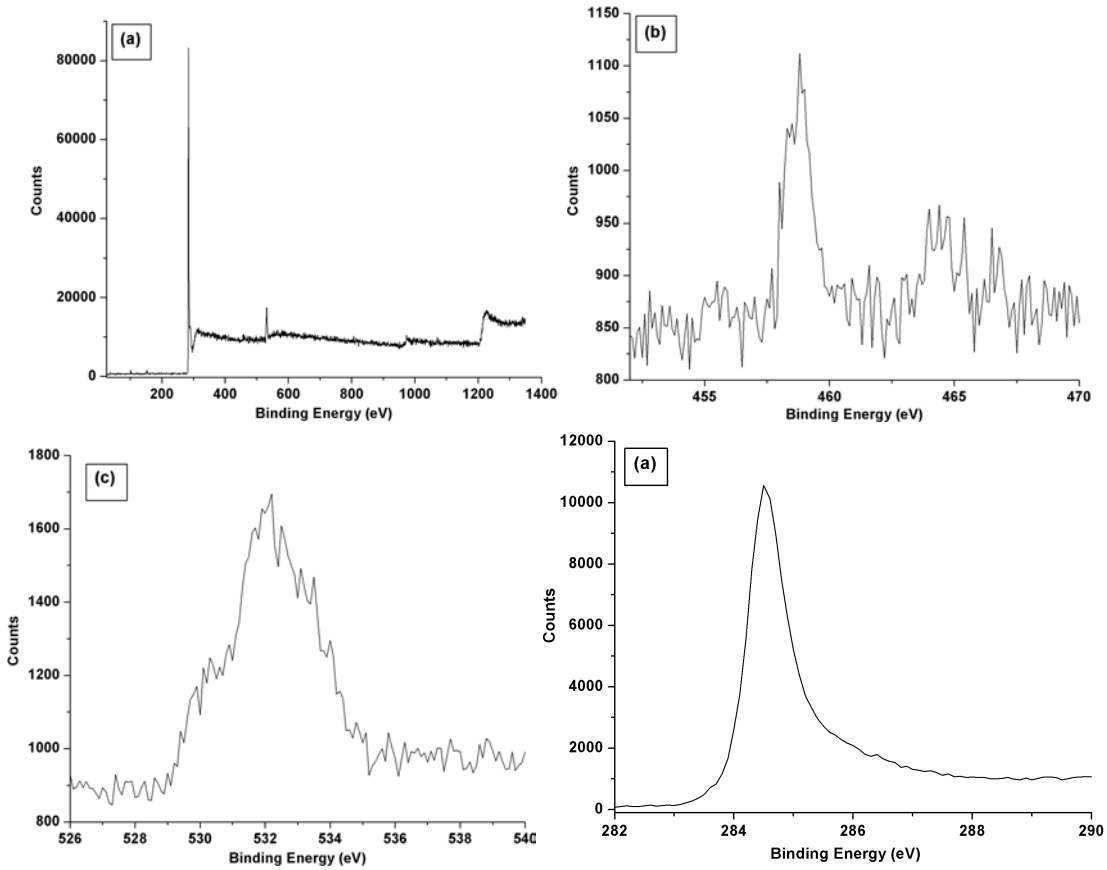

Figure 4.13: XPS spectra of titania - CNT composite (a) survey spectrum (b) titanium (2p3/2) (c) oxygen (O1s) and (d) carbon (C1s) spectrum.

The high degree of alignment is responsible for the absence of high intensity peak or graphitic (002) peak of carbon nanotubes. The spectrum is as shown in figure 4.12.

A composite of titania with CNTs enhances its photo catalytic activity. The titania phase as well as its composite formation with CNTs is cross examined by XPS spectroscopy (see figure 4.13). The survey spectrum obtained from XPS spectroscopy shows peaks for elements titanium, carbon and oxygen. The elemental peak of titanium (2p3/2) was recorded at 458.76 eV of binding energy and represent its tetra valent oxidized state. The oxygen peaks recorded at 532.02 eV of binding energy confirms the formation of titanium dioxide(TiO_2). Two peaks, carbon C1s at a binding energy of 284.5 eV and oxygen O1s shoulder peak at 530.15 eV, present graphitic carbon nanotubes from the support material.

4.2.2 Characterization of CNT - TiO_2 bilayer material

Similar to zinc oxide - CNT bilayer material, titanium dioxide CNT bilayer material composed of top layer of 100 to 200 nm oxidized film of titanium supported by carbon nanotube film

underneath. The metal was evaporated on glass substrate as well as on CNT film. Similar to zinc oxide process, film was oxidized in oven and as well in air. The upper limit for oxidation temperature was regulated to 500 °C, in order to avoid CNT oxidation as well as formation of rutile phase.

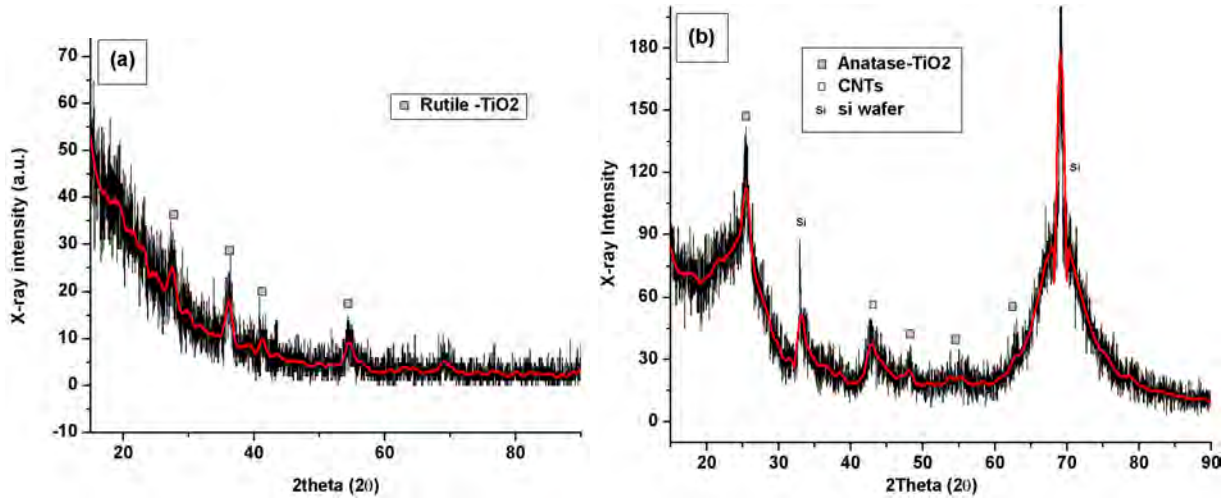

Figure 4.14: X-ray diffraction of titanium film oxidized on (a) glass and (b) CNT film. The red line is a smooth fit for better visualization.

As a preliminary step, 100 nm titanium was evaporated on glass and CNT film. These two films were then oxidized at 500 °C in air and investigated using x-ray diffraction. The oxidized film on glass substrate was light blue in color and one on CNT film was completely white. X-ray diffraction of both films, shows different phases clearly demonstrating predominant effect of porous nature CNT film as a substrate. On glass, the film was forced to undergo incomplete oxidation leading to formation of rutile phase. On the other hand, under better supply of oxygen

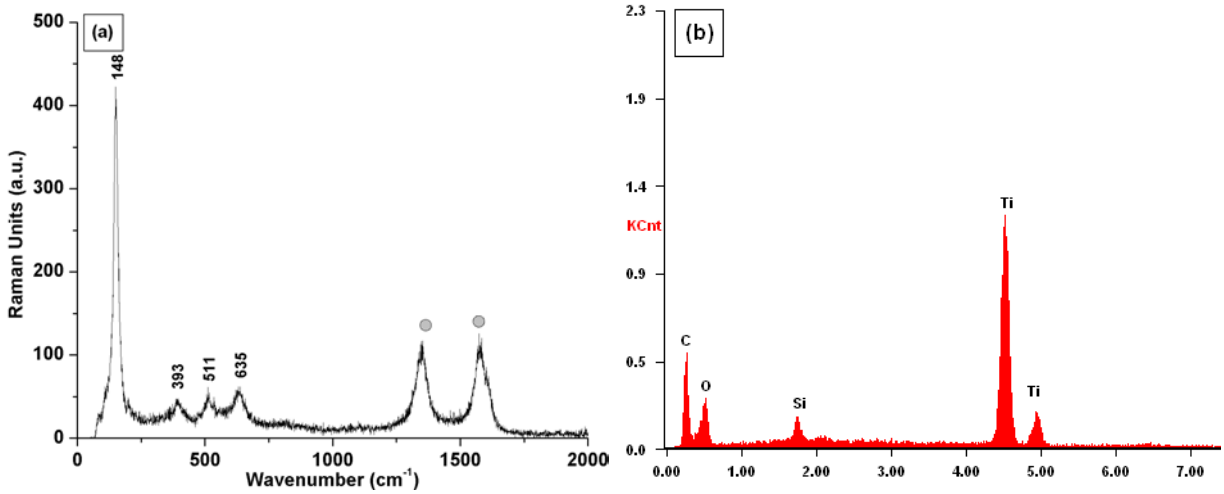

Figure 4.15: (a) Raman spectroscopy and (b) EDAX analysis of titania film grown on CNT film.

through nano porous CNT film, titanium film supported on carbon nanotube was oxidized to anatase phase. Both XRD plots are as shown in figure 4.14. Experiments were repeated in an oven under controlled oxygen atmosphere. Along with 100 sccm argon, oxygen in varied amount (5 to 100 sccm) was supplied. None of them could deliver a fruitful result. The CNT film used here as a substrate not only helps to form anatase phase, but also might helpful for better electron transport. The CNT film can act as a nano porous membrane helping to enhance the contact between the ruthenium dye and the photo active titania film in dye sensitized solar cell applications.

The phase of titania film grown on CNT is confirmed to be anatase by x-ray diffraction. Raman spectroscopy of same sample gives rise to peaks corresponding to anatase phase as shown in figure 4.15a. In the same spectrum, peaks marked with gray circles are originating from CNTs and represent defect and graphitic band peaks of carbon nanotubes. Parallely, EDAX analysis shows peaks for elements titanium, oxygen, carbon and silicon (see fig 4.15b). Titanium and

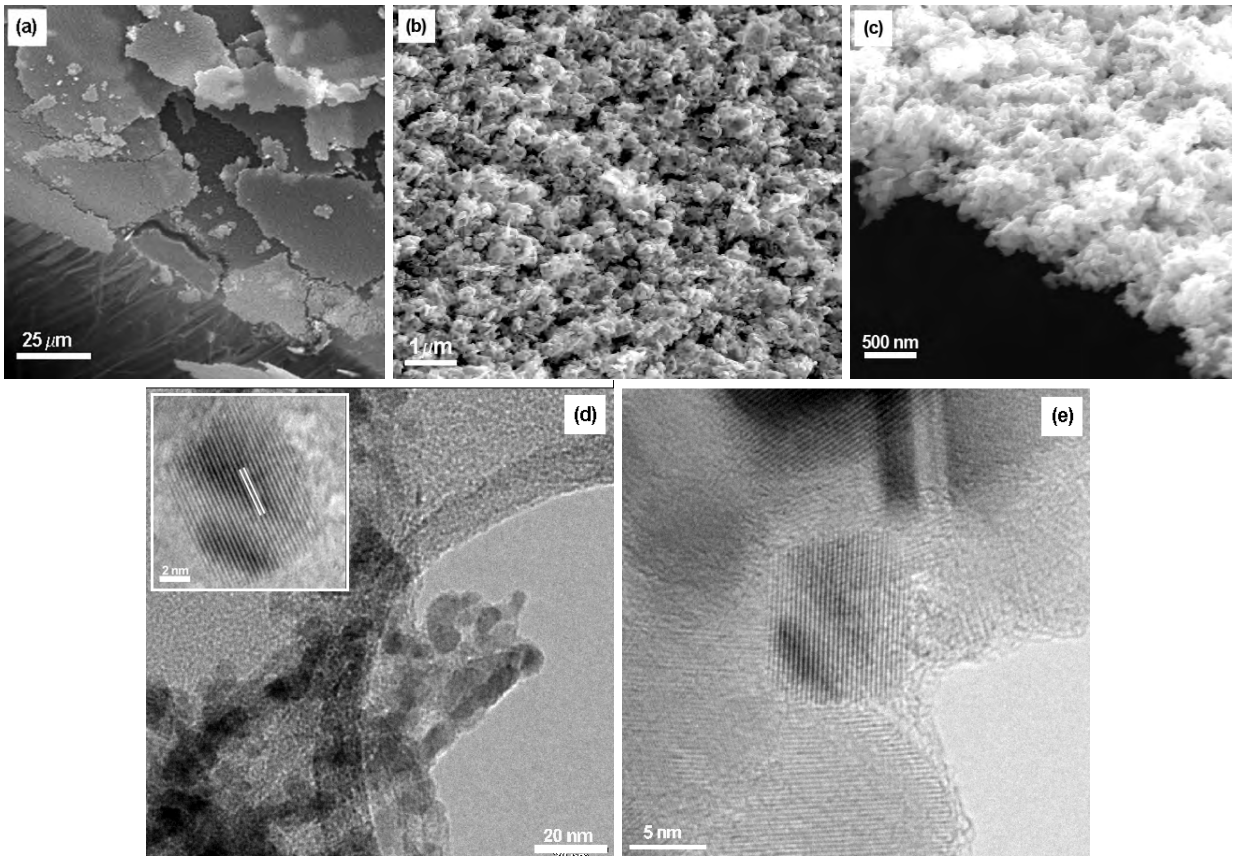

Figure 4.16: Electron micrographs of titania film grown on CNTs blocks. (a, b & c) SEM images and (d & e) TEM images.

oxygen peaks confirm the oxidation of titanium metal while carbon and silicon are from CNT and the Si-wafer substrate respectively.

The morphology of titania film as well as its average particle size plays a deciding role in photo catalysis or dye sensitized solar cells. If particles are too big, electron hole pair generated could not leave the particle fast enough increasing the risk of electron-hole recombination. SEM and TEM micrographs of titania film are displayed in figure 4.16. The low resolution image reveals titania on CNT film is indeed a porous film made up of nano crystalline titania. If resolved to higher magnification, titania film found to be made up of small particles similar to that of zinc oxide morphology explained before. In presence of nano porous and crystalline CNT film, supply of oxygen through these nano sized pores leads to uniform oxidation of titanium film and oxidation takes place at numerous places building up small nano particles. Similar to zinc oxide, titania nanoparticles also agglomerate together to build up bigger particles (see fig 4.16d). It might be advantageous as while oxidation, particles surely get intimate contact with each other necessary for better electron transport. TEM micrograph 4.16e reveal, film indeed made up of small titania nano particles interconnected to each other to form a bigger particle. The average size of single titania nano particle obtained from transmission electron microscopy is of order 5 to 10 nm. Titania nano particles were crystalline with major arrangement in direction (101) plane.

4.2.3 Characterization of TiO_2 thin film on CNT blocks

The sol - gel method is a solution based method and uses a titania sol in alcohol (iso-propanol) solvent. During infiltration the liquid sol can enter and cover the complete circumference of

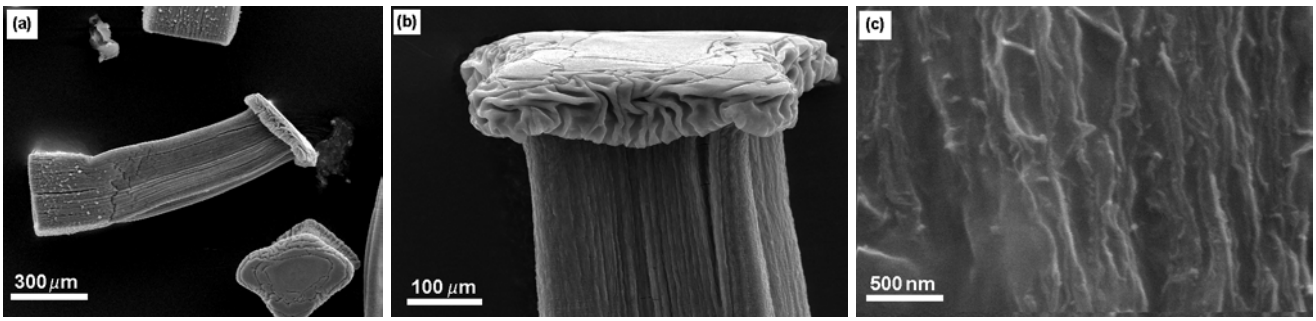

Figure 4.17: SEM micrographs of titania film deposited on CNTs blocks. (a and b) show low magnification images of composite, while (c) is high magnification image showing CNTs embedded in titania film.

individual carbon nanotube as well as the outer periphery of block structure. The viscosity of the solution and rate of evaporation of solvent after deposition on CNT are deciding factors to avoid the complete collapse of the CNT structure. The nano porous CNT structure can shrink upon solution evaporation leading to a complete destruction of the structure. However, if the viscosity of the sol is well controlled and solvent is evaporated in a controlled manner, the collapse of the CNT structure can be hindered. The method gives unique advantage to control the crystalline nature and possibility of dopant insertion.

The titania - CNT composite was characterized using using XRD and Raman spectroscopy. The extent of titania deposition was visualized with the help of SEM investigations (see figure 4.17). Titania is uniformly coated on the block and structure is intact even after crystallization of titania by thermal treatment. The high magnification image (figure 4.17c) of side wall of block confirms, CNTs are embedded inside the titania layer.

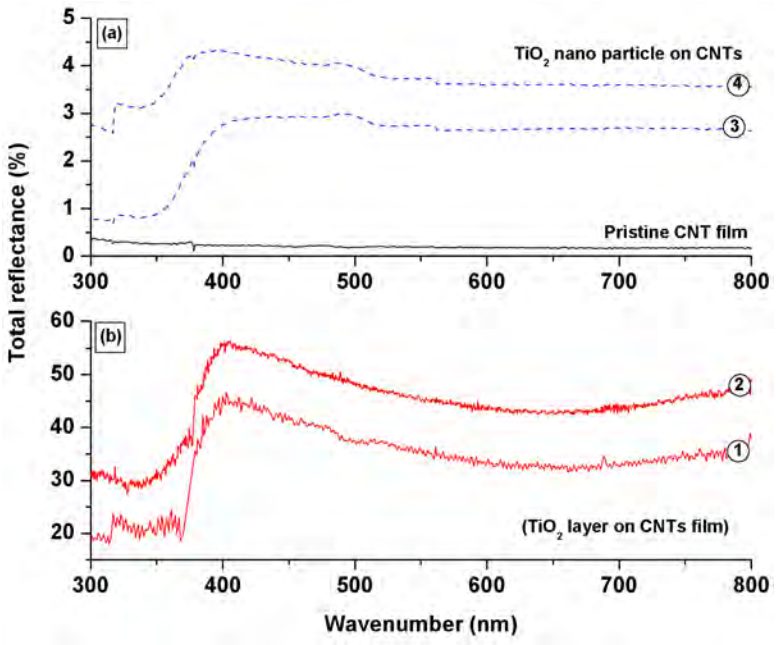

Figure 4.18: UV-Vis total reflectance of (a) TiO_2-CNT composite and (b) TiO_2-CNT bilayer material.

Titania - CNTs composite material synthesized using different methodologies was tested as a material for potential applications such as dye sensitized solar cells, photo catalysis and cold cathode emitters etc. CNT block structures coated by titania in the gas phase or by metal oxidation technique are quite suitable material for such applications due to narrow particle size distribution at nano scale. Efforts were taken to transfer CNT blocks on a transparent glass electrode after titania deposition. The titania particles will be then sensitized using a

commercially available ruthenium based dye and will be tested for harvesting the solar energy. The UV-Vis total reflectance of the composite as well as bilayer film of TiO_2-CNT is as shown in figure 4.18. Unlike to pristine CNT film, various samples prepared under different conditions show drop in total reflectance in range 350 to 450 nm. Also, primary tests to study the photo catalytic activity and enhanced stability in field emission applications have been successfully studied. Preliminary results are discussed in application part of this thesis.

4.3 Deposition of iron oxide on carbon nanotubes

Iron oxide, in magnetite form (Fe_3O_4) is a most interesting magnetic material. Below certain size, ($\sim$ <20 nm) magnetite behave super paramagnetic in nature. Various solution based reduction techniques using iron salts and appropriate surface functional groups are available to grow nano particles of magnetite [204, 210, 219]. These processes deliver optimal particle size, however, need critical control over experimental conditions (pH, inert atmosphere etc.), making the process complicated and tedious to control.

A molecular precursor Tri[2-(methoxyimino)propanoato]iron(III) also known as iron oximato was prepared in lab and used to grow nano particles of magnetite [220]. The precursor not only delivers optimal size in range of 5 to 15 nm, but also eliminates process complications such as working under inert atmosphere, surface functionalization, pH control etc. The precursor readily decomposes at relatively low temperature or by under UV radiations. The detailed preparation procedure for precursor is explained in experimental section of this thesis.

4.3.1 Characterization of iron oxide obtained from oximato precursor

The chemical structure as well as reaction path way explaining the decomposition of iron oximato precursor and formation of iron oxide nano particles is as shown in figure 4.19. The oximato precursor can be decomposed using thermal energy as well as by using UV radiations. The decomposition is clean, almost free of any chemical impurity. The thermal decomposition of the precursor was studied using thermogravimetric - mass spectrometry (TG - MS)analysis. The major product of the decomposition process is iron oxide in magnetite form. Along with

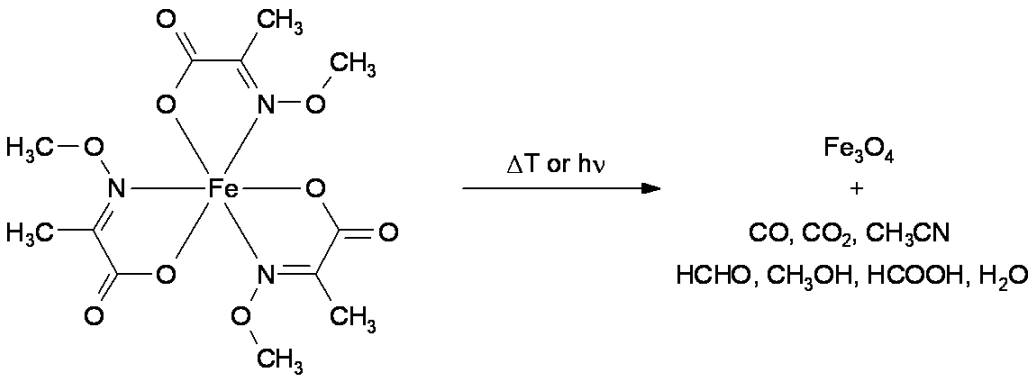

Figure 4.19: Decomposition of oximato(Tri[2-(methoxyimino)propanoato]iron(III)) precursor yielding iron oxide of magnetite phase [220].

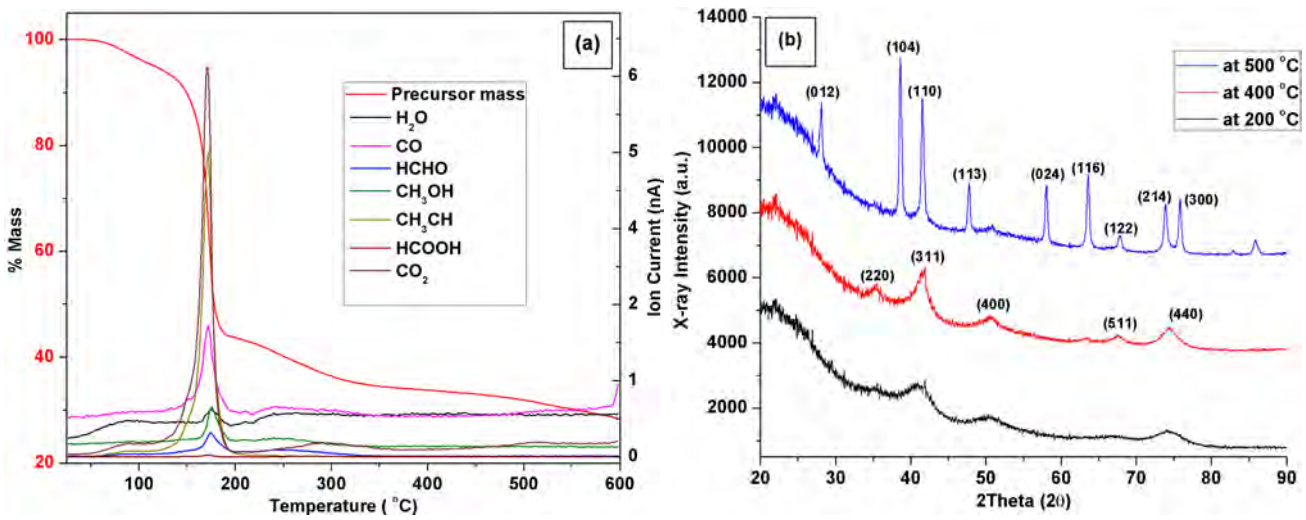

Figure 4.20: (a) Thermogravimetric - mass spectrometry analysis of oximato precursor yielding iron oxide (a) X-ray diffraction plot showing temperature dependent phases of iron oxide synthesized from same precursor.

it, carbon mono and dioxide gas, methyl cyanide and water are released as bi-products as a result of decomposition of the ligand. The decomposition follows second order Beckmann route [161, 221].

The TG - MS analysis of precursor (see fig 4.20a) carried out in helium atmosphere shows loss of water of crystallization below 100°C. At around 150 to 160°C, the precursor decomposes almost instantly leading to formation of iron oxide. The decomposition of precursor reaches final stage at around 200°C giving crystalline magnetite particles. During decomposition, bi - products such as acetonitrile, formic acid, methanol, formaldehyde, carbon mono and dioxide were detected using mass spectrometry. Acetonitrile and carbon dioxide were released simply by decomposition of oximato ligand where as formic acid and formaldehyde were presumed to be oxidative products of methanol generated by decomposition of oximato ligand itself. The oxidation of methanol can be co-related to the reduction of iron from Fe^{3+} (in oximato) to Fe^{2+} state [220]. Such reduction occurs partially as a mixture of Fe^{3+} and Fe^{2+} ion forming Fe_3O_4 is obtained as a final product. Past 200°C, a further loss in weight was observed and the process is complete with weight lose of about 70 to 75%. Past 400°C, magnetite become unstable transforming into hematite (α - iron oxide); explained as follows.

The temperature dependent phase transformation from magnetite to hematite was followed using x-ray diffraction technique (see fig 4.20b). The precursor was decomposed by heating to 200°C for an hour in air. Next, part of the product was heated to 400, 500 and 600°C for an

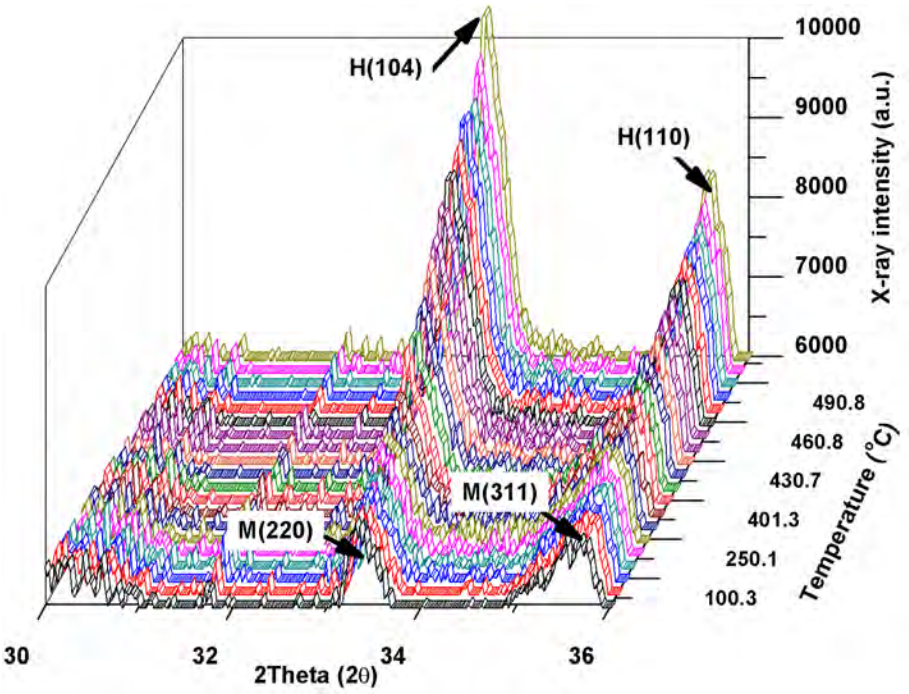

Figure 4.21: High temperature X-ray diffraction showing temperature induced phase transformation of iron oxide from magnetite to hematite.

hour. The decomposition carried out at 200°C, reveal formation of magnetite phase, however the peaks are broad and are of less intensity. It might be due to incomplete decomposition or presence of organic residue. Further heating to higher temperature leads to formation of crystalline nano particles of magnetite. This phase of iron oxide is found to be stable till a temperature up to 400°C. X-ray diffractogram of a sample heated to 500°C shows nice sharp peaks from the newly formed hematite phase of iron oxide. The exact temperature at which

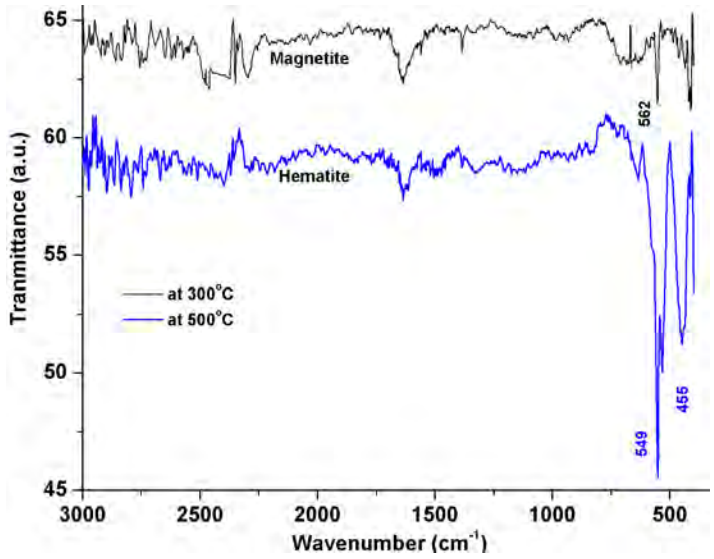

Figure 4.22: IR spectroscopy of oximato precursor, magnetite at 300°C and hematite 500°C.

change in crystal structure takes place is estimated by using high temperature X-ray diffraction method.

The measurement was carried out between the temperature range 29°C to 600°C and X-ray diffraction scan in range of 28 to 38° of 2θ (see figure 4.21). The region 28 to 38° of 2θ includes two peaks of magnetite and of hematite. Magnetite peaks at 35.05 and 41.36° of 2θ originating from (220) and (311) crystal planes. On the other hand, in case of hematite peaks at 38.69 and 41.59° of 2θ representing (104) and (110) crystal planes were seen. Till 400°C, magnetite peaks were recorded. With further rise in the temperature, the intensity of magnetite peaks starts decreasing with unanimous rise in hematite peaks. The complete lose of major intensity

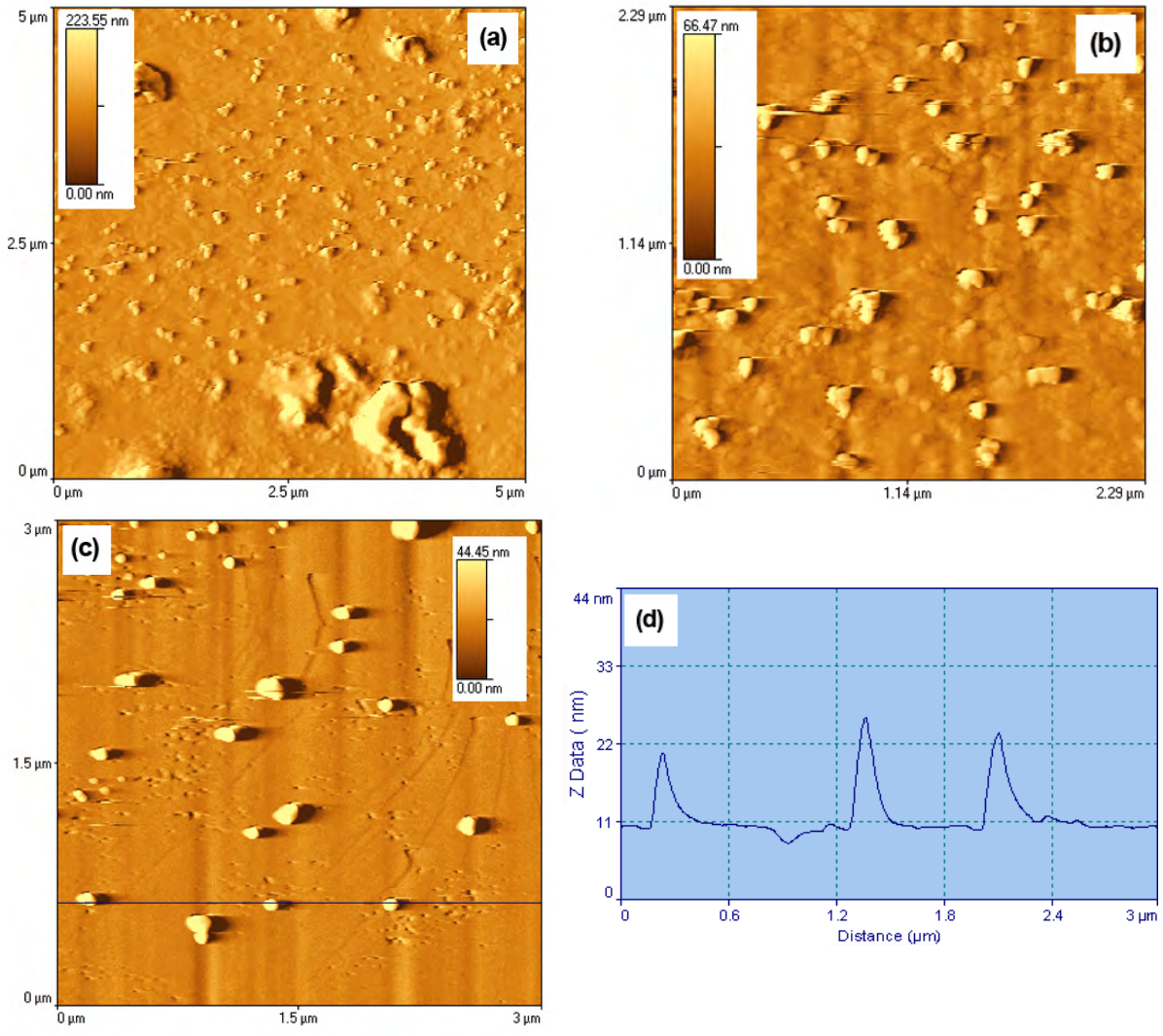

Figure 4.23: AFM micrographs of magnetite nano particles. (a and b) are micrographs of agglomerated magnetite particle. Big lumps in figure (a) are seen. (c) well dispersed single nano particles on substrate and (d) shows profile of particles in Z direction along the line marked in figure (c).

(311) peak of magnetite was recorded at temperature $\sim$ 460 °C. Therefore the transformation temperature of magnetite to hematite is confirmed to be $\sim$ 460 °C.

Iron oxide nano particles obtained by decomposition of the precursor at various temperatures were studied using the IR - spectroscopy (see figure 4.22). The decomposition product obtained at 300 and 500°C, both have almost negligible amount of organic contamination. The sample heated to 300°C, shows an absorption band at 562 cm-1 assigned to Fe-O stretching modes of magnetite lattice [207, 222]. On the other hand, at 500°C, nano particles have hematite phase giving rise to Fe-O absorption edge at wavenumber 549 and 455 cm^{-1} [222].

The size and the morphology of magnetite nano particles were determined with the help of atomic microscopy tool (See figure 4.23). Magnetite particles are obtained by thermal decomposition of precursor in air. In absence of proper surfactant, particles tend to agglomerate building bigger one or even a film over the silicon wafer. However, nano particles can be well dispersed in an alcohol solution by light ultra-sonication. The AFM image of well dispersed individual nano particles reveal spherical morphology and diameter of order 10 nm. The profile of particles in z direction is measured for three free standing particles is as shown in figure 4.23d. All three particles have diameter in range mentioned above.

4.3.2 Characterization of CNTs - Fe_3O_4 composite material

Magnetite nano particles of same size and morphology were deposited on carbon nanotubes. In order to do so, a CNT film was dipped into the oximato precursor solution in ethanol, dried and heated to 300°C or treated using UV-radiation to grow magnetite nano particles. In order to control the particle size and morphology, a ethanol based oximato solutions of different concentration (1.11, 2.23, 3.34, 4.45 and 8.91 mM) were tried. In ever solution, a CNT film (0.5x1 cm or 0.5 mg in weight) was dipped and solvent was evaporated. The process was repeated at least for 2 times. Finally, the semi-dried film was heated or treated using UV-radiations in order to decompose the precursor to form nano particles of magnetite. Composites prepared using different precursor concentrations were dispersed separately into a ethanol medium and drop casted on Si wafers for further examination.

Scanning electron microscopy was employed to examine the morphology, distribution and homogeneity of magnetite nano particles in each composite. SEM investigations of all samples using a solution concentration higher than 4.45 mM reveal formation of large agglomerate

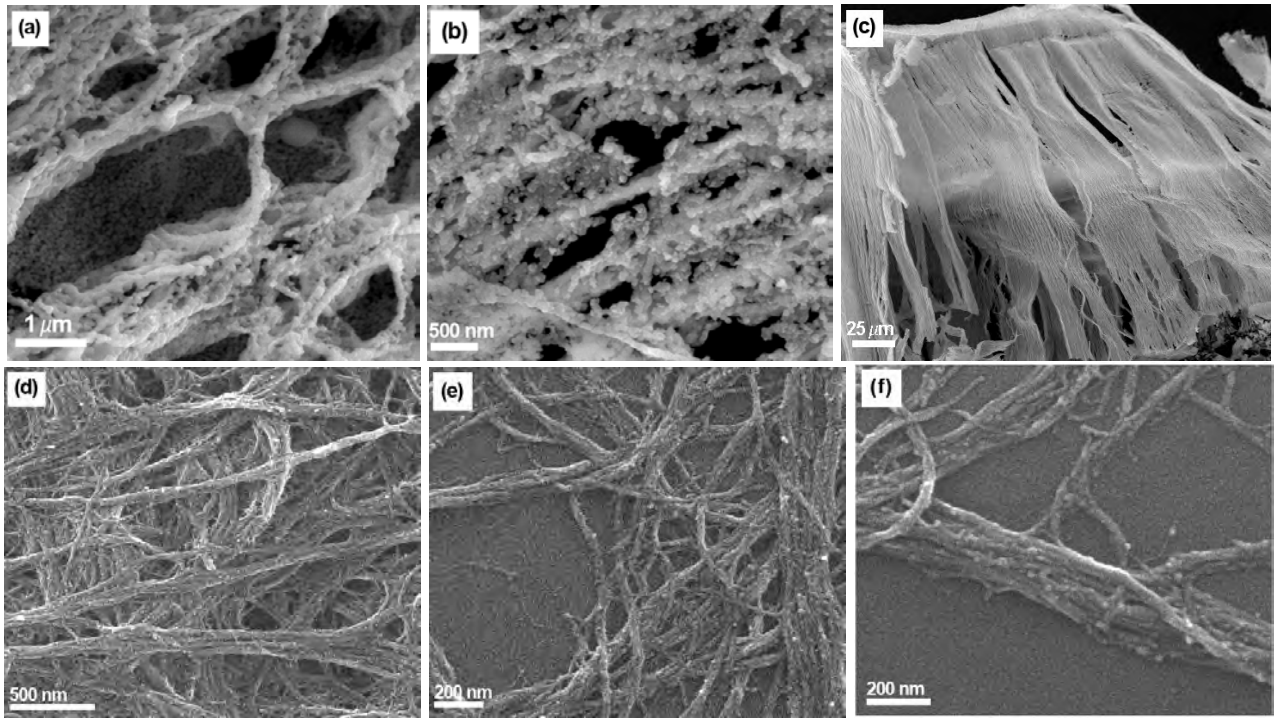

Figure 4.24: SEM micrographs of magnetite nano particles decorated CNTs. (a and b) are micrographs of CNTs hidden beneath aggregates of magnetite particles. (c) fiber structured magnetite - CNT composite, (d e & f) are well dispersed CNTs decorated by magnetite nano particles. (a,b & c) with solution concentration 4.45 mM and (c,d & e) from 1.11 mM solution.

of magnetite on the side wall of CNTs. CNTs were completely covered by bigger particles or aggregates of magnetite nano particles. The size determination of magnetite nano particle is a non trivial task due to lack of possibility of transmission electron microscopy because of their magnetic nature. For concentration lower than 4.45 mM, evenly distributed nano particle of magnetite were observed. The average particle size was found to be optimal ($\sim$ 10 nm) for the sample prepared by using 2.23 mM concentrated oximato solution. SEM micrographs of the CNT-magnetite composite prepared using various concentration are as shown in figure 4.24. For concentration lower than 2.23 mM, particles formed had average size below 10 nm, practically below resolution of SEM. SEM micrographs are displayed in figure 4.24e & f. The sample prepared using 2.23 mM solution concentration show optimal distribution of magnetite nano particles on side wall of CNT and this sample is chosen for SQUID measurement and referred as "FeCN-2a".

For solutions of concentration lower than 2.23 mM, the observed size of magnetite particles in the composite was very fine. Therefore, composites prepared using lower concentrations

(1.11, 2.23, and 3.34 mM) were examined using AFM to estimate the average size of magnetite nano particles. Same as before, the composite was dispersed in ethanol to form a very dilute dispersion, and one drop of such dispersion was deposited on Si-wafer and dried. Using AFM in non contact mode, the sample was scanned over different areas of drop casted composite. The AFM study confirms the observations of SEM investigations and it reveal that the size of nano particles as well as distribution over CNT decreases with decrease in the concentration of the solution (see figure 4.25). Using Z-scan technique, average size of the particle in various

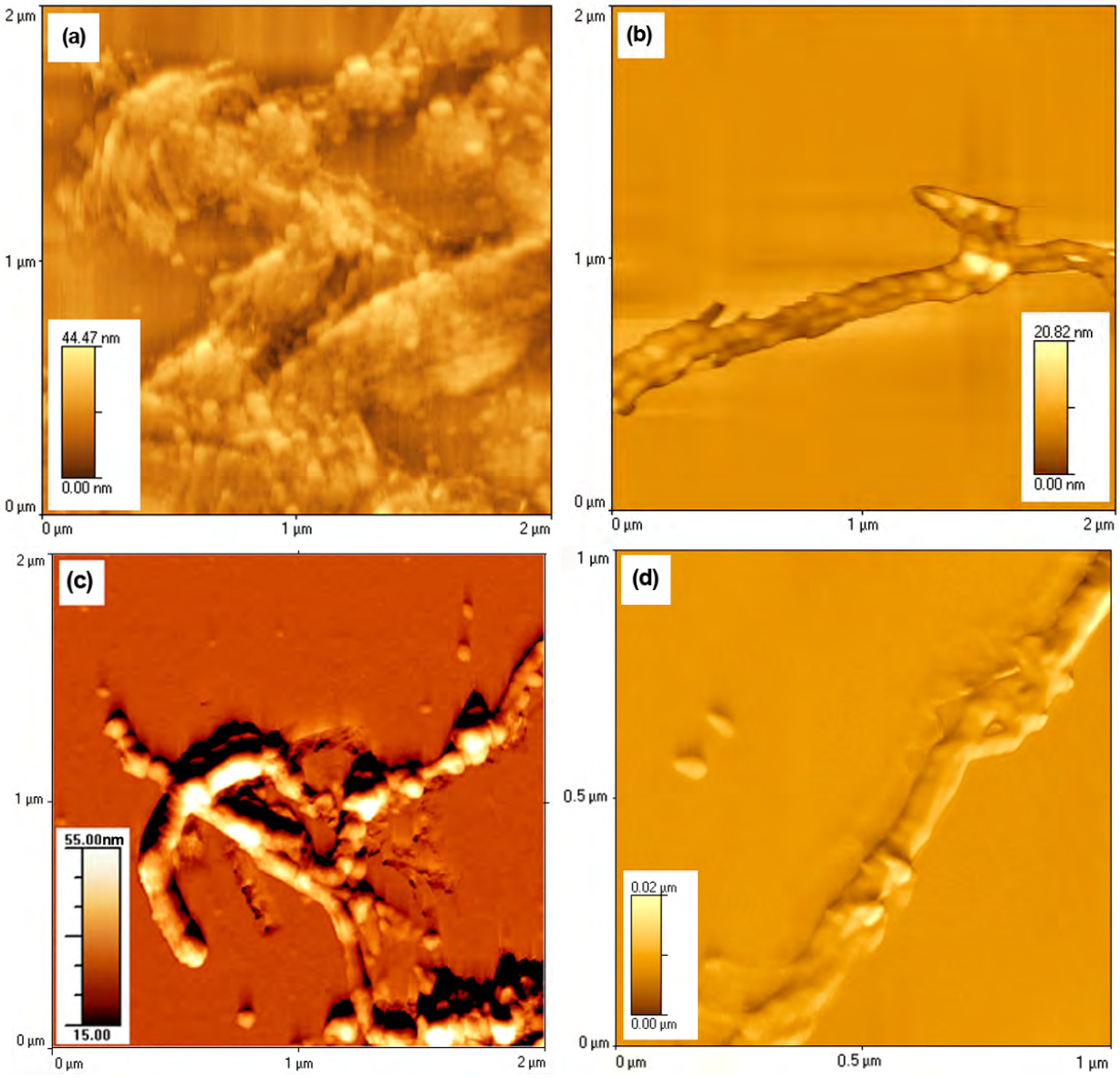

Figure 4.25: AFM micrographs of magnetite nano particles decorated CNTs. (a) an overview of composite, composite prepared using solution concentrations (b) 3.34 mM, (c) 2.23 mM and (d) 1.11 mM. Notice the decrease in average particle distribution with decrease in solution concentration.

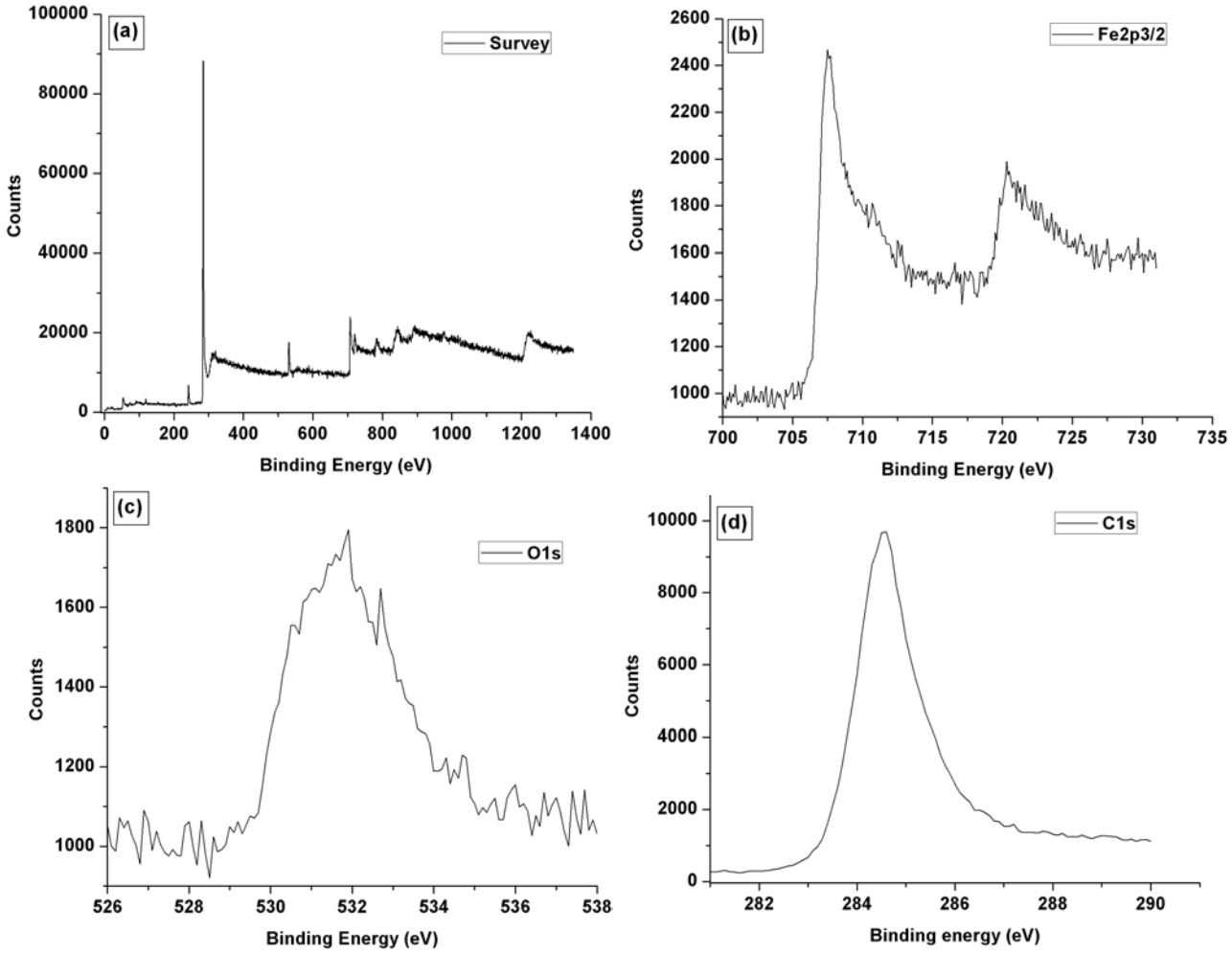

Figure 4.26: XPS spectra of magnetite - CNT composite (a) survey spectrum (b) iron (Fe2p3/2) (c) oxygen (O1s) and (d) carbon C1s spectrum.

solution was determined. The optimal particle size of an order 5 to 10 nm was found for samples prepared using a solution 1.11 and 2.23 mM. Although the particle size obtained from 3.34 mM solution had nearly the same mean distribution, particles were covering the CNT completely by forming a homogeneous layer on it. Such layered deposition will reduce the effective CNT - magnetite contact area which are optimal sites at which catalytic reactions can proceed.

The XPS spectrum (survey) of the composite (FeCN-2a) further confirms the elemental composition of the composite (figure 4.26). The survey spectrum had distinguishing peaks of iron and oxygen originating from magnetite along with a carbon peak originating from carbon nanotubes. The high resolution iron 2p3/2 signal has binary peak position. Peaks recorded at 707.7 eV and 720.3 eV of binding energy correspond magnetite composition of iron [223, 224]. The oxygen peak is broad encapsulating different oxygen species. Two major peaks of oxygen were recorded at 530.5 and 531.7 eV. The prior peak represents the oxygen

from magnetite [224] while the later one is assigned oxygen species present on CNTs [100]. The precursor deposited on CNTs was thermally decomposed at 300 °C in air. This might lead to oxidation of carbon atom presents at dangling sites. The carbon peak was positioned at 284.5 eV, attributed to graphitic structure of carbon, i.e. CNTs (see XPS study of CNTs in section 2).

4.3.3 SQUID investigation of Fe_3O_4 and CNT - Fe_3O_4 composite

The hysteresis loop obtained in SQUID measurement is basically a x-y plot of volume averaged magnetization against applied external magnetic field. The iron oxide obtained from the precursor is magnetite in phase (below 400 °C), and heating it to higher temperature will lead to formation hematite (at 500 °C or above). The hysteresis plot for the both phases is as shown in the figure 4.27a.

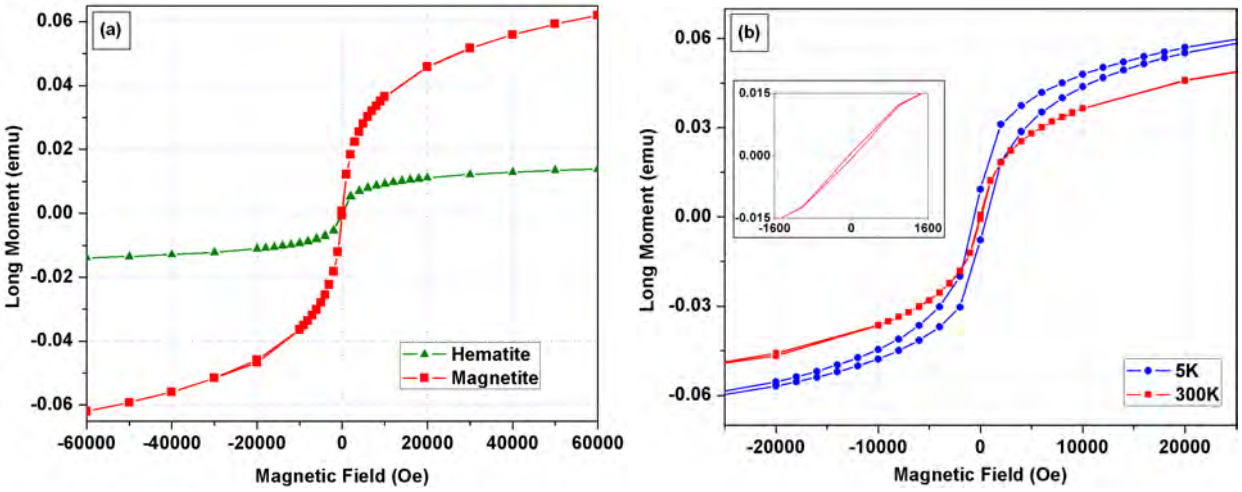

Figure 4.27: Magnetic hysteresis curves (a) of magnetite and hematite at 300 °C and (b) of magnetite at 300 and 5 K.

The particle size of magnetite is small enough to be made up of a single domain depicting super paramagnetic behavior [219]. Figure 4.27a shows the standard 'S' shaped hysteresis curve for magnetite (sample FeCN-1) and hematite (sample FeCN-1a). Both curves have no coercivity. The red curve, representing magnetite phase, do not reach the saturated state of magnetization even under strong external magnetic field (∼ 60000 Oersted). The lack of coercivity and remanence in the hysteresis loop corroborate the super paramagnetic nature of the as synthesized nano particles. On the other hand, although hematite has nearly the same particle size as it is obtained by air oxidation of magnetite nano particles, it reaches a state of magnetic saturation in presence of a very small external magnetic field (∼ 4000 Oersted).

The hysteresis curves of magnetite sample (FeCN-1) cooled down to 5 K using liquid helium and at room temperature are as shown in the figure 4.27b. The hysteresis curve at 300 K shows nice super paramagnetic behavior, however at 5 K, small coercivity was recorded. The appearance of the coercivity is due to lack of enough thermal energy to over come complete thermal equilibrium with the applied field during the time required for the measurement. The same effect is quite possible to observe if, at a given temperature, size of the particle is increased [209, 219]. The room temperature magnetic coercive field is 59 Oe, which is significantly small.

The magnetization curve of magnetite nano particles deposited on side walls of CNTs (sample FeCN-2a) using thermal decomposition of the precursor is as shown in figure 4.28. As the size and morphology of magnetite nano particles deposited on carbon nanotubes is more or less same as that of pure magnetite nano particles, they depict same super paramagnetic nature at room temperature. The average particle size obtained on CNTs was 6 to 10 nm. The coercivity of the magnetite nano particles obtained in powder form was measured to be 59 Oe. The magnetization curve of the composite FeCN-2a shows no traceable coercivity (see inset in figure 4.28). This indicates that, CNTs might help nano particles to get aligned to external magnetic field more easily compared to unsupported magnetite nano particles.

The magnetite - CNT composite shows good super paramagnetic properties. Thus the composite can be advantageously used to prepare a magnetic field induced micro actuator. For this, magnetite nano particles will be deposited on CNT blocks by using same method explained

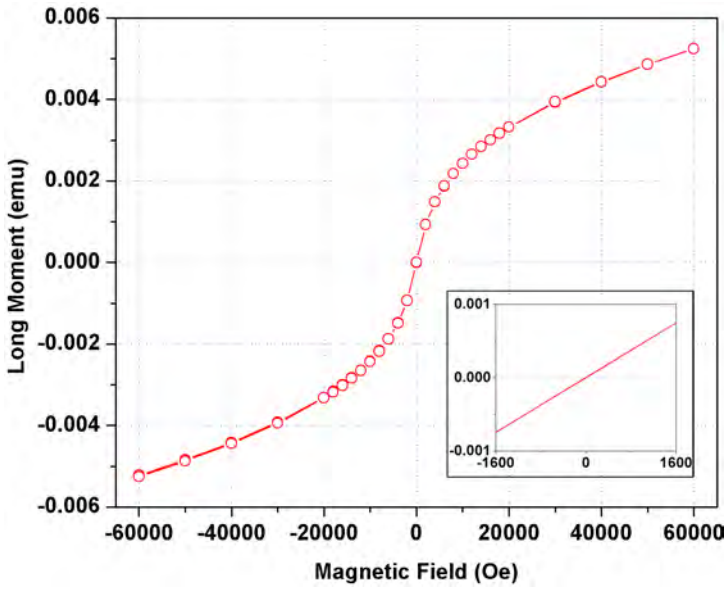

Figure 4.28: Magnetization curve for magnetite decorated CNTs composite.

before. The block will be subjected to reversible magnetic field using commercially available solenoids. A pictorial representation of magnetite - CNT actuator along 2 solenoids is as shown in figure 4.29. The as grown CNT blocks will be held fixed on Si wafer. Magnetite nano particles are deposited on CNT using molecular precursor. Upon the application of an external magnetic field, the magnetite particles adhered to CNT side walls will force the CNT block to bend towards the solenoid under the attractive force. If the direction of external magnetic field is continuously changed with a certain frequency, CNT block will tend to vibrate to and fro to form an actuator. Work in this direction is under progress.

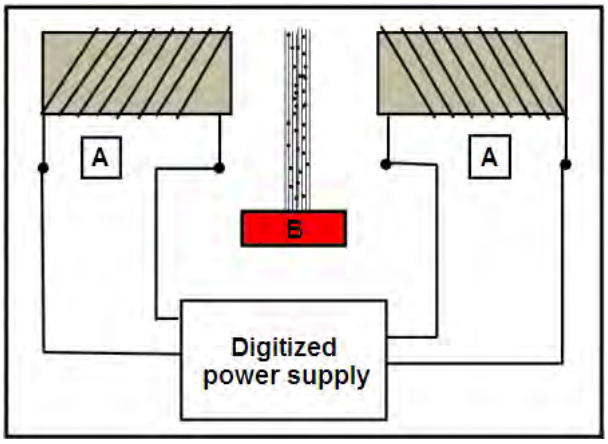

Figure 4.29: Pictorial representation of magnetite - CNT actuator. In figure (A) electro magnets and (B) magnetite - CNT composite supported on Si wafer.

The method explained here to prepare magnetite nano particles is straight forward, simple and effective. This process works under ambient conditions, eliminates critical control of work conditions and the need of surface functional groups to stabilize the size of magnetite nano particle and avoid agglomeration.

4.4 Platinum nano particle decorated carbon nanotubes film for PEM fuel cells

Proton exchange membrane (PEM) is one of the intensely researched low temperature fuel cell system. The membrane electrode assembly (MEA) is the heart of a PEM fuel cell. It incorporates central electrolyte film made up of nafion membrane sandwiched between two layers of platinum loaded electrodes. For a homogeneous dispersion, particle size control and enhanced electrical conductivity, carbon nanotubes are used as a principle part of these electrodes. The MEA is assembled between gas diffusion layers and end plates supplying hydrogen and oxygen gases (see figure 4.30). Hydrogen gas is oxidized by platinum nano particles and electrons generated during this process are carried to the outer circuit by carbon nanotubes. Protons generated during this process diffuse through the nafion film to anode side and combine with oxygen to generate water.

Platinum nano particles are often loaded on carbon nanotubes by employing a chemical route. Usage of a chemical method to deposit platinum nano particles from its salt solution demands functionalization of CNTs. Such a functionalization will lead to damage of CNTs structure and thereby increase in net electrical resistance of the cell. Apart from this, optimal size of platinum nano particles should be in range of 2 to 4 nm, which is hard to control. Normally, Pt decorated CNTs are drop casted on nafion film without any preferred orientation. With such a lack of orientation its hard to control the porosity of the film leading to loss of gas pressure, ineffective

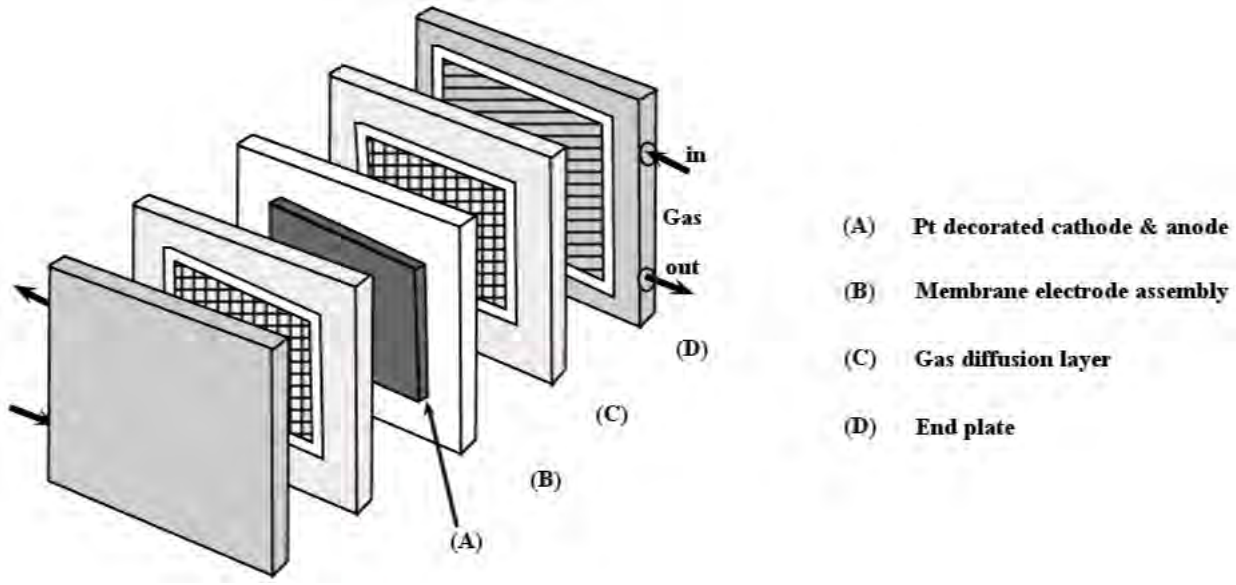

Figure 4.30: Schematic showing an exploded view of a PEM fuel cell stack.

use of platinum catalyst. CNT films grown using WCVD method can possibly be a solution two above mentioned problems in PEM fuel cell. The perfect CNTs alignment will not only improve the gas flow conditions, effective usage of the catalyst but also can lead to enhanced electrical conductivity. The process of MEA preparation incorporating a film of aligned CNTs is discussed below.

Carbon nanotube film grown on silicon wafer consists of 2 - dimensional arrangement of CNTs. CNTs as they grow perpendicular to the substrate, form a membrane with enormous nano porosity and high surface area. Also, due to their nano size, they readily form a redox pair with platinum in its salt solution, reducing platinum to its metallic state. By this way, platinum particles of an average size 2 to 4 nm is easily obtained. These properties can fruitfully used to build up membrane electrode assembly for fuel cell studies. The MEA for fuel cell can be build up by two ways as follows.

1. Two CNT films grown on si wafer were transferred to either side of a nafion membrane. Self reduction technique will be utilized to deposit platinum particles on CNTs. The cell is then ready for testing.

2. CNTs were grown on commercial carbon paper. Platinum nano particles were deposited on CNTs to build up a test cell.

4.4.1 Characterization of membrane electrode assembly (MEA)

Carbon nanotube film was grown on Si wafer using standard water assisted chemical vapor deposition method to a height of about 300 to 400 μm. The film was softly peeled off from the substrate and dipped in platinum salt solution. The film was kept swimming in the solution for an hour and then taken out, washed with distilled water and dried. During this one hour, platinum (Pt^{+4}) ion concentration will continuously decrease. This was monitored using the UV-VIS spectroscopy. The UV-VIS absorbance spectroscopy of the salt solution at initial time, after half an hour and at one hour is as shown in the figure 4.31a. The concentration of the solution decreases with the passage of time which is clearly seen in terms of drop in absorbance intensity of the salt solution. The drop in absorbance intensity can be directly correlated to reduction of platinum ions to its metallic state and getting deposited on CNTs.

The CNT film deposited by platinum nano particles was analyzed by using thermogravimetric analysis technique to find out the extent of platinum loading (see fig. 4.31b). The standard platinum loading used for fuel cell applications is of order 0.2 to 0.5 mg/cm^2. The CNTs film used in this study has exactly 1 cm^2 of surface area. 10 mg mass of platinum decorated CNTs was oxidized in oxygen atmosphere. CNTs grown using WCVD technique are clean and free from any impurity and sustain temperature as high as 550 °C without undergoing oxidation. However, platinum nano particles promote or catalyze the oxidation of CNTs at a temperature of about 400 °C. The mass left over after the complete oxidation of CNTs was around $\sim$ 57%, which in this case accounts for the platinum nano particles deposited.

A single CNT film possessing dimensions (1cm x 1cm x 500 μm) weighs approximately 1 milligram. Therefore the platinum loading on 1 cm^2 CNT film would be 0.57 mg which is in range of conventional amount of platinum loading for fuel cell applications. If necessary, a slightly diluted platinum salt solution or lower reaction time will be used to tune the loading rate of platinum.

Carbon nanotubes decorated using platinum nano particles were investigated using electron microscopy. For this purpose, a CNT film was halved into two parts, and then dipped in the platinum salt solution. First halve was taken out after a half an hour of reaction time and the second halve after an hour. Both films were washed, dried and studied using SEM. CNTs from both films found with very small nano particles of platinum on their side walls. The average size

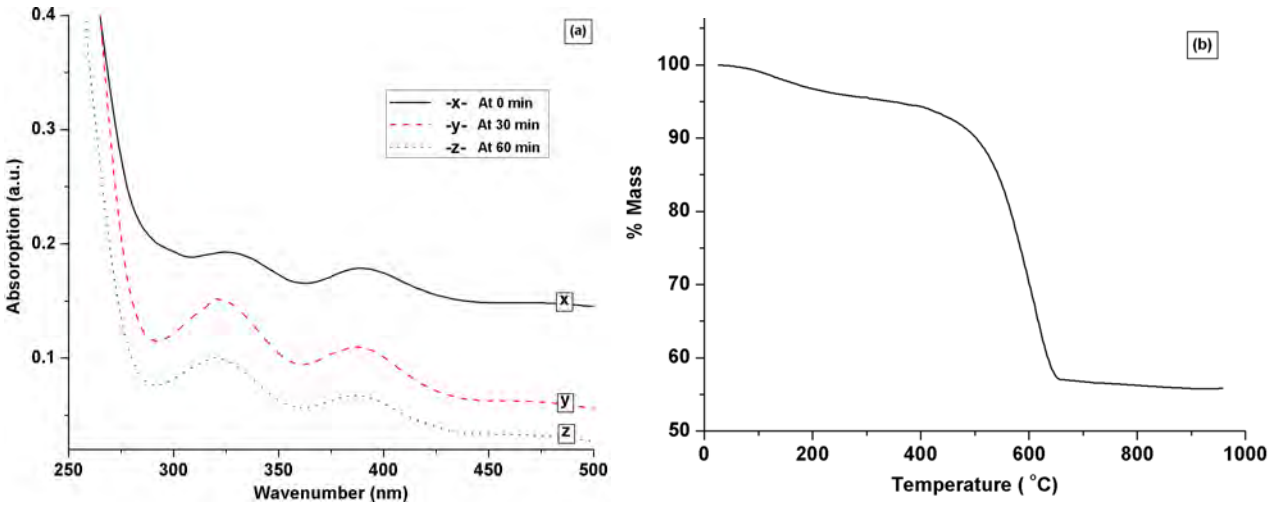

Figure 4.31: (a) UV-VIS spectroscopy of platinum salt solution during self-reduction and (b) thermogravimetric analysis of platinum decorated CNTs to confirm the loading rate.

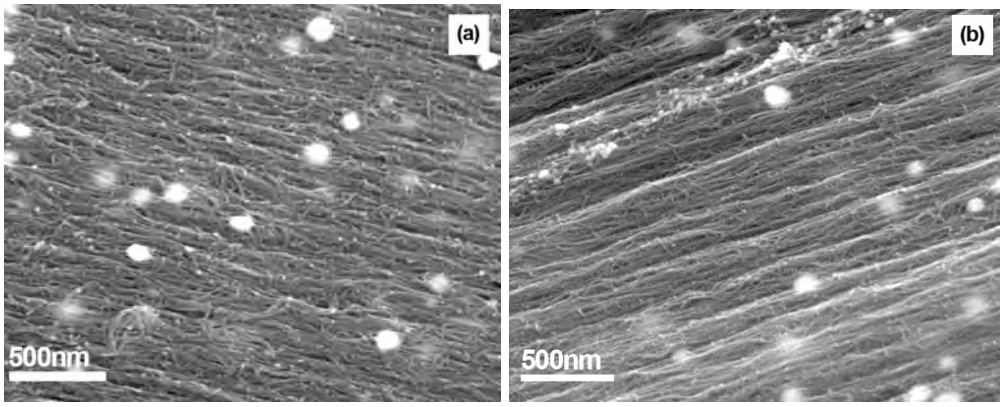

Figure 4.32: SEM micrographs of CNTs film loaded with platinum nano particles.

of platinum nano particles was of order 2 to 4 nm (confirmed using TEM), below the resolution limit of SEM machine. However, compared to CNTs, platinum atoms are much heavier and more conductive in nature. Thus, regular small white dots resembling morphologies on side walls of CNTs are confirmed to be platinum nano particles (see fig. 4.32). The bigger white particles ($\sim$ 100 nm) are of coarse agglomerates of platinum. During SEM investigation no major difference was found between two samples or halves of CNT film. The difference, naturally would be the size of platinum nano particle loaded. This can be only determined by using TEM investigations.

Transmission electron micrographs displayed in figure 4.33 elaborate the efficiency of the process. In the micrograph 4.33a, a blanket of CNTs decorated by small nano particles of platinum (black dots) can be easily seen. Due to huge difference between atomic sizes of Pt and carbon, its hard to gain a better contrast for CNTs which are composed of few atoms of

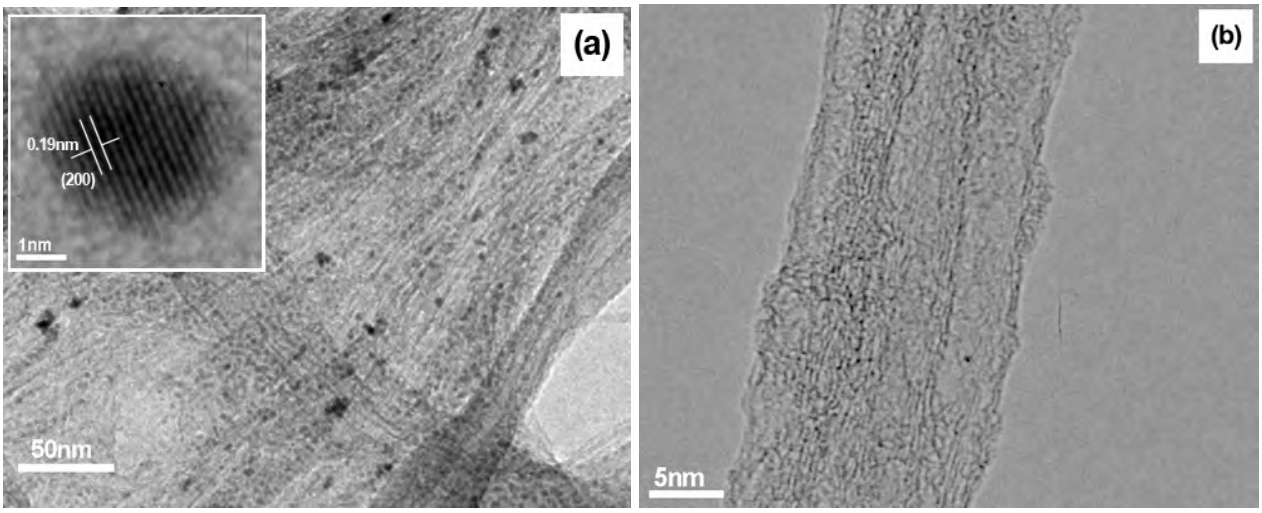

Figure 4.33: TEM micrographs of CNTs loaded with platinum nano particles. Inset in figure (a) show lattice fringes of platinum particle 2 nm in size.

lighter element carbon. The average size of platinum nano particles was about 2 nm. The inter planar distance of atomic fringes is about 0.196 nm, revealing crystal planes with (200) lattice parameters. Figure 4.33b show dark small nano particles of platinum on side wall of CNTs. The image is taken from the first halve sample dipped in salt solution for half an hour. The particles size is of order 1 to 2 nm. The rate of reaction is dependent upon the solution concentration. For optimal loading rate, reaction time of 1 complete hour is utilized. This make platinum particle size in a range of 2 to 5 nm.

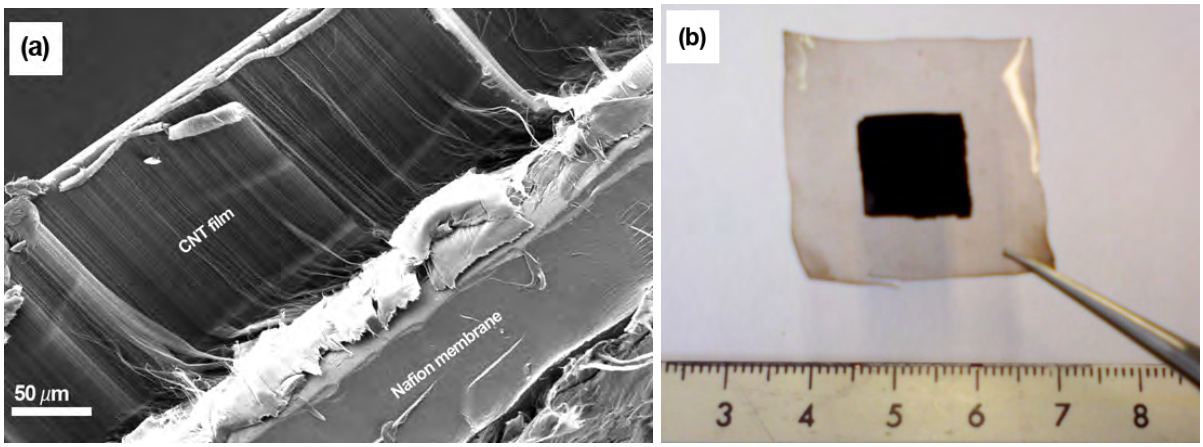

Figure 4.34: (a) SEM micrograph of nafion - CNT film forming a MEA assembly and (a) an optical image of the same assembly.

Finally, the membrane electrode assembly is prepared using fresh CNT films. CNT films of 1 cm^2 size were grown on silicon wafer. A 3 x 3 cm piece of nafion membrane was sandwiched between two fresh CNT films grown on silicon wafer in a way CNTs films will be located right at the center of nafion film. The whole assembly was clamped between glass plates and heated to 160 °C for half an hour. the nafion film, due to heat, melts and two CNT films on either sides get welded to this membrane upon cooling. The low magnification SEM micrograph of MEA along with its optical image is as shown in the figure 4.34. The complete assembly is then dipped in the platinum salt solution to deposit platinum nano particles on CNTs. The purpose of attaching CNT film first to nafion and then carrying out platinum deposition is to avoid the collapse of CNT film after removal from the salt solution. The nafion film will hold the CNT film intact not letting it shrink. After platinum deposition, a thin homogeneous layer of nafion solution will be sprayed on platinum deposited CNT film. The assembly is ready for testing its performance in a fuel cell test station.

4.4.2 Characterization of CNT growth on carbon paper

In a fuel cell, water is generated after the completion of a reaction cycle. The water generated will hamper the performance of the cell, if not drained out in time. The commonly used gas diffusion layer (GDL) materials such as carbon cloth or paper needed to be modified to increase their water handling capability. It can be achieved by growing carbon nanotubes directly on the paper itself. Such modification will not only help to drive the generated water efficiently out of the cell but the same paper can directly serve as a gas diffusion electrode. As an effort in this direction, CNTs were grown directly on the carbon paper. Carbon paper was deposited using bimetallic catalyst and growth was carried out at 750 to 800 °C for duration of 15 to 30 minutes and then system is cooled down to the room temperature. The samples were investigated in scanning electron microscope (4.35).

Scanning electron micrographs show a homogeneous growth of CNTs covering the complete graphite fiber of carbon paper. CNTs grown on graphite fibers have no particular alignment. The lack of proper alignment compared to the growth on silicon wafer is due to uneven morphology of graphite fibers present of the carbon paper. Therefore, after growth CNTs were found to be rolled along the graphite fibers. This results in dense layer of carbon nanotubes on the graphite fibers of carbon paper. Carbon nanotubes grown on graphite fibers have a uniform diameter of order 10 to 20 nm. The diameter of CNTs is bigger than those grown on Si wafer, as the uneven morphology of graphite fibers lead to building up bigger size of catalyst nano particle.

The modified carbon paper and MEA assembly composed of CNT film on nafion membrane were tested for their performance in a test cells. The carbon paper was first tested for its water handling capability, i.e. for its hydrophobic nature. To gain a better hydrophobic nature,

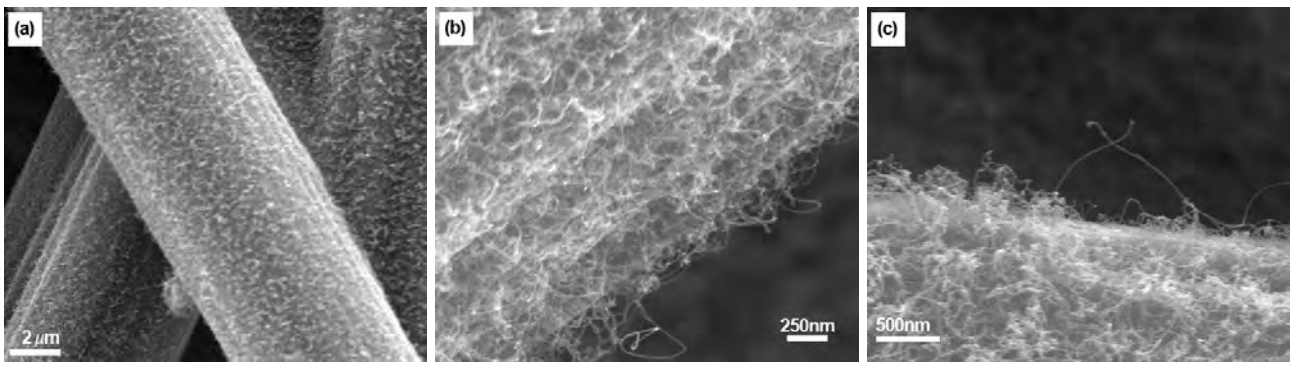

Figure 4.35: SEM micrographs of CNTs grown on carbon paper. CNTs grown were 1 to 5 μm in length.

CNT growth conditions were tuned to control the size and quality of CNTs synthesized. The carbon paper with growth optimized of CNTs were tested for their hydrophobic nature simply by measuring the contact angle of water droplet seating on it (Sessile drop technique). The contact angle of untreated carbon paper is around 100°. The growth of carbon nanotubes was carried out at two different temperatures, 750 and 800°C and for 15 and 30 minutes at each temperature. The contact angle measured for all four growth conditions is displayed in form of histogram in figure 4.36a. The contact angle measured for the sample grown under conditions 750°C and 15 minute show nominal rise in hydrophobicity with increase of 8° in contact angle. However for half an hour growth at 750°C, contact angle was found to increase to a value of 138°. The same amount of hydrophobicity was obtained in 15 minutes, if growth is carried out at 800°C. The further rise in growth temperature was ineffective. The growth temperature was limited to 800°C, as at higher temperature risk of amorphous carbon deposition will increase.

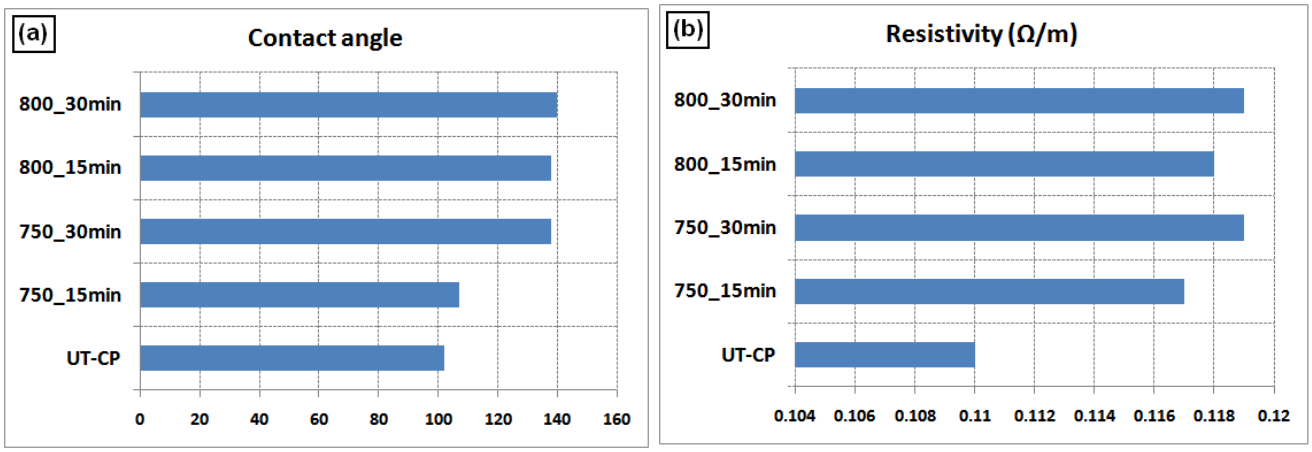

Figure 4.36: Histogram showing (a) increase in contact angle, demonstrating higher hydrophobicity (b) at same time, no major rise in electrical resistivity of carbon paper.

The rise of contact angle demonstrates the higher hydrophobicity of carbon paper. However, at same time, the resistance of carbon paper should not increase. As rise in electrical resistance will be accounted as a hindrance in electron path which will lead to a poor performance of the cell. Figure 4.36b shows a histogram of resistivity of same carbon papers. The resistivity, in any case, show no major change indicating that the growth of CNTs will not induce any negative impact on the performance of a cell. In ongoing work, platinum nano particles will be deposited on carbon nanotubes grown on carbon paper and the assembly will be tested for its performance in fuel cell test station.

4.5 Growth of neuron cells on structured carbon nanotubes blocks or films

The creativity and intelligence is gifted to the human race by its well developed brain. Different tasks such as daily activities, thought process, decision making ability are taken care by complex nervous system. In a network, millions of neurons interconnected to each other carry out these tasks. Depending upon its application, same network of neuron cells can store data, control important functions of the body, generate or even transfer signals. Although considerable information over the genetic codes of human is gathered, still it is insufficient to understand the functional behaviour of the central nervous system [225]. Therefore, an alternative way is necessary to unravel this information.

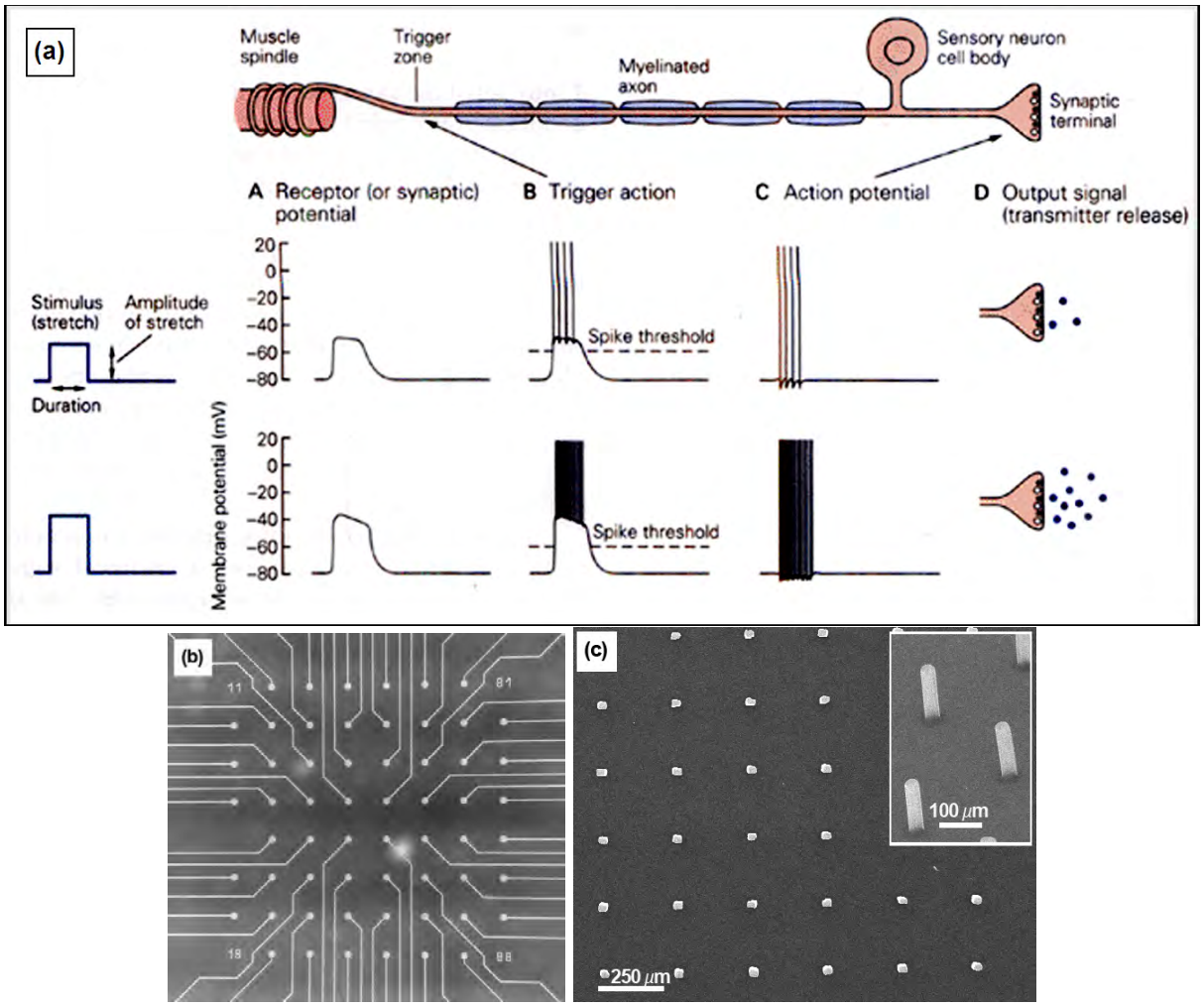

Figure 4.37: Schematic demonstrating functional behaviour of sensory neuron. Neuron cell working to transfer a stimulus into an electrical impulse [226]. (b) optical image of commonly used multi electrode array. Round dots are electrodes while lines are insulated leads. (c) Complimentary CNT block structure which can acts as a MEA.

The information is carried within or between neurons with the help of electrical or chemical signals. Electrical impulses control ion channels in the cell membrane [226]. Therefore, if the electrical signals and their role in a cell mechanism is scrutinized, it will help to understand the cell transport mechanism. Figure 4.37(a) shows a schematic, describing how the neuron cell converts physical stimulus into electrical activity in the cell. The input signal from the muscle (A) is graded in amplitude and duration, which is then transfered into frequency code of cation potential. This leads to release of chemical neurotransmitter that serves the output signal [226].

The possible option to study cell transport mechanism is to use multi electrode arrays (MEA) helping to investigate electrical signals, cells transfer between each other. As name signifies, In MEA, numerous electrodes are arranged in a matrix over which a neuronal network is grown. With the help of MEA, one can study not only electrical impulses between cells but also can stimulate cells using external power source. Often these electrodes are made up of noble metals. However, carbon nanotubes due to their bio-compatibility and high electrical conductivity can be an alternative option. If a structured growth is carried out, CNTs can perform task of MEA and can easily be modified for various bio-medical applications; neural prosthesis for example.

Various initiative studies in this direction have already been taken place. A successful growth of neuron cells on carbon nanotube film is demonstrated. Neuronal Cells show good affinity towards CNTs by forming a neurite branching at a local site. However, unaligned CNTs, their purity, lack of structure might question the reproducibility of results, signal sensitivity or detection ability.

The aim of the present work here is to demonstrate the growth of perfect neuronal network by using a film or block structure of aligned CNTs. Thereafter, fabrication of a device of consisting arrays of CNT electrodes inter-bridged by using a neuronal network will be demonstrated.

4.5.1 Characterization of neuron cells growth on structured CNT blocks or films

Neuronal cells used in present work are purchased or obtained from a chicken fetus. The details of experimental procedure are given in experimental part of this thesis. After the deposition of the cells, growth of neuron cells on carbon nanotubes is regularly monitored using a blind substrate. The optimal growth means regular inter branching between neuron cells by regeneration of axons. After complete regeneration of axons, the silicon wafer supporting CNT blocks and neuron cells on it, was taken out of the medium solution and washed carefully

using ethanol for numerous times. The repetitive washing will remove traces of medium solution. Neuron cells are then fixed on CNT blocks using a thin layer of polymer. This step is necessary to hold the cells right at their position to ease the investigation of samples using various characterization techniques. If the electrical measurement is to be carried out, this step will be simply avoided as it leads to death of cells. The ready samples are investigated using scanning electron microscopy.

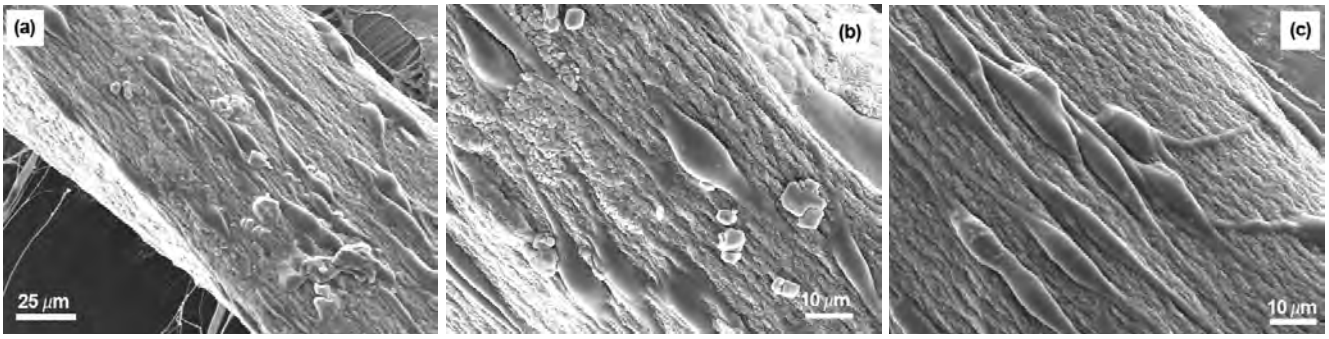

Figure 4.38: Neuron cell growth on a CNT film. As clearly seen, well developed axons are interconnecting neighboring neurons.

For primary investigation, an unstructured CNT film was used for neuron cell growth. SEM images show a sustainable growth of neuron cells on the CNT film (see fig. 4.38). The cell body, also referred as 'soma' was found to be well adhered to the CNT film. The oval shaped cells bodies have got nourished in a medium solution and axons from each cell have been grown connecting one cell to another. The length of a single axon or neurite do vary from nominal length of about 15 to 30 μm till 70 to 90 μm. The fact that cells are dead during the SEM investigation plays no major role in observed morphology of the neuronal network. To confirm this, a neuronal network of live cells grown under similar conditions was studied using Environmental SEM recommended for biological investigations. Matter of fact, similar network of cells was seen with no major difference in its structure and morphology.

The major point of this case study is, unlike to various previous reports using functionalized carbon nanotubes, nerve cells found to be growing on pristine CNTs [49, 227]. Also, nerve cells found to have absolutely no problem in growing either on the top of CNT film (i.e. on apex of CNTs) or on side wall of CNTs. It might be possible that functionalization of CNTs might improve the out growth and branching of axons. This would also be interesting to study. As a next step, CNT film was replaced by block structures of CNTs in order to visualize the growth of

neuron cells. Under optimal growth conditions, it would be intriguing to see if neuron cells can bridge two spatially divided CNT blocks.

For such study, CNT blocks with different aspect ratio and separation were utilized. Using the same procedure, cells were cultivated on CNT blocks for same duration. Scanning electron micrographs of neuron cells grown on CNT blocks are as shown in the figure 4.39. Initial visual conclusion from micrographs is preferential affinity of neuron cells towards CNTs. A dense growth of neuron cells was found on CNT blocks and rarely any cell was seen on the silicon

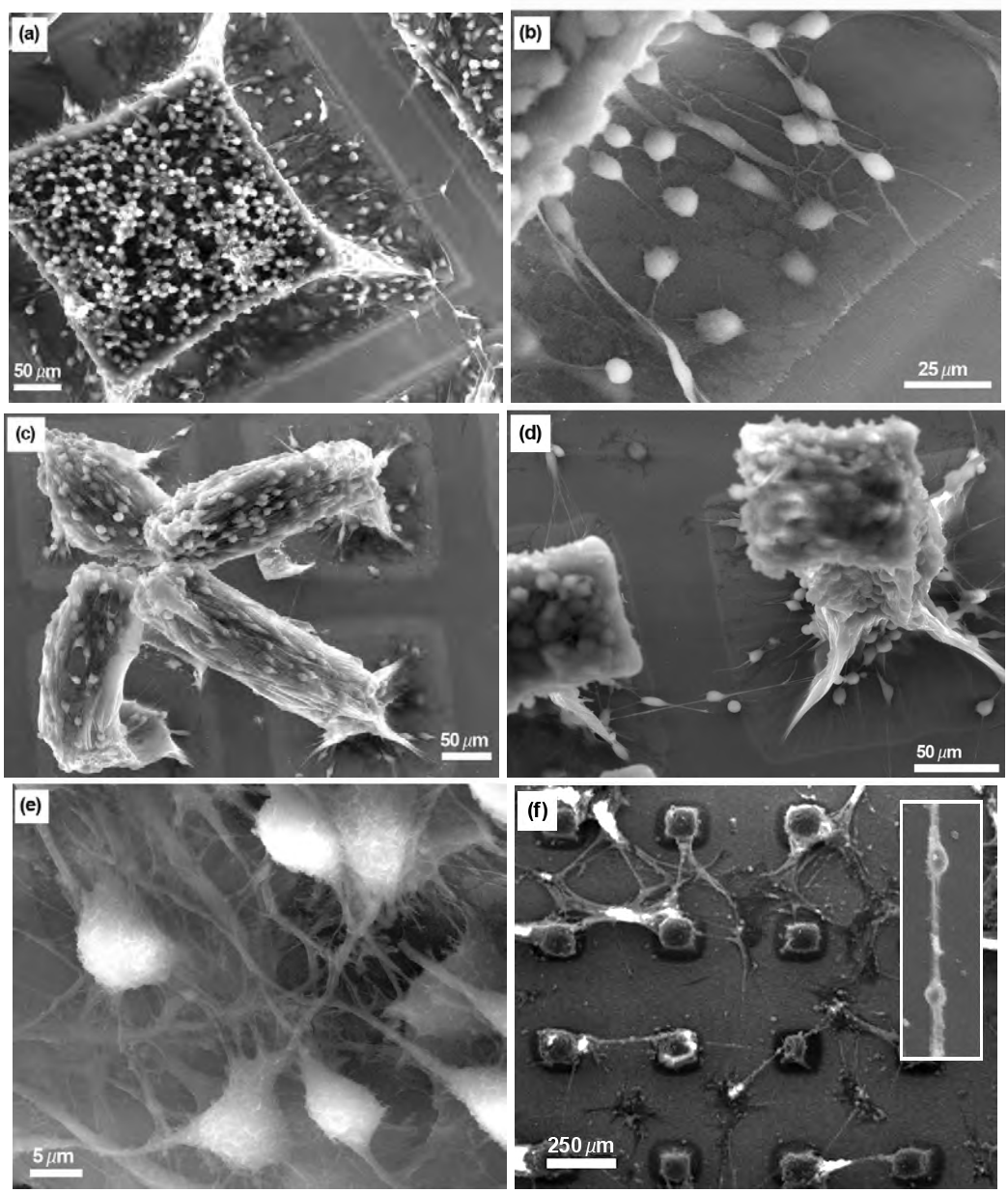

Figure 4.39: SEM micrographs of neuronal cells grown on CNT blocks. (a to d) growth of neuron cells on various CNT structures, (d and e) formation of numerous axons on each soma and (f) inter - bridging of CNT blocks with neuron cells network is clearly seen.

surface. Neuron cells have found their home not only on top of the CNT block but also on the side walls of CNTs. The figure 4.39a shows a single CNT block with numerous cells on the top as well as on the side wall. High magnification image of cells (see fig. 4.39b) adhered to side wall of CNTs shows distinguishing growth of axons originating from every soma. Neuron cells had number of neurites growing. A single soma is found to have on an average 3 to 5 neurites grown. Somas were connected with each other forming excellent network of cells.

In numerous cases, neuron cells were bridging the two neighboring CNT blocks. One of such splendid network of cells in between CNT blocks is displayed in figure 4.39d & f. In figure 4.39f, distance between two blocks is 5 folds bigger than in figure 4.39d. The inset in figure 4.39f shows high magnification image of cell bridge between two CNT blocks revealing with two inter connected somas. After comparing two above mentioned micrographs , one can see that the bridging took place favorably irrespective of distance between two blocks. If the distance between blocks is too big to bridge with single axon from one cell, two or more cells constitutes a single bridging network. Naturally, for this, the cell density deposited on CNT blocks plays a vital role. The bridging might have been carried out by the cells, those were swimming in medium solution and there by extending the regenerating axons to CNT blocks on either side. Another possibility would be, the actual migration of numerous somas from one block to another through the solution medium. Such phenomenon was observed in case of neuron cells present in spheroids, explained below.

Neuron cells or somas not only regenerate various axons but also their axons were often seen sub branched. The high magnification image of the somas displayed in figure 4.39e show proper sub-branching of axons forming a dense network. The formation of subbranches exemplifies the favorable conditions cells possess while growing on CNT blocks. It might be more interesting to see and learn the behavior of cells during their growth on CNTs functionalized by various functional end groups. For this purpose neuron cells with fluorescent tags or gold quantum dots could be used.

As a next part of study, instead of neuron cells, spheroids made up of neurons were allowed to settle on CNT blocks. For this purpose, CNT blocks with varying inter block distance were chosen. The standard diameter of such spheroids is about 200 μm. Therefore CNT structures with block spacing smaller and bigger than 200 μm were chosen. The micrographs of spheroids seating on CNT blocks is as shown in figure 4.40. In this case even, neuron cells have clear

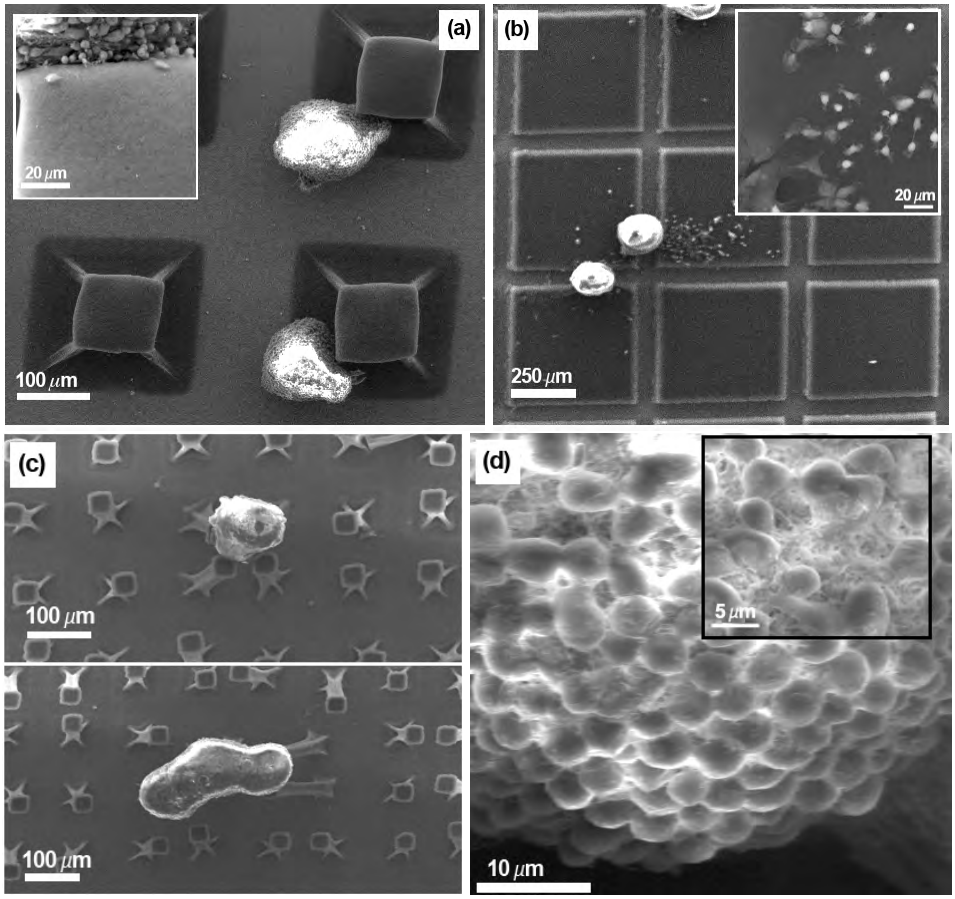

Figure 4.40: SEM micrographs showing adhered spheroids of neuron cells to carbon nanotubes blocks. (a and c) Selectivity of neuron cells towards CNT block is clearly seen, (b) bridging of CNT blocks by spheroids, inset show migration of cells from spheroid to CNT blocks (d) High resolution image of spheroids.

inclination towards the CNTs than towards the silicon wafer (see fig. 4.40a & c). Each and every spheroid deposited through the solution was found to be adhered to CNT blocks. Depending upon the time given for adhesion, neuron cells found migrating to CNT blocks leaving spheroid structure made up of purely neuron cells. The insets in figure 4.40a and b show migrated cells on the top of CNT blocks. The cells have grown good sub-branched neurite structures. They have extended their axons to CNT blocks in order to gain good adhesion. These neurites should have formed good bonds with carbon nanotubes to support such a mass of neuron cells adhered vertically to CNT block. It is quite possible only because these blocks consists of nano sized bio compatible carbon nanotubes.

Neuron cell spheroids bridge one or many carbon nanotube blocks as seen in micrographs displayed in figure 4.40b & c. This would be an ideal growth condition. Numerous CNT blocks can act as a individual electrode and a complete assembly can function to deliver

more knowledge about the cell transport mechanism or effect of various neuro-toxin drugs on human nervous system. Such device can be visualized by modifying present CNT block structure supported on a silicon wafer. In order to use single CNT block as one electrode, each block should be contacted individually from the bottom side. An initial plan to miniaturize such device structure is explained below.

4.5.2 Miniaturization of MEA for CNT - neuron cells structure

The important next step in this work is to develop a special multi electrode arrays (MEA) using each CNTs block as a individual electrode. This can be visualized only by growing or transferring the CNTs blocks on well insulated individual metal electrodes, lithographed on an insulating substrate. The growth of CNTs blocks having CNTs of same quality and typology on metal electrodes would be difficult as surface properties should match for water assisted growth of CNTs. Although CNTs can be grown on various metal foils, INCONEL foil for example [228]. However, bio compatibility of such alloys is questionable. Therefore, transfer of CNT blocks using a bio-compatible conducting adhesive paste would be the feasible option. A schematic of cross sectional view of such an electrode assembly is as shown in the figure 4.41. After a successful transfer CNT blocks on metal electrode, cells can be grown in usual manner and testing can be carried out using external ends of metal electrodes. The work in this direction is under progress.

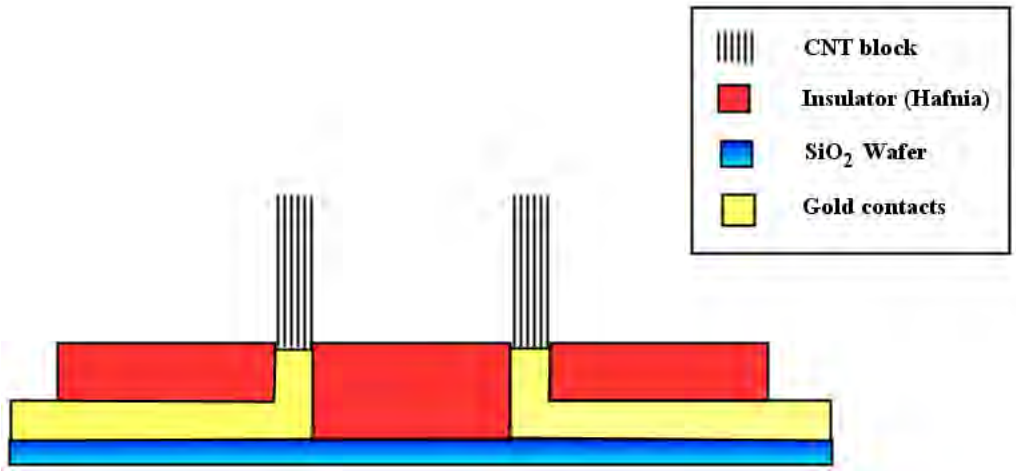

Figure 4.41: Schematic of a proposed multi electrode assembly (MEA) employing CNT blocks as individual electrodes.

The successful development of CNT-MEA device will give an option of testing of the CNT-neuron cell hybrid material. The next most intriguing problem would be to control the density of neuron cells per CNT block. With a high density of cells, the measured signal would result as noise signal as every cell from the bulk will contribute to the signal.

5 Studies towards functional applications of carbon nanotubes and its hybrid materials

Carbon nanotubes and their hybrid materials are investigated for their functional properties such as field emission, light sensors, gas sensor, field effect transistors. Preliminary results of obtained in various studies, methods used for studying the materials as well as device fabrication theories are discussed here.

5.1 Carbon nanotubes and their metal oxide composite for field emission applications.

Carbon nanotubes can have a very high aspect ratio up to 10^6. Apart from this, CNTs are electrically conductive, possess low threshold voltage, good emission stability and long emitter lifetime [229]. These properties make CNTs a potential candidate for field emission. Numerous studies have exemplified the potential of CNTs as field emitter [228]. As SWNT possesses only one layer of carbon atoms, it is prone to oxidation much easier upon application of high electrical field. Therefore, CNTs with two or few walls are considered ideal material for such applications [101]. Nonetheless, structured CNT growth and thereby possibility to tune size, shape and intermediate distance between two emitters is still a challenge.

Field emission studies were carried out in cooperation with University Wuppertal in Germany. Emission studies were carried out using a sophisticated setup built for studying emission of numerous field emitting materials. CNT block structures were studied for their homogeneous field emission properties as well as a single CNT block is examined using a locater anode tip

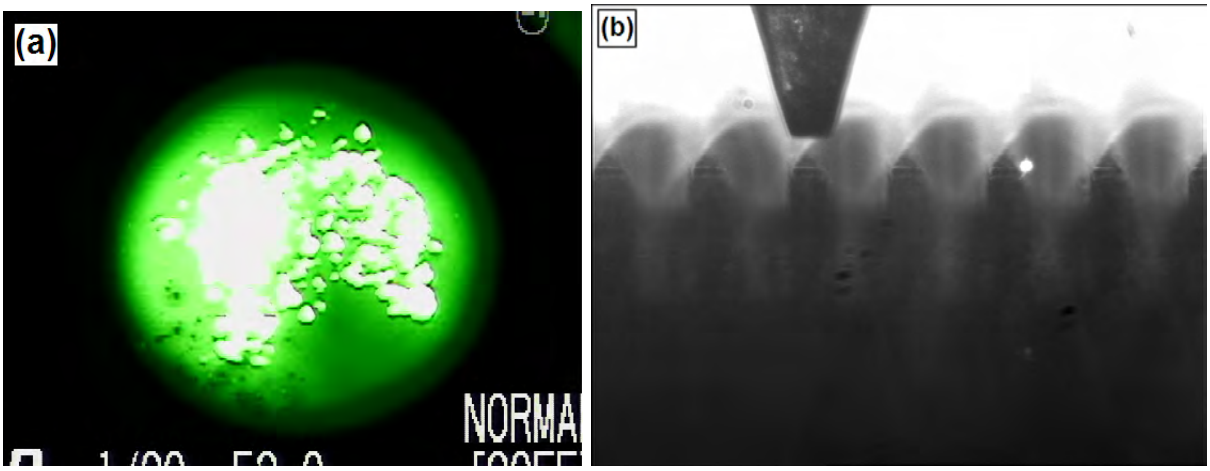

Figure 5.1: Optical images of (a) luminescent screen (IMLS) during the emission study of CNTs and (b) locater anode tip used for studying individual CNT block.

as shown in the figure 5.1b. This way, current emission studies starting from the threshold emission till the destruction of an emitter at higher current rates was undertaken.

Pristine CNT blocks were studied for field emission applications. CNT blocks of different size and varying intermediate distance were examined for field emission. Apart from this, metal oxides nano particles of ZnO and TiO_2 were deposited on CNT blocks, and composites were studied for emission stability and for emission at high oxygen pressure. The purpose of metal oxide deposition on CNTs is to enhance the life time stability of CNTs in presence of hight fields and lower operating vacuum. At first, field emission properties of pristine CNTs is reported, followed by emission studies of CNT metal oxide composite.

5.1.1 Field emission of CNT blocks.

Carbon nanotubes are synthesized in form of small blocks or pillars on Si wafer using a mask technique (see section 2.1.2). Three structures having different block dimensions and varying intermediate distance (as shown in the figure 5.2) were used for field emission studies. Three different structures consist of square shaped CNTs blocks of size 150x150 (sample 1), 100x100 (sample 2) and 50x50 (sample 3) μm^2 separated by distance 50 150 and 250 μm respectively. All three samples were tested individually for their emission characteristics. The size of a block

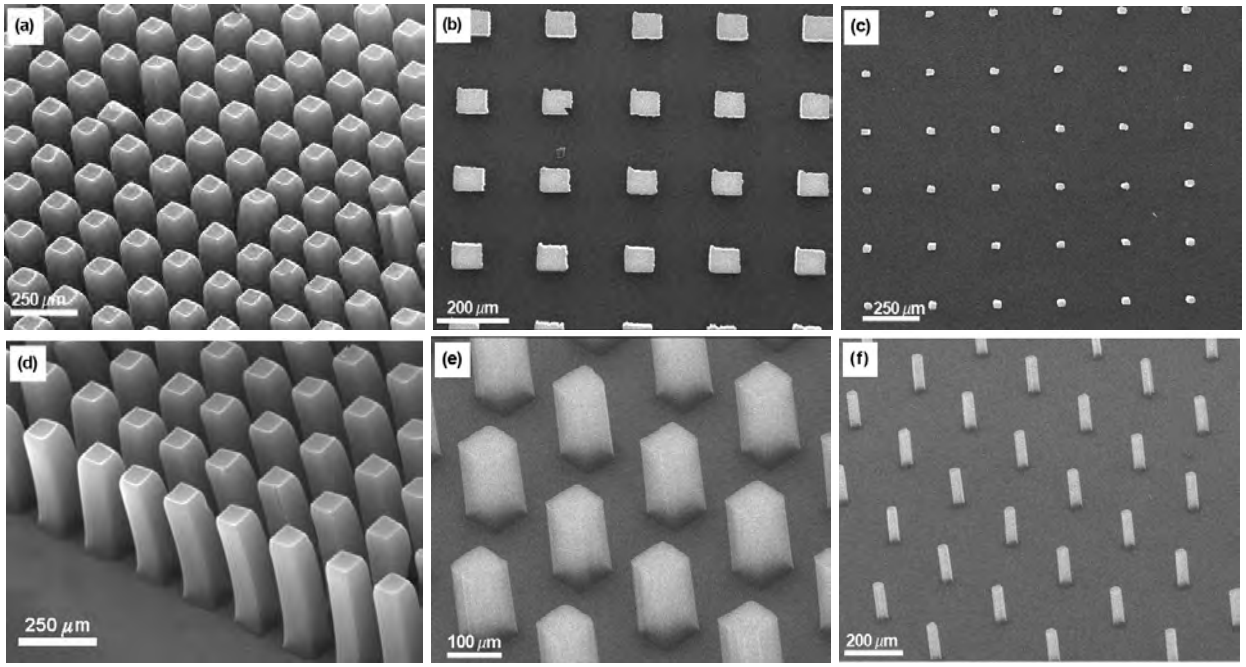

Figure 5.2: SEM micrographs of pristine CNTs blocks investigated for field emission characteristics.

as well as distance between two blocks carry importance in field emission studies as these two dimension determine the local enhancement in the field, referred as field enhancement factor, represented by symbol β. All three samples were found to emitting at fairly low on field voltage. The block with smaller intermediate distance (see figure 5.2a and d) starts emitting with turn on field in between 5-10 V/μm while for other two samples this value was in between 3-6 V/μm. All three structures were able to emit current up to an average value of 300 μA. During every up cycle (a cycle during which electron emission was increased from from 0 to 300 μA), occasionally partial destruction of the emitter was observed, however, complete destruction was never seen.

The voltage maps for two out of three samples are shown in figure 5.3. Using an anode of tip diameter 100 μm and located at distance of about 100μm from the emitting block, complete sample was scanned for its emission behavior. As it is seen from the voltage map, almost every emitter (CNT block) shows electrons emission. The maximum emission takes place from edges or contours of an emitter. This possibly explains the partial destruction of the emitter at higher emission currents. In order to avoid such destructions, instead of present CNT structures with sharp corners, round or conical blocks should be used. The another important point is, loss of emission from the emitters located close to edge of the Si substrate. At the periphery of the substrate, the field enhancement is not enough or requisite, leading to higher on set field. The quite possible reason for such a behavior would be inhomogeneous growth of CNTs at the edge of the substrate. As CNT growth is carried out at atmospheric condition, the improper fluid dynamics conditions at the edge of the substrate leads to loss of growth rate. Therefore, CNT

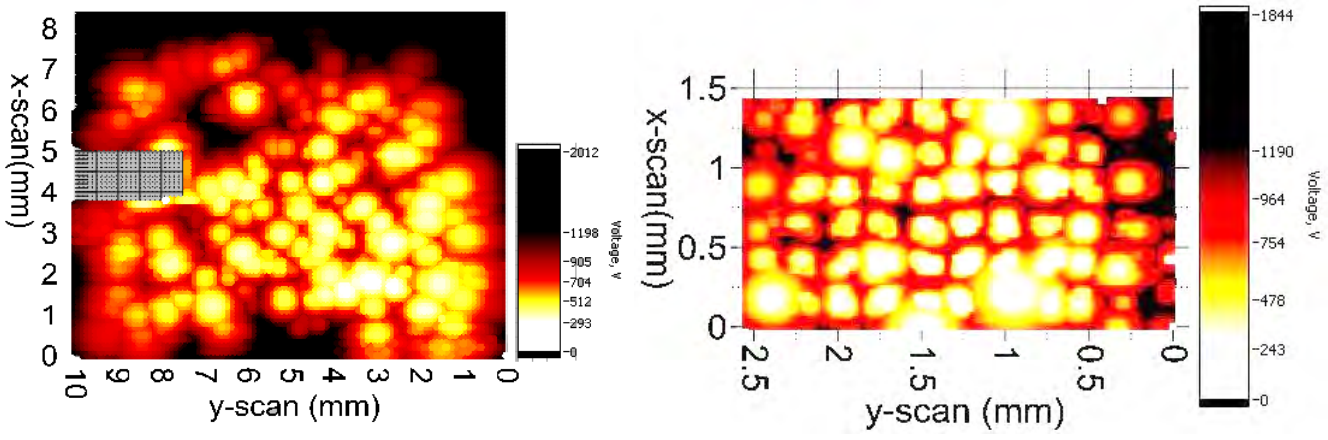

Figure 5.3: Voltage map of CNT block emitters (a) for sample 1 and (b) for sample 2 as well as 3.

blocks grown close to the edge of the substrate will have a height (or CNT length) bit smaller than those located at the middle of the wafer. Smaller height reduces the field enhancement factor, demanding higher applied field.

The height of a block in each structure was in range of 100 to 300 μm. Higher height of each block, helps to gain higher field enhancement factor (β). However, If the block height is increased enormously in order to gain higher β factor, blocks will become mechanically unstable and tends to bend. This will lead to inhomogeneous restructuring of blocks, decrease in the intermediate distance and upon all loss in emission, as from bent structures emission will take place from the side wall of CNTs rather than from their tip.

The current voltage (I - V) plot and Fowler - Nordheim (FN) plots of all three structures are a shown in the figure 5.4. The I - V plot shows the emission characteristics of an emitter. The Fowler - Nordheim plot on the other hand, is most the commonly used theory to model the emission of cold electrons. It explains the dependence of emitter current on local electric field and the work function (ϕ) of the emitter [230]. Consequently, a minute change in emitter geometry, chemical state or even in surrounding of an emitter carries a strong impact on its emission property. The FN plot is obtained by plotting $\ln(I/V^2)$ versus $(1/V)$. The standard FN plot for carbon nanotube is a straight line. The work function of the carbon nanotubes is $\phi = 5$ eV, similar to graphite or fullerene (C_{60}) [230, 231].

For every sample the I-V as well as FN plot are recorded for up and down cycles for emission of 50 μA. The FN plot shows straight line function for all three samples. Sample 1 shows the maximum emission of current up to 300 μA while the sample 2 up to 800 μA and the one with smallest tip diameter up to 1.46 mA. These emission values were obtained for each sample by testing the individual CNT block for their maximum emission ability before complete destruction of the emitter. The emitted current value shows that, smaller the emitter tip and larger the intermediate distance, higher will be the emission.

The local measurement carried out by using the tip sized anode shows the stepwise destruction of the emitter during up and down cycle, fluctuation in emitted current as well as activation and deactivation of the emission. The measured value of applied field required for the extraction of 100 μA of current varies from 35 to 65 MV/m for sample 2 and 25 to 110 MV/m for sample 3. These two sample shows more stable FN behavior and higher emission currents compared

to the first sample. Therefore these two samples were selected for the deposition of the metal oxides to study its impact on the field emission characteristics of the samples.

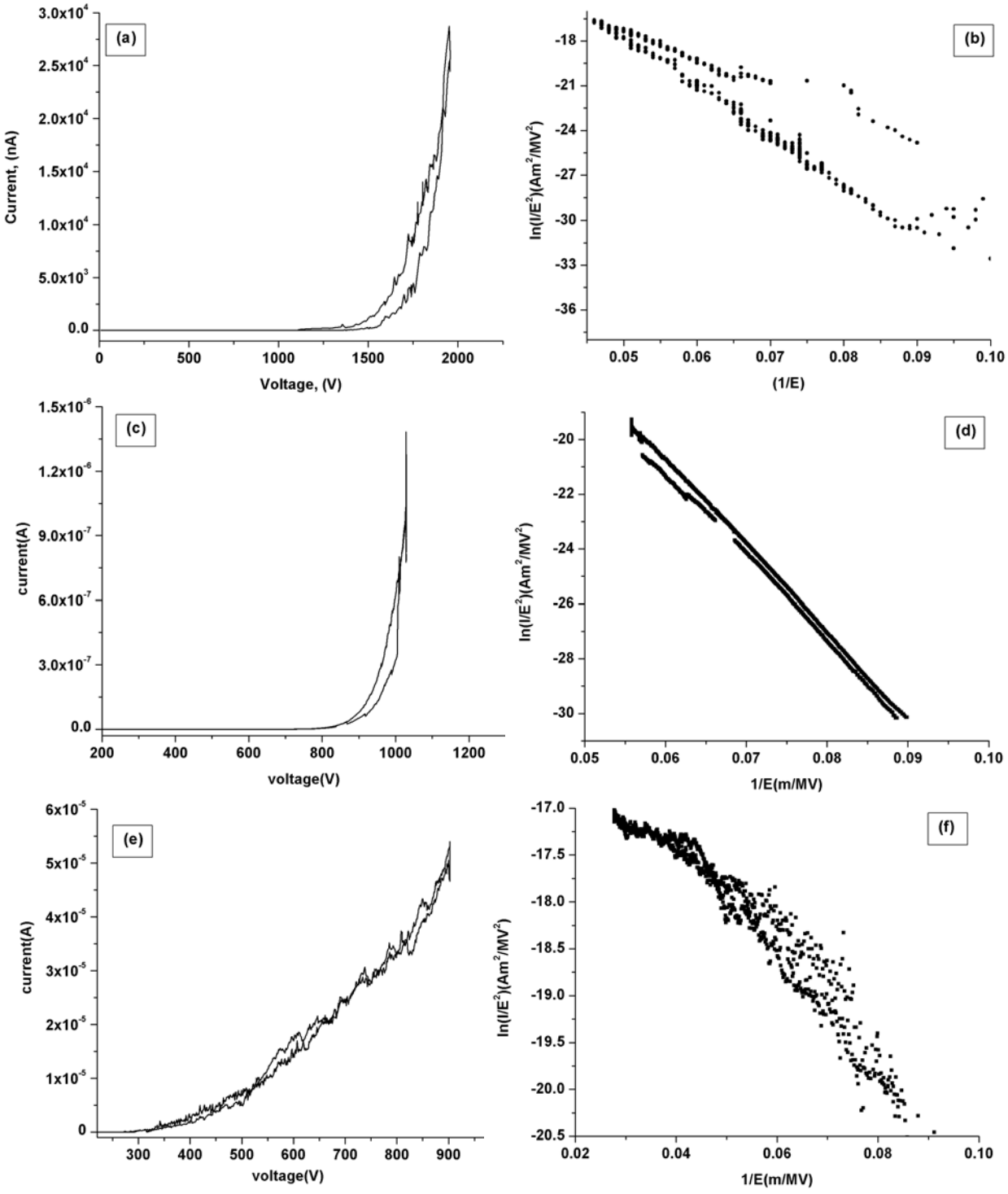

Figure 5.4: I-V plots (left) and Fowler - Nordheim plots (right) for above displayed CNT blocks. (a and b) for sample 1, (c and d) for sample 2 and (e and f) for sample 3 respectively.

5.1.2 Field emission of CNT - metal oxide composite blocks.

The purpose of studying titania and zinc oxide coated CNT block structures is to examine the emission characteristics of these composites materials, investigate the extend of insulating role oxide coatings can play, their impact on emission current during operation at lower vacuum. ZnO show nice individual field emission characteristics [162], therefore a composite of CNT and ZnO will have emission from both emitter materials. Titania, on the other hand, can protect the CNTs against oxidation during emission in lower vacuum conditions. As both oxides are photo active in nature, the emission can perhaps be controlled (or enhanced) by UV radiation.

The CNT - ZnO composite (sample ZnCN-1, see page No. 73) was prepared by depositing nano particles of ZnO using chemical vapor deposition method. In absence of ZnO nano particles, CNT blocks shows emission properties with a turn-on voltage of 0.36 V/μm. The on set field value for composite material is higher than that of pure CNT blocks. The sample ZnCN-1 shows on set field voltage value in range of 0.75 V/μm. The values are recorded for current emission of 1μ/cm^2. The oxide layer deposited on CNTs demands higher on set emission potential for the same amount of current. The I-V curve and FN curve recorded for sample ZnCN-1 is as shown in figure 5.5.

Upon application in potential between sample and anode, as observed often, the emission takes place from the tip of the emitter. The tip of composite material in this case is composed of nano particles of ZnO and carbon nanotubes. However electrons were tunneled through the CNTs with high aspect ratio to reach the apex of the block. With ongoing emission, partial

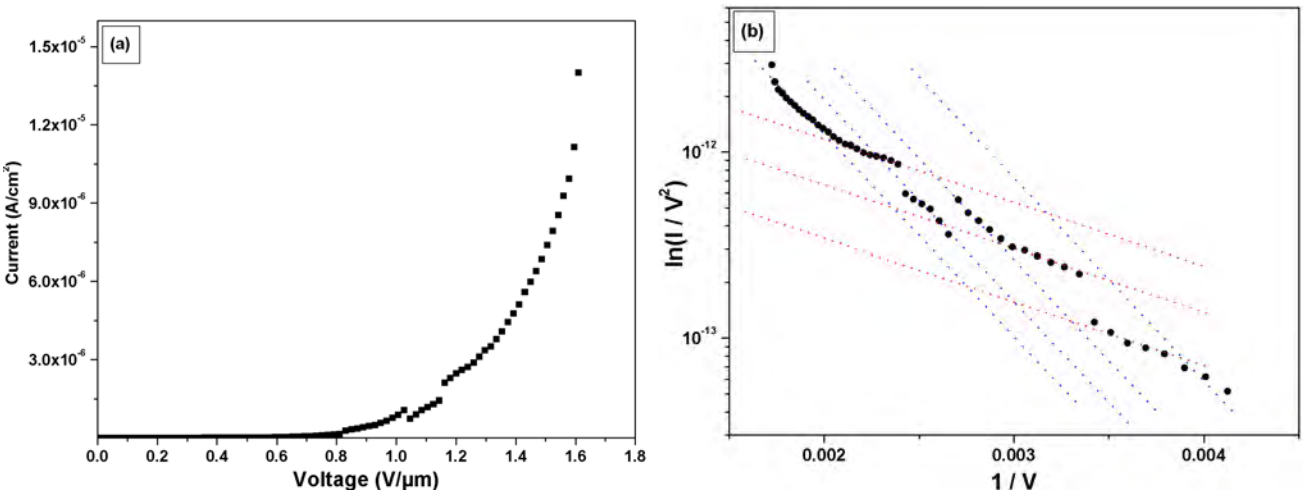

Figure 5.5: (a) I-V and (b) FN plot of CNT-ZnO field emission characteristics.

destruction of primarily emitting tips takes place and ZnO nano particles start emitting electrons. It is intriguing to investigate the exact reason of such a destruction. It might be due to the emission of high current or might be due to high density electron transfer between the ZnO - CNT through a small nano sized contact area.

The characteristic FN behavior indicates either partial but repetitive destruction of emitting tip or electron transfer barrier between the CNT and ZnO nano particles. Upon emission of electrons from ZnO, a small time lapse is occurring due to non continuous electron supply to ZnO nano particles from CNTs to refill the scavenged electrons. Further experiments are needed to conclude exact reason of such emission characteristics.

On the other hand, titanium dioxide coating seems to stabilize the emission characteristics of CNT blocks. The stability in field emission is observed for CNT - TiO_2 blocks for currents as high as 20 μm. For emission higher than this value, no major contribution from TiO_2 coating is seen. Also, the stability is gained at a cost of lose in emission current; 2 to 3 factors less than that of pristine CNT emission. The field emission for CNT - TiO_2 blocks was tested for varying oxygen pressure (see figure 5.6b). The emission at higher oxygen pressure was more of less stable but as stated before, at a cost of loss in emission current.

The stability during field electron emission is another important study parameter for emitting cathode. The emission seems to be stable after the conditioning effect. The emission behavior depicts stable FN behavior with a field emission factor almost same for currents from 1nA up to 50μA. The field required for stable emission of 100μA current for sample 2 and 3 is

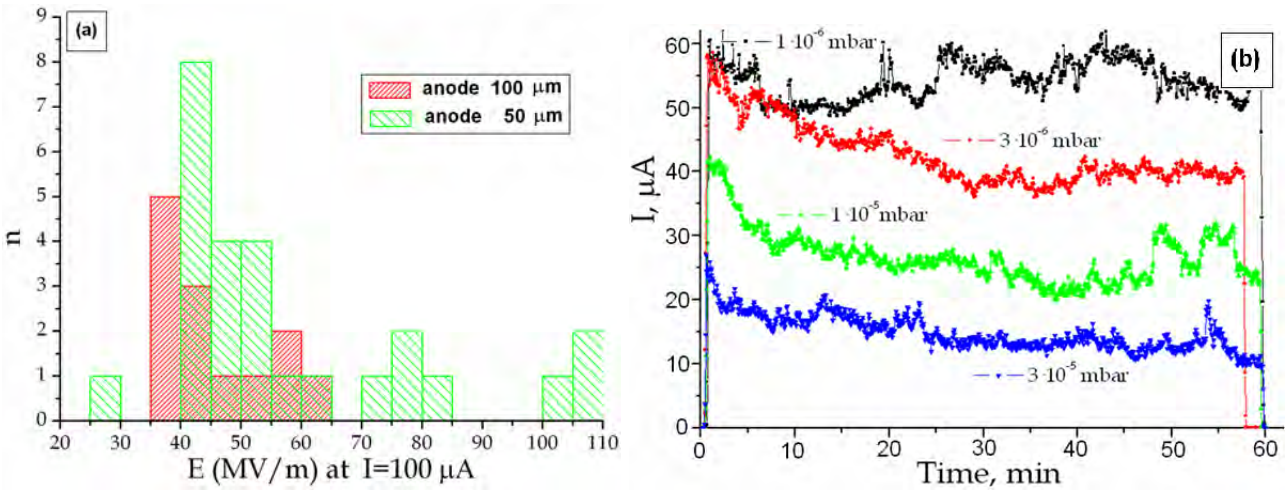

Figure 5.6: (a) Histogram representing field requirement for emission of 100μA current and (b) Plot showing emission stability of CNT-TiO_2 composite for varying oxygen pressure.

presented by histogram in figure 5.6a. Beside it, an emission stability measurement of the one of three emitters coated with titania is displayed (see fig. 5.6b). Long time emission stability measurements are under progress.

5.2 Carbon nanotubes based field effect transistors

Thin film transistors (TFTs) devices gaining important in electronic industries. TFTs are special kind of field effect transistors made by depositing a thin layer of semiconducting material, dielectric layer and metal contacts. As a semiconducting material, thin layer of micro crystalline silicon or polysilicon is used while, indium tin oxide is famous transperent electrodes. The research on TFTs is gaining speed in a demand of flexible displays. Apart from this, they are vital for touch screens displays and equally important in bio or chemio - sensors and solar cell technologies. Carbon nanotubes with flexible structure and semiconducting nature are interesting candidate for thin film transistors. Despite numerous demonstrations of successful use of CNTs for TFTs, majors challenges in this work are diameter selective growth of CNTs, alignment and reproducibility [27, 128]. Using classical CVD technique, CNTs are grown directly on and between two contact pads deposited on silicon wafer. Using various techniques reported in literature, after the growth, CNTs can be easily transfered to transperent and flexible substrates such as plastic. Among them, Ethanol - CVD [66] and Methane - CVD techniques [128, 129] not only ease the selective growth of semiconducting CNTs but also offer alignment during the growth itself. Apart from this, for applications such as chemical or biological sensors, selective growth of individual CNT can be easily achieved with the help of these tow synthesis techniques. Out of above mentioned two methods, depending upon requirement, either of them is used to grow CNTs for fabricating field effect transistors. The characterization of CNT based FET device is discussed here.

The horizontal growth process was used for growing CNTs between two gold pads. Using optical lithography, gold pads separated by a distance of 5 or 10 μm were deposited on SiO_2 layer. On these gold pads cobalt of 0.6 to 0.8 nm thickness was deposited. The substrate heated to 900 °C to grow the CNTs using vapors of ethanol as carbon source. Detailed growth process is explained in synthesis part of the thesis. Arrays of source - drain electrodes deposited on SiO_2 wafer is as shown in figure 5.7a and a high resolution image of one of such electrode pair is displayed in figure 5.7b. CNTs grown between two electrodes are single walled carbon

nanotubes. The average diameter was found to be in range of 1 to 2 nm (confirmed by using AFM technique). SEM micrographs of CNTs grown between two electrodes are displayed in figure 5.7c and 5.7d. CNTs lack in alignment and average length CNTs grow is about 10 to 20 μm. The exact length is hard to determine as CNTs rarely growth along a straight line.

After a successful growth , arrays where tested for their transistor characteristics. A varying voltage from -4 to +4 volts is applied between two electrodes, and the drain current is recorded. Next, for a given potential applied on gate electrode, change in drain current was recorded. A cumulative plot of drain current against source drain voltage and applied gate voltage is as shown in the figure 5.8.

The plot shows current - voltage (I_{ds} - V_{ds}) response of a transistor for different values of gate voltage (V_g). The plot (a) shows a gate effect for positive as well as negative drain voltage indicating smooth ohmic contacts on source and drain side. This is a result of in situ growth of CNTs on gold contact pads. During growth, as a consequence of atom by atom growth,

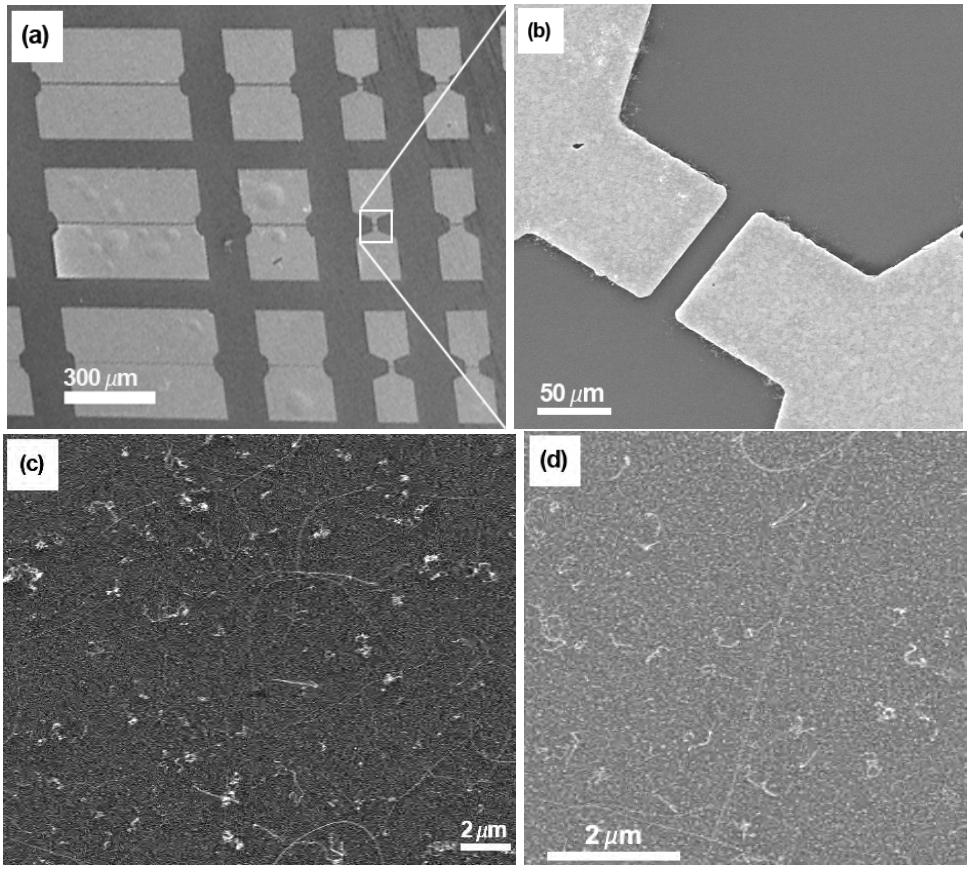

Figure 5.7: CNT based field effect transistor device. (a) Transistor source drain structure on Si wafer, (b) high resolution image of one such device and (c & d) semi conducting single walled CNTs grown between these two electrodes.

CNTs gain good ohmic contact. The drain voltage response is a consistent curve, offering moderate current output even at lower operating voltages. The current output can be tuned simply by increasing the number of CNTs per channel. The device is sensitive enough to respond to small change in the gate voltage. The good modulation is seen by using a gate voltage in a value of small fraction of applied drain voltage. In general CNTs, can have p type or n type semi conducting characteristics depending on the presence or absence of adsorbed oxygen molecules [232, 233]. The present device demonstrates p - type of characteristics as measured in air (oxygen) atmosphere. In p-type, holes are the charge carriers. Upon application of a source drain voltage, charge carriers form a conductive channel in semi conducting material (in CNTs) leading to a charge transport. This channel will deplete upon the application of positive gate voltage leading to lose of drain current. The effect can be reversed i.e. the drain current will increase, if a negative gate voltage is applied. Both effects are successfully demonstrated here for a CNT based transistor. The present transistor shows ON/OFF ratio of an order 2000 to 5000. The value can be further improved by reducing metallic CNTs count.

Carbon nanotube based transistors can be utilized as a memory storage applications. Such device can deliver high operational speed [29]. The standard hysteresis loop representing transfer characteristics for such a memory device is as shown in figure 5.9. The stable hysteresis loop has ON and OFF states separated by more than 2 orders of magnitude. It can be further enhanced by post growth top gate miniaturization. The work in this direction is under progress.

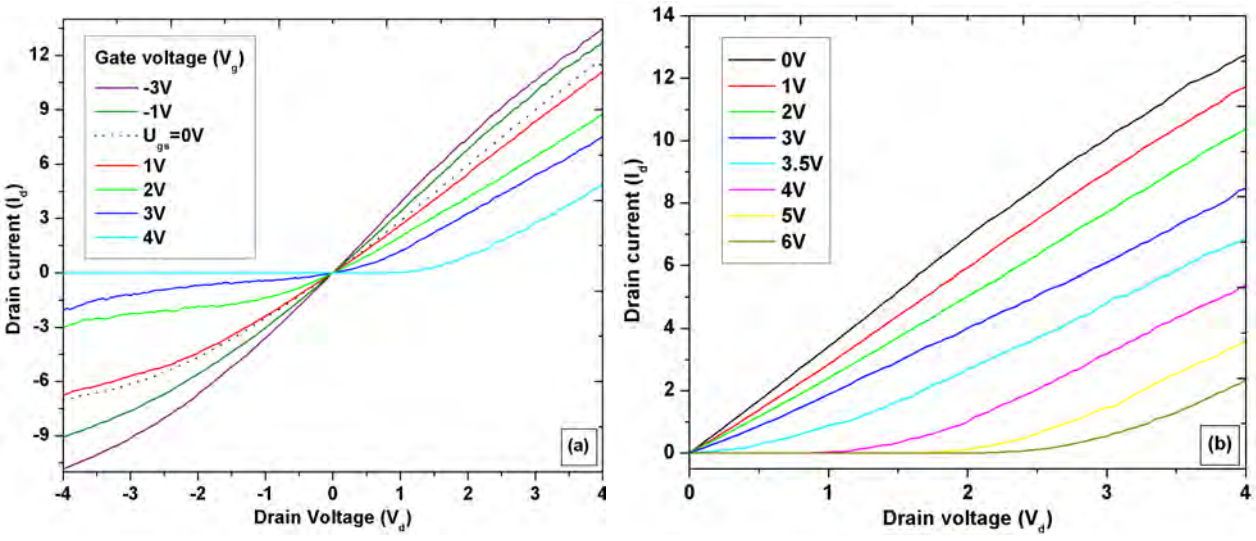

Figure 5.8: Current (in μA) - voltage (in volts) characteristics of CNT-based Field effect transistor.

Further tests to electrically characterize the transistor device for high on - off values, high frequency applications are under way. The device will be soon tested for gas sensing applications. In future, CNTs will be decorated using metal oxide nano particles, or biological molecules to visualize the advanced bio sensor, chemical sensors, and various other electronic devices.

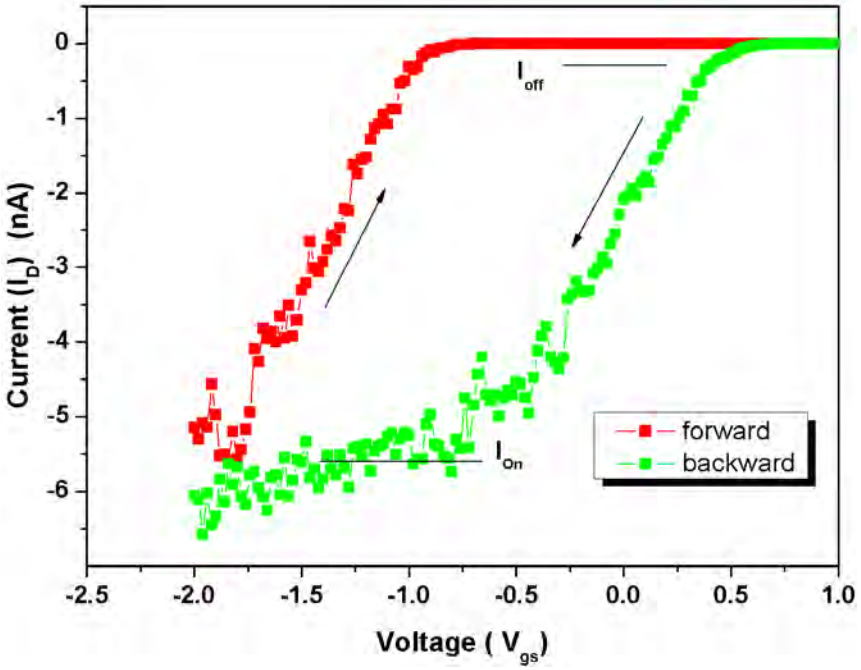

Figure 5.9: Hysteresis loop of a typical SWNT-FET device.

5.3 Carbon nanotubes or their block structures for gas sensing

Carbon nanotubes bundles or individual CNTs, show promising gas sensing characteristics [5,229,234]. For this purpose single walled or at least few wall (2 to 4 walled) CNTs are optimal choice. The reason behind such choice is their strong gas adsorption capacity exemplifying strong sensitivity against the gas, it needs to detect. The detection of the gas is accounted in terms of change in resistance of the complete system [234, 235]. Also, seldom studies demonstrate utilization of field ionization potential of the gas in order to detect it [236]. It is presumed that gas species to be detected get physio or chemio - adsorbed on the surface of the sensing material which leads to a localized charge transfer or shift in fermi level [229]. Such charge transfer across the length of CNTs leads to change in total resistance of the system.

Number of CNTs constituting a single device is an important factor. With increasing number of CNTs, net conductance of the module increases, or in other words total resistance decreases.

Smaller the resistance, smaller will be the net change in resistance upon adsorption of the gas making the measurement critical. On same path, relaxation time of a device depends upon number of CNTs in a device. In order to resolve both issues, a systematic study is undertaken. Two different gas sensing modules are idealized. Instead of a dense CNT film, numerous CNT blocks were utilized. This will not only limit the number of CNTs per module but also will give optimal gas flow path. In another case, individual CNT is grown between two silicon pillars. It will help in studying CNT gas adsorption properties to get more insight of gas sensing behaviour of carbon nanotubes.

Two sensor modules incorporating either CNT block structures or a individual CNT grown between nano pillars of silicon. Both modules are successfully fabricated and being tested for gas sensitivity and selectivity.

5.3.1 Palladium deposited CNT blocks as a gas sensing module

Each CNT block is composed of CNTs with average density of 1600 CNTs / μm^2. Each macroscopic CNT block can act as a single sensor element dedicated to a certain gas. The preferential detection is possible by decorating CNTs with different metals such as gold or platinum nano particles or with metal oxides nano particles. Therefore a single module consists of numerous CNT blocks those can detect various gases or chemicals.

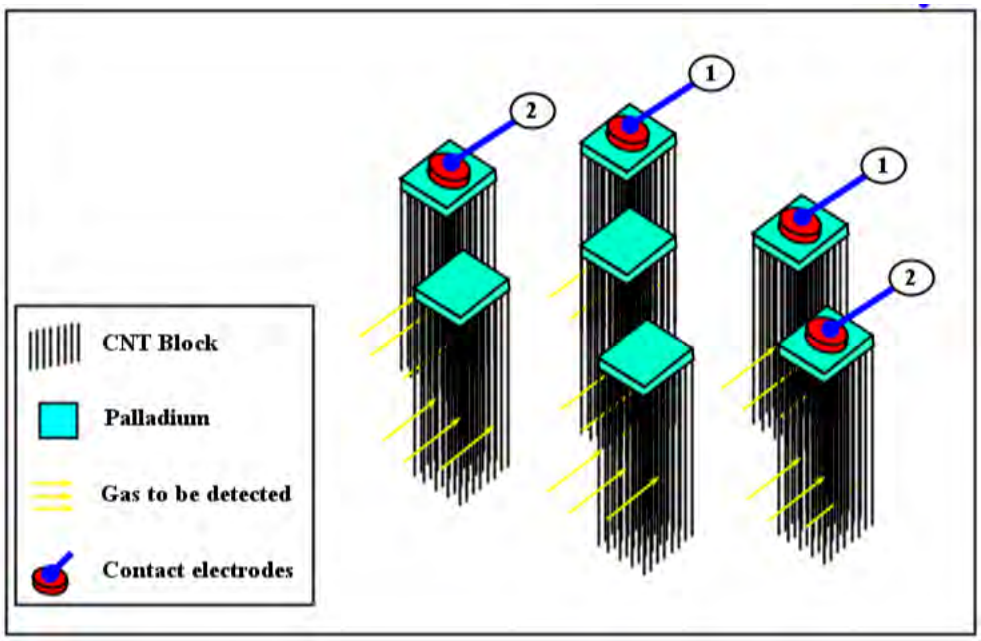

Figure 5.10: Schematics of CNT blocks as a gas sensing module. Numbers 1 and 2 define different modules for different gases.

The pictorial representation of one such module is as shown in figure 5.10. As grown CNTs blocks were deposited with thin layer of palladium using electron beam evaporation method. On well grown block structure, a 100 to 200 nm thick palladium layer was deposited on the tip of each block using metal evaporation technique. There after, complete module was annealed in argon atmosphere for 1 hour at 250 °C. The choice of palladium is obvious due to its ability to establish good ohmic contact with CNTs [26].

The block structure is grown on Si wafer by depositing the metal catalyst. The in situ growth of CNTs over nano particles of metal catalyst delivers a good (ohmic) contact between CNTs and Si wafer or substrate. The resistance between two blocks or across several blocks was measured simply by contacting two or more palladium pads using contact whiskers (see fig. 5.10). The resistance is found to be of order 150 to 300 Ω. The total resistance between two blocks is the sum of resistances between CNT-Pd, CNT-Si wafer and the Si wafer itself. The CNT-palladium is a ohmic contact and so does the CNT-wafer contacts. The substrate i.e. Si-wafer itself has

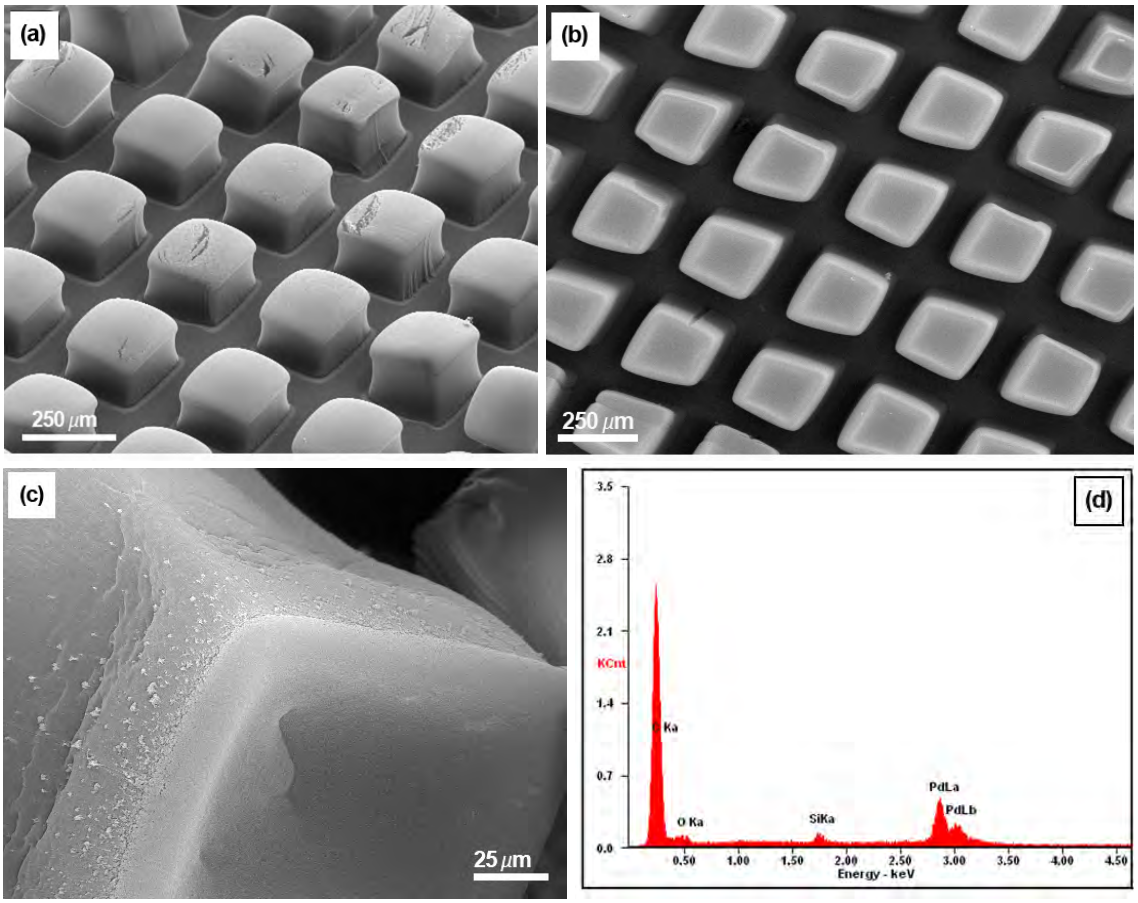

Figure 5.11: (a-c)CNT blocks deposited with palladium as a gas sensing module and (d) EDAX of palladium deposited on the CNT block tip.

standard resistance of 10 to 20 Ω-cm. Therefore, the total resistance is mostly contributed by CNT blocks. The resistance of CNT blocks can be further increased by depositing metal oxide nano particles of zinc oxide and can be decreased by depositing noble metal nano particles of platinum or gold. By doing so, a single substrate with can incorporate different sensor elements having a different selectivity for different gases.

Scanning electron micrographs of palladium deposited CNT blocks are as shown in figure 5.11. The top view as well as side view show the well ordered arrangement of CNTs blocks offering perfect canal system for the gas flow. This helps in gaining better contact between gas to be detected and the sensing element (CNTs). EDAX shows the presence of palladium at the tip of the CNT blocks (see fig 5.11d). The element concentration of Pd on CNTs falls below the detection limit if measurement was carried out at the bottom of the block, instead of at tip.

One of such well characterized block structure was tested for gas sensitivity at room temperature. In dry nitrogen atmosphere, the module was tested for sensitivity against 400 ppm of carbon monoxide and 475 ppm of hydrogen gas. The preliminary response of the gas sensing module is as shown in the figure 5.12. In nitrogen atmosphere (oxygen free atmosphere), CNTs shows n-type semiconducting characteristics. Therefore, upon coming in contact with CO, the gas will be chemisorbed on the side walls of CNTs. This will shift the Fermi level closer to valence band resulting a noticeable drop in resistance (increase in conductance)

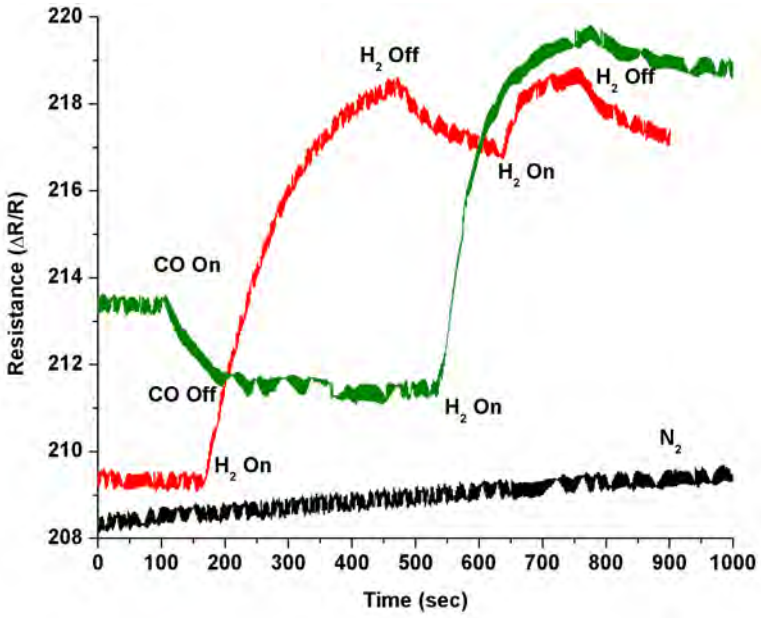

Figure 5.12: Preliminary gas sensing response of the CNT block module against carbon monoxide and hydrogen gas at room temperature.

of the module [237]. On the other hand, if module is tested for hydrogen gas, the resistance was found to be increasing. The rise or fall in resistance is majorly contributed by chemisorption of the detecting gases on the surface of carbon nanotubes and not by metal-CNT junction. The testing of other gases and at elevated temperature is under progress. At higher temperature, at about 200 to 300 °C detecting limit as well as sensitivity will increase reducing the response time.

5.3.2 Growth of individual CNTs on silicon nano pillars

The growth of individual CNT was carried on silicon pillars using horizontal growth technique employing Alcohol - CVD method. Silicon wafers etched in form of nano pillars were received from the RWTH Aachen University. The commercially available silicon wafer was etched in form of arrays of nano pillars using a nanosphere lithography technique [238]. SEM micrographs of Si wafer with nano sized pillars are displayed in figure 5.13 (a and b). On the tip of these pillars, cobalt (0.7 to 0.9 nm) is deposited which will acts as a catalyst for CNT growth. The temperature and duration of growth was 900 °C and 1 hour respectively.

CNTs are grown using different combinations of gas flow. The gas flow consists of hydrogen and argon and the mixture was was bubbled through a technical grade ethanol solution. The total gas flow rate was 300 sccm with argon to hydrogen ratio varying from 3 to 4:1. Although, the change in ratio of gas flow is minute, it carries a strong impact on the growth rate of CNTs. With higher argon content in the total gas flow, conditions are optimal to grow a dense network of CNTs on these silicon pillars.

The argon flow rate was optimized in order to grow very few CNTs (230 sccm argon + 70 sccm hydrogen). Argon gas has a higher molar mass compared that of to hydrogen, carrying more ethanol vapor in to the reaction zone. By decreasing the flow rate of argon and increasing that of hydrogen, favorable conditions were met to grow CNTs from one block to another. The growth of CNTs starts from one pillar and it continues to grow horizontally to reach another or even more silicon pillars in vicinity. In this case a single CNT is hanging between two Si pillars, an ideal condition for studying individual CNT for gas sensitivity. The gas can flow through nano channel between two pillars gaining better contact with CNTs, i.e. sensing element. Few well resolved SEM images of such CNTs is as shown in the figure 5.13c,d and e. Electron micrograph b and d are of same substrate, however, before and after the growth of carbon nanotubes. Single

CNT supported by Si pillars are marked with colors dots in figure 5.13d. CNTs are slender having average length of 1 to 5 μm. A high resolution image of CNTs bridging two si pillars or more is displayed in figure 5.13e.

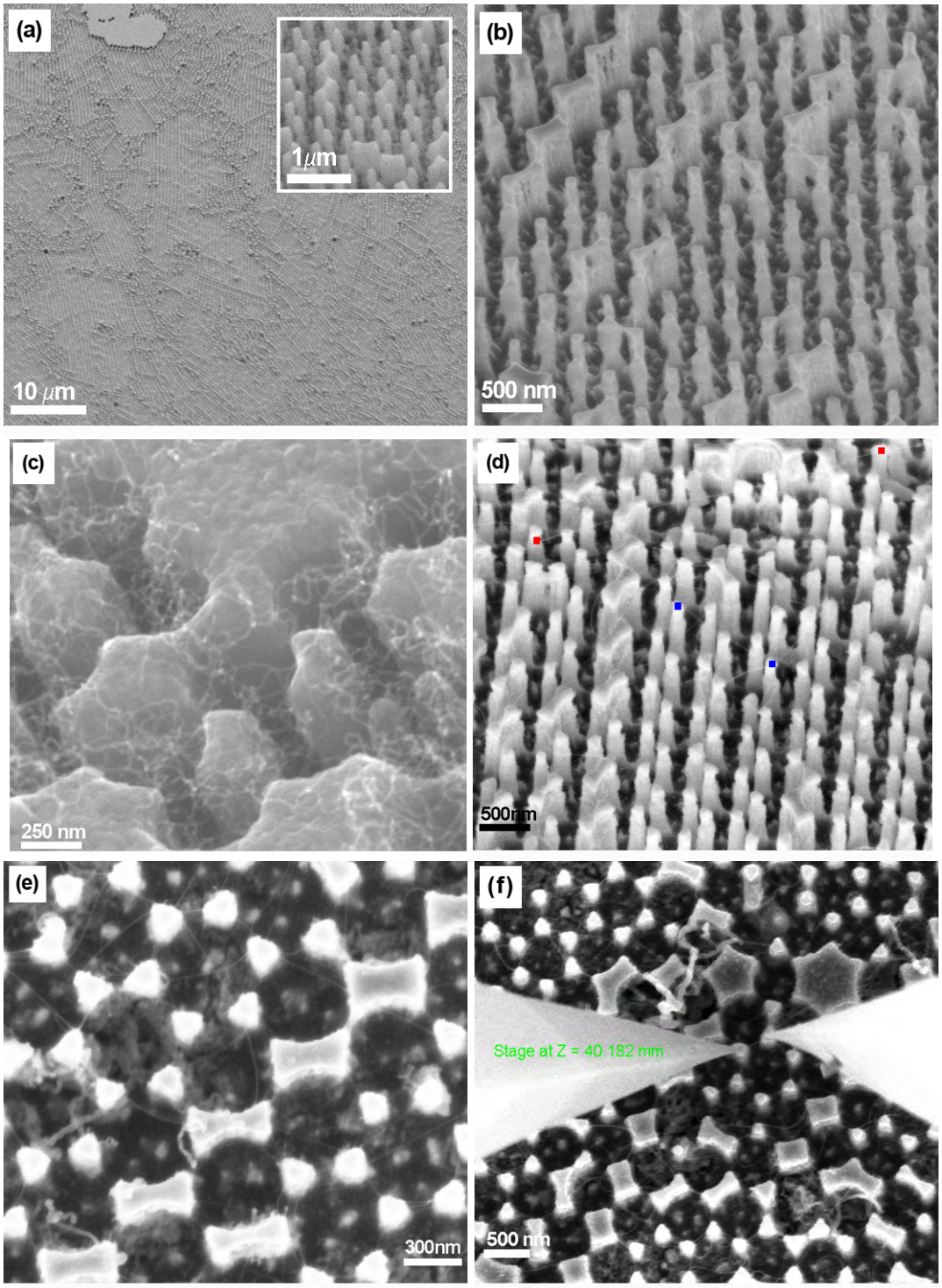

Figure 5.13: Horizontal growth of CNTs on silicon pillars. (a and b) as received pillar [238], (c) dense growth of CNTs on pillars (d and e) individual CNTs grown between two pillars (f) electrical contacting pillars using whiskers.

Using contact whiskers, two pillars incorporating single CNT were contacted and measurement is carried out(see figure 5.13f). The resistance between two pillars is of order several kilo ohms, majority of it is contributed by CNTs. The ready substrates are being tested for their sensitivity and selectivity at RWTH Aachen.

5.4 Carbon nanotubes - ZnO bilayer film as a light sensor

All four ZnO-CNT bilayer films (ZnCN-1 to ZnCN-4) obtained by evaporation and oxidation of zinc metal on CNT film were tested first for their electrical characteristics. The films were measured using four point method. The oxide film exemplify substrate dependent electrical behavior. The film on a glass substrate shows ohmic behavior. For a given applied field, the current tends to increase in a linear manner. On the other hand, the CNT-ZnO film delivers a non linear Schottky response. This is due to a contact between semi conducting zinc oxide and metallic nanotubes. The CNT film is a mixture of metallic and semi conducting CNTs, in which case, often metallic CNTs will be used as the charge carriers. The plot is as shown in the figure 5.14.

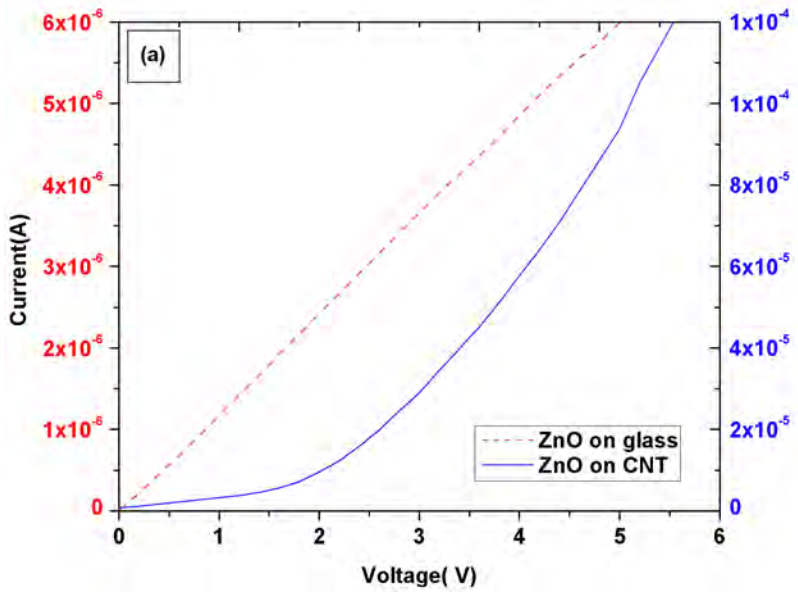

Figure 5.14: I-V characteristics of zinc oxide on glass (red curve) and on CNT (blue curve).

The exact reason of the such a change in the electrical character is unknown. The zinc oxide on glass substrate possess ZnO crystals oriented in one direction while the one on CNT film is poly-crystalline. Also, the size of crystal measured using Debye - Scherrer formula and x-ray diffraction, was relatively small in case of ZnO on CNT. This accounts for a higher amount of

edges and facets of crystals in zinc oxide compared to one on a glass substrate. Smaller crystal size and poly crystalline nature will automatically have a higher amount of grain boundaries. Such material will have higher work function demanding higher potential to conduct the charge carriers through the film.

The all four samples show strong green illumination in photo luminescence measurements. Therefore, samples were tested for possible light sensitivity by using various light sources. Few 5mW intensity laser diodes emitting light of predefined wavelength were used. Also, samples were tested against white incandescent light room light. Lasers emitting 365 nm, 530 nm, 650 and 780 nm were used. The first one is in ultraviolet zone, 530 is green laser, and 780 nm laser emits light in infra red range, invisible for human eye. The testing was carried out by measuring the sample first in dark conditions and alternately illuminated using various light sources. The I-V characteristics are as shown below (see figure 5.15)

The zinc oxide grown on glass substrate (ZnCN-2a and b) show no sensitivity against any kind of light. The CNT-ZnO bilayer film oxidized in oven (ZnCN-2c) also fail to show any sensitivity against incident photons. The only sample, sample ZnCN-4 was photo active against all light sources. The zinc oxide film grown on CNT film was contacted using whiskers and first measured in dark conditions (black curve in figure 5.15a). If the light was incidence of photons of various wavelength, a three to five fold rise in the current was seen. As the intensity of laser was too low, no wavelength dependent change in current flow was observed.

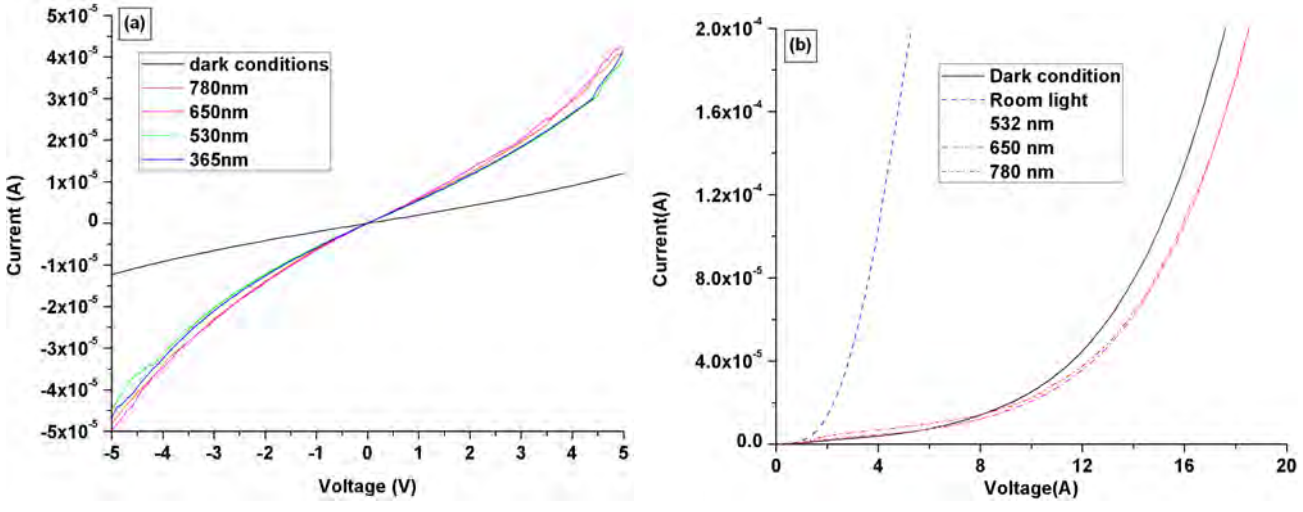

Figure 5.15: I-V characteristics of various ZnO-CNT bilayer film.

The ZnCN-2d was synthesized by oxidation time of 1 hour in open air. Instead the film was oxidized over night at 400 °C. After cooling down to room temperature the film was tested for photon sensitivity. The film was still sensitive against light of all wavelength. However, the film show strong rise in current in response to photons from the incandescent lamp emitting white light. The incandescent white light has spectrum similar to that of sun light. The bilayer film can be thus a good candidate for solar energy harvesting. The film of size 1x1cm was prepared and being tested for photo conversion efficiency.

A CNT-ZnO bilayer film offers light sensitivity over a broad spectrum. It is also possible to dope the zinc metal simply by replacing the zinc target by alloy of zinc and dopant materials; magnesium for example. The doping with appropriate elements might lead to increase in the observed photo conversion efficiency.

6 Summary and conclusion

The present work comprises a novel method for selective growth of carbon nanotubes, study of their growth mechanism as well as synthesis and application of their various hybrid materials. An experimental setup is established to grow carbon nanotubes using water assisted chemical vapor deposition method. Various growth parameters were scrutinized carefully and a growth mechanism is put forth for the same method. A new methodology to prepare different hybrid materials of aligned carbon nanotubes together with nano sized metal oxides particles, biological nerve cell, noble metal nano particles is demonstrated.

Growth of carbon nanotubes and study of its growth mechanism:

Carbon nanotubes are synthesized using water assisted chemical vapor deposition method, in which water acts as a weak oxidant. CNTs are crystalline, aligned, double walled and impurity free. The standard growth rate obtained was 30 to 40 μm per minute and the growth rate, quality and typology of the CNTs can be fine tuned by controlling hydrogen flow rate, quantity of iron and aluminum deposited and their deposition method. The present study confirms the precise role of hydrogen and aluminum in WCVD growth mechanism. The process follows the root growth mechanism with bimetallic catalyst composed of iron and aluminum. The small quantity of water acts as weak oxidant, held responsible for keeping catalyst active for longer time.

By employing advanced techniques such as EELS, tomography in transmission electron microscopy, catalyst nano particles were analyzed for their chemical composition. Each catalyst nano particle is made up of two phases; the central core made up of pure iron surrounded by intermixed phase of iron and aluminum. The two-phase catalyst was continuously hydrolyzed by supplied water vapor; confirmed by XRD and XPS measurements. Hydroxyl groups produced on surface of the catalyst utilized to selectively etch the amorphous carbon from the surface to keep the catalyst clean. Therefore, catalyst stays active for longer time leading the CNT growth up to millimeter long length.

Solid state nuclear magnetic resonance spectroscopy of pristine CNTs show majority of CNTs are double walled along with a small percentage of single walled carbon nanotubes. The shift to lower energy indicates most of the CNTs possess semiconducting characteristics. A split of 10

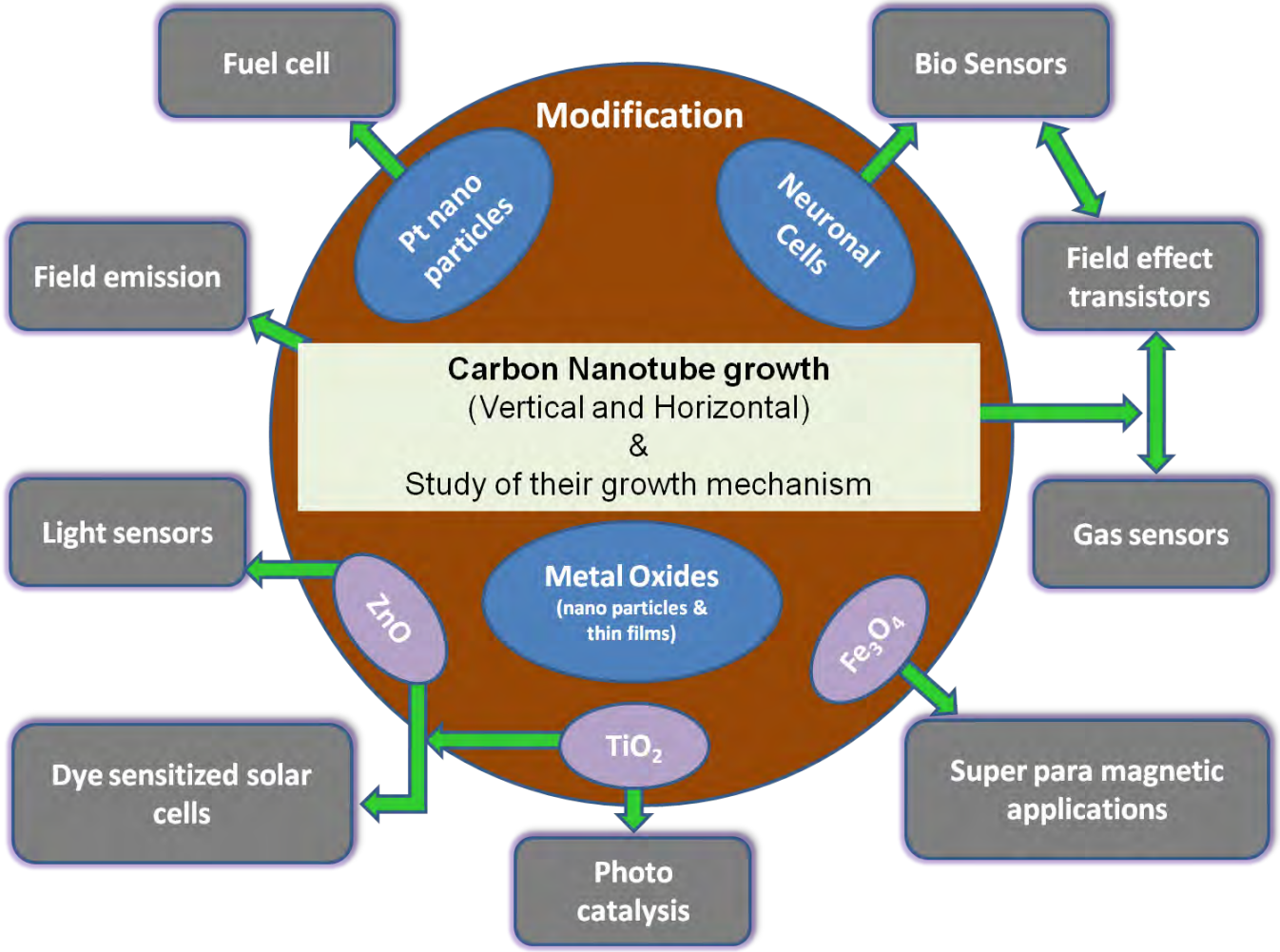

Pictorial overview exemplifying the present work undertaken in direction of growth, modification and various potential applications of carbon nanotubes and its hybrid materials.

ppm was recorded for DWNTs consisting one metallic and one semi conducting tube. Smaller tube diameter or metallic nature of CNTs shift the peak position to higher ppm.

Electronic applications of carbon nanotubes:

Carbon nanotubes can be grown vertically or even horizontally as required. The horizontally grown carbon nanotubes were used to fabricate field effect transistors. CNTs are single walled, semiconducting, p-type in nature delivering a device with high (2000 to 5000) on off ratio. Transistor is sensitive enough to depict good modulation of current for small value of gate voltage; ideal to realize various sensors. Also, using alcohol-CVD method, growth of single CNT bridging two silicon pillars is demonstrated. The CNT bridging two Si-pillars will be studied to gas sensor applications. On the other hand, vertically grown CNT blocks have already been tested for room temperature gas sensing. Vertically grown structured blocks of aligned carbon nanotubes exhibit excellent field emission characteristics. Current emission in milliampere range, stable emission and constant enhancement factor for up and down cycle are salient features. CNT blocks with appropriate size and intermediate distance are proposed for cold cathode applications.

Synthesis of metal oxide - CNT hybrid materials:

A new methodology is developed to prepare hybrid materials of metal oxides and carbon nanotubes. Using various techniques, metal oxide nano particles or film are deposited on previously grown carbon nanotubes blocks or films. In the present study, the ordered structure of carbon nanotubes is modified with nano particles of titanium dioxide, zinc oxide and iron oxide. The average distribution of particle size is of order 5 to 10 nm, covering the side walls of carbon nanotubes.

CNT blocks deposited with ZnO and TiO_2 particles show excellent field emission properties. Zinc oxide - CNT bilayer film is demonstrated as a light sensor. The bi-layer film is sensitive to light of different wavelength. A single step process to form magnetic composite of CNT and iron oxide is introduced. The particle size of iron oxide is small enough (5 to 15 nm) that the composite exhibits super paramagnetic properties. As the CNT and iron oxide both are bio compatible, composite shows potential in bio medical applications. Ordered CNT blocks deposited using ZnO and TiO_2 can serve as a potential material for solar energy harvesting or hydrogen generation by water splitting.

The electrode membrane assembly of as grown film of carbon nanotubes decorated using platinum nano particles is fabricated and being tested for fuel cell applications. The average size of the platinum nano particle is of order 2 to 4nm, obtained by self reduction technique.

Growth of Neuron cells on CNT blocks:

Carbon nanotube blocks are used as substrate to grow varieties of nerve cells. The growth takes place selectively on carbon nanotubes demonstrating affinity of cells towards CNTs. Unlike previous reports, growth is demonstrated on pristine CNTs. Somas found to have numerous neurites with several sub branching i.e. axons forming interconnects. Not only this, cells interconnect each other forming a cell bridge between two CNT blocks. The investigation using spheroids made up of neurons affirms the affinity of cells towards CNTs as many of the somas migrate to CNT blocks leaving spheroids. The complete study corroborates the potential of CNT structure as a electrode for the growth of neuron cell. CNTs are biocompatible, nano-sized and electrically conducting; in short, an ideal electrode for studying cell transport mechanism, neuron cell signaling and can even be a promising material for developing neuronal prosthesis.

As a center point of this work, water assisted chemical vapor deposition method is proved to be an optimal growth technique for multi-dimensional field of carbon nanotubes. This method not only offers the possibility to grow good quality CNTs of different typology or morphology, but also ease of maneuvering the experimental parameter to visualize different forms or architectures serving devices with high order sensitivity at sub micron scale. The study on composite of metal oxides and CNTs demonstrates the diversity of this field. Few potential applications were successfully demonstrated while many more can be thought of. The introductory work on growth of nerve cells shows exquisite potential of CNTs in the field of bio-nano-technology. By combining two fields; CNT based FET devices and growth of biological cells on CNTs; together, biosensors can be visualized. Nonetheless, CNTs put forth a wide range of properties addressing the constant demand of new or better materials to sustain the technological development.

6a Zusammenfassung

Die vorliegende Arbeit behandelt eine neuartige Methode zum selektiven Wachstum von Kohlenstoffnanoröhren (CNT), die Untersuchung des Wachstumsmechanismus sowie die Synthese und Anwendung verschiedener Hybrid-Materialien aus CNTs, Metalloxiden, Metallen und Biomaterialien.

Herstellung und Untersuchung des Wachstumsmechanismus von Kohlenstoffnanoröhren

Kohlenstoffnanröhren wurden mit dem Verfahren der Wasser unterstützten chemischen Gasphasenabscheidung (WCVD) synthetisiert, wobei das Wasser die Rolle eines schwachen Oxidationsmittel übernimmt. Die erhaltenen CNTs sind kristallin, vertikal angeordnet, zweiwandig und frei von amorphen Kohlenstoff. Die erzielte Wachstumsrate liegt bei 30 bis 40 μm pro Minute und die Wachstumsrate, die Qualität und Typologie der CNTs werden durch die Flußrate des Wasserstoffs, die Schichtdicke des Eisens und Aluminiums, die als Katalysatormetalle dienen, bestimmt. Der Wachstumsprozess erfolgt an bimetallischen Katalysatorpartikeln bestehend aus Eisen und Aluminium. Das zugegebene Wasser wirkt als schwaches Oxidationsmittel und ist verantwortlich für eine hohe Katalysatoraktivität und -standzeit. Die chemische Zusammensetzung und Morphologie der Katalysatornanopartikel wurden u.a. mittels EELS und mittels TEM Tomographie analysiert. Die Katalysatorpartikel bestehen aus zwei Phasen. Der Kern der Katalysatorpartikel besteht aus reinem Eisen, umgeben von einem intermetallischen Gemisch aus Eisen und Aluminium. Der zweiphasige Katalysator wird im Prozess durch den zugeführten Wasserdampf an der Oberfläche kontinuierlich verändert. Die dadruch erzeugten Hydroxyl-Gruppen auf der Oberfläche des Katalysators werden zu selektiven ätzung des amorphen Kohlenstoffs genutzt, wodurch die aktive Oberfläche des Katalysators im Prozess gereinigt wird. Festkörper-Kernspinresonanzspektroskopie (^{13}C - NMR - MAS) an ^{13}C angereicherten CNTs zeigt, dass die erhaltenen CNTs einen zweiwandigen Aufbau haben. Daneben liegt ein geringer Anteil an einwandigen CNTs vor. Ebenso gelang mit dieser Methode der Nachweis halbleitender, neben metallisch leitenden CNTs.

Untersuchungen zu den elektronischen Funktionseigenschaften von geordneten CNTs

CNTs können sowohl horizontal oder auch vertikal ausgerichtet wachsen. Horizontal gewachsene Kohlenstoffnanoröhren wurden verwendet um ein Feldeffekttransistor Bauteil (FET) herzustellen. Die erzeugten CNTs sind einwandig, halbleitend (p-Typ) und liefern

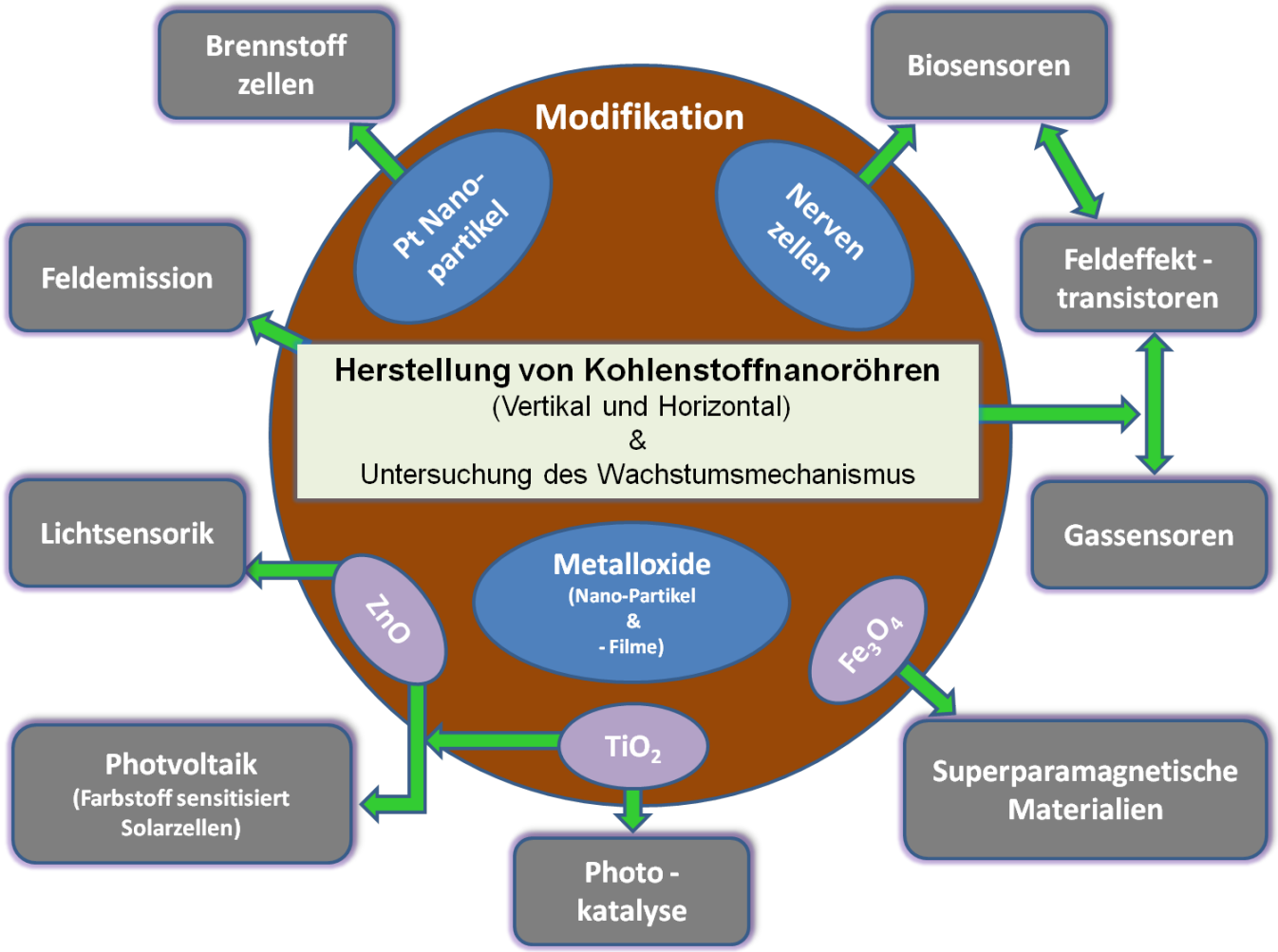

Schematische Darstellung der vorliegenden Arbeit in Bezug auf das Wachstum, Modifikation und verschiedener Anwendungen von CNTs und ihrer Hybridmaterialien.

FETs mit hohem ON/OFF Verhältnis. Die damit erzeugten FETs zeigen eine gute Modulation mit einer kleiner Gate Spannung in einer Transitorschaltung. Sie eignen sich daher prinzipiell zur Herstellung von sensorischen Bauteilen. Darüberhinaus wird unter Anwendung eines modifizierten CVD-Prozesses unter Verwendung von Ethanol als Kohlenstoffquelle das horizontale Wachstum von einzelnen CNTs zwischen isolierten Si-Säulen demonstriert. Die Eignung dieser vertikal gewachsenen CNTs für die Gassensorik wird derzeit untersucht.

Vertikale CNT Blöcke, die ebenfalls im Rahmen dieser Arbeit erzeugt wurden, weisen hervorragende Feldemissionseigenschaften auf. Der nachgewiesene Feldemissioneffekt liegt im Bereich von einigen mA, die stabile Emission und der erzielte, konstante Feldüberhöhungsfaktor (β) der CNT Blockstrukturen, sind hervorstechende Ergebnisse dieser Untersuchungen.

Herstellung von Metalloxid/ und Metall/CNT-Hybridmaterialien

Eine neue Methode zur Herstellung von Hybridmaterialien bestehend aus Metalloxiden und CNTs konnte im Rahmen dieser Arbeit entwickelt werden. Dazu wurden CNT-Blöcke oder großflächige CNT-Filme mit Metalloxid-Nanopartikeln oder Metalloxid-Filmen beschichtet. Es konnten so angeordnete CNT/Metalloxid Kompositstrukturen mit nanoskaligen Titan-, Zink- oder Eisenoxidpartikeln erhalten werden. Der mittlere Durchmesser der abgeschiedenen Nanopartikel beträgt 5 bis 10 nm.

CNT Blockstrukturen, beschichtet mit TiO2 und ZnO zeigen ebenfalls ausgezeichnete elektrische Feldemissionseigenschaften. Hybridische CNT/ZnO Filmstrukturen weisen zudem licht-abhängige Sensoreigenschaften über einen größeren Wellenlängenbereich auf. Diese konnten im Rahmen dieser Arbeit erstmals charakterisiert werden. Ein einstufiger Prozess zur Darstellung eines Hybridmaterials bestehend aus CNTs und Eisenoxidpartikeln führte zur Herstellung eines superparamagnetischen Materials auf Basis CNT/Fe_3O_4 bzw. CNT/Fe_2O_3. Die Größe der abgeschiedenen Eisenoxidpartikel liegt im Bereich zwischen 5 bis 15 nm.

CNT Filmstrukturen, die mit nanoskaligen Platinpartikeln beschichtet wurden, konnten als Elektrodenmaterialien in Niedertemperaturbrennstoffzellen getestet. Die Durchmesser der abgeschiedenen Partikel liegt im Bereich von 2 bis 4 nm.

Adherierung und Wachstum von Nervenzellen auf Kohlenstoffnanoröhren

Geordnete Blockstrukturen von Kohlenstoffnanröhren auf einkristallinen, planaren Siliciumsubstraten dienen als Substrate für das Wachstum von Nervenzellen. Das Wachstum der eingesetzten Zellen findet ausschließlich auf den CNT-Strukturen und nicht auf dem

Siliciumsubstrat statt. Im Unterschied zu bisherigen Untersuchungen wurde das Wachstum auf nativen, d.h. unbehandelten CNTs durchgeführt. Die verwendeten Nervenzellen zeigen ein verzweigtes Neuritenwachstum, welches die Zellen untereinander verbindet. Auf diese Art bilden Zellen eine Brücke aus mehreren Zellen, wenn der Abstand zwischen den CNT Blöcke zu groß gewählt wird. Untersuchungen mit Zellkugeln weisen die Affinität der Zellen zu den CNTs nach, wobei einzelne Zellen sogar die Zellkugeln verlassen, um auf den Blockstrukturen der CNTs gezielt weiterzuwachsen. Diese Untersuchungen zeigen erstmals direkt die Verwendbarkeit solcher CNT Blöcke zur Ausbildung eines Neuronalnetzwerkes auf der Basis von CNTs. Wegen der prinzipiellen Bioverträglichkeit und der guten elektrischen Leitfähigkeit von CNT-Strukturen sind diese ideale Elektroden für die zukünftige Untersuchung von Zelltransportmechanismen. Die Kombination der in dieser Arbeiten aufgezeigten Möglichkeit zur Herstellung von FETs, gekoppelt mit dem Wachstum von Neuriten auf CNT Blockstrukturen zeigt das große Potenzial dieser Materialkombination für zukünftige, neuratige Forschungen auf dem Gebiet der Biosensorik.

7 Experimental procedure

7.1 Growth of CNTs using water assisted chemical vapor deposition method

Carbon nanotubes were synthesized using a water assisted chemical vapor deposition method using silicon wafer as a substrate. The growth process starts with preparation of the substrate. The substrate used was single crystalline silicon wafer with $< 100 >$ crystal orientation. The wafer was p-type, light boron doped (Si-Mat,Silicon Materials). In present work, two types of such wafers were used. First one was called Si-wafer; without any oxide layer on it and another with 600 nm thick SiO_2 layer on it. This oxide layer was thermally grown and also has same orientation as that of Si-wafer. In order to prepare the substrate, on 1 cm^2 piece of Si or SiO_2 wafer a 10 nm thick layer of aluminum was deposited followed by 1 nm layer of iron. The deposition of metal was carried out using electron beam evaporation system (e-beam), and thickness of monitored using commercially available micro balance (Cressington MTM 10).

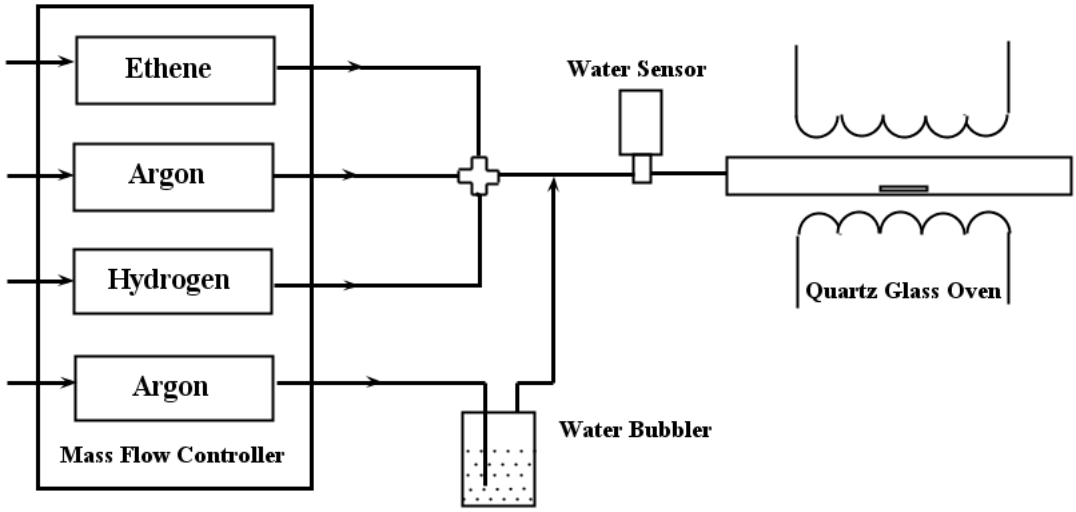

Figure 7.1: Schematic layout of experimental setup used for growing carbon nanotubes.

The CNT growth was carried out at temperature 800 °C using hydrogen (99.9990%), argon (99.996%), ethene (C_2H_4) (99.90%)) and small amount of water vapor. The complete process works at standard ambient (STP) conditions. The gas flow was controlled using commercially available mass flow controllers (MKS Instruments, 179B type flow meters with controller unit 647B). Four dedicated mass flow controllers were used for this purpose; one each for hydrogen, argon, ethene and fourth one for argon used to carry water vapor. Water vapor was carried inside the oven by bubbling small amount of carrier gas through a deionized water bubbler

built into the system. The gas bubbling through water was so controlled that it carries water vapor in amount 190 to 210 ppm (parts per million) of total gas flow rate. All the flowing gases were mixed together before supplying to an oven. A water sensor (Easidew transmitter EA2, range -100/+20, Michell Instrument) was built in the sytem just before the entrance to an oven in order to monitor the water vapor content. The reading was displayed in dew points of water, which was recalculated to ppm value. 190 to 210 ppm of water corresponds to dew point of -31 to -32 °C.

Carbon nanotubes were grown using a total gas flow rate of 1130 standard cm^3/min (sccm). Out of it, 600 sccm was argon, 400 sccm was hydrogen, 100 sccm ethene and 30±2 sccm argon through water bubbler. The ready substrate was heated to growth temperature (800°C) in a circular quartz glass oven (30 mm in diameter) consists of three zones, independent of each other. The sample was placed in another small quartz tube and inserted in side the oven tube. The purpose behind using the quartz tube as a sample holder was to minimize boundary layer conditions due to laminar flow of gases. The sample was heated to 800 °C in 20 minutes using constant heating ramp and under flow of argon (600 sccm) and hydrogen (400 sccm). At 800 °C, flow or 100 sccm ethylene along with 30 to 32 sccm of argon through water bubbler was started. Using this combination, a constant CNT growth rate of 30 to 40 μm/min was obtained. At the end of growth step, the flow of ethylene and water vapor was turned off and hydrogen flow was reduced to 100 sccm. The flow of hydrogen and argon was kept on for about 10 minutes and then the sample was cooled down to room temperature under nominal flow of 50 sccm of argon. This post growth hydrogen treatment will ease the peeling off of the CNT film from the substrate.

7.1.1 Growth of ^{13}C enriched CNTs for NMR studies

^{13}C enriched CNTs were synthesized using normal growth process explained above. On a standard SiO_2 wafer, 10 nm thick layer of aluminum and 0.8 nm thick iron layer on the top of aluminum layer was deposited. The ready substrate was then heated to CVD temperature under current of hydrogen and argon gas to form small catalyst nano particles. At CVD temperature, growth of CNTs was carried out using water assisted chemical vapor deposition method. A mixture of 400 sccm hydrogen and 600 sccm of argon gas was used as a carrier gas. Alike standard growth conditions, 100 sccm of ethene was used as a carbon source but coming from

two different sources; 68 sccm of $^{1}2C$ ethene together with 32 sccm of ^{13}C ethene (purchased from sigma aldrich 99.99% pure). Instead of argon gas, the 32 sccm part of ethene gas was bubbled through water bubbler. The change has no influence on the growth process and was made due to constraint in experimental setup, as at a time only four mass flow controllers can be operated simultaniously. In time span of 20 minutes, about 2.6 mg of ^{13}C enriched CNT mass was synthesized.

7.1.2 Growth of horizontally aligned CNTs

Horizontally aligned carbon nanotubes were grown using two different techniques; alcohol - CVD method and methane - CVD method. Both processes are explained as below.

Using alcohol - CVD method, CNT growth was carried out at 900 °C. The process begins as usual with substrate preparation. In this method, SiO_2-wafer having 230 nm thick oxide layer was used. Using optical lithography technique or standard masking method, contact electrodes made up of 100 nm thick gold film were deposited on the substrate. On such gold pads, 0.6 to 0.8 nm, cobalt was deposited using e-beam technique. The ready substrate was heated to growth temperature under the flow of argon (520 sccm) and hydrogen (65 sccm). At desired temperature, the gas flow was shifted to 230 sccm of argon and 70 sccm of hydrogen. The total gas flow was bubbled through a ethanol bubbler cooled using ice bath. The gas flow will carry ethanol vapor inside the oven and was used for the growth of carbon nanotubes catalyzed by cobalt nano particles. The growth period lasts for 1 hour, and then sample was cooled to room temperature under flow of argon.

In methane - CVD technique, 0.5 to 0.8 nm thick layer of iron was used instead of cobalt as a catalyst. The ready substrate was heated to 900 °C under flow of argon (100 sccm) and hydrogen (400 sccm). At 900 °C, gas flow was shifted to 1500 sccm of methane and 200 sccm of hydrogen. The standard duration of growth phase was about half an hour and then sample was cooled down to room temperature.

Both methods deliver good quality of single walled semiconducting carbon nanotubes. The average diameter of the SWNT was 1.5 to 1.7 nm. However, CNTs grown using ethanol - CVD method were less in number compared those grown using methane - CVD method. Suitable method was incorporated depending upon the need.

7.2 Modification of as grown carbon nanotubes

As grown carbon nanotubes were deposited using zinc oxide, titanium dioxide, iron oxide, nerve cells and platinum nano particles. The methodology to deposit various material on CNTs is as explained below.

7.2.1 Preparation of zinc oxide - CNTs hybrid material

Zinc oxide was deposited on as grown carbon nanotubes. The carbon nanotubes were grown using a standard technique of water assisted chemical vapor deposition method as explained before. Block structure or film structure, in both cases, the deposition was carried out on CNTs having length of about 400 to 500 μm. The experimental procedure is as follow.

- Deposition of zinc oxide nano particles on carbon nanotube blocks

  Carbon nanotubes in film or block structures, were inserted into a quartz tube oven and heated under the stream of argon to 500 to 700 °C within half an hour. Zinc acetylacetonate (Merck KGaA, 95% pure), precursor for zinc oxide, was placed in small around bottom flask and heated to 130 to 140 °C in same time using an oil bath. The flask was connected to quartz tube via a two way valve. Upon arrival of CVD temperature the argon flow was diverted into the flask and vapors of sublimated precursor were carried inside the reaction zone by using a gas flow. The precursor was decomposed immidiately after coming in contact with hot walls of an oven forming zinc oxide species and finally depositing a particulate layer of ZnO nano particles on side wall of carbon nanotubes.

  In solution method, zinc oximato precursor was dissolved into commonly available alcohols such as ethanol or iso-propanol forming a solution of 5 to 10 weight % concentration. The clear solution was dropped on CNT blocks grown on Si / SiO_2 wafer and let the solution to evaporate. After a while, the structure was heated to 250 to 300 °C to decompose the oximato precursor forming small nano particles of zinc oxide on the side wall of carbon nanotubes.

  Zinc oxide nano particles grown by chemical vapor deposition method were relatively bigger compared to that of by solution processing. However, solution processing impedes the shrinkage of CNT block structure.

- Deposition and oxidation of zinc metal on carbon nanotube film

  Pure zinc granules (sigma - aldrich 99.9%) were used as a starting material. A homogeneous layer of zinc metal was evaporated using electron beam metal evaporation system. 100 to 200 nm thick layer of zinc was deposited at a constant rate of 0.5 to 1 nm per second on previously grown CNT film or cleaned glass substrates. At standard evaporation conditions, zinc metal evaporates readily and uniformly at 2 to 2.5 KV of energy between two electrodes.

  Zinc film deposited on the various substrates was oxidized at temperature of 400 °C in open air or in a tubular oven under controlled supply of oxygen rich atmosphere. In both cases, the sample was placed in alumina petry dish and inserted in oven. The oven was heated to desired temperature with constant heating rate of 15 to 20 °C per minute. The films were held at oxidation temperature minimum for an hour in order to ensure enough time to oxidize the nanometer thick metal film. During oxidation in oven, the flow rate of oxygen and argon was controlled using commercially available mass flow controllers (MKS instruments). A gas flow consisting 100 sccm of argon and oxygen in varied amount of 5 to 100 sccm was supplied depending upon experimental conditions. Depending on the oxidation conditions, gray metallic zinc film was oxidized to form dark or light blue colored second layer on carbon nanotube or glass substrate.

The sample prepared using CVD method is termed as 'ZnCN-1', using solution method as 'ZnCN-2' and bilayer film of ZnO on CNT is designated as 'ZnCN-3'. The suffix a,b,c... after respective nomenclature represent same sample with minor change in experimental procedure defined as per need at proper time.

7.2.2 Preparation of titania - CNTs composite material

As grown carbon nanotubes were deposited with titania nano particles, a TiO_2 film or a layer using various methods. Chemical vapor deposition method was suitable to decorate CNTs with small nano particles of titania using a suitable titanium precursor. A sol-gel technique was used to deposit a film of titania on CNTs and evaporation of metal layer and oxidation in suitable atmosphere forms titania - CNT bilayer film. For all studies, as grown CNTs in form

of block structure or film structure of average height in range of 400 to 500 μm were used. The experimental procedure for titania deposition is explained as below.

- Deposition of titania nano particles on Carbon nanotube film/blocks

  Titanium iso-propoxide (Titanium tetra(isopropoxide)) (Merck, 99% pure) was used as a precursor to deposit titania nanoparticles on side walls of CNTs. As grown carbon nanotubes, film or blocked structure, was inserted into a quartz tube oven. The oven was heated to desired temperature under the flow of argon gas in order to avoid CNT burning at temperature above 550 °C. Few milliliters of precursor compound was poured a bubbler which was attached to quartz tube via two way valve. The flow of argon was diverted directly to an oven using two way valve and meanwhile, oven as well as precursor was heated to predetermined temperature. Upon arrival of desired temperature, argon gas (50 to 100 sccm) was bubbled to precursor heated using an oil bath. The gas flow carry vapors of the precursor into an oven depositing nano particles of titania on CNTs. In order to achieve appropriate loading rate, desired form and phase of titania, CVD temperature from 300 to 800 °C and precursor temperature from 90 to 140 °C were tried. The deposition time in every experiment was stipulated to an hour.

- Deposition of titania film using sol-gel technique

  A thin layer of titania film was deposited on carbon nanotubes in way a complete surface of CNT was covered using titania film. For this purpose, previously prepared titania sol was used. The process of sol preparation was adopted from [177]. The process utilizes titanium tetra(isopropoxide), iso-propanol, water along with hydrochloric acid and polyethylene glycol (PEG) as starting materials. 8 ml of titania precursor was added drop after drop into a 50 ml of iso-propanol containing 8 ml HCl. The solution was vigorously stirred for 10 minutes. Thereafter, iso-propanol quantity was increased to arrive final volume of 100 ml. Then, PEG (having 400 g/mol molecular weight) was added to the solution in a quantity 0.75 to 1 g per 100 ml of solution. The sample was stirred for minimum of two days prior usage at perfectly covered and ambient conditions.

  The sol with appropriate viscosity was drop casted on film or block structures of carbon nanotube. The solution was evaporated steadily under controlled conditions. Then the composite was calcinated in air at temperature 300 to 500 °C in order to crystallize the

titania sol. The upper end temperature of crystallization was kept below 550 °C in order to avoid oxidation of carbon nanotubes. Also, temperature above 600 °C increases risk of rutile phase formation.

- Deposition of titania layer by thermal oxidation method

  Similar to process explained in case of zinc oxide, titanium metal was evaporated using electron beam evaporation technique on CNT films as well as on glass substrates. The film was thereafter oxidized in an oven or simply in air at 400 to 500 °C. Every film was held at oxidation temperature minimum for an hour in order to ensure enough time to oxidize the nanometer thick metal film. During oxidation carried out inside an oven, the flow rate of oxygen and argon was controlled using commercially available mass flow controllers (MKS instruments). A gas flow consisting 100 sccm of argon and oxygen in varied amount from 5 sccm till 100 sccm was supplied depending upon experimental conditions. Depending on the oxidation condition, gray metallic titania film was turned into bluish or completely white oxidized film.

7.2.3 Synthesis of magnetite - CNTs composite material

- Synthesis of iron oximato (Tri[2-(methoxyimino)propanoato]iron(III)) precursor

  Synthesis of iron oximato began with synthesis of ligand, for which sodium pyruvate ($C_3H_3NaO_3$, 4.09g) and methoxyamine hydrochloride ($CH_3ONH_2 \cdot HCl$, 3.10g) were added in to 50 ml volume of distilled water in a molar ratio 1:1. Sodium bicarbonate ($NaHCO_3$, 3.68g) was added to same solution stepwise there after. The solution was stirred vigorously for an hour and product was dried using rotary evaporator under vacuum. The white colored ligand scratched off from the wall of a round bottom flask and dispersed into tetrahydrofuran (THF). To this, iron nitrate ($Fe(NO_3)_3 \cdot 9H_2O$, 5g) dissolved again in THF, was added. The reaction began immediately forming reddish brown iron oximato as the final product. The solution was stirred overnight to ensure completion of the reaction.

  The solvent (THF) was removed from the product using rotary evaporator and to left over dried compound, dichloromethane (CH_2Cl_2) together with 10% xylene ($C_6H_4C_2H_6$ or C_8H_{10}) was added. If the product was not crystallized upon cooling, solution was replaced by toluol and the product was precipitated out by adding hexane. Finally, iron

oximate precursor was centrifuged out from the solution and redish yellow powder was obtained by drying overnight at 60°C. The typical yield of the process was ∼ 60% having mole mass of 403.84 grams. The precursor easily dissolves in alcholic solution forming a dark red solution. The powder sample containing magnetite nano particles obtained by decomposition of the precursor was termed as FeCN-1.

- Synthesis of CNT-magnetite composite

  A alcohol based 5 wt% (89.1 mM) solution of oximato precursor was used for preparing the CNT-magnetite composite. Carbon nanotube blocks or films were peeled off the silicon wafer and immersed in same solution or one prepared by diluting it to a known concentration. Diluted solutions were prepared by mixing 25, 50, 75, 100, 200 μl of prepared oximate solution into 2 ml of fresh solvent. It gave solutions having 1.11, 2.23, 3.34, 4.45 and 8.91 mM concentrations respectively. The film was taken out of each solution, dried and heated to 200 to 300 °C or treated under UV radiation for 10 minutes to decompose the precursor and obtain iron oxide nano particles on the side wall of CNTs. This sample was termed at FeCN-2.

7.2.4 Procedure for growing neuron cells on CNT blocks or films

This part covers the methodology of growing purchased neuronal cells or neuron cells obtained from chicken fetus. Also a brief explanation about the process of obtaining neuron cells from the cortex of chicken fetus is given below.

Normally available chicken eggs were incubated in an oven at 37 °C for about 6 to 10 days. The ready egg was carefully broken, fetus was taken out and behead immediately. The cerebral cortex part of fetus was selected for the study purpose. The cortex mass was carefully cut into small pieces washed and then centrifuged at 9000 rpm for 3 minutes in an commercially available salt solution (Ham's F - 12 and Hank's salt solution). It will help to remove the blood residues and will weaken the cell bondage. Cells were then treated using another solution (Trypsin) to preferentially attack and etch all cell neurites or axons off. The duration of treatment was for about 8 to 10 minutes at 37 °C. Care must be taken by controlling the reaction time to ensure the stipulated attack on neurites without damaging the cell body. At the

end of treatment, cell mass dispersed in the solution was separated by centrifuge and rest of trypsin was neutralized and washed away.

Fresh neuron cells without axons were again dispersed into a salt solution and small amount of DNAse solution (200 μl) was supplied to regenerate the cells, those who in case have got damaged by trypsin attack. After appropriate time for regeneration (8 to 10 minutes), cell dispersion was filtered through 40 μm filter to remove the agglomerates. A drop of solution was put on previously grated glass slide and by using optical microscope, cell count per ml of the solution was determined. The optimal cell count used for this study was $\sim$ 3 million cells per ml of solution.

From this solution, around 150 μl of volume was carefully spread on CNT film or blocks grown on the Si wafer. The film was kept for about 4 to 5 hrs undisturbed to make sure that cells settle on CNT structure from the solution. Then, about 4 to 5 ml of neuro-basal medium was added into the solution. The medium mainly contains L-glutamine which will be consumed by cells to regrow its axons to build new interconnects again. On an average, one week to 10 days were allowed for building interconnects completely and forming proper neuronal networks. The growth and development of network was cross examined after few days. In order to do so, in same medium, a glass slide deposited with same amount of cells was kept. The medium is necessary for axon growth and was refreshed approximately 2 times a week.

A sphere of numerous cells was prepared from the remaining cells from the cell solution and are called as "spheroids" [239]. A cell spheroid is a spherical mass of neuron cells interconnected with each other forming a 3 dimensional sphere of size about 200 μm in diameter. Such properly grown spheroids were deposited on fresh CNT blocks.

The biological samples carry risk of destruction during electron microscopy if investigated in as grown condition. Therefore neuron cells were fixed using a polymer layer on CNTs making them stable for investigation. The process of cell fixing is explain here in short.

After complete regeneration of axons, the sample was taken out of the medium solution. A 2.5% concentrated glutaraldehyde solution was added and left for two and half an hour to work. The same process was repeated with phosphate buffer solution (PBS) for 3 times with 20 minutes of working time. Finally the sample was dehydrated using different water based ethanol solutions of increasing concentration. Care must be taken during this process that cells dont come in contact with air while changing the solution. As a last step, the sample was dipped

in HDMS solution in ethanol and dried in air. The sample was then ready for the microscopy investigation.

7.2.5 Preparation of membrane electrode assembly for Fuel cell

The growth of carbon nanotube was carried out on commercial carbon paper or on silicon wafer using standard chemical vapor deposition method. The bimetallic aluminum and iron catalyst was deposited on carbon paper or Si wafer. CNTs were grown at 800 °C using ethylene gas (for more information see synthesis part). The length of CNTs was stipulated to few tens of microns if grown on carbon paper. The carbon paper is a porous membrane made up of graphite fibers and for present study carbon paper was purchased from Toray international of grade TGP - H - 120. In order to limit the length of CNTs grown, no water vapor was passed through the system. However, if the CNTs were grown and transfered to Nafion membrane, CNTs films were grown to 300 to 400 μm height on 1cm^2 wafer pieces. A 0.2 mM concentrated aqueous solution of potassium tetrachloro platinate (K_2PtCl_4) was used for the study. Commercially available nafion membrane (Nafion 117) film was purchased from sigma - aldrich.

7.3 Characterization techniques

Various characterization tools those employed during this thesis work are listed below.

- Raman spectroscopy

  The instrument used for micro raman measurements was LabRAM HR high resolution microscope (Horiba Jobin Yvon, model HR 800). The excitation wavelength used was 488 nm. The spectrum was recorded in the range of 50 to 4000 cm^{-1} wavenumbers.

- Thermo-gravimetric and Mass spectrometry (TG - MS)

  TG-MS measurements were carried out using Netzsch instrument (TG 209N1 and Aelos QMS 403C). Thermo-gravimetric analysis was carried out in either oxygen or helium atmosphere while TG-MS in helium atmosphere starting from room temperature to 950 °C.

- UV-Vis spectroscopy

  UV-Vis spectroscopy was performed on a Perkin Elmer Lambda 900 spectrometer in a range 250 to 800 nm.

- IR spectroscopy

  IR spectroscopy was performed using Nicolet IR100 instrument in a range starting from 400 to 4000 cm^{-1} wavenumbers. Potassium bromide (KBr) was used as a binding agent.

- Photo luminescence spectroscopy

  PL spectroscopy was carried out using a Horiba Flurolog-3 instrument installed with a Xenon lamp.

- Nuclear magnetic resonance spectroscopy (NMR)

  Solid state NMR spectrosopy was performed using 400MHz Oxford instrument installed with Bruker spectrometer " AVANCE 2+".

- X-ray Diffraction (XRD)

  X-ray diffraction was carried out using different instruments. For normal 2θ scan, Siemens D5000 (copper Kα) or STADI P, STOE diffractometer (copper Kα) were used. The scan

range was in between 15 to 90 ° of 2θ with step size of 0.02 °. Gracing incidence X-ray diffraction was carried out using Philips (Panalytical) X'pert Pro MPD (Almelo, Netherlands). The radiation used was nickel-filtered Cu Kα, which was generated using an acceleration voltage of 40 kV and cathode current of 40 mA. The primary beam was collimated using a 0.25° axial divergence slit and a 10° equatorial mask. The instrument used for high temperature X-ray diffraction was a Bruker - AXS D8 instruments. The scan was carried out in range 26 to 36 ° of 2θ with step size 0.02°.

- Atomic force microscopy (AFM)

  AFM micrographs were recorded using DiCP-II, Veeco Instruments in non contact mode. A 5 μm scanner was used with standard scanning rate of 0.8 to 1 Hz. Commercially available silicon cantilevers (Phosphor doped Si tip, 40N/m, 300kHz, Symmetric Tip, Al Reflective Coating, MPP-11120-10 type, Veeco Instruments) were used for this purpose.

- Scanning electron microscopy (SEM)

  SEM investigation were performed using a Philips XL 30 FEG microscope with an acceleration voltage of 20 KV. The same instrument can be operated in scattered electron and back scattered electron modes. Energy dispersive analysis of x-rays (EDAX) spectrum was recorded using same instrument.

- X-ray photo electron spectroscopy (XPS)

  X-ray photoelectron spectroscopy was carried out using an instrument ESCALab 250 (Thermo VG Scientific) using monochromated Al Kα radiation (1486.6 eV) and Mg Kα radiation for aluminum (1253.6 eV) in constant analyser energy (CAE) mode with a pass energy of 50 eV for all spectra.

- Transmission electron microscopy (TEM)

  For normal measurements, a Phillip CM200 machine installed with a LaB_6 cathode excited using 200 KV or FEI Tecnai F20 ST electron microscope installed with field emission gun were utilized. Special studies such as tomography, spectroscopy was carried out on FEI Tecnai F20 ST electron microscope and a probe-side aberration-corrected FEI Titan 80-300 STEM. The procedure of differnt studies is as follows. High-resolution tomograms of the nanoparticles were reconstructed from a tilt series of bright-field images. Tilt-angle series

of FeAl nanoparticles were recorded manually at 2° intervals over a range from -60° to 60° with a Tecnai F20 (FEI) operated at 200 kV. Custom-written software was used for image alignment and reconstruction. A refinement of the image alignment to the re-projection of the tomogram was done. The 3D reconstruction was carried out using a the simultaneous iterative reconstruction technique (SIRT). STEM images and EEL spectroscopy line profiles were taken in the probe-side corrected Titan-80-300 microscope at 300 kV acceleration voltage and a Gatan GIF Tridiem spectrometer. A probe semi-collection angle of 25 mrad corresponding to a beam diameter of less than 0.08 nm and a spectrometer semi-collection angle of 43 mrad were adjusted. Elemental profiles were extracted by integration of detector counts over a 20 eV and 80 eV wide window.for the Fe L23 core loss at 707 eV and the Al K core loss at 1645 eV, respectively, after background subtraction. Special measurements such as tomography, EELS etc. were carried out at FZ Juelich under a cooperative project.

Curriculum Vitae

Personal information

Name: Ravi K. Joshi

Date of Birth: 28 / 03 / 1982

Address: 17, Poonam Nagar Near Dynaneshwar Nagar, jule solapur, Manjarewadi post, Solapur, Maharashtra, India. Pin - 413225.

Work experience

2003 - 2004: Graduate Engineer Trainee
Kirloskar Oil Engines Limited (KOEL), Casting division Solapur India

Education

03/2007 - till date: Doctor of philosophy (Ph.D.)
"Synthesis, alignment, growth mechanism and functional properties of carbon nanotubes and their hybrid materials with inorganic and biomaterials"
Technical University Darmstadt, Darmstadt Germany.

2004 - 2007: Master of Science (by research)
"Modified and alternate approaches to synthesize carbon nanotubes"
Indian Institute of Technology Madras, Chennai India - 600036

1999 - 2003: Bachelor of Mechanical Engineering
Shivaji University Kolhapur, Kolhapur India.
First class with distinction

School education

1997 - 1999: Higher Secondary Examination
Pune University, Pune India.
First class with distinction

1987 - 1997: Secondary School Examination
Pune University, Pune India.
First class with distinction

Personal skill and competence

Languages: Marathi(mother tongue), English(fluent), German(good), Hindi, Kannada, Persian(basic)

Awards and achievement:

- Received DAAD scholarship awarded by German Government.
- Awarded by HTTA, a scholarship from HR ministry, Govt. of India.
- Received 2nd prize for Paper “Robotics in spraying” in national level paper presentation contest.
- Second best outgoing student of bachelor class.

Darmstadt 06.09.2010

List of publications

Publications in International Journals

1. **R. Joshi**, J. Engstler, L. Houben, M. B. Sadan, A. Weidenkaff, P. Mandaliev, A. Issanin and J. J. Schneider, "Catalyst composition, morphology andrReaction pathway in the growth of super-long carbon nanotubes" ChemCatChem, (2010) DOI: 10.1002/cctc.201000037.
2. **R. Joshi**, J. J. Schneider, O. Yilmazoglu, and D. Pavlidis "Patterned growth of ultra long carbon nanotubes. Properties and systematic investigation into their growth process" J. Mater. Chem. 20 (2010) 1717.
3. H. Tempel, **R. Joshi**, J. J. Schneider, "Ink jet printing of ferritin as method for selective catalyst patterning and growth of multiwalled carbon nanotubes" Mater. Chem. Phy., 121 (2010) 178.
4. J. Schneider, N. Maksimova, J. Engstler, **R. Joshi**, R. Schierholz, R. Feile, "Catalyst free growth of a carbon nanotubeŰalumina composite structure" Inorg. Chim. Acta, 361 (2008) 1770.
5. **R. Joshi**, H. Tempel, J. J. Schneider, "Template assisted synthesis of transition metal oxide nanotubes via chemical vapor deposition" submitted.

Publications in International conference proceedings

1. **R. Joshi**, J. Engstler, L. Houben, M. B. Sadan, A. Weidenkaff, P. Mandaliev, A. Issanin and J. J. Schneider, "Unraveling the bimetallic nature of the Fe/Al catalyst in the super long growth of carbon nanotubes" accepted for oral talk in Nano - 2010, Sept. 13 - 17th 2010, Rome, Italy.
2. **R. Joshi**, H. Tempel, J. Engstler, J. J. Schneider "Water assisted chemical vapor deposition for millimeter long growth of 2D aligned carbon nanotubes", Oral presentation in ISRS - 2008, Dec. 10-12th 2008, IIT Madras, Chennai India.
3. O. Yilmazoglu, **R. Joshi**, A. Popp, D. Pavlidis, J. J. Schneider "Vertically aligned carbon nanotube bundles with pronounced field emission" submitted for poster presentation to IVNC - 2010,June 26-30th Palo Alto, California USA.

4. A. Navitski, P. Serbun, G. Müller, J. Engstler, **R. K. Joshi**, J. J. Schneider "Field emission properties of aligned pure and TiO_2-coated carbon nanotube block arrays" submitted for poster presentation to IVNC - 2010,June 26-30th Palo Alto, California USA.

Dt: 06.09.2010

Ravi Joshi
Annastrasse 59
64285 Darmstadt

Eidesstattliche Erklärung

Ich erkläre hiermit an Eides Statt, daß ich meine Dissertation selbständig und nur mit den angegebenen Hilfamitteln angefertigt habe.

Ravi K. Joshi

Dt: 06.09.2010

Ravi Joshi

Annastrasse 59

64285 Darmstadt

Erklärung

Ich erkläre hiermit, noch keinen Promotionsversuch undernommen zu haben.

Ravi K. Joshi

References

[**1**] F. Bundy, "Pressure-temperature phase diagram of elemental carbon," *Physica A: Statistical Mechanics and its Applications*, vol. 156, no. 1, pp. 169 – 178, 1989.

[**2**] J. Steinbeck, G. Braunstein, M. S. Dresselhaus, T. Venkatesan, and D. C. Jacobson, "A model for pulsed laser melting of graphite," *Journal of Applied Physics*, vol. 58, no. 11, pp. 4374–4382, 1985.

[**3**] T. W. Ebbesen, ed., *Carbon Nanotubes:Preperation and properties*. CRC Press Florida, 1997.

[**4**] S. Iijima, "Helical microtubules of graphitic carbon," *Nature*, vol. 354, pp. 56–58, Nov. 1991.

[**5**] C. Hierold, ed., *Carbon Nanotube Devices*. Wiley-VCH Verlag GmbH & Co. KGaA, 2008.

[**6**] M. Meyyappan, ed., *Carbon Nanotubes: Science and applications*. CRC Press Florida, 2004.

[**7**] K. Hata, D. N. Futaba, K. Mizuno, T. Namai, M. Yumura, and S. Iijima, "Water-assisted highly efficient synthesis of impurity-free single-walled carbon nanotubes," *Science*, vol. 306, no. 5700, pp. 1362–1364, 2004.

[**8**] J. Huang, D. H. Kim, R. Seelaboyina, B. K. Rao, D. Wang, M. Park, and W. Choi, "Catalysts effect on single-walled carbon nanotube branching," *Diamond and Related Materials*, vol. 16, no. 8, pp. 1524 – 1529, 2007.

[**9**] Z. Yao, H. W. C. Postma, L. Balents, and C. Dekker, "Carbon nanotube intramolecular junctions," *Nature*, vol. 402, pp. 273–276, Nov. 1999.

[**10**] H. W. C. Postma, T. Teepen, Z. Yao, M. Grifoni, and C. Dekker, "Carbon Nanotube Single-Electron Transistors at Room Temperature," *Science*, vol. 293, no. 5527, pp. 76–79, 2001.

[**11**] S. lijima, T. Ichihashi, and Y. Ando, "Pentagons, heptagons and negative curvature in graphite microtubule growth," *Nature*, vol. 356, pp. 776–778, Apr. 1992.

[**12**] M. M. J. Treacy, T. W. Ebbesen, and J. M. Gibson, “Exceptionally high young’s modulus observed for individual carbon nanotubes,” *Nature*, vol. 381, pp. 678–680, June 1996.

[**13**] A. Krishnan, E. Dujardin, T. W. Ebbesen, P. N. Yianilos, and M. M. J. Treacy, “Young’s modulus of single-walled nanotubes,” *Phys. Rev. B*, vol. 58, p. 14013, Nov 1998.

[**14**] E. W. Wong, P. E. Sheehan, and C. M. Lieber, “Nanobeam Mechanics: Elasticity, Strength, and Toughness of Nanorods and Nanotubes,” *Science*, vol. 277, no. 5334, pp. 1971–1975, 1997.

[**15**] H. J. Lu Jian Ping, “Carbon nanotubes and nanotube based nano devices,” *International Journal of high speed electronics and systems*, vol. 9, pp. 101–123, 1998.

[**16**] Y. Hayamizu, T. Yamada, K. Mizuno, R. C. Davis, D. N. Futaba, M. Yumura, and K. Hata, “Integrated three-dimensional microelectromechanical devices from processable carbon nanotube wafers,” *Nat Nano*, vol. 3, pp. 289–294, May 2008.

[**17**] J. H. Bak, Y. D. Kim, S. S. Hong, B. Y. Lee, S. R. Lee, J. H. Jang, M. Kim, K. Char, S. Hong, and Y. D. Park, “High-frequency micromechanical resonators from aluminium-carbon nanotube nanolaminates,” *Nat Mater*, vol. 7, pp. 459–463, June 2008.

[**18**] S. L. Hellstrom, H. W. Lee, and Z. Bao, “Polymer-assisted direct deposition of uniform carbon nanotube bundle networks for high performance transparent electrodes,” *ACS Nano*, vol. 3, pp. 1423–1430, June 2009.

[**19**] N. Ferrer-Anglada, M. Kaempgen, V. Skákalová, U. Dettlaf-Weglikowska, and S. Roth, “Synthesis and characterization of carbon nanotube-conducting polymer thin films,” *Diamond and Related Materials*, vol. 13, no. 2, pp. 256 – 260, 2004.

[**20**] C. Park, J. H. Kang, J. S. Harrison, R. C. Costen, and S. E. Lowther, “Actuating single wall carbon nanotube-polymer composites: Intrinsic unimorphs,” *Advanced Materials*, vol. 20, no. 11, pp. 2074–2079, 2008.

[**21**] L. Yang, K. Setyowati, A. Li, S. Gong, and J. Chen, “Reversible infrared actuation of carbon nanotube-liquid crystalline elastomer nanocomposites,” *Advanced Materials*, vol. 20, no. 12, pp. 2271–2275, 2008.

[**22**] J. N. Coleman, U. Khan, and Y. K. Gun'ko, "Mechanical reinforcement of polymers using carbon nanotubes," *Advanced Materials*, vol. 18, no. 6, pp. 689–706, 2006.

[**23**] C. Li, E. T. Thostenson, and T.-W. Chou, "Sensors and actuators based on carbon nanotubes and their composites: A review," *Composites Science and Technology*, vol. 68, no. 6, pp. 1227 – 1249, 2008.

[**24**] X.-L. Xie, Y.-W. Mai, and X.-P. Zhou, "Dispersion and alignment of carbon nanotubes in polymer matrix: A review," *Materials Science and Engineering: R: Reports*, vol. 49, no. 4, pp. 89 – 112, 2005.

[**25**] J. W. Mintmire and C. T. White, "Universal density of states for carbon nanotubes," *Phys. Rev. Lett.*, vol. 81, p. 2506, Sept. 1998.

[**26**] A. Javey, J. Guo, Q. Wang, M. Lundstrom, and H. Dai, "Ballistic carbon nanotube field-effect transistors," *Nature*, vol. 424, pp. 654–657, Aug. 2003.

[**27**] M. C. LeMieux, M. Roberts, S. Barman, Y. W. Jin, J. M. Kim, and Z. Bao, "Self-Sorted, Aligned Nanotube Networks for Thin-Film Transistors," *Science*, vol. 321, no. 5885, pp. 101–104, 2008.

[**28**] X. Wang, Q. Li, J. Xie, Z. Jin, J. Wang, Y. Li, K. Jiang, and S. Fan, "Fabrication of ultralong and electrically uniform single-walled carbon nanotubes on clean substrates," *Nano Letters*, vol. 9, pp. 3137–3141, Sept. 2009.

[**29**] M. Rinkiö, A. Johansson, G. S. Paraoanu, and P. Törmä, "High-speed memory from carbon nanotube field-effect transistors with high-k gate dielectric," *Nano Letters*, vol. 9, pp. 643–647, Feb. 2009.

[**30**] R. H. Baughman, A. A. Zakhidov, and W. A. de Heer, "Carbon Nanotubes–the Route Toward Applications," *Science*, vol. 297, no. 5582, pp. 787–792, 2002.

[**31**] V. L. Pushparaj, M. M. Shaijumon, A. Kumar, S. Murugesan, L. Ci, R. Vajtai, R. J. Linhardt, O. Nalamasu, and P. M. Ajayan, "Flexible energy storage devices based on nanocomposite paper," *Proceedings of the National Academy of Sciences*, vol. 104, no. 34, pp. 13574–13577, 2007.

[**32**] D. R. Kauffman, C. M. Shade, H. Uh, S. Petoud, and A. Star, “Decorated carbon nanotubes with unique oxygen sensitivity,” *Nat Chem*, vol. 1, pp. 500–506, Sept. 2009.

[**33**] S. W. Lee, B.-S. Kim, S. Chen, Y. Shao-Horn, and P. T. Hammond, “Layer-by-layer assembly of all carbon nanotube ultrathin films for electrochemical applications,” *Journal of the American Chemical Society*, vol. 131, pp. 671–679, Jan. 2009.

[**34**] S. Berber, Y.-K. Kwon, and D. Tománek, “Unusually high thermal conductivity of carbon nanotubes,” *Phys. Rev. Lett.*, vol. 84, p. 4613, May 2000.

[**35**] J. Hone, M. Whitney, C. Piskoti, and A. Zettl, “Thermal conductivity of single-walled carbon nanotubes,” *Phys. Rev. B*, vol. 59, p. R2514, Jan. 1999.

[**36**] S. Maruyama, “A molecular dynamics simulation of heat conduction of a finite length single-walled carbon nanotube,” *Microscale Thermophysical Engineering*, vol. 7, no. 1, pp. 41–50, 2003.

[**37**] M. T. Pettes and L. Shi, “Thermal and structural characterizations of individual single-, double-, and multi-walled carbon nanotubes,” *Advanced Functional Materials*, vol. 19, no. 24, p. 3918, 2009.

[**38**] Q. Li, C. Liu, and S. Fan, “Thermal boundary resistances of carbon nanotubes in contact with metals and polymers,” *Nano Letters*, vol. 9, pp. 3805–3809, Nov. 2009.

[**39**] W. Yi, L. Lu, Z. Dian-lin, Z. W. Pan, and S. S. Xie, “Linear specific heat of carbon nanotubes,” *Phys. Rev. B*, vol. 59, p. R9015, Apr. 1999.

[**40**] J. Chen, V. Perebeinos, M. Freitag, J. Tsang, Q. Fu, J. Liu, and P. Avouris, “Bright Infrared Emission from Electrically Induced Excitons in Carbon Nanotubes,” *Science*, vol. 310, no. 5751, pp. 1171–1174, 2005.

[**41**] M. Freitag, J. C. Tsang, J. Kirtley, A. Carlsen, J. Chen, A. Troeman, H. Hilgenkamp, and P. Avouris, “Electrically excited, localized infrared emission from single carbon nanotubes,” *Nano Letters*, vol. 6, pp. 1425–1433, July 2006.

[**42**] M. B. Tzolov, T.-F. Kuo, D. A. Straus, A. Yin, and Xu, “Carbon nanotubes silicon heterojunction arrays and infrared photocurrent responses,” *The Journal of Physical Chemistry C*, vol. 111, no. 15, pp. 5800–5804, 2007.

[**43**] W. A. deHeer, W. S. Bacsa, A. Chatelain, T. Gerfin, R. Humphrey-Baker, L. Forro, and D. Ugarte, “Aligned Carbon Nanotube Films: Production and Optical and Electronic Properties,” *Science*, vol. 268, no. 5212, pp. 845–847, 1995.

[**44**] E. Adam, C. M. Aguirre, L. Marty, B. C. St-Antoine, F. Meunier, P. Desjardins, D. Menard, and R. Martel, “Electroluminescence from single-wall carbon nanotube network transistors,” *Nano Letters*, vol. 8, pp. 2351–2355, Aug. 2008.

[**45**] C.-W. Liang and S. Roth, “Electrical and optical transport of GaAs/carbon nanotube heterojunctions,” *Nano Letters*, vol. 8, pp. 1809–1812, July 2008.

[**46**] K. Gong, F. Du, Z. Xia, M. Durstock, and L. Dai, “Nitrogen-Doped Carbon Nanotube Arrays with High Electrocatalytic Activity for Oxygen Reduction,” *Science*, vol. 323, no. 5915, pp. 760–764, 2009.

[**47**] H. C. Choi, M. Shim, S. Bangsaruntip, and H. Dai, “Spontaneous reduction of metal ions on the sidewalls of carbon nanotubes,” *Journal of the American Chemical Society*, vol. 124, pp. 9058–9059, Aug. 2002.

[**48**] A. Lobo, E. Antunes, A. Machado, C. Pacheco-Soares, V. Trava-Airoldi, and E. Corat, “Cell viability and adhesion on as grown multi-wall carbon nanotube films,” *Materials Science and Engineering: C*, vol. 28, no. 2, pp. 264 – 269, 2008.

[**49**] G. Cellot, E. Cilia, S. Cipollone, V. Rancic, A. Sucapane, S. Giordani, L. Gambazzi, H. Markram, M. Grandolfo, D. Scaini, F. Gelain, L. Casalis, M. Prato, M. Giugliano, and L. Ballerini, “Carbon nanotubes might improve neuronal performance by favouring electrical shortcuts,” *Nat Nano*, vol. 4, pp. 126–133, Feb. 2009.

[**50**] L. Ge, S. Sethi, L. Ci, P. M. Ajayan, and A. Dhinojwala, “Carbon nanotube-based synthetic gecko tapes,” *Proceedings of the National Academy of Sciences*, vol. 104, no. 26, pp. 10792–10795, 2007.

[**51**] A. Thess, R. Lee, P. Nikolaev, H. Dai, P. Petit, J. Robert, C. Xu, Y. H. Lee, S. G. Kim, A. G. Rinzler, D. T. Colbert, G. E. Scuseria, D. Tomanek, J. E. Fischer, and R. E. Smalley, “Crystalline Ropes of Metallic Carbon Nanotubes,” *Science*, vol. 273, no. 5274, pp. 483–487, 1996.

[**52**] Z. F. Ren, Z. P. Huang, J. W. Xu, J. H. Wang, P. Bush, M. P. Siegal, and P. N. Provencio, "Synthesis of Large Arrays of Well-Aligned Carbon Nanotubes on Glass," *Science*, vol. 282, no. 5391, pp. 1105–1107, 1998.

[**53**] P. J. Harris, ed., *Carbon Nanotubes and Related Structures*. Cambridge University Press, 1999.

[**54**] P. M. Ajayan, T. W. Ebbesen, T. Ichihashi, S. Iijima, K. Tanigaki, and H. Hiura, "Opening carbon nanotubes with oxygen and implications for filling," *Nature*, vol. 362, pp. 522–525, Apr. 1993.

[**55**] T. W. Ebbesen and P. M. Ajayan, "Large-scale synthesis of carbon nanotubes," *Nature*, vol. 358, pp. 220–222, July 1992.

[**56**] H. Zhang, X. Xue, D. Wang, Y. He, and S. Peng, "The effect of different kinds of inert gases and their pressures on the preparation of carbon nanotubes by carbon arc method," *Materials Chemistry and Physics*, vol. 58, no. 1, pp. 1 – 5, 1999.

[**57**] S. Iijima and T. Ichihashi, "Single-shell carbon nanotubes of 1-nm diameter," *Nature*, vol. 363, pp. 603–605, June 1993.

[**58**] S. Cui, P. Scharff, C. Siegmund, D. Schneider, K. Risch, S. Klötzer, L. Spiess, H. Romanus, and J. Schawohl, "Investigation on preparation of multiwalled carbon nanotubes by dc arc discharge under N_2 atmosphere," *Carbon*, vol. 42, no. 5-6, pp. 931 – 939, 2004.

[**59**] A. P. Dresselhaus M.S., Dresselhaus G., ed., *Carbon nanotubes: Synthesis, structure, properties and applications*. Springer Series, Berlin, 2001.

[**60**] T. Guo, P. Nikolaev, A. G. Rinzler, D. Tomanek, D. T. Colbert, and R. E. Smalley, "Self-assembly of tubular fullerenes," *The Journal of Physical Chemistry*, vol. 99, pp. 10694–10697, July 1995.

[**61**] A. Srivastava, O. N. Srivastava, S. Talapatra, R. Vajtai, and P. M. Ajayan, "Carbon nanotube filters," *Nat Mater*, vol. 3, pp. 610–614, Sept. 2004.

[**62**] P. Nikolaev, M. J. Bronikowski, R. K. Bradley, F. Rohmund, D. T. Colbert, K. A. Smith, and R. E. Smalley, "Gas-phase catalytic growth of single-walled carbon nanotubes from carbon monoxide," *Chemical Physics Letters*, vol. 313, no. 1-2, pp. 91 – 97, 1999.

[**63**] F. Keller, M. S. Hunter, and D. L. Robinson, “Structural features of oxide coatings on aluminum,” *Journal of The Electrochemical Society*, vol. 100, no. 9, pp. 411–419, 1953.

[**64**] G. Che, B. B. Lakshmi, C. R. Martin, E. R. Fisher, and R. S. Ruoff, “Chemical vapor deposition based synthesis of carbon nanotubes and nanofibers using a template method,” *Chemistry of Materials*, vol. 10, pp. 260–267, Jan. 1998.

[**65**] K. P. Budna, “Darstellung, charakterisierung und eigenschaften mesoporöser, freitragender aluminiumoxid-membranen,” Master’s thesis, Karl-Franzens-Universität Graz, 2003.

[**66**] S. Maruyama, R. Kojima, Y. Miyauchi, S. Chiashi, and M. Kohno, “Low-temperature synthesis of high-purity single-walled carbon nanotubes from alcohol,” *Chemical Physics Letters*, vol. 360, no. 3-4, pp. 229 – 234, 2002.

[**67**] M. Cantoro, S. Hofmann, S. Pisana, V. Scardaci, A. Parvez, C. Ducati, A. C. Ferrari, A. M. Blackburn, K.-Y. Wang, and J. Robertson, “Catalytic chemical vapor deposition of single-wall carbon nanotubes at low temperatures,” *Nano Letters*, vol. 6, pp. 1107–1112, June 2006.

[**68**] L. Ci, S. Manikoth, X. Li, R. Vajtai, and P. Ajayan, “Ultrathick freestanding aligned carbon nanotube films,” *Advanced Materials*, vol. 19, no. 20, pp. 3300–3303, 2007.

[**69**] T. Belin and F. Epron, “Characterization methods of carbon nanotubes: A Review,” *Materials Science and Engineering B*, vol. 119, no. 2, pp. 105 – 118, 2005.

[**70**] A. M. Rao, E. Richter, S. Bandow, B. Chase, P. C. Eklund, K. A. Williams, S. Fang, K. R. Subbaswamy, M. Menon, A. Thess, R. E. Smalley, G. Dresselhaus, and M. S. Dresselhaus, “Diameter-Selective Raman Scattering from Vibrational Modes in Carbon Nanotubes,” *Science*, vol. 275, no. 5297, pp. 187–191, 1997.

[**71**] S. Bandow, S. Asaka, Y. Saito, A. M. Rao, L. Grigorian, E. Richter, and P. C. Eklund, “Effect of the growth temperature on the diameter distribution and chirality of single-wall carbon nanotubes,” *Phys. Rev. Lett.*, vol. 80, p. 3779, Apr. 1998.

[**72**] P. T. Araujo, I. O. Maciel, P. B. C. Pesce, M. A. Pimenta, S. K. Doorn, H. Qian, A. Hartschuh, M. Steiner, L. Grigorian, K. Hata, and A. Jorio, “Nature of the constant factor in the

relation between radial breathing mode frequency and tube diameter for single-wall carbon nanotubes," *Phys. Rev. B*, vol. 77, p. 241403, June 2008.

[**73**] M. Milnera, J. Kürti, M. Hulman, and H. Kuzmany, "Periodic resonance excitation and intertube interaction from quasicontinuous distributed helicities in single-wall carbon nanotubes," *Phys. Rev. Lett.*, vol. 84, p. 1324, Feb. 2000.

[**74**] A. G. Souza Filho, A. Jorio, A. K. Swan, M. S. Ünlü, B. B. Goldberg, R. Saito, J. H. Hafner, C. M. Lieber, M. A. Pimenta, G. Dresselhaus, and M. S. Dresselhaus, "Anomalous two-peak G' band raman effect in one isolated single-wall carbon nanotube," *Phys. Rev. B*, vol. 65, no. 8, p. 085417, 2002.

[**75**] A. M. Rao, A. Jorio, M. A. Pimenta, M. S. S. Dantas, R. Saito, G. Dresselhaus, and M. S. Dresselhaus, "Polarized raman study of aligned multiwalled carbon nanotubes," *Phys. Rev. Lett.*, vol. 84, p. 1820, Feb. 2000.

[**76**] X. Zhang, W. Zhang, L. Liu, and Z. X. Shen, "Surface-enhanced Raman of Z-vibration mode in single-walled and multi-walled carbon nanotube," *Chemical Physics Letters*, vol. 372, no. 3-4, pp. 497 – 502, 2003.

[**77**] P. Lambin, A. Loiseau, C. Culot, and L. P. Biró, "Structure of carbon nanotubes probed by local and global probes," *Carbon*, vol. 40, no. 10, pp. 1635 – 1648, 2002.

[**78**] X. Zhang, X. Zhang, S. Amelinckx, G. V. Tendeloo, and J. V. Landuyt, "The reciprocal space of carbon tubes: a detailed interpretation of the electron diffraction effects," *Ultramicroscopy*, vol. 54, no. 2-4, pp. 237 – 249, 1994.

[**79**] S. Amelinckx, A. Lucas, and P. Lambin, "Electron diffraction and microscopy of nanotubes," *Reports on Progress in Physics*, vol. 62, no. 11, p. 1471, 1999.

[**80**] M. Liu and J. M. Cowley, "Structures of the helical carbon nanotubes," *Carbon*, vol. 32, no. 3, pp. 393 – 403, 1994.

[**81**] Z. Liu and L.-C. Qin, "A practical approach to determine the handedness of chiral carbon nanotubes by electron diffraction," *Chemical Physics Letters*, vol. 405, no. 4-6, pp. 265 – 269, 2005.

[**82**] L. Qin, T. Ichihashi, and S. Iijima, “On the measurement of helicity of carbon nanotubes,” *Ultramicroscopy*, vol. 67, no. 1-4, pp. 181 – 189, 1997. Frontiers in Electron Microscopy in Materials Science.

[**83**] M. Gao, J. M. Zuo, R. D. Twesten, I. Petrov, L. A. Nagahara, and R. Zhang, “Structure determination of individual single-wall carbon nanotubes by nanoarea electron diffraction,” *Applied Physics Letters*, vol. 82, no. 16, pp. 2703–2705, 2003.

[**84**] J. M. Cowley, P. Nikolaev, A. Thess, and R. E. Smalley, “Electron nano-diffraction study of carbon single-walled nanotube ropes,” *Chemical Physics Letters*, vol. 265, no. 3-5, pp. 379 – 384, 1997.

[**85**] E. D. Minot, Y. Yaish, V. Sazonova, J.-Y. Park, M. Brink, and P. L. McEuen, “Tuning carbon nanotube band gaps with strain,” *Phys. Rev. Lett.*, vol. 90, p. 156401, Apr. 2003.

[**86**] P. Lambin, V. Meunier, L. Henrard, and A. A. Lucas, “Measuring the helicity of carbon nanotubes,” *Carbon*, vol. 38, no. 11-12, pp. 1713 – 1721, 2000.

[**87**] K. T. Lau, M. Lu, and D. Hui, “Coiled carbon nanotubes: Synthesis and their potential applications in advanced composite structures,” *Composites Part B: Engineering*, vol. 37, no. 6, pp. 437 – 448, 2006.

[**88**] A. Cao, C. Xu, J. Liang, D. Wu, and B. Wei, “X-ray diffraction characterization on the alignment degree of carbon nanotubes,” *Chemical Physics Letters*, vol. 344, no. 1-2, pp. 13 – 17, 2001.

[**89**] F.-H. Ko, C.-Y. Lee, C.-J. Ko, and T.-C. Chu, “Purification of multi-walled carbon nanotubes through microwave heating of nitric acid in a closed vessel,” *Carbon*, vol. 43, no. 4, pp. 727 – 733, 2005.

[**90**] Y.-Q. Xu, E. Flor, H. Schmidt, R. E. Smalley, and R. H. Hauge, “Effects of atomic hydrogen and active carbon species in 1 mm vertically aligned single-walled carbon nanotube growth,” *Applied Physics Letters*, vol. 89, no. 12, p. 123116, 2006.

[**91**] R. T. K. Baker, M. A. Barber, P. S. Harris, F. S. Feates, and R. J. Waite, “Nucleation and growth of carbon deposits from the nickel catalyzed decomposition of acetylene,” *Journal of Catalysis*, vol. 26, no. 1, pp. 51 – 62, 1972.

[**92**] R. T. K. Baker, P. S. Harris, R. B. Thomas, and R. J. Waite, "Formation of filamentous carbon from iron, cobalt and chromium catalyzed decomposition of acetylene," *Journal of Catalysis*, vol. 30, no. 1, pp. 86 – 95, 1973.

[**93**] A. Magrez, J. W. Seo, V. L. Kuznetsov, and L. Forró, "Evidence of an equimolar C_2H_2 -CO_2 reaction in the synthesis of carbon nanotubes," *Angewandte Chemie International Edition*, vol. 46, no. 3, pp. 441–444, 2007.

[**94**] D. N. Futaba, J. Goto, S. Yasuda, T. Yamada, M. Yumura, and K. Hata, "General rules governing the highly efficient growth of carbon nanotubes," *Advanced Materials*, vol. 21, no. 47, pp. 4811–4815, 2009.

[**95**] S. R. C. Vivekchand, A. Govindaraj, M. M. Seikh, and C. N. R. Rao, "New method of purification of carbon nanotubes based on hydrogen treatment," *The Journal of Physical Chemistry B*, vol. 108, pp. 6935–6937, June 2004.

[**96**] A. J. Hart and A. H. Slocum, "Rapid growth and flow-mediated nucleation of millimeter-scale aligned carbon nanotube structures from a thin-film catalyst," *The Journal of Physical Chemistry B*, vol. 110, pp. 8250–8257, Apr. 2006.

[**97**] D. N. Futaba, K. Hata, T. Yamada, K. Mizuno, M. Yumura, and S. Iijima, "Kinetics of water-assisted single-walled carbon nanotube synthesis revealed by a time-evolution analysis," *Phys. Rev. Lett.*, vol. 95, pp. 056104–, July 2005.

[**98**] D. N. Futaba, K. Hata, T. Yamada, T. Hiraoka, Y. Hayamizu, Y. Kakudate, O. Tanaike, H. Hatori, M. Yumura, and S. Iijima, "Shape-engineerable and highly densely packed single-walled carbon nanotubes and their application as super-capacitor electrodes," *Nat Mater*, vol. 5, pp. 987–994, Dec. 2006.

[**99**] A. Popp and J. Schneider, "A chip-sized nanoscale monolithic chemical reactor," *Angewandte Chemie International Edition*, vol. 47, no. 46, pp. 8958–8960, 2008.

[**100**] T. Okpalugo, P. Papakonstantinou, H. Murphy, J. McLaughlin, and N. Brown, "High resolution XPS characterization of chemical functionalised MWCNTs and SWCNTs," *Carbon*, vol. 43, no. 1, pp. 153 – 161, 2005.

[**101**] T. Yamada, T. Namai, K. Hata, D. N. Futaba, K. Mizuno, J. Fan, M. Yudasaka, M. Yumura, and S. Iijima, "Size-selective growth of double-walled carbon nanotube forests from engineered iron catalysts," *Nat Nano*, vol. 1, pp. 131–136, Nov. 2006.

[**102**] R. Brajpuriya, A. Sharma, S. Tripathi, V. R. Reddy, and S. M. Chaudhari, "Temperature induced structural changes at interfaces and their influence on magnetic and electronic properties of ultrathin Fe/Al structures," *Journal of Physics: Condensed Matter*, vol. 18, no. 4, p. 1197, 2006.

[**103**] R. Brajpuriya and T. Shripathi, "Investigation of Fe/Al interface as a function of annealing temperature using XPS," *Applied Surface Science*, vol. 255, no. 12, pp. 6149 – 6154, 2009.

[**104**] F. Bonnet, F. Ropital, P. Lecour, D. Espinat, Y. Huiban, L. Gengembre, Y. Berthier, and P. Marcus, "Study of the oxide/carbide transition on iron surfaces during catalytic coke formation," *Surface and Interface Analysis*, vol. 34, no. 1, pp. 418–422, 2002.

[**105**] P. C. Wong, Y. S. Li, and K. A. R. Mitchell, "Investigations of the interface between magnesium and polyethyleneterephthalate by x-ray photoelectron spectroscopy," *Applied Surface Science*, vol. 84, no. 3, pp. 245 – 252, 1995.

[**106**] K.-H. Ernst, J. Patscheider, R. Hauert, and M. Tobler, "XPS study of the a-; H/Al_2O_3 interface," *Surface and Interface Analysis*, vol. 21, no. 1, pp. 32–37, 1994.

[**107**] M. Eggersmann and H. Mehrer, "Diffusion in intermetallic phases of the Fe-Al system," *Philosophical Magazine A*, vol. 80, no. 5, pp. 1219–1244, 2000.

[**108**] F. Bournel, C. Laffon, P. Parent, and G. Tourillon, "Adsorption of acrylic acid on aluminium at 300 K: a multi-spectroscopic study," *Surface Science*, vol. 352-354, pp. 228 – 231, 1996. Proceedings of the 15th European Conference on Surface Science.

[**109**] S. Akhter, X. L. Zhou, and J. M. White, "XPS study of polymer/organometallic interaction: Trimethyl aluminum on polyvinyl alcohol polymer," *Applied Surface Science*, vol. 37, no. 2, pp. 201 – 216, 1989.

[**110**] L. Sandrin and E. Sacher, "X-ray photoelectron spectroscopy studies of the evaporated aluminum / corona-treated polyethylene terephthalate interface," *Applied Surface Science*, vol. 135, no. 1-4, pp. 339 – 349, 1998.

[**111**] B. M. DeKoven and P. L. Hagans, "XPS studies of metal/polymer interfaces – thin films of Al on polyacrylic acid and polyethylene," *Applied Surface Science*, vol. 27, no. 2, pp. 199 – 213, 1986.

[**112**] M. Bou, J. Martin, T. L. Mogne, and L. Vovelle, "Chemistry of the interface between aluminium and polyethyleneterephthalate by XPS," *Applied Surface Science*, vol. 47, no. 2, pp. 149 – 161, 1991.

[**113**] J. Chenavas, J. C. Joubert, J. J. Capponi, and M. Marezio, "Synthese de nouvelles phases denses d'oxyhydroxydes $M^{3+}OOH$ des metaux de la premiere serie de transition, en milieu hydrothermal átres haute pression," *Journal of Solid State Chemistry*, vol. 6, no. 1, pp. 1 – 15, 1973.

[**114**] J. L. Hazemann, J. F. Berar, and A. Manceau, "Rietveld studies of the aluminum-iron substitution in synthetic geothite," *Material Science Forum*, vol. 79-82, pp. 821–826, 1991.

[**115**] P. J. Roach, W. H. Woodward, J. Castleman, A. W., A. C. Reber, and S. N. Khanna, "Complementary Active Sites Cause Size-Selective Reactivity of Aluminum Cluster Anions with Water," *Science*, vol. 323, no. 5913, pp. 492–495, 2009.

[**116**] G. C. Bond, C. Louis, and D. T. Thompson, eds., *Catalysis by Gold*. Imperial College Press, 2006.

[**117**] C. Costello, J. Yang, H. Law, Y. Wang, J.-N. Lin, L. Marks, M. Kung, and H. Kung, "On the potential role of hydroxyl groups in co oxidation over Au/Al_2O_3," *Applied Catalysis A: General*, vol. 243, pp. 15–24, 2003.

[**118**] H. H. Kung, M. C. Kung, and C. K. Costello, "Supported Au catalysts for low temperature CO oxidation," *Journal of Catalysis*, vol. 216, no. 1-2, pp. 425 – 432, 2003. 40th Anniversary Commemorative Issue.

[**119**] A. R. Harutyunyan, O. A. Kuznetsov, C. J. Brooks, E. Mora, and G. Chen, "Thermodynamics behind carbon nanotube growth via endothermic catalytic decomposition reaction," *ACS Nano*, vol. 3, pp. 379–385, Feb. 2009.

[**120**] M. Colaianni, P. Chen, and J. Y. Jr., "Spectroscopic studies of the thermal modification of the Fe/Al_2O_3 interface," *Surface Science*, vol. 238, no. 1-3, pp. 13 – 24, 1990.

[**121**] C. Goze-Bac, S. Latil, P. Lauginie, V. Jourdain, J. Conard, L. Duclaux, A. Rubio, and P. Bernier, "Magnetic interactions in carbon nanostructures," *Carbon*, vol. 40, no. 10, pp. 1825 – 1842, 2002.

[**122**] X.-P. Tang, A. Kleinhammes, H. Shimoda, L. Fleming, K. Y. Bennoune, S. Sinha, C. Bower, O. Zhou, and Y. Wu, "Electronic Structures of Single-Walled Carbon Nanotubes Determined by NMR," *Science*, vol. 288, no. 5465, pp. 492–494, 2000.

[**123**] S. Hayashi, F. Hoshi, T. Ishikura, M. Yumura, and S. Ohshima, "13C NMR study of 13C-enriched single-wall carbon nanotubes synthesized by catalytic decomposition of methane," *Carbon*, vol. 41, no. 15, pp. 3047 – 3056, 2003.

[**124**] B. Waldschmidt, "Oberflächen-induzierte dissoziation von massenselektierten pb-clusterkationen an graphit," Master's thesis, Technical University Darmstadt, Germany, 2007.

[**125**] B. Waldschmidt, S. Barman, C. Rajesh, C. Majumder, G. P. Das, and R. Schäfer, "Energetics and fragmentation of single-doped tin and lead clusters," *Phys. Rev. B*, vol. 79, p. 045422, Jan. 2009.

[**126**] M. Turra, B. Waldschmidt, B. Kaiser, and R. Schafer, "An improved time-of-flight method for cluster deposition and ion-scattering experiments," *Review of Scientific Instruments*, vol. 79, no. 1, p. 013905, 2008.

[**127**] T. Tanaka, H. Jin, Y. Miyata, S. Fujii, H. Suga, Y. Naitoh, T. Minari, T. Miyadera, K. Tsukagoshi, and H. Kataura, "Simple and scalable gel-based separation of metallic and semiconducting carbon nanotubes," *Nano Letters*, vol. 9, pp. 1497–1500, Apr. 2009.

[**128**] S. J. Kang, C. Kocabas, T. Ozel, M. Shim, N. Pimparkar, M. A. Alam, S. V. Rotkin, and J. A. Rogers, "High-performance electronics using dense, perfectly aligned arrays of single-walled carbon nanotubes," *Nat Nano*, vol. 2, pp. 230–236, Apr. 2007.

[**129**] N. R. Franklin and H. Dai, "An enhanced CVD approach to extensive nanotube networks with directionality," *Advanced Materials*, vol. 12, no. 12, pp. 890–894, 2000.

[**130**] Z. Song, T. Cai, Z. Chang, G. Liu, J. A. Rodriguez, and J. Hrbek, "Molecular Level Study of the Formation and the Spread of MoO_3 on Au (111) by Scanning Tunneling Microscopy and X-ray Photoelectron Spectroscopy," *Journal of the American Chemical Society*, vol. 125, pp. 8059–8066, July 2003.

[**131**] S. Surnev, G. Kresse, M. G. Ramsey, and F. P. Netzer, "Novel Interface-Mediated Metastable Oxide Phases: Vanadium Oxides on Pd(111)," *Phys. Rev. Lett.*, vol. 87, pp. 086102–, Aug. 2001.

[**132**] A. D. Yoffe, "Low-dimensional systems: quantum size effects and electronic properties of semiconductor microcrystallites (zero-dimensional systems) and some quasi-two-dimensional systems," *Advances in Physics*, vol. 42, no. 2, pp. 173–262, 1993.

[**133**] L. Brus, "Electronic wave functions in semiconductor clusters: experiment and theory," *The Journal of Physical Chemistry*, vol. 90, pp. 2555–2560, June 1986.

[**134**] J. M. McHale, A. Auroux, A. J. Perrotta, and A. Navrotsky, "Surface Energies and Thermodynamic Phase Stability in Nanocrystalline Aluminas," *Science*, vol. 277, no. 5327, pp. 788–791, 1997.

[**135**] T. Bredow, E. Aprá, M. Catti, and G. Pacchioni, "Cluster and periodic ab-initio calculations on K/TiO_2(110)," *Surface Science*, vol. 418, no. 1, pp. 150 – 165, 1998.

[**136**] J. A. Rodriguez and A. Maiti, "Adsorption and Decomposition of H_2S on MgO(100), NiMgO (100), and ZnO (0001) Surfaces: A First-Principles Density Functional Study," *The Journal of Physical Chemistry B*, vol. 104, pp. 3630–3638, Apr. 2000.

[**137**] J. A. Rodriguez and M. Fernandez-Garcia, *Synthesis Properties and Applications of Oxide Nanomaterials*. wiley-interscience A john Wiley & Sons, Inc. Publication, 2007.

[**138**] Y. Wang, Z. Zhang, Y. Zhu, Z. Li, R. Vajtai, L. Ci, and P. M. Ajayan, "Nanostructured VO_2 Photocatalysts for Hydrogen Production," *ACS Nano*, vol. 2, pp. 1492–1496, July 2008.

[**139**] X. Liu, C. Täschner, A. Leonhardt, M. H. Rümmeli, T. Pichler, T. Gemming, B. Büchner, and M. Knupfer, "Structural, optical, and electronic properties of vanadium oxide nanotubes," *Phys. Rev. B*, vol. 72, pp. 115407–, Sept. 2005.

[**140**] Z. Gu, M. P. Paranthaman, J. Xu, and Z. W. Pan, "Aligned ZnO Nanorod Arrays Grown Directly on Zinc Foils and Zinc Spheres by a Low-Temperature Oxidization Method," *ACS Nano*, vol. 3, pp. 273–278, Feb. 2009.

[**141**] H. Morkoc and U. Özqür, *Zinc Oxide - Fundamental Materials and Device Technology*. Wiley-VCH Verlag GmbH & Co. KGaA, 2008.

[**142**] S. Mathur, S. Barth, H. Shen, J.-C. Pyun, and U. Werner, "Size-Dependent Photoconductance in SnO_2 Nanowires," *Small*, vol. 1, no. 7, pp. 713–717, 2005.

[**143**] J. C. Park, J. Kim, H. Kwon, and H. Song, "Gram-Scale Synthesis of Cu_2O Nanocubes and Subsequent Oxidation to CuO Hollow Nanostructures for Lithium-Ion Battery Anode Materials," *Advanced Materials*, vol. 21, no. 7, pp. 803–807, 2009.

[**144**] A. Ghicov and P. Schmuki, "Self-ordering electrochemistry: a review on growth and functionality of TiO_2 nanotubes and other self-aligned MO_x structures.," *Chemical Communications*, no. 20, pp. 2791–2808, 2009.

[**145**] B. H. Meekins and P. V. Kamat, "Got TiO_2 Nanotubes? Lithium Ion Intercalation Can Boost Their Photoelectrochemical Performance," *ACS Nano*, vol. 3, pp. 3437–3446, Nov. 2009.

[**146**] S. Brehme, F. Fenske, W. Fuhs, E. Nebauer, M. Poschenrieder, B. Selle, and I. Sieber, "Free-carrier plasma resonance effects and electron transport in reactively sputtered degenerate ZnO:Al films," *Thin Solid Films*, vol. 342, pp. 167–173, Mar. 1999.

[**147**] B. Sun and H. Sirringhaus, "Solution-processed zinc oxide field-effect transistors based on self-assembly of colloidal nanorods," *Nano Letters*, vol. 5, pp. 2408–2413, Dec. 2005.

[**148**] S. Mathur and S. Barth, "Molecule-Based Chemical Vapor Growth of Aligned SnO_2 Nanowires and Branched SnO_2/V_2O_5 Heterostructures," *Small*, vol. 3, no. 12, pp. 2070–2075, 2007.

[**149**] X. Du, Z. Mei, Z. Liu, Y. Guo, T. Zhang, Y. Hou, Z. Zhang, Q. Xue, and A. Y. Kuznetsov, "Controlled Growth of High-Quality ZnO-Based Films and Fabrication of Visible-Blind and Solar-Blind Ultra-Violet Detectors," *Advanced Materials*, vol. 21, no. 45, pp. 4625–4630, 2009.

[**150**] J. M. Macák, H. Tsuchiya, and P. Schmuki, "High-Aspect-Ratio TiO_2 Nanotubes by Anodization of Titanium," *Angewandte Chemie International Edition*, vol. 44, no. 14, pp. 2100–2102, 2005.

[**151**] J. Wang and Z. Lin, "Anodic Formation of Ordered TiO_2 Nanotube Arrays: Effects of Electrolyte Temperature and Anodization Potential," *The Journal of Physical Chemistry C*, vol. 113, pp. 4026–4030, Mar. 2009.

[**152**] A. Nattestad, A. J. Mozer, M. K. R. Fischer, Y.-B. Cheng, A. Mishra, P. Bauerle, and U. Bach, "Highly efficient photocathodes for dye-sensitized tandem solar cells," *Nat Mater*, vol. 9, pp. 31–35, Jan. 2010.

[**153**] G. K. Mor, O. K. Varghese, R. H. T. Wilke, S. Sharma, K. Shankar, T. J. Latempa, K.-S. Choi, and C. A. Grimes, "p-Type Cu-Ti-O Nanotube Arrays and Their Use in Self-Biased Heterojunction Photoelectrochemical Diodes for Hydrogen Generation," *Nano Letters*, vol. 8, pp. 1906–1911, July 2008.

[**154**] J. H. Park, S. Kim, and A. J. Bard, "Novel carbon-doped tio_2 nanotube arrays with high aspect ratios for efficient solar water splitting," *Nano Letters*, vol. 6, pp. 24–28, Jan. 2006.

[**155**] T. F. Jaramillo, S.-H. Baeck, A. Kleiman-Shwarsctein, K.-S. Choi, G. D. Stucky, and E. W. McFarland, "Automated Electrochemical Synthesis and Photoelectrochemical Characterization of $Zn_{1-x}Co_xO$ Thin Films for Solar Hydrogen Production," *Journal of Combinatorial Chemistry*, vol. 7, pp. 264–271, Mar. 2005.

[**156**] R. Jose, V. Thavasi, and S. Ramakrishna, "Metal oxides for dye-sensitized solar cells," *Journal of the American Ceramic Society*, vol. 92, no. 2, pp. 289–301, 2009.

[**157**] F. Cheng, Z. Tao, J. Liang, and J. Chen, "Template-directed materials for rechargeable lithium-ion batteries," *Chemistry of Materials*, vol. 20, pp. 667–681, Feb. 2008.

[**158**] Y. Yamaguchi, M. Yamazaki, S. Yoshihara, and T. Shirakashi, "Photocatalytic ZnO films prepared by anodizing," *Journal of Electroanalytical Chemistry*, vol. 442, pp. 1–3, Jan. 1998.

[**159**] G. R. Bamwenda, T. Uesigi, Y. Abe, K. Sayama, and H. Arakawa, "The photocatalytic oxidation of water to O_2 over pure CeO_2, WO_3, and TiO_2 using Fe^{3+} and Ce^{4+} as electron acceptors," *Applied Catalysis A: General*, vol. 205, pp. 117–128, Jan. 2001.

[**160**] O. K. Varghese, M. Paulose, T. J. LaTempa, and C. A. Grimes, "High-Rate Solar Photocatalytic Conversion of CO_2 and Water Vapor to Hydrocarbon Fuels," *Nano Letters*, vol. 9, pp. 731–737, Feb. 2009.

[**161**] J. J. Schneider, R. C. Hoffmann, J. Engstler, O. Soffke, W. Jaegermann, A. Issanin, and A. Klyszcz, "A Printed and Flexible Field-Effect Transistor Device with Nanoscale Zinc Oxide as Active Semiconductor Material," *Advanced Materials*, vol. 20, no. 18, pp. 3383–3387, 2008.

[**162**] X. Fang, Y. Bando, U. K. Gautam, C. Ye, and D. Golberg, "Inorganic semiconductor nanostructures and their field-emission applications.," *Journal of Materials Chemistry*, vol. 18, no. 5, pp. 509–522, 2008.

[**163**] M. H. Huang, S. Mao, H. Feick, H. Yan, Y. Wu, H. Kind, E. Weber, R. Russo, and P. Yang, "Room-temperature ultraviolet nanowire nanolasers," *Science*, vol. 292, no. 5523, pp. 1897–1899, 2001.

[**164**] A. P. Ramirez, "Applied physics: Oxide electronics emerge," *Science*, vol. 315, no. 5817, pp. 1377–1378, 2007.

[**165**] P. Chen, X. Ma, D. Li, Y. Zhang, and D. Yang, "Bidirectional direct-current electroluminescence from i-$Mg_xZn_{1-x}O$/n-ZnO/SiO_x double-barrier heterostructures on Si," *Applied Physics Letters*, vol. 94, no. 6, p. 061110, 2009.

[**166**] G. Sberveglieri, "Classical and novel techniques for the preparation of SnO_2 thin-film gas sensors," *Sensors and Actuators B: Chemical*, vol. 6, pp. 239–247, Jan. 1992.

[**167**] R. krishna Bhakta, *Rational Development of Precursors for MOCVD of TiO_2 : Precursor Chemistry, Thin film deposition, Mechanistic Studies.* PhD thesis, Ruhr-Universität Bochum, Deutschland., 2005.

[**168**] A. Navrotsky, J. C. Jamieson, and O. J. Kleppa, "Enthalpy of transformation of a high-pressure polymorph of titanium dioxide to the rutile modification," *Science*, vol. 158, no. 3799, pp. 388–389, 1967.

[**169**] K.-N. P. Kumar, K. Keizer, A. J. Burggraaf, T. Okubo, H. Nagamoto, and S. Morooka, "Densification of nanostructured titania assisted by a phase transformation," *Nature*, vol. 358, pp. 48–51, July 1992.

[**170**] K. Woan, G. Pyrgiotakis, and W. Sigmund, "Photocatalytic Carbon-Nanotube-TiO_2 Composites," *Advanced Materials*, vol. 21, no. 21, pp. 2233–2239, 2009.

[**171**] N. Kopidakis, E. A. Schiff, N.-G. Park, J. van de Lagemaat, and A. J. Frank, "Ambipolar Diffusion of Photocarriers in Electrolyte-Filled, Nanoporous TiO_2," *The Journal of Physical Chemistry B*, vol. 104, pp. 3930–3936, Apr. 2000.

[**172**] D. C. Hurum, K. A. Gray, T. Rajh, and M. C. Thurnauer, "Recombination Pathways in the Degussa P25 Formulation of TiO_2: Surface versus Lattice Mechanisms," *The Journal of Physical Chemistry B*, vol. 109, pp. 977–980, Jan. 2005.

[**173**] D. C. Hurum, A. G. Agrios, K. A. Gray, T. Rajh, and M. C. Thurnauer, "Explaining the Enhanced Photocatalytic Activity of Degussa P25 Mixed-Phase TiO_2 Using EPR," *The Journal of Physical Chemistry B*, vol. 107, pp. 4545–4549, May 2003.

[**174**] D. Hurum, A. Agrios, S. Crist, K. Gray, T. Rajh, and M. Thurnauer, "Probing reaction mechanisms in mixed phase TiO_2 by EPR," *Journal of Electron Spectroscopy and Related Phenomena*, vol. 150, pp. 155–163, Feb. 2006.

[**175**] O. Carp, C. L. Huisman, and A. Reller, "Photoinduced reactivity of titanium dioxide," *Progress in Solid State Chemistry*, vol. 32, no. 1-2, pp. 33–177, 2004.

[**176**] S. K. Poznyak, A. I. Kokorin, and A. I. Kulak, "Effect of electron and hole acceptors on the photoelectrochemical behaviour of nanocrystalline microporous tio_2 electrodes," *Journal of Electroanalytical Chemistry*, vol. 442, pp. 99–105, Jan. 1998.

[**177**] M. Rincón, J. Molina, M. Sánchez, C. Arancibia, and E. Garcia, "Optical characterization of tandem absorber/reflector systems based on titanium oxide-carbon coatings," *Solar Energy Materials and Solar Cells*, vol. 91, pp. 1421–1425, Sept. 2007.

[**178**] A. C. Jones and P. R. Chalker, "Some recent developments in the chemical vapour deposition of electroceramic oxides," *Journal of Physics D: Applied Physics*, vol. 36, no. 6, p. R80, 2003.

[**179**] R. van de Krol, A. Goossens, and J. Schoonman, "Mott-Schottky Analysis of Nanometer-Scale Thin-Film Anatase TiO_2," *J. Electrochem. Soc.*, vol. 144, pp. 1723–1727, May 1997.

[**180**] A. Smith and R. Rodriguez-Clemente, "Morphological differences in zno films deposited by the pyrosol technique: effect of hcl," *Thin Solid Films*, vol. 345, pp. 192–196, May 1999.

[**181**] I. A. Md and S. S. Bhattacharya, "Effect of process parameters on the chemical vapour synthesis of nanocrystalline titania," *Journal of Physics D: Applied Physics*, vol. 41, no. 15, p. 155313, 2008.

[**182**] A. Ghicov, H. Tsuchiya, J. M. Macak, and P. Schmuki, "Titanium oxide nanotubes prepared in phosphate electrolytes," *Electrochemistry Communications*, vol. 7, pp. 505–509, May 2005.

[**183**] T.-S. Kang, A. P. Smith, B. E. Taylor, and M. F. Durstock, "Fabrication of Highly-Ordered TiO_2 Nanotube Arrays and Their Use in Dye-Sensitized Solar Cells," *Nano Letters*, vol. 9, pp. 601–606, Feb. 2009.

[**184**] I. A. Md., S. S. Bhattacharya, and H. Hahn, "Structure, thermal stability, and optical properties of boron modified nanocrystalline anatase prepared by chemical vapor synthesis," *J. Appl. Phys.*, vol. 105, pp. 113526–8, June 2009.

[**185**] D. Buso, M. Post, C. Cantalini, P. Mulvaney, and A. Martucci, "Gold Nanoparticle-Doped TiO_2 Semiconductor Thin Films: Gas Sensing Properties," *Advanced Functional Materials*, vol. 18, no. 23, pp. 3843–3849, 2008.

[**186**] M. R. Hoffmann, S. T. Martin, W. Choi, and D. W. Bahnemann, "Environmental applications of semiconductor photocatalysis," *Chemical Reviews*, vol. 95, pp. 69–96, Jan. 1995.

[**187**] W. Wang, P. Serp, P. Kalck, and J. L. Faria, "Visible light photodegradation of phenol on MWNT-TiO_2 composite catalysts prepared by a modified sol-gel method," *Journal of Molecular Catalysis A: Chemical*, vol. 235, pp. 194–199, July 2005.

[**188**] C. Klingshirn, "ZnO: From basics towards applications," *physica status solidi (b)*, vol. 244, no. 9, pp. 3027–3073, 2007.

[**189**] T. Makino, K. Tamura, C. Chia, Y. Segawa, M. Kawasaki, A. Ohtomo, and H. Koinuma, "Optical Properties of ZnO:Al Epilayers and of Undoped Epilayers Capped by Wider-Gap MgZnO Grown by Laser MBE," *physica status solidi (b)*, vol. 229, no. 2, pp. 853–857, 2002.

[**190**] Y. R. Ryu, T. S. Lee, J. A. Lubguban, A. B. Corman, H. W. White, J. H. Leem, M. S. Han, Y. S. Park, C. J. Youn, and W. J. Kim, "Wide-band gap oxide alloy: BeZnO," *Appl. Phys. Lett.*, vol. 88, pp. 052103–2, Jan. 2006.

[**191**] Y. S. Choi, C. G. Lee, and S. M. Cho, "Transparent conducting $Zn_xCd_{1-x}O$ thin films prepared by the sol-gel process," *Thin Solid Films*, vol. 289, pp. 153–158, Nov. 1996.

[**192**] D. C. Look and B. Claflin, "P-type doping and devices based on ZnO," *physica status solidi (b)*, vol. 241, no. 3, pp. 624–630, 2004.

[**193**] A. Dadgar, N. Oleynik, J. Bläsing, S. Deiter, D. Forster, F. Bertram, A. Diez, M. Seip, A. Greiling, J. Christen, and A. Krost, "Heteroepitaxy and nitrogen doping of high-quality ZnO," *Journal of Crystal Growth*, vol. 272, pp. 800–804, Dec. 2004.

[**194**] K. Minegishi, Y. Koiwai, Y. Kikuchi, K. Yano, M. Kasuga, and A. Shimizu, "Growth of p-type zinc oxide films by chemical vapor deposition," *Jpn. J. Appl. Phys.*, vol. 36, no. Part 2, No. 11A, p. L1453, 1997.

[**195**] C. Jagadish and S. Pearton, eds., *ZInc Oxide Bulk, Thin films and Nanostructures*. Elsevier, 2006.

[**196**] Y. Hu, Y. Gao, S. Singamaneni, V. V. Tsukruk, and Z. L. Wang, "Converse piezoelectric effect induced transverse deflection of a free-standing zno microbelt," *Nano Letters*, vol. 9, pp. 2661–2665, July 2009.

[**197**] Y. Qin, X. Wang, and Z. L. Wang, “Microfibre-nanowire hybrid structure for energy scavenging,” *Nature*, vol. 451, pp. 809–813, Feb. 2008.

[**198**] Q. Zhang, C. S. Dandeneau, X. Zhou, and G. Cao, “ZnO Nanostructures for Dye-Sensitized Solar Cells,” *Advanced Materials*, vol. 21, no. 41, pp. 4087–4108, 2009.

[**199**] A. Nadarajah, R. C. Word, J. Meiss, and R. Konenkamp, “Flexible inorganic nanowire light-emitting diode,” *Nano Letters*, vol. 8, pp. 534–537, Feb. 2008.

[**200**] K. C. Jin Hyung Jun, Byoungjun Park and S. Kim, “Flexible TFTs based on solution-processed ZnO nanoparticles,” *Nanotechnology*, vol. 20, no. 50, p. 505201, 2009.

[**201**] Y.-K. Chang and F. C.-N. Hong, “The fabrication of ZnO nanowire field-effect transistors by roll-transfer printing,” *Nanotechnology*, vol. 20, no. 19, p. 195302, 2009.

[**202**] Y. I. Alivov, D. C. Look, B. M. Ataev, M. V. Chukichev, V. V. Mamedov, V. I. Zinenko, Y. A. Agafonov, and A. N. Pustovit, “Fabrication of ZnO-based metal-insulator-semiconductor diodes by ion implantation,” *Solid-State Electronics*, vol. 48, pp. 2343–2346, Dec. 2004.

[**203**] J. Khanderi, R. C. Hoffmann, A. Gurlo, and J. J. Schneider, “Synthesis and sensoric response of ZnO decorated carbon nanotubes.,” *Journal of Materials Chemistry*, vol. 19, no. 28, pp. 5039–5046, 2009.

[**204**] P. Majewski and B. Thierry, “Functionalized Magnetite Nanoparticles: Synthesis, Properties, and Bio-Applications,” *Critical Reviews in Solid State and Materials Sciences*, vol. 32, no. 3, pp. 203–215, 2007.

[**205**] S. Klotz, G. Steinle-Neumann, T. Strässle, J. Philippe, T. Hansen, and M. J. Wenzel, “Magnetism and the Verwey transition in Fe_3O_4 under pressure,” *Phys. Rev. B*, vol. 77, pp. 012411–, Jan. 2008.

[**206**] R. Mantovan, A. Lamperti, M. Georgieva, G. Tallarida, and M. Fanciulli, “Cvd synthesis of polycrystalline magnetite thin films: structural, magnetic and magnetotransport properties,” *Journal of Physics D: Applied Physics*, vol. 43, no. 6, p. 065002, 2010.

[**207**] X. Sun, C. Zheng, F. Zhang, Y. Yang, G. Wu, A. Yu, and N. Guan, "Size-Controlled Synthesis of Magnetite (Fe_3O_4) Nanoparticles Coated with Glucose and Gluconic Acid from a Single Fe(III) Precursor by a Sucrose Bifunctional Hydrothermal Method," *The Journal of Physical Chemistry C*, vol. 113, pp. 16002–16008, Sept. 2009.

[**208**] A. S. Teja and P.-Y. Koh, "Synthesis, properties, and applications of magnetic iron oxide nanoparticles," *Progress in Crystal Growth and Characterization of Materials*, vol. 55, pp. 22–45, Mar. 2009.

[**209**] D. S. Yi Liu, David J. Sellmyer, ed., *Handbook of advanced magnetic materials*. Springer Science+Business Media, Inc., 2006.

[**210**] M. Das, P. Dhak, S. Gupta, D. Mishra, T. K. Maiti, A. Basak, and P. Pramanik, "Highly biocompatible and water-dispersible, amine functionalized magnetite nanoparticles, prepared by a low temperature, air-assisted polyol process: a new platform for bio-separation and diagnostics," *Nanotechnology*, vol. 21, no. 12, p. 125103, 2010.

[**211**] Y. Lee, M. A. Garcia, N. A. Frey Huls, and S. Sun, "Synthetic Tuning of the Catalytic Properties of Au-Fe_3O_4 Nanoparticles," *Angewandte Chemie*, vol. 122, no. 7, pp. 1293–1296, 2010.

[**212**] D. Weller and A. Moser, "Thermal effect limits in ultrahigh-density magnetic recording," *Magnetics, IEEE Transactions on DOI - 10.1109/20.809134*, vol. 35, no. 6, pp. 4423–4439, 1999.

[**213**] X. Wang, J. Zhuang, Q. Peng, and Y. Li, "A general strategy for nanocrystal synthesis," *Nature*, vol. 437, pp. 121–124, Sept. 2005.

[**214**] A. Faiyas, E. Vinod, J. Joseph, R. Ganesan, and R. Pandey, "Dependence of pH and surfactant effect in the synthesis of magnetite (Fe_3O_4) nanoparticles and its properties," *Journal of Magnetism and Magnetic Materials*, vol. 322, pp. 400–404, Feb. 2010.

[**215**] H. Yu, Z. Zhang, M. Han, X. Hao, and F. Zhu, "A General Low-Temperature Route for Large-Scale Fabrication of Highly Oriented ZnO Nanorod/Nanotube Arrays," *Journal of the American Chemical Society*, vol. 127, pp. 2378–2379, Mar. 2005.

[**216**] V. L. Pushparaj, L. Ci, S. Sreekala, A. Kumar, S. Kesapragada, D. Gall, O. Nalamasu, A. M. Pulickel, and J. Suhr, "Effects of compressive strains on electrical conductivities of a macroscale carbon nanotube block," *Applied Physics Letters*, vol. 91, no. 15, p. 153116, 2007.

[**217**] J. Li, R. Stevens, L. Delzeit, H. T. Ng, A. Cassell, J. Han, and M. Meyyappan, "Electronic properties of multiwalled carbon nanotubes in an embedded vertical array," *Applied Physics Letters*, vol. 81, no. 5, pp. 910–912, 2002.

[**218**] J. Zhang, M. Li, Z. Feng, J. Chen, and C. Li, "UV Raman Spectroscopic Study on TiO_2. I. Phase Transformation at the Surface and in the Bulk," *The Journal of Physical Chemistry B*, vol. 110, pp. 927–935, Jan. 2006.

[**219**] A. G. Roca, J. F. Marco, M. d. P. Morales, and C. J. Serna, "Effect of nature and particle size on properties of uniform magnetite and maghemite nanoparticles," *The Journal of Physical Chemistry C*, vol. 111, pp. 18577–18584, Dec. 2007.

[**220**] C. Vogel, "schiff-base komplexe der uebergangsmetalle (cr, mn, fe, co und ni) sowie seltenerdmetalle (la, ce, eu und yb) als molekulare vorlaeufer fuer metalloxide," Master's thesis, Technical University Darmstadt, Germany, 2010.

[**221**] M. R. Hill, A. W. Jones, J. J. Russell, N. K. Roberts, and R. N. Lamb, "Towards new precursors for ZnO thin films by single source CVD: the X-ray structures and precursor properties of zinc ketoacidoximates," *Inorganica Chimica Acta*, vol. 358, no. 1, pp. 201 – 206, 2005.

[**222**] I. Chamritski and G. Burns, "Infrared- and raman-active phonons of magnetite, maghemite, and hematite: A computer simulation and spectroscopic study," *The Journal of Physical Chemistry B*, vol. 109, pp. 4965–4968, Mar. 2005.

[**223**] D. Brion, "Etude par spectroscopie de photoelectrons de la degradation superficielle de FeS_2, $CuFeS_2$, ZnS et PbS a l'air et dans l'eau," *Applications of Surface Science*, vol. 5, no. 2, pp. 133 – 152, 1980.

[**224**] N. S. McIntyre and D. G. Zetaruk, "X-ray photoelectron spectroscopic studies of iron oxides," *Analytical Chemistry*, vol. 49, pp. 1521–1529, Sept. 1977.

[**225**] C. Nick, “Elektrische stimulation von biologischen, neuronalen netzwerken,” Master’s thesis, HOCHSCHULE ASCHAFFENBURG, 2009.

[**226**] E. Kandel, J. Schwartz, and T. Jessell, eds., *Principles of Neural Science, Fourth Edition*. McGraw-Hill, Health Professions Division, 2000.

[**227**] H. Hu, Y. Ni, V. Montana, R. C. Haddon, and V. Parpura, “Chemically functionalized carbon nanotubes as substrates for neuronal growth,” *Nano Letters*, vol. 4, pp. 507–511, Mar. 2004.

[**228**] T. Hiraoka, T. Yamada, K. Hata, D. N. Futaba, H. Kurachi, S. Uemura, M. Yumura, and S. Iijima, “Synthesis of single- and double-walled carbon nanotube forests on conducting metal foils,” *Journal of the American Chemical Society*, vol. 128, pp. 13338–13339, Oct. 2006.

[**229**] M. Endo, M. Strano, and P. Ajayan, *Carbon Nanotubes*, ch. Potential Applications of Carbon Nanotubes, pp. 13–61. Topics in Applied Physics, 2008.

[**230**] J.-M. Bonard, M. Croci, C. Klinke, R. Kurt, O. Noury, and N. Weiss, “Carbon nanotube films as electron field emitters,” *Carbon*, vol. 40, no. 10, pp. 1715 – 1728, 2002.

[**231**] J.-M. Bonard, J.-P. Salvetat, T. Stockli, W. A. de Heer, L. Forro, and A. Chatelain, “Field emission from single-wall carbon nanotube films,” *Applied Physics Letters*, vol. 73, no. 7, pp. 918–920, 1998.

[**232**] M. Shim, A. Javey, N. W. Shi Kam, and H. Dai, “Polymer functionalization for air-stable n-type carbon nanotube field-effect transistors,” *Journal of the American Chemical Society*, vol. 123, pp. 11512–11513, Nov. 2001.

[**233**] A. Bachtold, P. Hadley, T. Nakanishi, and C. Dekker, “Logic circuits with carbon nanotube transistors,” *Science*, vol. 294, no. 5545, pp. 1317–1320, 2001.

[**234**] Y. Lu, J. Li, J. Han, H.-T. Ng, C. Binder, C. Partridge, and M. Meyyappan, “Room temperature methane detection using palladium loaded single-walled carbon nanotube sensors,” *Chemical Physics Letters*, vol. 391, no. 4-6, pp. 344 – 348, 2004.

[**235**] J. Li, Y. Lu, Q. Ye, M. Cinke, J. Han, and M. Meyyappan, “Carbon nanotube sensors for gas and organic vapor detection,” *Nano Letters*, vol. 3, pp. 929–933, July 2003.

[**236**] S. Kim, S. Pal, P. M. Ajayan, T. Borca-Tasciuc, and N. Koratkar, "Electrical breakdown gas detector featuring carbon nanotube array electrodes," *Journal of Nanoscience and Nanotechnology*, vol. 8, pp. 416–419, 2008.

[**237**] J. Kong, N. R. Franklin, C. Zhou, M. G. Chapline, S. Peng, K. Cho, and H. Dai, "Nanotube Molecular Wires as Chemical Sensors," *Science*, vol. 287, no. 5453, pp. 622–625, 2000.

[**238**] A. Sinitskii, S. Neumeier, J. Nelles, M. Fischler, and U. Simon, "Ordered arrays of silicon pillars with controlled height and aspect ratio," *Nanotechnology*, vol. 18, no. 30, p. 305307, 2007.

[**239**] A. Daus and C. Thielemann, "Spheroids on microelectrode arrays: A highly sensitive system for biosensing applications," *European Journal of Cell Biology*, vol. 89(S1), pp. 67–68, 2010.